galenos
yayınevi

TURKISH SOCIETY OF NUCLEAR MEDICINE
1975

Scientific Advisory Board

MIRT

Molecular Imaging and Radionuclide Therapy

Maria Lyra Georgosopoulou
University of Athens, 1st Department of Radiology, Aretaieion Hospital, Radiation Physics Unit, Athens, Greece

Gevorg Gevorgyan
The National Academy of Sciences of Armenia, H. Buniatian Institute of Biochemistry, Yerevan, Armenia

Seza Güleç
Florida International University Herbert Wertheim College of Medicine, Departments of Surgery and Nuclear Medicine, Miami, USA

Liselotte Højgaard
University of Copenhagen, Department of Clinical Physiology, Nuclear Medicine and PET, Rigshospitalet, Copenhagen, Denmark

Ora Israel
Tel Aviv University Sackler Medical School, Assaf Harofeh Medical Center, Clinic of Otolaryngology-Head and Neck Surgery, Haifa, Israel

Csaba Juhasz
Wayne State University Medical School, Children's Hospital of Michigan, PET Center and Translational Imaging Laboratory, Detroit, USA

Gamze Çapa Kaya
Dokuz Eylül University, Medical School, Department of Nuclear Medicine, İzmir, Turkey

Metin Kır
Ankara University, Medical School, Department of Nuclear Medicine, Ankara, Turkey

Irena Dimitrova Kostadinova
Alexandrovska University Hospital, Clinic of Nuclear Medicine, Sofia, Bulgaria

Lale Kostakoğlu
The Mount Sinai Hospital, Clinic of Nuclear Medicine, New York, USA

Rakesh Kumar
All India Institute of Medical Sciences, Department of Nuclear Medicine, New Delhi, India

Georgios S. Limouris
Athens University, Medical School, Department of Nuclear Medicine, Athens, Greece

Luigi Mansi
Second University of Naples, Medical School, Department of Nuclear Medicine, Naples, Italy

Yusuf Menda
University of Iowa Health Care, Carver College of Medicine, Department of Radiology, Iowa City, USA

Vladimir Obradović
University of Belgrade, Faculty of Organizational Sciences, Department of Human Development Theory, Business Administration, Organizational Studies, Belgrade, Serbia

Zehra Özcan
Ege University Faculty of Medicine, Department of Nuclear Medicine, İzmir, Turkey

Yekta Özer
Hacettepe University, Faculty of Pharmacy, Department of Radiopharmaceutical, Ankara, Turkey

Francesca Pons
Hospital Clinic, Clinic of Nuclear Medicine, Barcelona, Spain

Monica Rossleigh
Sydney Children's Hospital, Clinic of Nuclear Medicine, Sydney, Australia

Dragana Sobic Saranovic
University of Belgrade, Medical School, Departments of Radiology, Oncology and Cardiology, Belgrade, Serbia

Mike Sathekge
University of Pretoria, Steve Biko Academic Hospital, Department of Nuclear Medicine, Pretoria, South Africa

Kerim Sönmezoğlu
İstanbul University, Cerrahpaşa Medical School, Department of Nuclear Medicine, İstanbul, Turkey

Zsolt Szabo
The Johns Hopkins Hospital, Divisions of Radiology and Radiological Science, Baltimore, USA

Istvan Szilvasi
Semmelweis University, Medical School, Department of Nuclear Medicine, Budapest, Hungary

Berna Okudan Tekin
Ankara Numune Trainig and Research Hospital, Clinic of Nuclear Medicine, Ankara, Turkey

Mathew L. Thakur
Thomas Jefferson University, Department of Radiology, Pennsylvania, USA

Bülent Turgut
Cumhuriyet University, Medical School, Department of Nuclear Medicine, Sivas, Turkey

Turgut Turoğlu
Marmara University, Medical School, Department of Nuclear Medicine, İstanbul, Turkey

Gülin Uçmak
University of Health Sciences Turkey, Ankara Oncology Training and Research Hospital, Clinic of Nuclear Medicine, Ankara,Turkey

Doğangün Yüksel
Pamukkale University, Medical School, Department of Nuclear Medicine, Denizli, Turkey

ABOUT US

Molecular Imaging and Radionuclide Therapy (formerly Turkish Journal of Nuclear Medicine) is the official publication of Turkish Society of Nuclear Medicine.

Focus and Scope

Molecular Imaging and Radionuclide Therapy (Mol Imaging Radionucl Ther, MIRT) is a double-blind peer-review journal published in English language. It publishes original research articles, invited reviews, editorials, short communications, letters, consensus statements, guidelines and case reports with a literature review on the topic, in the field of molecular imaging, multimodality imaging, nuclear medicine, radionuclide therapy, radiopharmacy, medical physics, dosimetry and radiobiology. MIRT is published three times a year (February, June, October). Audience: Nuclear medicine physicians, medical physicists, radiopharmaceutical scientists, radiobiologists.

The editorial policies are based on the "Recommendations for the Conduct, Reporting, Editing, and Publication of Scholarly Work in Medical Journals (ICMJE Recommendations)" by the International Committee of Medical Journal Editors (2016, archived at http://www.icmje.org/) rules.

Molecular Imaging and Radionuclide Therapy is indexed in **Pubmed, Pubmed Central (PMC), Emerging Sources Citation Index (ESCI), TUBITAK-ULAKBIM, DOAJ, Scopus, Gale/Cengage Learning, EBSCO databases, Embase, ProQuest Health & Medical Complete, CINAHL, Index Copernicus, J-Gate, IdealOnline, ROOT INDEXING, Türkiye Atıf Dizini-Turkiye Citation Index, Turk Medline, EuroPub, Hinari, GOALI, ARDI, OARE** and **AGORA.**

Open Access Policy

This journal provides immediate open access to its content on the principle that making research freely available to the public supports a greater global exchange of knowledge.

Open Access Policy is based on rules of Budapest Open Access Initiative (BOAI) (http://www.budapestopenaccessinitiative.org/). By "open access" to [peer-reviewed research literature], we mean its free availability on the public internet, permitting any users to read, download, copy, distribute, print, search, or link to the full texts of these articles, crawl them for indexing, pass them as data to software, or use them for any other lawful purpose, without financial, legal, or technical barriers other than those inseparable from gaining access to the internet itself. The only constraint on reproduction and distribution, and the only role for copyright in this domain, should be to give authors control over the integrity of their work and the right to be properly acknowledged and cited.

Subscription Information

Manuscripts can only be submitted electronically through the Journal Agent website (http://www.journalagent.com/mirt/?plng=eng) after creating an account. This system allows online submission and review.

All published volumes in full text can be reached free of charge through the website http://mirt.tsnmjournals.org

Copyight Statement

Turkish Society of Nuclear Medicine holds the international copyright of all the content published in the journal.

Republication and reproduction of images or tables in any published material should be done with proper citation of source providing authors names; article title; journal title; year (volume) and page of publication; copyright year of the article.

The author(s) hereby affirms that the manuscript submitted is original, that all statement asserted as facts are based on author(s) careful investigation and research for accuracy, that the manuscript does not, in whole or part, infringe any copyright, that it has not been published in total or in part and is not being submitted or considered for publication in total or in part elsewhere.

Completed Copyright Statement form should be submitted to the online article system.

By signing this form,

1. Each author acknowledge that he/she participated in the work in a substantive way and is prepared to take public responsibility for the work.

2. Each author further affirms that he or she has read and understands the "Ethical Guidelines for Publication of Research".

3. The author(s), in consideration of the acceptance of the manuscript for publication, does hereby assign and transfer to the Molecular Imaging and Radionuclide Therapy all of the rights and interest in and the copyright of the work in its current form and in any form subsequently revised for publication and/or electronic dissemination.

This work is licensed under a Creative Commons Attribution-NonCommercial-NoDerivatives 4.0 International License.

Instructions for Authors

Instructions for authors are published in the journal and on the website http://mirt.tsnmjournals.org

Material Disclaimer

Scientific and legal responsibilities pertaining to the papers belong to the authors. Contents of the manuscripts and accuracy of references are also the author's responsibility. The Turkish Society of Nuclear Medicine, the Editor, the Editorial Board or the publisher do not accept any responsibility for opinions expressed in articles.

Financial expenses of the journal are covered by Turkish Society of Nuclear Medicine.

Correspondence Address

Editor in Chief Prof. Murat Fani Bozkurt, MD, FEBNM Hacettepe University, Medical School, Department of Nuclear Medicine, Ankara, Turkey

E-mail: fanibozkurt@gmail.com

Web page: http://mirt.tsnmjournals.org/

Publisher Corresponding Address

Galenos Yayınevi Tic. Ltd. Şti.
Address: Molla Gürani Mah. Kaçamak Sk. No: 21/1 34093 Fındıkzade, İstanbul, Turkey
Phone: +90 212 621 99 25
Fax: +90 212 621 99 27
E-mail: info@galenos.com.tr

INSTRUCTIONS TO AUTHORS

Molecular Imaging and Radionuclide Therapy (Mol Imaging Radionucl Ther, MIRT) publishes original research articles, short communications, invited reviews, editorials, case reports with a literature review on the topic, interesting images, consensus statements, guidelines, letters in the field of molecular imaging, multimodality imaging, nuclear medicine, radionuclide therapy, radiopharmacy, medical physics, dosimetry and radiobiology. MIRT is published by the Turkish Society of Nuclear Medicine three times a year (February, June, October).

Molecular Imaging and Radionuclide Therapy does not charge any article submission or processing fees.

GENERAL INFORMATION

MIRT commits to rigorous peer review, and stipulates freedom from commercial influence, and promotion of the highest ethical and scientific standards in published articles. Neither the Editor(s) nor the publisher guarantees, warrants or endorses any product or service advertised in this publication. All articles are subject to review by the editors and peer reviewers. If the article is accepted for publication, it may be subjected to editorial revisions to aid clarity and understanding without changing the data presented.

Manuscripts must be written in English and must meet the requirements of the journal. The journal is in compliance with the uniform requirements for manuscripts submitted to biomedical journals published by the International Committee of Medical Journal Editors (NEJM 1997; 336:309-315, updated 2016). Manuscripts that do not meet these requirements will be returned to the author for necessary revision before the review. Authors of manuscripts requiring modifications have a maximum of two months to resubmit the revised text. Manuscripts returned after this deadline will be treated as new submissions.

It is the authors' responsibility to prepare a manuscript that meets ethical criteria. The Journal adheres to the principles set forth in the Helsinki Declaration October 2013 (https://www.wma.net/policies-post/wma-declaration-of-helsinki-ethical-principles-for-medical-research-involving-human-subjects/) and holds that all reported research involving "Human beings" conducted in accordance with such principles.

Reports describing data obtained from research conducted in human participants must contain a statement in the MATERIALS AND METHODS section indicating approval by the ethical review board (including the approval number) and affirmation that INFORMED CONSENT was obtained from each participant.

All manuscripts reporting experiments using animals must include a statement in the MATERIALS AND METHODS section giving assurance that all animals have received humane care in compliance with the Guide for the Care and Use of Laboratory Animals (www.nap.edu) and indicating approval by the ethical review board.

If the study should have ethical approval, authors asked to provide ethical approval in order to proceed the review process. If they provide approval, review of the manuscript will continue.

In case report(s) and interesting image(s) a statement regarding the informed consent of the patients should be included in the manuscript and the identity of the patient(s) should be hidden.

Subjects must be identified only by number or letter, not by initials or names. Photographs of patients' faces should be included only if scientifically relevant. Authors must obtain written consent from the patient for use of such photographs. In cases of image media usage that potentially expose patients' identity requires obtaining permission for publication from the patients or their parents/guardians. If the proposed publication concerns any commercial product, the author must include in the cover letter a statement indicating that the author(s) has (have) no financial or other interest with the product or explaining the nature of any relations (including consultancies) between the author(s) and editor the manufacturer or distributor of the product.

All submissions will be screened by Crossref Smilarity Check powered by "iThenticate". Manuscripts with an overall similarity index of greater than 25%, or duplication rate at or higher than 5% with a single source will be returned back to authors.

MANUSCRIPT CATEGORIES

1. Original Articles

2. Short Communications are short descriptions of focused studies with important, but very straightforward results.

3. Reviews address important topics in the field. Authors considering the submission of uninvited reviews should contact the editor in advance to determine if the topic that they propose is of current potential interest to the Journal. Reviews will be considered for publication only if they are written by authors who have at least three published manuscripts in the international peer reviewed journals and these studies should be cited in the review. Otherwise only invited reviews will be considered for peer review from qualified experts in the area.

4. Editorials are usually written by invitation of the editor by the editors on current topics or by the reviewers involved in the evaluation of a submitted manuscript and published concurrently with that manuscript.

5. Case Report and Literature Reviews are descriptions of a case or small number of cases revealing a previously undocumented disease process, a unique unreported manifestation or treatment of a known disease process, unique unreported complications of treatment regimens or novel and important insights into a condition's pathogenesis, presentation, and/or management. The journal's policy is to accept case reports only if it is accompanied by a review of the literature on the related topic. They should include an adequate number of images and figures.

6. Interesting Image

One of the regular parts of Molecular Imaging and Radionuclide Therapy is a section devoted to interesting images. Interesting image(s) should describe case(s) which are unique and include interesting findings adding insights into the interpretation of patient images, a condition's pathogenesis, presentation, and/or management.

7. Consensus Statements or Guidelines may be submitted by professional societies. All such submissions will be subjected to peer review, must be modifiable in response to criticisms, and will be published only if they meet the Journal's usual editorial standards.

8. Letters to the Editor may be submitted in response to work that has been published in the Journal. Letters should be short commentaries related to specific points of agreement or disagreement with the published work.

Note on Prior Publication

Articles are accepted for publication on the condition that they are original, are not under consideration by another journal, or have not been previously published. Direct quotations, tables, or illustrations that have appeared in

INSTRUCTIONS TO AUTHORS

copyrighted material must be accompanied by written permission for their use from the copyright owner and authors. Materials previously published in whole or in part shall not be considered for publication. At the time of submission, authors must report that the manuscript has not been published elsewhere. Abstracts or posters displayed at scientific meetings need not be reported.

MANUSCRIPT SUBMISSION PROCEDURES

MIRT only accepts electronic manuscript submission at the web site http://www.journalagent.com/mirt/. After logging on to the website Click the 'online manuscript submission' icon. All corresponding authors should be provided with a password and a username after entering the information required. If you already have an account from a previous submission, enter your username and password to submit a new or revised manuscript. If you have forgotten your username and/or password, please send an e-mail to the editorial office for assistance. After logging on to the article submission system please read carefully the directions of the system to give all needed information and attach the manuscript, tables and figures and additional documents.

All Submissions Must Include:

1. Completed Copyright Assignment & Disclosure of Potential Conflict of Interest Form; This form should be downloaded from the website (provided in the author section), filled in thoroughly and uploaded to the website during the submission.

2. All manuscripts describing data obtained from research conducted in human participants must be accompanied with an approval document by the ethical review board.

3. All manuscripts reporting experiments using animals must include approval document by the animal ethical review board.

4. All submissions must include the authorship contribution form which is signed by all authors.

Authors must complete all online submission forms. If you are unable to successfully upload the files please contact the editorial office by e-mail.

MANUSCRIPT PREPARATION

General Format

The Journal requires that all submissions be submitted according to these guidelines:

• Text should be double spaced with 2.5 cm margins on both sides using 12-point type in Times Roman font.

• All tables and figures must be placed after the text and must be labeled.

• Each section (abstract, text, references, tables, figures) should start on a separate page.

• Manuscripts should be prepared as a word document (*.doc) or rich text format (*.rtf).

• Please make the tables using the table function in Word.

• Abbreviations should be defined in parenthesis where the word is first mentioned and used consistently thereafter.

• Results should be expressed in metric units. Statistical analysis should be done accurately and with precision. Please consult a statistician if necessary.

• Authors' names and institutions should not be included in the manuscript text and should be written only in the title page.

Title Page

The title page should be a separate form from the main text and should include the following:

• Full title (in English and in Turkish). Turkish title will be provided by the editorial office for the authors who are not Turkish speakers.

• Authors' names and institutions.

• Short title of not more than 40 characters for page headings.

• At least three and maximum eight keywords. (in English and in Turkish). Do not use abbreviations in the keywords. Turkish keywords will be provided by the editorial office for the authors who are not Turkish speakers. If you are not a native Turkish speaker, please reenter your English keywords to the area provided for the Turkish keywords. English keywords should be provided from http://www.nlm.nih.gov/mesh (Medical Subject Headings) while Turkish keywords should be provided from http://www.bilimterimleri.com.

• Word count (excluding abstract, figure legends and references).

• Corresponding author's e-mail and address, telephone and fax numbers.

• Name and address of person to whom reprint requests should be addressed.

Original Articles

Authors are required to state in their manuscripts that ethical approval from an appropriate committee and informed consents of the patients were obtained.

Original Articles should be submitted with a structured abstract of no more than 250 words. All information reported in the abstract must appear in the manuscript. The abstract should not include references. Please use complete sentences for all sections of the abstract. Structured abstract should include background, objective, methods, results and conclusions. Turkish abstract will be provided by the editorial office for the authors who are not Turkish speakers. If you are not a native Turkish speaker, please reenter your English abstract to the area provided for the Turkish abstract.

- Introduction
- Materials and Methods
- Results
- Discussion
- Study Limitations
- Conclusion

May be given for contributors who are not listed as authors, or for grant support of the research.

References should be cited in numerical order (in parentheses) in the text and listed in the same numerical order at the end of the manuscript on a separate page or pages. The author is responsible for the accuracy of references. Examples of the reference style are given below. Further examples will be found in the articles describing the Uniform Requirements for Manuscripts Submitted to Biomedical Journals (Ann Intern Med.1988; 208:258-265, Br Med J. 1988; 296:401-405). The titles of journals should be abbreviated according to the style used in the Index Medicus. Journal Articles and Abstracts: Surnames and initials of author's name, title of the article, journal name, date, volume number, and pages. All authors should be listed regardless of number. The citation of unpublished papers, observations or personal communications is not permitted. Citing an abstract is not recommended. Books: Surnames and initials of author's names, chapter title, editor's name, book title, edition, city, publisher, date and pages.

INSTRUCTIONS TO AUTHORS

Sample References

Journal Article: Sayit E, Söylev M, Capa G, Durak I, Ada E, Yilmaz M. The role of technetium-99m-HMPAO-labeled WBC scintigraphy in the diagnosis of orbital cellulitis. Ann Nucl Med 2001;15:41-44.

Erselcan T, Hasbek Z, Tandogan I, Gumus C, Akkurt I. Modification of Diet in Renal Disease equation in the risk stratification of contrast induced acute kidney injury in hospital inpatients. Nefrologia 2009 doi: 10.3265/Nefrologia.2009.29.5.5449.en.full.

Article in a journal published ahead of print: Ludbrook J. Musculovenous pumps in the human lower limb. Am Heart J 2009;00:1-6. (accessed 20 February 2009).

Lang TF, Duryea J. Peripheral Bone Mineral Assessment of the Axial Skeleton: Technical Aspects. In: Orwoll ES, Bliziotes M (eds). Osteoporosis: Pathophsiology and Clinical Management. New Jersey, Humana Pres Inc, 2003;83-104.

Books: Greenspan A. Orthopaedic Radiology a Pratical Approach. 3th ed. Philadelphia, Lippincott Williams Wilkins 2000, 295-330.

Website: Smith JR. 'Choosing Your Reference Style', Online Referencing 2(3), http://orj.sagepub.com (200, accessed October 2008).

- Tables

Tables must be constructed as simply as possible. Each table must have a concise heading and should be submitted on a separate page. Tables must not simply duplicate the text or figures. Number all tables in the order of their citation in the text. Include a title for each table (a brief phrase, preferably no longer than 10 to 15 words). Include all tables in a single file following the manuscript.

– Figure Legends

Figure legends should be submitted on a separate page and should be clear and informative.

– Figures

Number all figures (graphs, charts, photographs, and illustrations) in the order of their citation in the text. At submission, the following file formats are acceptable: AI, EMF, EPS, JPG, PDF, PPT, PSD, TIF. Figures may be embedded at the end of the manuscript text file or loaded as separate files for submission. All images MUST be at or above intended display size, with the following image resolutions: Line Art 800 dpi, Combination (Line Art + Halftone) 600 dpi, Halftone 300 dpi. Image files also must be cropped as close to the actual image as possible.

Short Communications:

Short communications should be submitted with a structured abstract of no more than 200 words. These manuscripts should be no longer than 2000 words, and include no more than two figures and tables and 20 references. Other rules which the authors are required to prepare and submit their manuscripts are the same as described above for the original articles.

Invited Review Articles:

- Title page (see above)
- Abstract: Maximum 250 words; without structural divisions; in English and in Turkish . Turkish abstract will be provided by the editorial office for the authors who are not Turkish speakers. If you are not a native Turkish speaker, please reenter your English abstract to the area provided for the Turkish abstract.
- Text
- Conclusion

- Acknowledgements (if any)
- References

Editorial:

- Title page (see above)
- Abstract: Maximum 250 words; without structural divisions; in English and in Turkish. Turkish abstract will be provided by the editorial office for the authors who are not Turkish speakers. If you are not a native Turkish speaker, please re enter your English abstract to the area provided for the Turkish abstract.
- Text
- References

Case Report and Literature Review

- Title page (see above)
- Abstract: Approximately 100-150 words; without structural divisions; in English and in Turkish. Turkish abstract will be provided by the editorial office for the authors who are not Turkish speakers. If you are not a native Turkish speaker, please re-enter your English abstract to the area provided for the Turkish abstract.
- Introduction
- Case report
- Literature Review and Discussion
- References

Interesting Image:

No manuscript text is required. Interesting Image submissions must include the following:

Title Page: (see Original article section)

Abstract: Approximately 100-150 words; without structural divisions; in English and in Turkish. Turkish abstract will be provided by the editorial office for the authors who are not Turkish speakers. If you are not a native Turkish speaker, please re-enter your English abstract to the area provided for the Turkish abstract.

Image(s): The number of images is left to the discretion of the author. (See Original article section)

Figure Legend: Reference citations should appear in the legends, not in the abstract. Since there is no manuscript text, the legends for illustrations should be prepared in considerable detail but should be no more than 500 words total. The case should be presented and discussed in the Figure legend section.

References: Maximum eight references (see original article section).

Letters to the Editor:

- Title page (see above)
- Short comment to a published work, no longer than 500 words, no figures or tables.
- References no more than five.

Consensus Statements or Guidelines: These manuscripts should typically be no longer than 4000 words and include no more than six figures and tables and 120 references.

Proofs and Reprints

Proofs and a reprint orders are sent to the corresponding author. The author should designate by footnote on the title page of the manuscript the name and

INSTRUCTIONS TO AUTHORS

address of the person to whom reprint requests should be directed. The manuscript when published will become the property of the journal.

Archiving

The editorial office will retain all manuscripts and related documentation (correspondence, reviews, etc.) for 12 months following the date of publication or rejection.

Submission Preparation Checklist

As part of the submission process, authors are required to check off their submission's compliance with all of the following items, and submissions may be returned to authors that do not adhere to these guidelines.

1. The submission has not been previously published, nor is it before another journal for consideration (or an explanation has been provided in Comments to the Editor).

2. The submission file is in Microsoft Word, RTF, or WordPerfect document file format. The text is double-spaced; uses a 12-point font; employs italics, rather than underlining (except with URL addresses); and the location for all illustrations, figures, and tables should be marked within the text at the appropriate points.

3. Where available, URLs for the references will be provided.

4. All authors should be listed in the references, regardless of the number.

5. The text adheres to the stylistic and bibliographic requirements outlined in the Author Guidelines, which is found in About the Journal.

6. English keywords should be provided from http://www.nlm.nih.gov/mesh(Medical Subject Headings), while Turkish keywords should be provided fromhttp://www.bilimterimleri.com

7. The title page should be a separate document from the main text and should be uploaded separately.

8. The "Affirmation of Originality and Assignment of Copyright/The Disclosure Form for Potential Conflicts of Interest Form" and Authorship Contribution Form should be downloaded from the website, filled thoroughly and uploaded during the submission of the manuscript.

TO AUTHORS

Copyright Notice

The author(s) hereby affirms that the manuscript submitted is original, that all statement asserted as facts are based on author(s) careful investigation and research for accuracy, that the manuscript does not, in whole or part, infringe any copyright, that it has not been published in total or in part and is not being submitted or considered for publication in total or in part elsewhere. Completed

Copyright Assignment & Affirmation of Originality Form will be uploaded during submission. By signing this form;

1. Each author acknowledges that he/she participated in the work in a substantive way and is prepared to take public responsibility for the work.

2. Each author further affirms that he or she has read and understands the "Ethical Guidelines for Publication of Research".

3. The author(s), in consideration of the acceptance of the manuscript for publication, does hereby assign and transfer to the Molecular Imaging and Radionuclide Therapy all of the rights and interest in and the copyright of the work in its current form and in any form subsequently revised for publication and/or electronic dissemination.

Privacy Statement

The names and email addresses entered in this journal site will be used exclusively for the stated purposes of this journal and will not be made available for any other purpose or to any other party.

Peer Review Process

1. The manuscript is assigned to an editor, who reviews the manuscript and makes an initial decision based on manuscript quality and editorial priorities.

2. For those manuscripts sent for external peer review, the editor assigns at least two reviewers to the manuscript.

3. The reviewers review the manuscript.

4. The editor makes a final decision based on editorial priorities, manuscript quality, and reviewer recommendations.

5. The decision letter is sent to the author.

Contact Address

All correspondence should be directed to the Editorial Office:

Cinnah Caddesi Pilot Sokak No:10/12 06650 Çankaya / Ankara, Turkey

Phone: +90 312 441 00 45

Fax: +90 312 441 12 97

E-mail: info@tsnmjournals.org

MIRT

Molecular Imaging and Radionuclide Therapy

MIRT

Molecular Imaging and Radionuclide Therapy

CONTENTS

The Role of ^{18}F-FDOPA PET/CT in Recurrent Medullary Thyroid Cancer Patients with Elevated Serum Calcitonin Levels

Serum Kalsitonin Yüksekliği Bulunan Rekürren Medüller Tiroid Kanseri Hastalarında ^{18}F-FDOPA PET/BT'nin Rolü

🆔 *Mine Araz[1]*, 🆔 *Çiğdem Soydal[1]*, 🆔 *Özgür Demir[2]*, 🆔 *Mustafa Kürşat Gökcan[3]*, 🆔 *Nuriye Özlem Küçük[1]*

[1]*Ankara University Faculty of Medicine, Department of Nuclear Medicine, Ankara, Turkey*
[2]*Ankara University Faculty of Medicine, Department of Endocrinology and Metabolism, Ankara, Turkey*
[3]*Ankara University Faculty of Medicine, Department of Otorhinolaryngology and Head and Neck Surgery, Ankara, Turkey*

Abstract

Objectives: To evaluate the diagnostic performance of ^{18}F-dihydroxyphenylalanine (FDOPA) positron emission tomography/computed tomography (PET/CT) in the detection of medullary thyroid carcinoma (MTC) recurrence in patients with elevated calcitonin levels.

Methods: The patients who had undergone ^{18}F-FDOPA PET/CT imaging for elevated calcitonin levels after primary surgery of MTC were included in the study. addition, if available ^{18}F-fluorodeoxyglucose (FDG) PET/CT and Gallium-68 (^{68}Ga)- DOTATATE PET/CT images of the patients were evaluated retrospectively. The sensitivity and diagnostic performance of ^{18}F-DOPA PET/CT were investigated.

Results: A total of 14 patients (9 F and 5 M; median age: 45) were included in the analysis. Three patients had MEN IIA syndrome and 1 patient had MEN IIB syndrome, 10 patients had a diagnosis of sporadic MTC. Median calcitonin levels of the patients were calculated as 757.5 (min-max: 28.5-7911) pg/mL. Nine patients and 5 patients had undergone ultrasound and contrast-enhanced computed tomography (ceCT) of the neck, respectively, before ^{18}F-FDOPA PET/CT imaging. ^{18}F-FDOPA PET/CT revealed pathological uptake in the thyroid bed, lymph nodes, and distant organs in three, five and two patients, respectively. Median maximum standardized uptake value for the recurrent or metastatic lesions were calculated as 6.4 (min-max: 1.9-18.4). The sensitivity of ^{18}F-FDOPA PET/CT in the detection of recurrent disease was calculated as 64%. Eight patients had ^{68}Ga-DOTATATE PET/CT and 7 of them had ^{18}F-FDG PET/CT within 3 months period before ^{18}F-FDOPA PET/CT. ^{18}F-FDOPA PET/CT revealed recurrent disease in 4 of 5 and 2 of the 5 patients who had negative ^{18}F-FDG PET/CT and negative ^{68}Ga- DOTATATE PET/CT, respectively.

Conclusion: ^{18}F-FDOPA PET/CT can detect recurrence in about two-thirds of patients with elevated calcitonin levels after primary surgery for MTC. Due to variable differentiation degree, different receptor status, and clinical behavior of MTC, all three radiopharmaceuticals can be beneficial and are complementary to each other in patient management.

Keywords: Medullary thyroid cancer, PET/CT, ^{18}F-FDOPA, calcitonin

Öz

Amaç: Serum kalsitonin yüksekliği bulunan medüller tiroid kanseri (MTK) tanılı hastalarda rekürrensin saptanmasında ^{18}F-dihidroksifenilalanin (FDOPA) pozitron emisyon tomografisi/bilgisayarlı tomografinin (PET/BT) performansının değerlendirilmesidir.

Yöntem: Primer MTK cerrahisi sonrasında yüksek kalsitonin düzeyi olan ve ^{18}F-FDOPA PET/BT uygulanmış olan hastalar çalışmaya dahil edildi. Ek olarak, eğer varsa ^{18}F-florodeoksiglukoz (FDG) PET/BT ve Galyum-68 (^{68}Ga)-DOTATATE PET/BT bulguları da retrospektif olarak değerlendirildi.^{18}F-FDOPA PET/BT'nin duyarlılığı ve tanısal performansı araştırıldı.

Bulgular: Toplam 14 hasta (9 K, 5 E, medyan yaş: 45) analize dahil edildi. Üç hastada MEN IIA, 1 hastada MEN IB sendromu, 10 hastada sporadik MTK mevcuttu. Hastaların medyan kalsitonin seviyeleri 757,5 (min-maks: 28.5-7911) pg/mL bulundu. ¹⁸F-FDOPA PET/BT görüntülemesinden önce 9 hastaya boyun ultrasonu, 5 hastaya kontrastlı boyun BT uygulanmıştı. ¹⁸F-FDOPA PET/BT'de 3 hastada tiroid yatağında nüks, 5 hastada lenf nodu metastazı ve 2 hastada uzak metastaz saptandı. Rekürren veya metastatik lezyonlarda medyan maksimum standartlaştırılmış alım değeri: 6,4 (min-maks: 1,9-18,4) olarak hesaplandı. Rekürren hastalığın saptanmasında ¹⁸F-FDOPA PET/BT'nin duyarlılığı %64 bulundu. ¹⁸F-FDOPA PET/BT'den önceki 3 ay içerisinde 8 hastanın ⁶⁸Ga-DOTATATE, 7 hastanın ¹⁸F-FDG PET/BT görüntülemeleri mevcuttu. ¹⁸F-FDOPA PET/BT, negatif ¹⁸F-FDG PET/BT'si olan 5 hastanın 4'ünde ve negatif ⁶⁸Ga-DOTATATE PET/BT'si olan 5 hastanın 2'sinde rekürren hastalığı gösterdi.

Sonuç: ¹⁸F-FDOPA PET/BT, MTK için primer cerrahi sonrası yüksek kalsitonin düzeyi bulunan hastaların yaklaşık 2/3'ünde rekürrens saptayabilir. Tiroid medüller karsinomunun değişken diferansiyasyon derecesi, farklı reseptör durumu ve klinik davranışına bağlı olarak, her üç radyofarmasötik de hasta yönetiminde faydalı olabilir ve birbirine tamamlayıcıdır.

Anahtar kelimeler: Medüller tiroid kanseri, PET/BT, ¹⁸F-FDOPA, kalsitonin

Introduction

Medullary thyroid carcinoma (MTC) is a neuroendocrine tumor of the thyroid gland, originating from parafollicular C-cells with a frequency of 5% among all thyroid cancers. Sporadic (75%) and familial (25%) forms have been defined (1). The only curative therapy for medullary thyroid cancer is total resection of the primary tumor and metastatic lesions, and the prognosis is strongly related to the performance of surgery (2). However, despite all aggressive and effective surgeries performed, persistent or recurrent disease is commonly seen during medullary thyroid cancer. Serum calcitonin and carcinoembryonic antigen (CEA) are the tumor markers that are used in the follow-up. CEA has also been reported to be as a marker of dedifferentiation (1,3).

Biochemical recurrence necessitates accurate detection of the recurrent or the metastatic focus. In patients with increased serum calcitonin and/or CEA levels in the follow-up, a thorough examination and imaging of the whole body is crucial because early detection of recurrent disease enables clinicians and surgeons to perform effective surgeries, local or systemic therapies of the limited disease. With ultrasonography of the neck, computed tomography (CT) of the thorax, abdomen, and pelvis are usually performed for the detection of recurrence. When the levels of serum calcitonin exceeded 150 pg/mL, radionuclide whole-body imaging methods are also indicated because distant metastasis is likely (1,3,4).

Positron emission tomography (PET)/CT with ¹⁸F-fluorodeoxyglucose (FDG) is the most common radionuclide imaging tool in oncology. However, it has been reported that the performance of ¹⁸F-FDG PET/CT is highly related to serum calcitonin levels and is recommended for cases with serum calcitonin >500-1000 (5). Alternative tracers using different uptake pathways have been tested. Somatostatin receptor imaging with (Gallium-68) ⁶⁸Ga labeled somatostatin analogs (DOTATATE, DOTATOC or DOTANOC) and ¹⁸F-dihydroxyphenylalanine (FDOPA) have been proposed for restaging in case of biochemical recurrence. Being a cyclotrone-produced radiopharmaceutical, which can be highly expensive, ¹⁸F-FDOPA is not easily maintained throughout the world and the literature is still a lack of data about the role of ¹⁸F-FDOPA PET/CT in medullary thyroid cancer, a relatively rare tumor type of thyroid.

In this study, we evaluated the role of ¹⁸F-FDOPA PET/CT in the detection of recurrence in medullary thyroid cancer patients with elevated serum calcitonin levels.

Materials and Methods

Patients

This retrospective study was approved by the Ankara University Review Board (approval no: İ7-522-21, date: 06.09.2021). Medullary thyroid cancer patients who were referred to the nuclear medicine department for ¹⁸F-FDOPA PET/CT between January 2018 and January 2021 were included in the study. Inclusion criteria were i) >18 years old male or females with histopathologically confirmed medullary thyroid cancer diagnosis after thyroidectomy, ii) elevated levels of serum calcitonin in the follow-up after surgery for primary tumor, iii) clinical follow-up results of at least 2 years for confirmation of recurrence. Exclusion criteria were, i) age <18 years, ii) history of secondary malignancy, iii) lack of clinical follow-up.

¹⁸F-FDOPA PET/CT Protocol and Image Interpretation

Premedication with carbidopa was not performed. Following a minimum of 4 h fasting, 2 to 4 MBq/kg of ¹⁸F-FDOPA was intravenously administered by slow injection. Whole-body PET/CT images from the vertex to the upper thigh were obtained 60 min after radiopharmaceutical injection by using a hybrid PET/CT scanner (GE Discovery 710, General Electric Company, USA). PET images were acquired for 2 min per bed position. PET images were reconstructed with non-contrast low-dose CT images. CT images were obtained with a standardized protocol of 140 kV, 70 mA,

tube rotation time of 0.5 s per rotation, a pitch of 6 and a slice thickness of 5 mm. Patients were allowed to breathe normally during the procedure. Attenuation-corrected PET/CT fusion images were reviewed in three planes (transaxial, coronal and sagittal) on Advanced Workstation Volumeshare 5 (GE Medical Systems).

All PET/CT images were reevaluated by two nuclear medicine specialists with consensus. Any area of focal uptake higher than the adjacent background activity outside the areas of physiological distribution of the radiotracer with a corresponding nodular lesion on CT were considered as pathological. Maximum standardized uptake value (SUV_{max}) was measured for all lesions for semiquantitative analysis.

Statistical Analysis

In this retrospective analysis, with demographics, serum calcitonin levels, results of any radiological or functional imaging studies, including neck US, CT of the thorax, abdomen or pelvis, Tc-99m methylenediphosphanate whole body bone scan, ^{18}F-FDG PET/CT, or [68]Ga- DOTATATE PET/CT were recorded. Clinical follow-up or histopathological examination results in patients who underwent surgeries after ^{18}F-FDOPA PET/CT were used for confirmation of results. Patient-based sensitivity, specificity, and accuracy were calculated for ^{18}F-FDOPA PET/CT in the detection of disease recurrence.

Results

A total of 14 patients (9 F and 5 M; median age: 45) were included in the analysis. Three patients had MEN IIA syndrome and 1 patient MEN IIB syndrome, 10 patients had a diagnosis of sporadic MTC. Median calcitonin levels of patients were calculated as 757.5 (min-max: 28.5-7911) pg/mL. Nine patients and 5 patients had undergone ultrasound and contrast-enhanced computed tomography (ceCT) of the neck, respectively, before PET/CT imaging. Eight patients had [68]Ga- DOTATATE and 7 patients had ^{18}F-FDG PET/CT within 3 months period before ^{18}F-DOPA PET/CT. Results were confirmed histopathologically in 7 patients. Clinical follow-up results were used for confirmation in 7 patients. Four of these patients showed no sign of recurrence, and in 3 patients, progression was recorded on radiological examinations [CT and/or magnetic resonance imaging (MRI)] in the follow-up. Patient characteristics, details of PET/CT and follow-up results are given in Table 1.

^{18}F-FDG PET/CT Findings

^{18}F-FDG PET/CT was normal in 5 patients. In 1 patient, ^{18}F-FDG PET/CT revealed cervical metastatic lymph node, and in 1 patient ^{18}F-FDG was positive in both cervical and mediastinal lymph nodes. In these 2 patients, ^{18}F-FDOPA PET/CT was negative for lymph node metastasis and ^{68}Ga PET/CT was not available.

^{68}Ga-DOTATATE PET/CT Findings

^{68}Ga-DOTATATE was negative in 5 patients. In patients with a positive ^{68}Ga-DOTATATE PET/CT, cervical lymph nodes were detected in all 3 of them, mediastinal lymph nodes in one patient, and pathological uptake was recorded in the thyroid bed in 1 patient. In 1 patient with cervical lymph node metastasis, ^{18}F-FDOPA PET/CT was negative and ^{18}F-FDG PET/CT was not performed.

^{18}F-FDOPA PET/CT Findings

^{18}F-FDOPA PET/CT was normal in 5 patients. ^{18}F-FDOPA PET/CT revealed pathological uptake on the thyroid bed, lymph nodes and distant organs in 3, 5, and 2 patients, respectively. Median SUV_{max} for the recurrent lesions were calculated as 6.4 (min-max: 1.9-18.4). Although not statistically significant, serum calcitonin levels in ^{18}F-FDOPA PET/CT-positive patients were higher than ^{18}F-FDOPA PET/CT-negative patients (800 pg/mL min: 47, max: 7911 vs. 98.2 pg/mL, min: 28.5, max: 800, respectively, p=0.30).

^{18}F-FDOPA PET/CT detected recurrent disease in 4 of 5 and 2 of the 5 patients who had negative ^{18}F-FDG PET/CT and negative ^{68}Ga-DOTATATE PET/CT, respectively. In 5 patients with negative ^{18}F-FDG PET/CT, ^{18}F-FDOPA was positive in the thyroid bed in 2 patients, in regional lymph nodes in 2 patients, and in lung metastasis in 1 patient. In 2 patients with a negative ^{68}Ga-DOTA PET/CT scan, ^{18}F-FDOPA was positive in the thyroid bed (Figure 1). The sensitivity of ^{18}F-FDOPA PET/CT in the detection of recurrent disease was calculated as 64%.

Discussion

Medullary thyroid cancer is a relatively rare malignancy of the thyroid. Disease progression is usually slow, and overall survival rates are acceptable if an effective surgical resection at the time of diagnosis could be achieved. However, calcitonin recurrence or persistence is observed in up to 80% of the patients. Detection and accurate localization of structural diseases in patients with biochemical recurrence is important for further therapies (6). Reoperation aims to total resection of recurrent or persistent malignant tissues and to achieve undetectable calcitonin levels. Even with experienced operators and excellent surgeries, complete remission could be maintained in only 30% of patients (7). Thus, imaging studies are expected to detect insignificant-volume diseases with high accuracy for differentiating candidates of surgery/local therapies or systemic therapy (8).

Table 1. Patient characteristics, PET/CT findings and Follow-up results

Patient number	Gender	Age	^{18}F-FDOPA PET/CT		^{18}F-FDG PET/CT		^{68}Ga-DOTATATE PET/CT		CEA	Calcitonin	Syndrome	Follow-up results
			Location	SUV$_{max}$	Location	SUV$_{max}$	Location	SUV$_{max}$				
1	M	47	Cervical LN	3.5	(-)	NA	Cervical LN	4.4	2.48	800	Sporadic	Right central lymph node dissection revealed metastasis
2	M	36	Thyroid bed	5.8	(-)	NA	Thyroid bed, cervical LN	17.4	5.16	48.4	MEN IIA	Left central revision lymph node dissection revealed lymph node metastasis and thyroid bed recurrence
3	F	68	Bone, mediastinal LN, liver, adrenal gland	13.3	(-)	NA	(-)	NA	4079.6	800	MEN IIA	Progression on CT and MR in the follow-up
4	M	53	Normal	NA	(-)	NA	Normal	0	920	457	Sporadic	No recurrence in clinical follow-up
5	F	45	Thyroid bed	2.2	Normal	0	Normal	0	NA	1372	MEN IIA	Biopsy revealed local recurrence
6	F	54	Normal	NA	Cervical LN	5	(-)	NA	1.31	43.4	Sporadic	Cervical lymph node biopsy revealed metastasis
7	F	78	Normal	NA	(-)	NA	Normal	0	NA	28.5	Sporadic	No recurrence in clinical follow-up
8	F	45	Cervical LN	2.2	(-)	NA	(-)	NA	1.74	47	Sporadic	Left cervical lymph node dissection revealed lymph node metastasis
9	F	34	Lung	1.9	Cervical LN, mediastinal LN	3.5	(-)	NA	7.27	1800	Sporadic	Progression in lung nodule and lymph node dimensions on CT
10	M	30	Normal	NA	Normal	NA	Normal	0	7.75	800	MEN IIB	No recurrence in clinical follow-up
11	F	19	Cervical LN	2.8	Normal	NA	(-)	NA	3.48	138.1	Sporadic	Right cervical lymph node dissection revealed metastasis
12	M	71	Thyroid bed	18.4	Normal	NA	Normal	NA	7.4	715	Sporadic	Biopsy revealed local recurrence
13	F	44	Cervical lymph node, mediastinal lymph node	6.4	Normal	NA	Cervical LN, mediastinal LN	2.8	174	7911	Sporadic	Progression in cervical and mediastinal lymph node dimensions on CT
14	F	46	Normal	NA	(-)	NA	(-)	NA	2.28	98.2	Sporadic	No recurrence in clinical Follow-up

M: Male, F: Female, LN: Lymph node, PET/CT: Positron emission tomography/computed tomography, FDOPA: ¹⁸F-dihydroxyphenylalanine, ^{68}Ga: Gallium-68, FDG: Fluorodeoxyglucose, SUV$_{max}$: Maximum standardized uptake value, CEA: Carcinoembryonic antigen, MR: Magnetic resonance
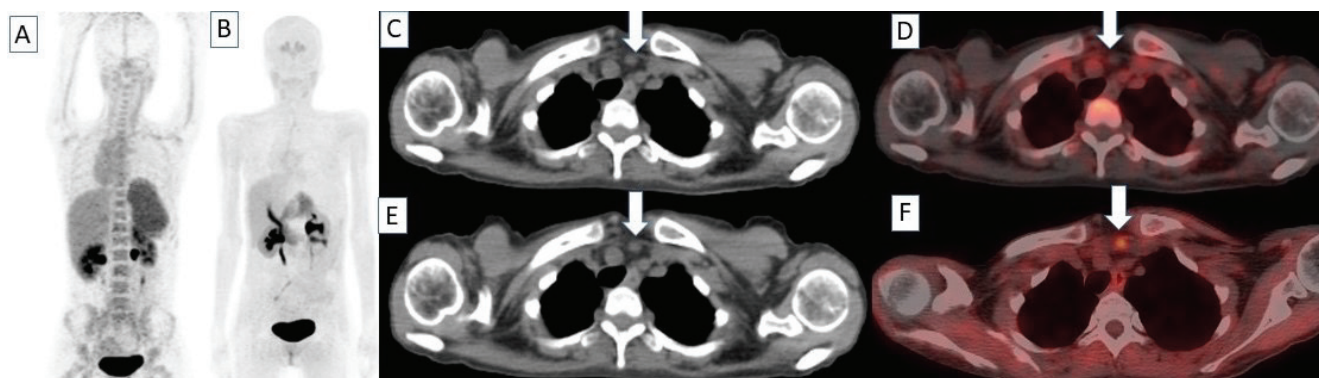
Figure 1. 68Ga- DOTATATE and 18F-FDOPA PET/CT images of patient number 5. Forty-five years old female diagnosed with MEN IIA syndrome (medullary thyroid carcinoma and adrenal paraganglioma) was referred with elevated serum calcitonin levels (1372 pg/mL) following total thyroidectomy. On maximum intensity projection (A, B), axial CT, and fusion images of 68Ga-DOTATATE (C, D) and 18F-FDOPA (E, F) PET/CT studies, focal pathological 18F-FDOPA uptake was detected on a nodular lesion located in the thyroid bed (SUV$_{max}$: 2.2), which was 68Ga-DOTATATE negative (arrows). A biopsy revealed local recurrence in the thyroid bed

68Ga: Gallium-68, FDOPA: 18F-dihydroxyphenylalanine, PET/CT: Positron emission tomography/computed tomography, SUV$_{max}$: Maximum standardized uptake value

18F-FDOPA has gained importance in medullary thyroid cancer recently. In a meta-analysis, the patient-based and lesion- based detection rates of 18F-FDOPA in patients with increased tumor markers were calculated as 66% and 71% respectively. The performance of 18F-FDOPA PET/CT was related to serum calcitonin levels. The detection rate of 18F-FDOPA was found 86% in patients with serum calcitonin levels >1000 pg/mL (9). In another study comparing the diagnostic utility of 18F-FDOPA and 18F-FDG PET/CT, the sensitivity of 18F-FDOPA was significantly higher in patients with serum calcitonin levels >150 pg/mL compared to <150 pg/mL (90.9% vs. 28.6%; p=0.013) (10). In our study, compatible with the literature, patient-based sensitivity of 18F-FDOPA PET/CT in medullary thyroid cancer patients with elevated serum calcitonin levels was found to be 64%. Serum calcitonin levels were relatively higher in 18F-FDOPA PET/CT-positive patients compared to others (800 pg/mL vs. 98.2), but this difference could not be proved statistically due to the very small number of patients in the subgroups.

In comparative studies with 18F-FDG PET/CT and 68Ga-DOTATATE PET/CT, 18F-FDOPA PET/CT was reported to be superior (11,12,13). This is why the European Association of Nuclear Medicine recommends 18F-FDOPA PET/CT in the first line in medullary thyroid cancer patients with elevated serum calcitonin levels after initial treatment (14). In this study, because not all patients had 68Ga-DOTATATE PET/CT and 18F-FDG PET/CT, no direct comparison of patient or lesion-based sensitivity or detection rates of these three modalities could be possible. In regional analysis, it is shown that 18F-FDOPA was positive in lymph nodes in 2 patients and in the thyroid bed in 2 patients with negative 18F-FDG PET/

CT and in the thyroid bed in 2 patients with negative 68Ga-DOTATATE PET/CT. However, there were 2 patients (patients 6 and 9) with 18F-FDG positive but 18F-FDOPA negative lymph node metastasis and 1 patient (patient 2) with 68Ga-DOTATATE-positive but 18F-FDOPA negative lymph nodes. According to the literature, 18F-FDOPA has a higher performance in the neck compared to both 18F-FDG and 68Ga-DOTATATE. This is probably due to a higher ratio of tumor/background counts compared to the other two radiopharmaceuticals. Another thing is that the uptake mechanisms of these three radiopharmaceuticals are different, and 18F-FDOPA is rather positive in relatively differentiated medullary thyroid cancer. While 18F-FDG uptake is related to dedifferentiation, 68Ga-DOTATATE uptake is a measure of somatostatin receptor expression of the tumor cells (11,12,15,16). Our results partly confirm previous reported data, as there are patients with locoregional disease either 18F-FDG or 68Ga-DOTATATE positive but 18F-FDOPA negative.

Regarding distant metastasis, only 18F-FDOPA was positive in a single patient with lung metastasis, which was also reported on ceCT (patient 9). Because 68Ga-DOTATE PET/CT was not performed in this patient, a comparison between 68Ga-DOTATATE PET/CT and 18F-FDOPA PET/CT could not be made but, this lung nodule was 18F-FDG negative. No other patients had lung metastasis detectable by any radiological or functional imaging modality. In lung metastasis, as it is the case in our study, ceCT seems adequate enough to detect lung lesions. No significant superiority of 18F-FDOPA PET/CT was reported over other imaging modalities. However, 18F-FDG PET/CT is sometimes insufficient in the evaluation of lesions with low metabolic rate or small nodules (<1cm) (17).

^{18}F-FDOPA was found superior to ^{68}Ga-DOTATATE PET/CT in the detection of liver metastasis (11). There was only one patient in our study (patient 3) who had liver metastasis shown by ^{18}F-FDOPA PET/CT. Although no comparison with ^{18}F-FDG or ^{68}Ga-DOTATATE could be possible in our study, in the follow-up liver lesions showed progression on both CT and MRI and accuracy of ^{18}F-FDOPA PET/CT was confirmed. This result was compatible with previous data in the literature (11).

Study Limitations

The major limitation of this study is that few patients were enrolled. Further statistical analysis would be possible including subgroup analysis if a larger patient population could be achieved. Another limitation is that the study was designed retrospectively. Thus, head-to-head comparison of ^{18}F-FDOPA with ^{18}F-FDG and ^{68}Ga-DOTATATE was not possible for all patients. Although patients involved in this study were scanned at 60 min, as recommended in the guideline, in recent studies, higher detection rates with the earlier acquisition for ^{18}F-FDOPA PET/CT in medullary thyroid cancer was reported (14,18). Calculated sensitivity could have been higher if dual time point imaging could be performed. Despite these limitations, in our opinion, clinical results of a relatively specific and hard- to- reach radiopharmaceutical in a rare patient group are still valuable and would contribute to the literature.

Conclusion

^{18}F-FDOPA PET/CT can detect recurrence in about two-thirds of the patients with elevated calcitonin levels after primary surgery for MTC. Due to variable differentiation degree, different receptor status, and clinical behavior of MTC, all three radiopharmaceuticals can be beneficial and are complementary to each other in patient management.

Ethics

Ethics Committee Approval: Ankara University Ethics Committee approval was received for this study (decision no: İ7-522-21, date: 06.09.2021).

Informed Consent: The patient consent was obtained.

Peer-review: Externally and internally peer-reviewed.

Authorship Contributions

Surgical and Medical Practices: M.K.G., Concept: Ç.S., N.Ö.K., Ö.D., Design: Ç.S., M.A., Data Collection or Processing: Ç.S., M.A., Analysis or Interpretation: Ç.S., M.A., Literature Search: M.A., Writing: M.A.

Conflict of Interest: No conflict of interest was declared by the authors.

References

1. Pitt SC, Moley JF. Medullary, anaplastic, and metastatic cancers of the thyroid. Semin Oncol 2010;37:567-579.

2. Machens A, Dralle H. Surgical treatment of medullary thyroid cancer. Recent Results Cancer Res 2015;204:187-205.

3. Pacini F, Castagna MG, Brilli L, Pentheroudakis G; ESMO Guidelines Working Group. Thyroid cancer: ESMO Clinical Practice Guidelines for diagnosis, treatment and follow-up. Ann Oncol. 2012;23(Suppl 7):vii110-vii119.

4. American Thyroid Association Guidelines Task Force; Kloos RT, Eng C, Evans DB, Francis GL, Gagel RF, Gharib H, Moley JF, Pacini F, Ringel MD, Schlumberger M, Wells SA Jr. Medullary thyroid cancer: management guidelines of the American Thyroid Association. Thyroid 2009;19:565-612. Erratum in: Thyroid 2009;19:1295.

5. Ong SC, Schöder H, Patel SG, Tabangay-Lim IM, Doddamane I, Gönen M, Shaha AR, Tuttle RM, Shah JP, Larson SM. Diagnostic accuracy of 18F-FDG PET in restaging patients with medullary thyroid carcinoma and elevated calcitonin levels. J Nucl Med 2007;48:501-507.

6. Wells SA Jr, Asa SL, Dralle H, Elisei R, Evans DB, Gagel RF, Lee N, Machens A, Moley JF, Pacini F, Raue F, Frank-Raue K, Robinson B, Rosenthal MS, Santoro M, Schlumberger M, Shah M, Waguespack SG; American Thyroid Association Guidelines Task Force on Medullary Thyroid Carcinoma. Revised American Thyroid Association guidelines for the management of medullary thyroid carcinoma. Thyroid 2015;25:567-610.

7. Fialkowski E, DeBenedetti M, Moley J. Long-term outcome of reoperations for medullary thyroid carcinoma. World J Surg 2008;32:754-765.

8. Klain M, Hadoux J, Nappi C, Finessi M, Ambrosio R, Schlumberger M, Cuocolo A, Deandreis D, Salvatore D. Imaging medullary thyroid cancer patients with detectable serum markers: state of the art and future perspectives. Endocrine 2022;75:330-337.

9. Treglia G, Cocciolillo F, Di Nardo F, Poscia A, de Waure C, Giordano A, Rufini V. Detection rate of recurrent medullary thyroid carcinoma using fluorine-18 dihydroxyphenylalanine positron emission tomography: a meta-analysis. Acad Radiol 2012;19:1290-1299.

10. Romero-Lluch AR, Cuenca-Cuenca JI, Guerrero-Vázquez R, Martínez-Ortega AJ, Tirado-Hospital JL, Borrego-Dorado I, Navarro-González E. Diagnostic utility of PET/CT with 18F-DOPA and 18F-FDG in persistent or recurrent medullary thyroid carcinoma: the importance of calcitonin and carcinoembryonic antigen cutoff. Eur J Nucl Med Mol Imaging 2017;44:2004-2013.

11. Treglia G, Castaldi P, Villani MF, Perotti G, de Waure C, Filice A, Ambrosini V, Cremonini N, Santimaria M, Versari A, Fanti S, Giordano A, Rufini V. Comparison of 18F-DOPA, 18F-FDG and 68Ga-somatostatin analogue PET/CT in patients with recurrent medullary thyroid carcinoma. Eur J Nucl Med Mol Imaging 2012;39:569-580.

12. Treglia G, Rufini V, Salvatori M, Giordano A, Giovanella L. PET imaging in recurrent medullary thyroid carcinoma. Int J Mol Imaging 2012;2012:324686.

13. Slavikova K, Montravers F, Treglia G, Kunikowska J, Kaliska L, Vereb M, Talbot JN, Balogova S. What is currently the best radiopharmaceutical for the hybrid PET/CT detection of recurrent medullary thyroid carcinoma? Curr Radiopharm 2013;6:96-105.

14. Bozkurt MF, Virgolini I, Balogova S, Beheshti M, Rubello D, Decristoforo C, Ambrosini V, Kjaer A, Delgado-Bolton R, Kunikowska J, Oyen WJG, Chiti A, Giammarile F, Sundin A, Fanti S. Guideline for PET/CT imaging of neuroendocrine neoplasms with 68Ga-DOTA-conjugated somatostatin receptor targeting peptides and 18F-DOPA. Eur J Nucl Med Mol Imaging 2017;44:1588-1601. Erratum in: Eur J Nucl Med Mol Imaging 2017.

15. Chondrogiannis S, Marzola MC, Al-Nahhas A, Venkatanarayana TD, Mazza A, Opocher G, Rubello D. Normal biodistribution pattern and physiologic variants of 18F-DOPA PET imaging. Nucl Med Commun 2013;34:1141-1149.

16. S. Hoegerle, C. Altehoefer, N. Ghanem, I. Brink, E. Moser, and E. Nitzsche, "18F-DOPA positron emission tomography for tumour detection in patients with medullary thyroid carcinoma and elevated calcitonin levels," European Journal of Nuclear Medicine, 2001;28:64-71.

17. Tan BB, Flaherty KR, Kazerooni EA, Iannettoni MD; American College of Chest Physicians. The solitary pulmonary nodule. Chest. 2003;123(Suppl 1):89S-96S.

18. Soussan M, Nataf V, Kerrou K, Grahek D, Pascal O, Talbot JN, Montravers F. Added value of early 18F-FDOPA PET/CT acquisition time in medullary thyroid cancer. Nucl Med Commun 2012;33:775-779.

Oxidized Regenerated Cellulose can be a Cause of False Tumor Recurrence on PET/CT in Patients with Lung Cancer Treated Surgically

Cerrahi Olarak Tedavi Edilen Akciğer Kanserlerinde Okside Rejenere Selüloz, PET/BT'de Yalancı Tümör Nüksünün Bir Sebebi Olabilir

Ⓘ *Muhammet Sayan[1],* Ⓘ *Ali Çelik[1],* Ⓘ *Merve Şatır Türk[1],* Ⓘ *Dilvin Özkan[1],* Ⓘ *Irmak Akarsu[1],* Ⓘ *Ozan Yazıcı[2],* Ⓘ *Uğuray Aydos[3],*
Ⓘ *Nilgün Yılmaz Demirci[4],* Ⓘ *Gülen Akyol[5],* Ⓘ *İsmail Cüneyt Kurul[1],* Ⓘ *Abdullah İrfan Taştepe[1]*

[1]*Gazi University Faculty of Medicine, Department of Thoracic Surgery, Ankara, Turkey*
[2]*Gazi University Faculty of Medicine, Department of Medical Oncology, Ankara, Turkey*
[3]*Gazi University Faculty of Medicine, Department of Nuclear Medicine, Ankara, Turkey*
[4]*Gazi University Faculty of Medicine, Department of Chest Diseases, Ankara, Turkey*
[5]*Gazi University Faculty of Medicine, Department of Pathology, Ankara, Turkey*

Abstract

Objectives: Regular follow-up of patients with lung cancer treated surgically is crucial to detect local recurrence or distant metastasis of the tumor. Postoperative follow-ups are performed with thorax computed tomography (CT) and, if necessary, positron emission tomography (PET)/CT. Sometimes, inflammatory tissue reactions due to the materials used during the surgery for hemostasis may cause the appearance of tumor recurrence in imaging modalities. In this study, we presented that oxidized regenerated cellulose (ORC) used intraoperatively may cause false tumor recurrence on PET/CT.

Methods: The records of patients who had local tumor recurrence after lung cancer surgery was reviewed retrospectively. Inclusion criteria were the presence of local recurrence of cancer on PET/CT, specification of using ORC in the surgical notes, and histopathological diagnosis of the recurrence site of tumor was reported as a foreign body reaction. Data of patients were collected according to age, gender, surgery performed, adjuvant therapy status, resolution status and time ORC, and standard uptake value of ^{18}F-fluorodeoxyglucose on PET/CT.

Results: Eleven patients (1 female, 10 males) who met the criteria were included in the study. The median age was 64. Histopathological results of all patients were reported as foreign body reactions. The median detection time of PET/CT positivity after surgery was 139 days (range: 52-208 days). False tumor recurrence was resolved in 8 patients (72.7%) in their control radiological examinations and median resolution time was 334 days (range: 222-762 days). The median maximum standard uptake value of the lesions was 6.2 (1.7-11) on the PET/CT.

Conclusion: ORC used intraoperatively in patients undergoing surgery for lung cancer may cause false tumor recurrence in imaging modalities in postsurgical follow-ups. When tumor recurrence is suspected in the follow-up of these patients, histopathological confirmation is necessary to prevent unnecessary operations and treatments.

Keywords: Lung cancer, positron emission tomography/computed tomography, false recurrence, and oxidized regenerated cellulose

Öz

Amaç: Cerrahi olarak tedavi edilen akciğer kanserli hastaların düzenli takibi, lokal nüks ve uzak metastaz saptanmasında oldukça önemlidir. Postoperatif takipler toraks bilgisayarlı tomografi (BT) ve gerekirse pozitron emisyon tomografisi (PET)/BT ile yapılır. Bazen hemostaz sağlamak

için ameliyat sırasında kullanılan materyallere bağlı enflamatuvar doku reaksiyonları görüntüleme modalitelerinde tümör nüksü görünümüne neden olabilir. Bu çalışmada intraoperatif kullanılan oksitlenmiş rejenere selülozun (ORS), PET/BT'de yalancı tümör nüksüne neden olabileceğini göstermeyi amaçladık.

Yöntem: Akciğer kanseri cerrahisi sonrası lokal tümör nüksü gelişen hastaların kayıtları geriye dönük olarak incelendi. Dahil edilme kriterleri, PET/BT'de lokal kanser nüksü varlığı, cerrahi notlarda ORS kullanımının belirtilmesi ve tümörün nüks bölgesinin histopatolojik tanısının yabancı cisim reaksiyonu olarak bildirilmesiydi. Hastalara ait yaş, cinsiyet, yapılan cerrahi, adjuvan tedavi durumu, rezolüsyon durumu ve ORC süresi ve PET/BT'deki ^{18}F-florodeoksiglukoz standart uptake değeri verileri toplandı.

Bulgular: Kriterleri karşılayan 11 hasta (1 kadın, 10 erkek) çalışmaya dahil edildi. Ortanca yaş 64 idi. Tüm hastaların histopatolojik raporları yabancı cisim reaksiyonu olarak rapor edildi. Ameliyattan sonra PET/BT pozitifliğinin ortanca tespit süresi 139 gündü (dağılım: 52-208 gün). Kontrol radyolojik incelemelerinde 8 hastada (%72,7) tümör görünümü düzeldi ve ortanca iyileşme süresi 334 gündü (dağılım: 222-762 gün). PET/BT'de lezyonların ortanca maksimum standard tutulum değeri 6,2 idi (dağılım: 1,7-11).

Sonuç: Cerrahi olarak tedavi edilen akciğer kanserli hastaların takibinde tümör nüksünden şüphelenildiğinde, gereksiz operasyon ve tedavileri önlemek için histopatolojik doğrulama gereklidir.

Anahtar kelimeler: Akciğer kanseri, pozitron emisyon tomografi bilgisayarlı tomografi, yalancı nüks

Introduction

Surgery is the optimal treatment option for patients with clinically early-stage non-small-cell lung cancer (NSCLC). However, adjuvant treatment such as chemotherapy and/or radiotherapy, may be required depending on the patient's pathological tumor stage, complete resection status, and tumor histopathology. Despite all efforts, the 5-year survival in all stages of NSCLC is less than 50%, and the median expected survival after tumor recurrence has been reported as 11.5 months (1,2,3). Follow-up of patients after surgery for detecting local tumor recurrence or distant metastasis is usually performed with computed tomography (CT) and/or positron emission tomography (PET)/CT. PET/CT is the preferred method for follow-up due to its high sensitivity and specificity for tumor recurrence. Furthermore, it is also a suitable procedure for evaluating the response to adjuvant therapy (4,5). Oxidized regenerated cellulose (ORC) is an absorbable hemostatic material that has long been used for bleeding control in neurosurgery, hepatic surgery, renal surgery, and cardiothoracic surgery. Although some studies in the literature have reported that ORC can cause false tumor recurrence, its PET/CT findings of false tumor recurrence after lung cancer surgery are unclear (6,7,8,9). In this study, we presented ORC used intraoperatively may cause false tumor recurrence on PET/CT.

Materials and Methods

Patient Selection

Following the approval of the Gazi University Ethics Committee (no: 91610558-604.01.02, research code no: 2020-366), the medical records of patients who underwent surgery for NSCLC between January 2018 and August 2020 were examined retrospectively. An informed consent form was obtained from the patients or their relatives included in the study. During the study period, data of patients with cancer recurrence detected on imaging modality, were collected. Inclusion criteria were, detection of local recurrence of lung cancer at the surgical side on PET/CT, specification of using ORC in the surgical notes, and reporting of histopathological diagnosis of biopsy taken from the recurrence site was the foreign body reaction. Patients whose histopathological result were reported as only "non-malignant" were not included in the study. In addition, patients whose follow-up records could not be obtained, and those whose surgical notes did not indicate the use of ORC, were excluded from the study. Data of patients were collected according to age, gender, localization of recurrence, adjuvant therapy status, smoking status, resolution status, total resolution time (day) of agent, maximum standard uptake value (SUV_{max}) on the PET/CT, stage of the tumor, comorbidity status, postoperative complication, and the detection time of false tumor recurrence.

Statistical Analysis

All analyses were performed using the IBM SPSS version 20.0 software (IBM Corp., Armonk, NY, USA). Due to the small sample size, we only performed descriptive analysis. Descriptive data were expressed in mean ± standard deviation (SD), median (minimum-maximum) or number and frequency. The distribution of numeric variables was evaluated by histogram and Kolmogrov-Smirnov test. The mean ± SD was used for normal distributions and median value with range (minimum-maximum) was used for skewed distributions.

Results

During the study period, we detected 293 patients undergoing surgery for NSCLC in our clinic, and 160 of them (54.7%) required adjuvant treatment. Eleven of the

Table 1. Characteristics of the patients included in the study

Case	Age	Sex	Smoking P/Y	Co-morbidity	Diagnosis	Surgery	Post-op course	Induction therapy	Adjuvant therapy	Localization	PET/CT SUV$_{max}$	pTNM[1]	Detection time[2] (day)	Resolution time (day)
1	59	M	90	-	TTNA	BLI	Pneumonia	-	CRT	Intercostal	9.6	T1cN2M0	128	Unknown
2	65	M	60	CAD, HT	EBUS-TBNA	RUSL	-	CT	CT	RPT	11	T1cN1M0	120	762
3	69	M	100	COPD	EBUS-TBNA	RUSL	-	-	CT	RPT	6.2	T3N0M0	52	222
4	63	M	30	HT	EBUS-TBNA	V-RUL	-	-	CRT	Hilar	2.9	T1N2M0	208	No resolved (progression)
5	60	F	15	HT, DM	EBUS-TBNA	RUL + S6	-	CT	CRT	SC, RPT	9.3	T1aNoM0	139	519
6	66	M	30	HT, Arrhythmia	T	RML	Pneumonia	-	-	Bronchial stump	5.9	No viable tumor	154	343
7	55	M	60		EBUS-TBNA	LP	Pneumonia Pl. effusion	CT	CT	Hilar	2.9	T2bN0M0	149	No resolved
8	62	M	45	CAD	EBUS-TBNA	VRS1	-	-	CT	RPT	6.2	T1bN0M0	149	326
9	64	M	-	HT	EBUS-TBNA	RUL	-	-	CRT	RPT	1.7	T4N2M0	105	316
10	77	M	90	-	EBUS-TBNA	LUL	Pneumonia	-	-	SC	4.4	T2bN0M0	135	431
11	66	M	50	-	EBUS-TBNA	BLI	COVID-19pneumonia	-	CT	SC	10.4	T3N0M0	132	317

1: According to the 8th tumor-node-metastasis system.
2: Detection time after the surgery.
BLI: Bilobectomy inferior, CAD: Coronary artery diseases, CRT: Chemo-Radiotherapy, COPD: Chronic obstructive pulmonary diseases, CT: Chemotherapy, EBUS-TBNA: Endobronchial ultrasound-guided transbronchial needle aspiration, HT: Hypertension, LP: Left pneumonectomy, LUL: Left upper lobectomy, P/Y: Pack/year, Pl: Pleural, RML: Right middle lobectomy, RPT: Right paratracheal, RUL.: Right upper lobectomy, RUSL: Right upper sleeve lobectomy, S6: Lower lobe superior segmentectomy, SC: Subcarinal, T: Thoracotomy, TTNA: Transthoracic needle aspiration, VRS1: VATS right upper anterior segmentectomy, V-RUL: VATS right upper lobectomy

patients who met the inclusion criteria were included in the study. The general characteristics of the patients are given in Table 1. There was 1 female (9.1%) and 10 males (90.9%); the median age was 64 (age range: 55-77). The median SUV$_{max}$ was 6.4 (range: 1.7-11, Figure 1) on PET/CTs. Diagnosis was made with transthoracic tru-cut needle biopsy in 1 patient (9.1%), thoracotomy in 1 patient (9.1%), and EBUS-TBNA in 9 patients (81.8%) (Figure 2a). Histopathological results of all patients were reported as foreign body reactions (Figure 2b). Nine patients (81.8%) received adjuvant therapy. The most common area of false tumor recurrence was the right paratracheal area in 5 patients (45.4%). The median detection time of PET/CT positivity after surgery was 139 days (range: 52-208 days). False tumor images improved in 8 patients (72.7%) in their control radiological examinations. ORC was not resorbed radiologically in 2 patients. The median resolution time of ORC was 334 days (range: 222-762 days). Radiological progression was detected in one patient, and the histopathological report of the biopsy taken by EBUS-TBNA indicated a true tumor recurrence in the same region 18 months after the initial surgery. One of the patients included in the study died and the survival was 31 months. Other patients were alive at the date of the study and the median survival was 34 months (Table 2).

Discussion

In this study, we demonstrated that ORC can cause false tumor recurrence in some patients due to delayed absorption. Tumor recurrence is not rare in patients who underwent surgery for NSCLC. About 40% of all tumor recurrences is isolated in distant metastases, while the remaining recurrences are local or combined (local and distant). The incidence of isolated local tumor recurrence after surgery has been reported to range between 6 and 28% and 20%-40% for stage I and stage II tumors, respectively. Unfortunately, in the case of local tumor recurrence or distant metastasis, treatment success is low and the median survival time is 8.1-18.7 months (7,8). There is no definitive consensus on the postoperative follow-up period and optimal imaging modality
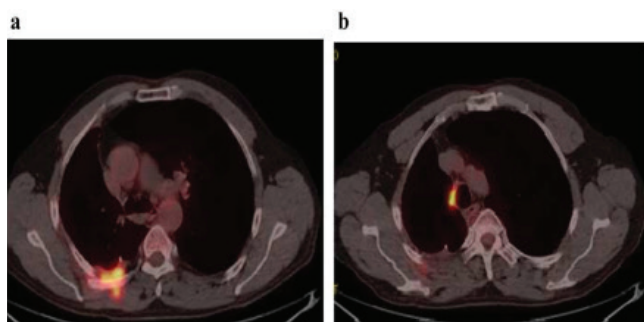
Figure 1. (a) PET/CT image of case 1. A pathological increased uptake at right posterior chest wall with SUV_{max} 9.3. Result of histopathologic examination of biopsy taken by trans-thoracic tru-cut biopsy was foreign body reaction. (b) A pathologic increased uptake (SUV_{max}: 11) was detected at the right paratracheal area on PET/CT of case 2

PET/CT: Positron emission tomography/computed tomography, SUV_{max}: Maximum standard uptake value
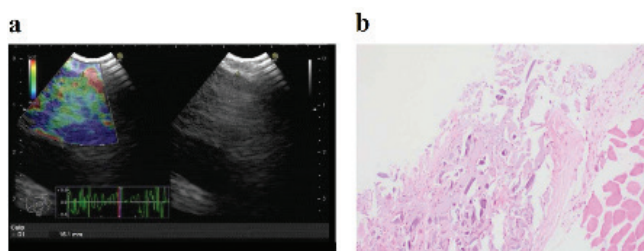
Figure 2. (a) EBUS-image of case 3 shows; indistinct margin, oval shape and heterogeneous echogenicity, partially blue partially non-blue (green, yellow and red) elastographic type in the right paratracheal area. (b) Histopathologically; granulation tissue characterized by numerous multinucleated giant cells is seen in the area adjacent to the normal muscle tissue (hematoxylin-eosin stain x100)

EBUS: Endobronchial ultrasound

Table 2. Survival time, date of surgery, and date of false positivity on PET/CT of patients

Case	Date of surgery	Date of detection	Survivability	Survival time* (month)
1	27/03/2019	02/08/2019	Alive	36
2	13/12/2018	14/04/2019	Exitus	31
3	28/06/2019	19/08/2019	Alive	32
4	11/04/2019	05/11/2019	Alive	35
5	03/07/2019	19/11/2019	Alive	32
6	02/02/2019	06/07/2019	Alive	37
7	08/05/2019	14/10/2019	Alive	34
8	06/04/2019	02/09/2019	Alive	35
9	31/01/2019	16/05/2019	Alive	37
10	31/08/2020	13/01/2021	Alive	18
11	25/08/2020	04/01/2021	Alive	18

*Survival time was calculated according to the current date for living patients. PET/CT: Positron emission tomography/computed tomography

for patients after lung cancer surgery. The common tendency is that patients are followed up with thoraco-abdominal CT or PET/CT at intervals of 3-6 months in the first 2 years, postoperatively. In our department, postsurgical follow-up is performed out in accordance with the National Comprehensive Cancer Network guidelines (radiological follow-up is performed once every 3 months in the first 2 years and PET/CT is performed in the presence of suspected tumor recurrence). The time of local recurrence and distant metastasis after surgery are similar. Boyd et al. (7) reported that the mean durations of distant metastasis and local tumor recurrence were 12.5% and 13.6 months, respectively. However, in our study, the median time of false PET/CT positivity after surgery was 139 days. The possible reason for this difference may be that early radiological tumor recurrence tends to be false positives.

In lung cancer surgery, cellulose hemostatic agents, such as ORC, are placed to provide hemostasis, particularly in the subcarinal and paratracheal areas after lymph node dissection. It may also be necessary to place it in the posterior intercostal space in patients undergoing thoracotomy. ORC is a self-absorbable product and it completely dissolves within 2-4 weeks without causing an inflammatory reaction. However, the reabsorption time of ORC may be prolonged by some reasons, and it may cause inflammation in the localizations where it is placed, thus it may give the appearance of a false tumor recurrence in PET/CT (6,10). The presence of pneumonia or pleural infection in patients during the postoperative period may cause increased inflammation around the materials. Adjuvant treatments (chemotherapy and/or radiotherapy) may also have a similar effect. In our study, most of the patients (81.8%) had a history of adjuvant therapy, and postoperative infection was only considered as the cause of false PET/CT positivity in 2 cases. Some studies in the literature have reported that these agents have the appearance of an abscess on radiological imaging, and their unnecessary use may result in the mediastinal infection (6,10,11). In our series, there were no radiological findings of an abscess, and the histopathological results were incompatible with the infection. In addition, there was no case of mediastinitis related to the use of ORC during the study period.

Study Limitations

This study had some limitations. It is a retrospective, single-center study, and it included few patients. Thus, we could not determine whether there were any correlations between false tumor recurrence and some variables, such as smoking habit, adjuvant/neoadjuvant treatment regimens, and tumor histopathology. However, this study may be

Sayan et al. False Tumor Recurrence on PET/CT

Mol Imaging Radionucl Ther 2023;32:8-12

deemed a preliminary report that may inspire researchers to conduct multicenter studies with many patients.

Conclusion

Surgeons should specify whether using ORC and its localization in the surgical notes of patients undergoing pulmonary resections for lung cancer. False tumor recurrence should be considered when radiologic early tumor recurrence is detected in the postsurgical follow-up, particularly in patients receiving adjuvant therapy and those with a history of postoperative infection. Thus, unnecessary treatment and re-surgical interventions can be prevented.

Ethics

Ethics Committee Approval: Gazi University Ethics Committee (no: 91610558-604.01.02, research code no: 2020-366).

Informed Consent: An informed consent form was obtained from the patients or their relatives included in the study.

Peer-review: Externally peer-reviewed.

Authorship Contributions

Surgical and Medical Practices: M.S., A.Ç., N.Y.D., G.A., İ.C.K., Concept: M.S., A.Ç., M.Ş.T., D.Ö., I.A., O.Y., N.Y.D., G.A., İ.C.K., A.İ.T., U.A., Design: M.S., A.Ç., M.Ş.T., D.Ö., I.A., O.Y., N.Y.D., G.A., İ.C.K., A.İ.T., U.A., Data Collection or Processing: M.S., A.Ç., M.Ş.T., D.Ö., I.A., O.Y., N.Y.D., G.A., İ.C.K., A.İ.T., U.A., Analysis or Interpretation: M.S., A.Ç., M.Ş.T., D.Ö., I.A., O.Y., N.Y.D., G.A., İ.C.K., A.İ.T., U.A., Literature Search: M.S., A.Ç., I.A., O.Y., Writing: M.S., A.Ç., O.Y.

Conflict of Interest: No conflict of interest was declared by the authors.

References

1. Martin J, Ginsberg RJ, Venkatraman ES, Bains MS, Downey RJ, Korst RJ, Kris MG, Rusch VW. Long-term results of combined-modality therapy in resectable non-small-cell lung cancer. J Clin Oncol 2002;20:1989-1995.

2. Sekihara K, Hishida T, Yoshida J, Oki T, Omori T, Katsumata S, Ueda T, Miyoshi T, Goto M, Nakasone S, Ichikawa T, Matsuzawa R, Aokage K, Goto K, Tsuboi M. Long-term survival outcome after postoperative recurrence of non-small-cell lung cancer: who is 'cured' from postoperative recurrence? Eur J Cardiothorac Surg 2017;52:522-528.

3. Yuan Q, Wang W, Zhang Q, Wang Y, Chi C, Xu C. Clinical features and prognostic factor of thoracic postoperative oligo-recurrence of non-small-cell lung cancer. Cancer Manag Res 2020;12:1397-1403.

4. Israel O, Kuten A. Early detection of cancer recurrence: 18F-FDG PET/CT can make a difference in diagnosis and patient care. J Nucl Med 2007;48(Suppl 1):28S-35S.

5. Weber WA, Figlin R. Monitoring cancer treatment with PET/CT: does it make a difference? J Nucl Med 2007;48(Suppl 1):36S-44S.

6. Haidari TA, Petersen RH, Skov BG, Ravn J. Oxidized resorbable cellulose (Gelita-cel) causing foreign body reaction in the mediastinum. Interact Cardiovasc Thorac Surg 2018;27:881-883. Erratum in: Interact Cardiovasc Thorac Surg 2019;29:495.

7. Boyd JA, Hubbs JL, Kim DW, Hollis D, Marks LB, Kelsey CR. Timing of local and distant failure in resected lung cancer: implications for reported rates of local failure. J Thorac Oncol 2010;5:211-214.

8. Okami J, Nishiyama K, Fujiwara A, Konishi K, Kanou T, Tokunaga T, Teshima T, Higashiyama M. Radiotherapy for postoperative thoracic lymph node recurrence of non-small-cell lung cancer provides better outcomes if the disease is asymptomatic and a single-station involvement. J Thorac Oncol 2013;8:1417-1424.

9. Williams BA, Sugimura H, Endo C, Nichols FC, Cassivi SD, Allen MS, Pairolero PC, Deschamps C, Yang P. Predicting postrecurrence survival among completely resected nonsmall-cell lung cancer patients. Ann Thorac Surg 2006;81:1021-1027.

10. Melamed JW, Paulson EK, Kliewer MA. Sonographic appearance of oxidized cellulose (Surgicel): pitfall in the diagnosis of postoperative abscess. J Ultrasound Med 1995;14:27-30.

11. Cantero M, Parra LM, Sierra-Marticorena J, Ramos A, Ganga B, Asensio A. Cellulose-derived absorbable hemostatic product as a risk factor for mediastinitis after cardiac surgery. Surg Infect (Larchmt) 2019;20:378-381.

Axillary Lymph Node Uptake on ^{18}F-FDG PET/CT after COVID-19 Vaccination: A Direct Comparison Study with Influenza Vaccination

COVID-19 Aşısından Sonra ^{18}F-FDG PET/BT'de Aksiller Lenf Nodu Tutulumu: Grip Aşısı ile Doğrudan Karşılaştırma Çalışması

 Yoichi Otomi[1], *Takayoshi Shinya[1],* *Hiroto Kasai[1],* *Naoko Okada[2],* *Tomoki Matsushita[1],* *Kohei Higashi[1],*
 Saya Matsuzaki[1], *Yuka Hiroshima[1],* *Michiko Kubo[1],* *Hideki Otsuka[1],* *Masafumi Harada[1]*

[1]*Tokushima University Hospital, Department of Radiology, Tokushima, Japan*
[2]*Tokushima Prefectural Central Hospital, Department of Radiology, Tokushima, Japan*

Abstract

Objectives: To compare vaccinated-side axillary lymph node uptake on ^{18}F-fluorodeoxyglucose (FDG) positron emission tomography/computed tomography (PET/CT) after coronavirus disease-2019 (COVID-19) and influenza vaccination.

Methods: We retrospectively analyzed 177 patients who underwent ^{18}F-FDG PET/CT after COVID-19 or influenza vaccination. We compared the uptake of the vaccinated-side axillary lymph nodes of 109 COVID-19 vaccinated patients with those of a lot of influenza-vaccinated patients. We also compared the uptake between 66 patients who received the first COVID-19 vaccination with 43 who received the second COVID-19 vaccination.

Results: ^{18}F-FDG-avid axillary lymph nodes on the vaccinated side were significantly more frequently observed in the COVID-19 group (45%) than in the influenza group (19%) (p<0.001). When the interval between vaccination to PET/CT was within 7 days, there was no significant difference in the frequency of ^{18}F-FDG-avid vaccinated-side axillary lymph nodes between the groups (COVID-19 group: 41% vs. influenza group: 45%, p=0.724). When the interval was over 7 days, ^{18}F-FDG-avid lymph nodes were much more frequent in the COVID-19 group (47%) than in the influenza group (7%) (p<0.001). Comparing the first and second COVID-19 groups, ^{18}F-FDG-avid lymph nodes were more frequent in the second vaccination group than in the first vaccination group, but the difference was not significant.

Conclusion: ^{18}F-FDG-avid vaccinated-side axillary lymph nodes were more frequently observed in the COVID-19 group than in the influenza group. In the case of the COVID-19 vaccine, a delay of ^{18}F-FDG PET/CT examination is recommended by a longer interval from vaccination than in the influenza vaccine.

Keywords: COVID-19, influenza, vaccination, ^{18}F-FDG PET/CT, axillary lymph node

Öz

Amaç: Koronavirüs hastalığı-2019 (COVID-19) aşısı ve grip aşısı sonra ^{18}F-florodeoksiglukoz (FDG) pozitron emisyon tomografisi/bilgisayarlı tomografi (PET/BT) ile aşılanan taraf aksiller lenf nodu tutulumunu karşılaştırmaktır.

Yöntemler: COVID-19 veya influenzaya yönelik aşılamadan sonra ^{18}F-FDG PET/BT uygulanan 177 hastayı retrospektif olarak inceledik. COVID-19 aşısı yapılan 109 hastanın aşılanmış taraftaki aksiller lenf nodlarındaki ^{18}F-FDG tutulumunu, grip aşısı yapılan hastalardaki tutulum ile karşılaştırdık. Ayrıca ilk COVID-19 aşısını olan 66 hasta ile ikinci COVID-19 aşısını olan 43 hasta arasındaki alımı karşılaştırdık.

Bulgular: Aşılanan taraftaki ^{18}F-FDG tutulumu olan aksiller lenf nodları, COVID-19 grubunda (%45) influenza grubuna (%19) göre anlamlı derecede daha sık gözlendi (p<0,001). PET/BT ile aşılama arasındaki aralık 7 gün içinde olduğunda, gruplar arasında ^{18}F-FDG tutulumu olan aşılı taraf aksiller

Otomi et al. Effects of vaccines on PET/CT

Mol Imaging Radionucl Ther 2023;32:13-19

lenf nodu sıklığında anlamlı bir fark yoktu (COVID-19 grubu: %41 vs. influenza grubu: %45, p=0,724). Aralık 7 günden fazla olduğunda, ^{18}F-FDG tutulumlu lenf nodları, COVID-19 grubunda (%47) influenza grubuna (%7) göre çok daha sıktı (p<0,001). Birinci ve ikinci COVID-19 grupları karşılaştırıldığında, ^{18}F-FDG tutulumlu lenf nodları ikinci aşılama grubunda birinci aşılama grubuna göre daha sıktı ancak aradaki fark anlamlı değildi.

Sonuç: ^{18}F-FDG tutulumlu aşılanmış taraf aksiller lenf nodları, COVID-19 grubunda influenza grubuna göre daha sık gözlendi. COVID-19 aşısı söz konusu olduğunda, ^{18}F-FDG PET/BT incelemesinin, grip aşısına göre daha uzun bir aralıkla ertelenmesi önerilir.

Anahtar Kelimeler: COVID-19, influenza, aşılama, ^{18}F-FDG PET/BT, aksiller lenf nodu

Introduction

The coronavirus disease-2019 (COVID-19) pandemic caused by severe acute respiratory syndrome coronavirus-2 is rampant worldwide (1). Safe and effective vaccines are urgently needed against this disease (2,3). Currently, mass COVID-19 vaccination is being conducted worldwide (4). Recently, there have been many reports of increased uptake of axillary lymph nodes on the vaccinated side on ^{18}F-fluorodeoxyglucose (FDG) positron emission tomography/computed tomography (PET/CT) after COVID-19 vaccination (5,6,7,8,9,10,11,12,13). Apart from case reports, there are also comprehensive reports on the frequency and degree of uptake. Some studies have reported differences among the types of COVID-19 vaccines. Before the report of increased axillary lymph node uptake on ^{18}F-FDG PET/CT after COVID-19 vaccination, there were several reports on increased axillary lymph node uptake after influenza vaccination (14,15,16,17). The increased uptake of axillary lymph nodes after seasonal influenza vaccination on ^{18}F-FDG PET/CT has been reported, especially within 1 week after vaccination (14,15). However, in the case of the COVID-19 vaccine, it was observed more than 1 month or 6 weeks after vaccination (12,13). As aforementioned, some studies have compared uptake after influenza vaccination; however, there have been no reports directly comparing the uptake of axillary lymph nodes on ^{18}F-FDG PET/CT after COVID-19 vaccination and after influenza vaccination.

In this study, we compared axillary lymph node uptake on ^{18}F-FDG PET/CT after COVID-19 vaccination with that after influenza vaccination.

Materials and Methods

We retrospectively analyzed 177 patients who underwent ^{18}F-FDG PET/CT after COVID-19 vaccination (BNT162b2 mRNA vaccine, Pfizer) or influenza vaccination. We compared the uptake of the vaccinated side axillary lymph nodes of 109 patients who received COVID-19 vaccine with 68 patients who received influenza vaccine. To investigate the effect of the interval from vaccination to PET examination on the positive accumulation of axillary lymph nodes, the frequency of positive accumulation within 7 days and after 7 or more days was compared for

each vaccine.

Before the above comparison, we also compared the uptake of vaccinated side axillary lymph nodes of 66 patients who received the first COVID-19 vaccination with those of 43 patients who received the second COVID-19 vaccination.

Patients

Based on the medical interview sheet for ^{18}F-FDG PET/CT examination, patients were placed in the COVID-19 and influenza vaccine groups. The COVID-19 vaccine group comprised patients who received COVID-19 vaccination within 50 days before undergoing ^{18}F-FDG PET/CT examination from May 10, 2021, to July 5, 2021. The influenza vaccine group comprised patients who received influenza vaccination within 50 days before undergoing ^{18}F-FDG PET/CT examination from October 1, 2020, to December 8, 2020. Patients with insufficient information on the date of vaccination and the vaccinated site were excluded. Patients with hyperglycemia (>150 mg/dL), suspected axillary lymph node metastases, or suspected malignant lymphoma lesions, and those with rheumatoid arthritis were excluded. A total of 109 patients (51 men and 58 women) after COVID-19 vaccination (after the first vaccination: 66 cases, after the second vaccination: 43 cases) and 68 patients after influenza vaccination (24 men and 44 women) were evaluated.

The Ethics Committee of Tokushima University Hospital approved this study (no: 4080). Informed consent was waived owing to the retrospective nature of the study.

^{18}F-FDG PET/CT Scanning

The patients fasted for at least 6 h before the ^{18}F-FDG PET/CT. after that, the patients received an intravenous injection of 3.0 MBq/kg of body weight of ^{18}F-FDG. ^{18}F-FDG PET/CT image acquisition was started 1 h after the ^{18}F-FDG injection with the patient in a relaxed supine position using an integrated PET/CT scanner (Discovery PET/CT 710; GE Healthcare, Milwaukee, WI, USA). A CT scan was obtained from the head to mid-thigh level, using a standardized protocol involving 120 kV, tube-rotation time of 0.6 s per rotation, and section thickness of 3.75 mm, and used for anatomical localization and attenuation correction. The PET acquisition time was 2 min per table position, with 7-9 bed

Mol Imaging Radionucl Ther 2023;32:13-19

Otomi et al. Effects of vaccines on PET/CT

positions per patient. PET reconstructions were generated using penalized likelihood reconstruction (Q.Clear, GE Healthcare) with a β value of 550. All PET datasets were reconstructed with a 192×192 matrix using an ordered-subset expectation maximization iterative reconstruction algorithm.

Evaluating the ¹⁸F-FDG Uptake of the Axillary Lymph Nodes of the Two Groups

A board-certified nuclear medicine physician with PET/CT experience of 12 years evaluated the ¹⁸F-FDG PET/CT images. The maximum standardized uptake values (SUV$_{max}$) of the axillary lymph nodes with the highest uptake, normalized for body weight, were calculated on the viewer (AW server 2.0; GE Healthcare, Milwaukee, WI, USA). Positive axillary lymph node uptake was defined as a ratio ≥1.5 between SUV$_{max}$ on the vaccinated side and the contralateral side, a method previously used (11,16). The size of the largest hypermetabolic lymph node was also measured on CT images in millimeters in short-axis diameter.

Statistical Analysis

Categorical variables are expressed as frequencies and percentages. Continuous variables are expressed as mean ± standard deviation. The normality of the distribution of variables was tested using Levene's test. The Student's t-test for normally distributed data and Welch's t-test or chi-square test for non-normally distributed data were applied to evaluate the differences in the variables. All statistical tests were performed using the SPSS Statistics software version 25 (IBM, Armonk, NY, USA). For all comparisons, a p value of < 0.05 was considered statistically significant.

Results

A comparison of the clinical characteristics related to PET/CT and vaccination of 66 patients from the post-first COVID-19 vaccination group and 43 from the post-second COVID-19 vaccination group are shown in Table 1. Sex, weight, height, blood glucose, ¹⁸F-FDG dose on PET/CT examination, time interval PET/CT examination from last vaccination, rate of PET/CT examinations within 7 days from the last vaccination, and injected side of the upper arm of the vaccine were not significantly different between the two groups. The rate of patients with ¹⁸F-FDG-avid axillary lymph nodes on the vaccinated side in the post-second COVID-19 vaccine group was higher than that in the post-first COVID-19 vaccine group, but not significantly (p=0.148). The average SUV$_{max}$ of the ¹⁸F-FDG-avid axillary lymph nodes on the vaccinated side in the second COVID-19 vaccine group was slightly higher than that in the first

COVID-19 vaccine group, but not significantly (p=0.630). The average short-axis of the largest ¹⁸F-FDG-avid axillary lymph nodes on the vaccinated side in the first and second COVID-19 vaccine groups was not significantly different (p=0.815).

The details of the clinical characteristics related to PET/CT and vaccination of 109 patients from the COVID-19 vaccine group and 68 from the influenza vaccine group are shown in Table 2. Patient age, sex, weight, height, blood glucose, ¹⁸F-FDG dose, interval time to PET/CT exam from the last vaccination, and the rate of PET/CT examinations

Table 1. Comparison of post-first and-second COVID-19 vaccination groups

	Post first COVID-19 vaccination group (n=66)	Post second COVID-19 vaccination group (n=43)	p value
Patient age, years	72.2±8.6	69.5±13.2	0.240
Sex			
Female	35	23	0.132
Male	31	20	
Weight (kg)	55.3±10.2	56.7±10.0	0.473
Height (cm)	158.2±8.7	158.4±7.5	0.918
Blood glucose (mg/dL)	104.4±14.4	101.4±15.7	0.310
¹⁸F-FDG (MBq)	165.9±31.2	168.8±31.0	0.630
Time interval to PET/CT exam from the last vaccination, days	12.0±7.8	15.5±11.9	0.094
Within 7 days from the last vaccination	18 (27%)	14 (33%)	0.554
Injected side of upper arm			
Right	7 (11%)	10 (23%)	0.075
Left	59 (89%)	33 (77%)	
Patients with ¹⁸F-FDG-avid axillary LN of vaccinated-side	26 (39%)	23 (53%)	0.148
SUV$_{max}$ of ¹⁸F-FDG-avid axillary LN of vaccinated-side	5.1±2.9	5.5±3.1	0.630
Short-axis of the largest ¹⁸F-FDG-avid axillary LN of vaccinated-side (mm)	5.3±1.4	5.2±1.5	0.815

Data are presented as mean ± standard deviation. Statistical significance was set at p<0.05. COVID-19: Coronavirus disease-2019; FDG: Fluorodeoxyglucose, LN: Lymph node, SUV$_{max}$: Maximum standardized uptake value

Table 2. Comparison of COVID-19 and influenza vaccination groups

	COVID-19 vaccine group (n=109)	Influenza vaccine group (n=68)	p value
Patient age, years	71.1±10.6	67.3±13.7	0.056
Sex			
Female	58	44	0.132
Male	51	24	
Weight (kg)	55.8±10.1	57.6±13.7	0.363
Height (cm)	158.3±8.2	157.1±9.1	0.402
Blood glucose (mg/dL)	103.2±14.9	103.4±17.3	0.957
PET/CT indication			
Lung malignancy	23 (21%)	13 (19%)	
Breast malignancy	21 (19%)	21 (31%)	
Head and neck malignancy	18 (17%)	10 (15%)	
Digestive/gastrointestinal malignancy	12 (11%)	9 (13%)	
Hematological malignancy	7 (6%)	4 (6%)	
Gynecological malignancy	5 (5%)	4 (6%)	
Genitourinary malignancy	4 (4%)	4 (6%)	
Musculoskeletal malignancy	4 (4%)	1 (1%)	
Others	15 (14%)	2 (3%)	
^{18}F-FDG (MBq)	167.0±31.0	175.3±44.3	0.179
Interval time to PET/CT exam from the last vaccination, days	13.4±9.7	16.7±11.8	0.053
Within 7 days from the last vaccination	32 (29%)	22 (32%)	0.674
Injected side of the upper arm			
Right	17	20	0.028*
Left	92	48	
Patients with ^{18}F-FDG-avid axillary LN on the vaccinated-side	49 (45%)	13 (19%)	<0.001*
SUV$_{max}$ of ^{18}F-FDG-avid axillary LN on the vaccinated-side	5.3±3.0	4.4±3.3	0.319
Short-axis of the largest ^{18}F-FDG-avid axillary LN on the vaccinated-side (mm)	5.2±1.4	5.0±1.6	0.647

Data are presented as mean ± standard deviation. *Statistical significance was set at p<0.05. COVID-19: Coronavirus disease-2019; FDG:Fluorodeoxyglucose, LN: Lymph node, SUV$_{max}$: Maximum standardized uptake value

within 7 days of the last vaccination were not significantly different between the two groups. There was a significant difference in the vaccine-injected side of the upper arm between the two groups. The number of patients with ^{18}F-FDG-avid axillary lymph nodes on the vaccinated side in the COVID-19 and influenza vaccine groups was 49 (45%) and 13 (19%), respectively (p<0.001).

The average SUV$_{max}$ of the ^{18}F-FDG-avid axillary lymph node on the vaccinated side in the COVID-19 vaccine group was higher than that in the influenza vaccine group, but the difference was not significant (p=0.319). The average short-axis of the largest ^{18}F-FDG-avid axillary lymph node on the vaccinated side in the COVID-19 vaccine group was slightly larger than that in the influenza vaccine group, but not significantly (p=0.647). A comparison of the number of cases of ^{18}F-FDG-avid axillary lymph nodes on the vaccinated side by the interval from the last vaccination in the COVID-19 and influenza vaccine groups is shown in Table 3. Thirteen of the 32 patients (41%) with PET/CT performed within 7 days from the last vaccination in the COVID-19 vaccine group showed ^{18}F-FDG-avid axillary lymph node on the vaccinated side. Ten of the 22 patients (45%) with PET/CT performed within 7 days from the last vaccination in the influenza vaccine group showed ^{18}F-FDG-avid axillary lymph nodes on the vaccinated side. There was no significant difference between the two groups (p=0.724). Thirty-six of the 77 patients (47%) with PET/CT performed after over 7 days from the last vaccination in the COVID-19 vaccination group showed ^{18}F-FDG-avid axillary lymph nodes of the vaccinated side. Three of the 46 patients (7%) with PET/CT performed after over 7 days from the last vaccination in the influenza vaccination group showed ^{18}F-FDG-avid axillary lymph node on the vaccinated

Table 3. Comparison of the number of cases of ^{18}F-FDG-avid axillary LNs on the vaccinated-side by time interval from the last vaccination to PET/CT in COVID-19 and influenza vaccination groups

	COVID-19 vaccine group (n=109)	Influenza vaccine group (n=68)	p value
0-7 days			
^{18}F-FDG-avid axillary LN (+)	13 (41%)	10 (45%)	0.724
^{18}F-FDG-avid axillary LN (-)	19 (59%)	12 (55%)	
>7 days			
^{18}F-FDG-avid axillary LN (+)	36 (47%)	3 (7%)	<0.001*
^{18}F-FDG-avid axillary LN (-)	41 (53%)	43 (93%)	

Data are presented as mean ± standard deviation. *Statistical significance was set at p<0.05. COVID-19: Coronavirus disease 2019, FDG: Fluorodeoxyglucose, LN: Lymph node

side. There was a significant difference between the two groups (p<0.001).

Figure 1 shows the PET/CT images of a patient after COVID-19 vaccination showing ^{18}F-FDG-avid vaccinated-side axillary lymph node. Figure 2 shows the PET/CT images of a patient after influenza vaccination showing ^{18}F-FDG-avid vaccinated-side axillary lymph node.

Discussion

^{18}F-FDG-avid axillary lymph node of the vaccinated side on PET/CT was significantly more frequent in the patients after COVID-19 vaccination than in those after influenza vaccination. Of the total, 45% of the patients showed ^{18}F-FDG-avid axillary lymph node on the vaccinated-side on PET/CT after COVID-19 vaccination and 19% of the patients after influenza vaccination. In a previous study, the frequency of ^{18}F-FDG-avid axillary lymph nodes on the vaccinated side on PET/CT after COVID-19 vaccination (Pfizer-BioNTech) was reported to be 43% (12). In another study, the type of COVID-19 vaccine was not specified, but the frequency of uptake was 45% (11). Yet another study reported a frequency of 45.6% (9). The results of COVID-19 vaccination in our study were similar to previous reports. Burger et al. (17) reported that 17 of the 58

(29.3%) patients who were vaccinated for influenza within 4 weeks before PET/CT (mean, 14.5±8.7 days) had ^{18}F-FDG-avid vaccinated-side axillary lymph nodes. The frequency of 29.3% in the previous report was higher than the result of our study on influenza vaccination. Skawran et al. (12) reported that ^{18}F-FDG PET/CT after COVID-19 vaccination had a higher frequency of ^{18}F-FDG-avid axillary lymph node compared with the findings of a previous paper on PET/CT after influenza vaccination. Since our study was a comparison between the axillary lymph node uptake after COVID-19 vaccination and influenza vaccination under the same imaging conditions with the same equipment in the same facility, the comparison of values, such as the frequency and SUV$_{max}$ could be more accurate.

In comparison with PET examinations within 7 days from the last vaccination, there was no significant difference in the frequency of ^{18}F-FDG-avid axillary lymph nodes on the vaccinated side between the COVID-19 and influenza groups. On PET/CT, 41% of the patients showed ^{18}F-FDG-avid axillary lymph nodes on the vaccinated side after COVID-19 vaccination and 45% of the patients after influenza vaccination. However, compared with PET examinations over 7 days from the last vaccination, there was a significant difference in the frequency of ^{18}F-FDG-
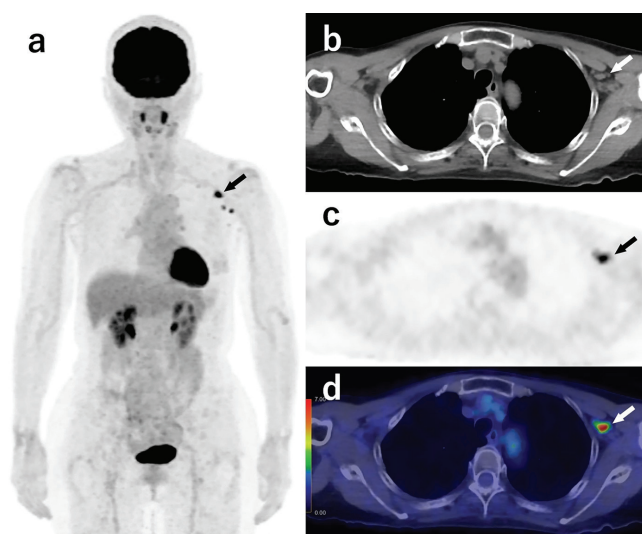
Figure 1. (a) MIP, (b) CT, (c) PET, and (d) fused PET/CT. ^{18}F-FDG PET/CT images of the representative case of a 67-year-old female in which ^{18}F-FDG uptake was observed in the axillary LN on the ipsilateral side to the COVID-19 vaccination arm (arrows). The interval time from vaccination to PET/CT exam was 19 days. The SUV$_{max}$ was 11.2. The size of the largest hypermetabolic LN was 4.2 mm in short-axis diameter
MIP: Maximum intensity projection, PET: Positron emission tomography, CT: Computed tomography, FDG: Fluorodeoxyglucose, LN: Lymph node, COVID-19: Coronavirus disease-2019, SUV$_{max}$: Maximum standardized uptake value
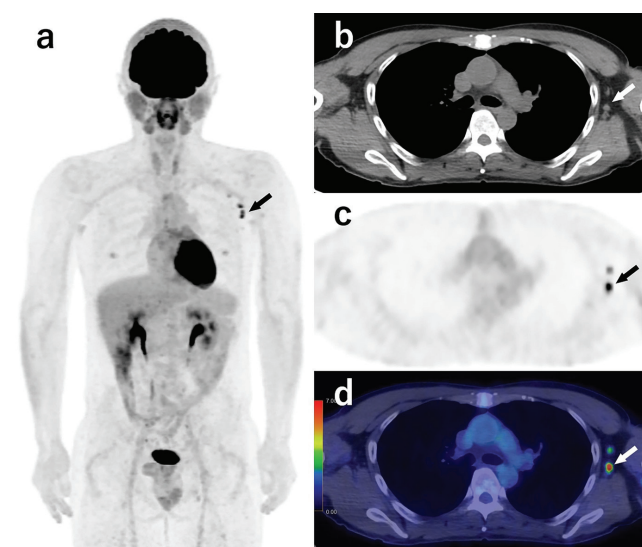
Figure 2. (a) MIP, (b) CT, (c) PET, and (d) fused PET/CT. ^{18}F-FDG PET/CT images of the representative case of a 39-year-old male in which ^{18}F-FDG uptake was observed in the axillary LN on the ipsilateral side to the influenza vaccination arm (arrows). The interval time from vaccination to PET/CT exam was 3 days. The SUV$_{max}$ was 7.7. The size of the largest hypermetabolic LN was 5.2 mm in short-axis diameter
MIP: Maximum intensity projection, PET: Positron emission tomography, CT: Computed tomography, FDG: Fluorodeoxyglucose, LN: Lymph node, COVID-19: Coronavirus disease-2019, SUV$_{max}$: Maximum standardized uptake value

avid axillary lymph nodes on the vaccinated-side between the COVID-19 and influenza groups. Of the total, 47% of the patients showed ^{18}F-FDG-avid axillary lymph nodes on the vaccinated-side on PET/CT after COVID-19 vaccination and 7% of the patients after influenza vaccination.

Although ^{18}F-FDG PET/CT after COVID-19 vaccination had a higher frequency of ^{18}F-FDG-avid vaccinated-side axillary lymph nodes than that after influenza vaccination, there was no difference in the frequency of ^{18}F-FDG-avid vaccinated-side axillary lymph nodes on PET/CT examination in the COVID-19 vaccine group and the influenza vaccine group when the PET/CT was performed within 7 days after the vaccine. When there were long intervals of more than 7 days from vaccination to examination, ^{18}F-FDG-avid vaccinated-side axillary lymph nodes on PET/CT were much more frequently observed in the COVID-19 vaccine group than in the influenza vaccine group, suggesting that the lymphadenopathy status could last longer in COVID-19 vaccination. This could be the reason why PET/CT examination after COVID-19 vaccination showed a higher positive rate of axillary lymph nodes on the vaccinated side than after influenza vaccination. In addition to the frequency, we compared the SUV$_{max}$ and size of the axillary lymph nodes in the COVID-19 and influenza groups and found that the SUV$_{max}$ was higher and the size was slightly larger in the COVID-19 vaccination group than in the influenza group, although the difference was not significant. Based on these results, in the case of the COVID-19 vaccine, it should be better to leave a longer period from vaccination to ^{18}F-FDG PET/CT examination than in the case of the influenza vaccine. In the case of COVID-19 vaccination, ^{18}F-FDG PET/CT examination after vaccination should probably be performed with a delay of several weeks to one month or more if there is little risk of the progression of the disease. Ferrari et al. (18) recommended that, if possible, ^{18}F-FDG PET/CT be examined at least 20 days after vaccination because the frequency of vaccine-related ^{18}F-FDG-avid lymph nodes decreases when the period from COVID-19 vaccination to ^{18}F-FDG PET/CT examination exceeds 20 days. Additionally, the National Comprehensive Cancer Network guidelines recommend the delay in imaging studies by 4 to 6 weeks following the COVID-19 vaccine if it does not result in a delay that will affect patient outcomes (19). To perform ^{18}F-FDG PET/CT examination at an appropriate time to evaluate lymph nodes more correctly, it is necessary to correctly grasp the vaccination date and information on the vaccination-side in advance.

The frequency of ^{18}F-FDG-avid axillary lymph nodes on the vaccinated side in the post-second COVID-19 vaccine group was higher than that in the post-first COVID-19 vaccine group, but not significantly (53% in the second

vaccination vs. 39% in the first vaccination group). Cohen et al. (9) reported that the frequency was significantly higher after the second vaccination (45.8%) than after the first vaccination (26.3%). In contrast, Skawran et al. (12) reported that the frequency was not significant in the Pfizer-BioNTech COVID-19 vaccination (44% after the second vaccination vs. 39% after the first vaccination). In addition to the frequency, we compared the SUV$_{max}$ and size of the axillary lymph node in the post-first and post-second COVID-19 vaccine groups and found that the SUV$_{max}$ was slightly higher in the post-second COVID-19 vaccination group than in the first group. There were no significant differences between the groups. The size was similar in both the groups.

Study Limitations

This study had some limitations. First, there was a selection bias because of the retrospective nature of the study. Second, the subject of this study was a PET/CT examination performed for cancer treatment, the results of which might be different from those of healthy individuals. The association between vaccinated-side axillary lymph node uptake, immune status, and hematologic malignancy has been reported in COVID-19 vaccinatio; however, but our study might include the effects of these factors (11,20). However, despite these limitations, this study is the first to directly compare vaccinated-side axillary lymph node uptake on ^{18}F-FDG PET/CT after COVID-19 vaccination and after influenza vaccination. This study revealed that there was no difference in the frequency of vaccinated-side axillary lymph node uptake on PET/CT examinations after COVID-19 vaccination and after influenza vaccination for a relatively short time interval of 7 days after the vaccination. It also revealed that the frequency was much higher on PET/CT after COVID-19 vaccination than after influenza vaccination for a longer interval time of over 7 days between the PET/CT and the vaccination. A more accurate interpretation of the axillary region could be expected by understanding the characteristics and differences of each type of vaccine, such as the frequency, uptake degree, and size of axillary lymph node uptake after vaccination.

Conclusion

There is no significant difference in the frequency of the ^{18}F-FDG-avid vaccinated-side axillary lymph nodes, SUV$_{max}$, or size between the first and second COVID-19 vaccinations. Therefore, careful interpretation of vaccinated-side axillary lymph nodes in ^{18}F-FDG PET/CT images after vaccination is required in both the first and second COVID-19 vaccinations.

To avoid false positives in the axillary lymph nodes, it is important to confirm the date of the recent vaccination

when scheduling an ^{18}F-FDG PET/CT examination. In the case of influenza vaccine, ^{18}F-FDG PET/CT examination should be performed at an interval of at least one week or more from vaccination. In the case of COVID-19 vaccine, ^{18}F-FDG PET/CT examination should probably be performed at a longer interval of several weeks to one month or more from vaccination. However, there are many cases where the early performance of ^{18}F-FDG PET/CT is necessary because treatment is urgent. In that case, it is better to perform without waiting.

Acknowledgments

Ethics

Ethics Committee Approval: The study was approved by the Ethics Committee of Tokushima University Hospital (no: 4080).

Informed Consent: Informed consent was waived owing to the retrospective nature of the study.

Peer-review: Externally and internally peer-reviewed.

Authorship Contributions

Medical Practices: Y.O., H.K., N.O., T.M., K.H., S.M., Y.H., M.K., Concept: Y.O., T.S., Design: Y.O., M.H., Data Collection, or Processing: Y.O., T.S., H.O., Analysis, or Interpretation: Y.O., T.S., M.K., H.O., M.H., Literature Search: Y.O., H.K., N.O., T.M., K.H., S.M., Writing: Y.O.

Conflict of Interest: No conflicts of interest was declared by the authors.

Financial Disclosure: The authors declare that this study received no financial support.

References

1. Johns Hopkins University Coronavirus Resource Center. COVID-19 dashboard by the Center for Systems Science and Engineering (CSSE) at Johns Hopkins University, https://coronavirus.jhu.edu/map.html (accessed April 2022).

2. Polack FP, Thomas SJ, Kitchin N, Absalon J, Gurtman A, Lockhart S, Perez JL, Pérez Marc G, Moreira ED, Zerbini C, Bailey R, Swanson KA, Roychoudhury S, Koury K, Li P, Kalina WV, Cooper D, Frenck RW Jr, Hammitt LL, Türeci Ö, Nell H, Schaefer A, Ünal S, Tresnan DB, Mather S, Dormitzer PR, Şahin U, Jansen KU, Gruber WC; C4591001 Clinical Trial Group. Safety and efficacy of the BNT162b2 mRNA Covid-19 vaccine. N Engl J Med 2020;383:2603-2615.

3. Baden LR, El Sahly HM, Essink B, Kotloff K, Frey S, Novak R, Diemert D, Spector SA, Rouphael N, Creech CB, McGettigan J, Khetan S, Segall N, Solis J, Brosz A, Fierro C, Schwartz H, Neuzil K, Corey L, Gilbert P, Janes H, Follmann D, Marovich M, Mascola J, Polakowski L, Ledgerwood J, Graham BS, Bennett H, Pajon R, Knightly C, Leav B, Deng W, Zhou H, Han S, Ivarsson M, Miller J, Zaks T; COVE Study Group. Efficacy and safety of the mRNA-1273 SARS-CoV-2 Vaccine. N Engl J Med 2021;384:403-416.

4. Dagan N, Barda N, Kepten E, Miron O, Perchik S, Katz MA, Hernán MA, Lipsitch M, Reis B, Balicer RD. BNT162b2 mRNA Covid-19 vaccine in a nationwide mass vaccination setting. N Engl J Med 2021;384:1412-1423.

5. Eifer M, Eshet Y. Imaging of COVID-19 vaccination at FDG PET/CT. Radiology 2021;299:248.

6. Xu G, Lu Y. COVID-19 mRNA vaccination-induced lymphadenopathy mimics lymphoma progression on FDG PET/CT. Clin Nucl Med 2021;46:353-354.

7. Nawwar AA, Searle J, Hagan I, Lyburn ID. COVID-19 vaccination induced axillary nodal uptake on [18F]FDG PET/CT. Eur J Nucl Med Mol Imaging 2021;48:2655-2656.

8. Johnson BJ, Van Abel KM, Ma DJ, Johnson DR. 18F-FDG-avid axillary lymph nodes after COVID-19 vaccination. J Nucl Med 2021;62:1483-1484.

9. Cohen D, Krauthammer SH, Wolf I, Even-Sapir E. Hypermetabolic lymphadenopathy following administration of BNT162b2 mRNA Covid-19 vaccine: incidence assessed by [18F]FDG PET-CT and relevance to study interpretation. Eur J Nucl Med Mol Imaging 2021;48:1854-1863.

10. Bernstine H, Priss M, Anati T, Turko O, Gorenberg M, Steinmetz AP, Groshar D. Axillary Lymph Nodes Hypermetabolism After BNT162b2 mRNA COVID-19 vaccination in cancer patients undergoing 18F-FDG PET/CT: a cohort study. Clin Nucl Med 2021;46:396-401.

11. Eifer M, Tau N, Alhoubani Y, Kanana N, Domachevsky L, Shams J, Keret N, Gorfine M, Eshet Y. COVID-19 mRNA vaccination: age and immune status and its association with axillary lymph node PET/CT uptake. J Nucl Med 2022;63:134-139.

12. Skawran S, Gennari AG, Dittli M, Treyer V, Muehlematter UJ, Maurer A, Burger IA, Mader C, Messerli O, Grünig H, Gebhard C, Huellner MW, Curioni-Fontecedro A, Berger C, Messerli M. [18F]FDG uptake of axillary lymph nodes after COVID-19 vaccination in oncological PET/CT: frequency, intensity, and potential clinical impact. Eur Radiol 2022;32:508-516.

13. Eshet Y, Tau N, Alhoubani Y, Kanana N, Domachevsky L, Eifer M. Prevalence of increased FDG PET/CT axillary lymph node uptake beyond 6 weeks after mRNA COVID-19 vaccination. Radiology 2021;300:345-347.

14. Panagiotidis E, Exarhos D, Housianakou I, Bournazos A, Datseris I. FDG uptake in axillary lymph nodes after vaccination against pandemic (H1N1). Eur Radiol 2010;20:1251-1253.

15. Shirone N, Shinkai T, Yamane T, Uto F, Yoshimura H, Tamai H, Imai T, Inoue M, Kitano S, Kichikawa K, Hasegawa M. Axillary lymph node accumulation on FDG-PET/CT after influenza vaccination. Ann Nucl Med 2012;26:248-252.

16. Thomassen A, Lerberg Nielsen A, Gerke O, Johansen A, Petersen H. Duration of 18F-FDG avidity in lymph nodes after pandemic H1N1v and seasonal influenza vaccination. Eur J Nucl Med Mol Imaging 2011;38:894-898.

17. Burger IA, Husmann L, Hany TF, Schmid DT, Schaefer NG. Incidence and intensity of F-18 FDG uptake after vaccination with H1N1 vaccine. Clin Nucl Med 2011;36:848-853.

18. Ferrari C, Nappi AG, Santo G, Mammucci P, Rubini D, Tucci M, Pisani AR. The day after mass COVID-19 vaccination: higher hypermetabolic lymphadenopathy detection on PET/CT and impact on oncologic patients management. Cancers (Basel) 2021;13:4340.

19. Website: National Comprehensive Cancer Network. COVID-19 Resources, https://www.nccn.org/covid-19 (accessed June 2022).

20. Cohen D, Hazut Krauthammer S, Cohen YC, Perry C, Avivi I, Herishanu Y, Even-Sapir E. Correlation between BNT162b2 mRNA Covid-19 vaccine-associated hypermetabolic lymphadenopathy and humoral immunity in patients with hematologic malignancy. Eur J Nucl Med Mol Imaging 2021;48:3540-3549.

Characteristics of Radiopharmaceutical Uptake in Primary Tumor and Metastatic Lesions of Prostate Carcinoma: Comparison of Oligometastatic with Multimetastatic Disease

Prostat Kanserinin Primer Tümör ve Metastatik Lezyonlarında Radyofarmasötik Tutulumunun Karakteristikleri: Oligometastatik ve Multimetastatik Hastalıkların Karşılaştırılması

 Gonca Kara Gedik, Farise Yılmaz, Hasan Önner

Selçuk University Faculty of Medicine, Department of Nuclear Medicine, Konya, Turkey

Abstract

Objectives: Oligometastases may generate secondary to indolent tumor biology. In this study, we investigated whether semiquantitative measures of ^{18}F-fluorodeoxyglucose (FDG) and gallium-68 (^{68}Ga) prostate-specific membrane antigen (PSMA) uptake of metastatic lesions and prostatic sites are different between oligometastatic (OM) and multimetastatic (MM) disease of prostate carcinoma (PC).

Methods: Patients with PC, who underwent positron emission tomography/computed tomography (PET/CT) from October 2012 to February 2020 were retrospectively reviewed. Patients, whose reports were consistent with metastatic diseases were selected. Patients classified as with MM or OM disease. Maximum standardized uptake values (SUV_{max}) were calculated from metastatic lesions and the prostatic site. The median of the SUV_{max} results between patients with OM and MM disease were compared.

Results: A totally 145 patients with a mean age of 71.46±9.26, were evaluated. In 59 of 145 patients, ^{18}F-FDG PET/CT was performed; 86 patients had gone through ^{68}Ga PSMA PET/CT. Thirty-seven of 145 patients were OM, whereas 108 patients were MM. The median of the SUV_{max} of metastatic lesions in patients with OM and MM disease in the ^{18}F-FDG group were 5.60 and 9.51, respectively. The results of the calculated median SUV_{max} values in OM and MM disease in the Ga-68 PSMA group were 13.44 and 29.84, respectively. A significant difference was observed in the median SUV_{max} results of metastatic lesions between OM and MM disease (p<0.05). Median values of SUV_{max} calculated from the prostatic site in OM and MM disease were 7.83 and 12.29 respectively in ^{18}F-FDG; 26.23 and 26.74 in the ^{68}Ga PSMA group. No significant difference was found in the SUV_{max} results of the prostatic site between OM and MM disease (p>0.05).

Conclusion: SUV_{max} results of metastatic lesions are significantly higher in patients with MM than in patients with OM disease in patients with PC, which may be secondary to their different biological contents in terms of aggressiveness.

Keywords: Oligometastasis, prostate carcinoma, SUV_{max}, PET/CT

Öz

Amaç: Oligometastazlar, tümörün sınırlı metastatik kapasitesini ifade etmekte olup hastalığın yavaş biyolojisine sekonder gelişebildikleri düşünülmektedir. Bu çalışma, prostat kanserinde (PK) prostat bölgesi ve metastatik lezyonların ^{18}F-florodeoksiglukoz (FDG) ve galyum-68 (^{68}Ga) prostat spesifik membran antijeni (PSMA) tutulumunun semikantitatif ölçümlerinin oligometastatik (OM) ve multimetastatik (MM) hastalık arasında farklı olup olmadığını araştırmak için tasarlanmıştır.

Yöntem: Ekim 2012-Şubat 2020 tarihleri arasında pozitron emisyon tomografisi/bilgisayarlı tomografi (PET/BT) incelemesi yapılan PK'li hastaların verileri retrospektif olarak incelendi. Sonuç raporları metastatik hastalık ile uyumlu olan hastalar seçildi. Hastalar MM veya OM hastalığı olanlar olarak iki gruba

Address for Correspondence: Prof. Gonca Kara Gedik, MD, Selçuk University Faculty of Medicine, Department of Nuclear Medicine, Konya, Turkey

Phone: +90 332 224 40 77 **E-mail:** goncakara@yahoo.com ORCID ID: https://orcid.org/0000-0003-4607-8615

ayrıldı. İlgi alanı, görsel olarak en yüksek radyofarmasötik tutulumu gösteren metastatik lezyondan ve prostat bölgesinden çizilerek maksimum standartlaştırılmış tutulum değerleri (SUV$_{maks}$) hesaplandı. OM ve MM'li hastalarda prostat bölgesi ve metastatik lezyonların medyan SUV$_{maks}$ değerleri karşılaştırıldı.

Bulgular: Yaş ortalaması 71,46±9,26 olan, 47-90 yaş aralığında toplam 145 hasta değerlendirildi. Yüz kırk beş hastanın 59'una ^{18}F-FDG PET/BT uygulandı; kalan 86 hastaya ^{68}Ga PSMA PET/BT incelemesi yapıldı. Yüz kırk beş hastanın 37'si OM, 108 hasta MM hasta grubundaydı. ^{18}F-FDG uygulanmış OM ve MM hastalığı olan hastalarda metastatik lezyonların medyan SUV$_{maks}$ değeri sırasıyla 5,60 (aralık: 1,72-17,40) ve 9,51 (aralık: 4,13-56,01) olarak hesaplandı. ^{68}Ga PSMA grubundaki OM ve MM hastalığı olanlarda hesaplanan metastatik lezyondan hesaplanan medyan SUV$_{maks}$ değerleri sırasıyla 13,44 ve 29,84 olarak bulundu. ^{18}F-FDG ve ^{68}Ga PSMA gruplarında OM ve MM hastalığı olan hastaların metastatik lezyonlarının medyan SUV$_{maks}$ değerleri istatistiksel olarak anlamlı fark gözlenirken (p<0,05), prostat bölgesinden hesaplanan medyan SUV$_{maks}$ değerleri ^{18}F-FDG grubunda sırasıyla 7,83 ve 12,29; ^{68}Ga PSMA grubunda ise 26,23 ve 26,74 olarak bulundu ve aralarında istatistiksel olarak fark saptanmadı (p>0,05).

Sonuç: Prostat kanserinde metastatik lezyonların SUV$_{maks}$ değerleri MM hastalarda OM hastalardan anlamlı olarak daha yüksek olup bu sonuç, OM ve MM yayılım gösteren tümörlerin agresiflik açısından farklı biyolojik içeriklerinden kaynaklanıyor olabilir.

Anahtar kelimeler: Oligometastaz, prostat kanseri, SUV$_{maks}$, PET/BT

Introduction

Prostate-specific membrane antigen (PSMA) is a type II transmembrane glycoprotein that is overexpressed in prostate carcinoma (PC) (1). Nearly all adenocarcinomas of the prostate demonstrate PSMA expression in most primary and metastatic lesions (2). Expression levels of PSMA are directly associated with PC aggressivenessand with higher expression in higher-grade and metastatic castration-resistant disease (1).

The correct staging of PC is important for treatment planning and patient management. Positron emission tomography/computed tomography (PET/CT) with ^{18}F-fluorodeoxyglucose (FDG) is the standard imaging modality for staging, restaging, and the evaluation of therapy response in various tumors. Besides enabling visual interpretation, this modality gives quantitative information about the level of metabolic activity and biological aggressiveness of the tumor by calculating the degree of ^{18}F-FDG uptake known as the standardized uptake value (SUV). In PC, however, due to the reported less than favorable results than those from other cancer, the role of ^{18}F-FDG PET/CT is not well recognized (3). Recently, gallium-68 (^{68}Ga) labeled PSMA ligands for PET imaging have been introduced and ^{68}Ga PSMA is the most abundantly used agent for PSMA-targeted PET imaging. High diagnostic sensitivity and high accuracy for detecting metastases of ^{68}Ga-PSMA PET/CT in PC have been well established (2,4). Like in ^{18}F-FDG PET/CT, a three-dimensional distribution of ^{68}Ga PSMA is produced, and quantitative measures allowing non-invasive assessment of PSMA expression can be calculated.

It has been reported that the number and location of metastatic sites impact survival in patients with PC (3). Observing worse outcomes for the increasing number of nodal and distant metastases and obtaining remission or possibly cure using intensive treatment in patients with a limited number of metastatic site, introduced the concept of oligometastatic (OM) disease in the PC armamentarium (5,6). Besides clinical diagnosis, the biological component of this entity has also been an area of interest; questions looking for an answer whether the tumors that cause the OM disease might be biologically different from those that induce multimetastatic (MM) lesions or the entity is improved detection of existing distant metastatic disease because of more sensitive imaging modalities or not, have been arisen (7).

Recently, a significant correlation with the grade group of the primary tumor and SUV values was shown, higher SUV results in higher Gleason scores (GS) of 8 and 9, were observed in patients with PC with ^{68}Ga PSMA PET/CT imaging (8). Taking from this point, we wanted to investigate whether semiquantitative measures of ^{18}F-FDG and Ga-6 PSMA uptake differs or not between OM and MM disease in patients with PC.

Materials and Methods

Patients

Data of patients with prostate adenocarcinoma who underwent ^{18}F-FDG or ^{68}Ga PSMA PET/CT imaging between October 2012 and February 2020 in Selcuk University Medical Faculty Department of Nuclear Medicine, were retrospectively reviewed. Patients, whose reports were consistent with metastatic diseases, were selected. The study was approved by the Selcuk University Faculty of Medicine Ethics Committee (meeting date: 25.12.2019, decision number: 2019/382), and written informed consent was obtained in all patients under our institution's rules.

^{18}F-FDG and ^{68}Ga-PSMA PET/CT Imaging

PET/CT body images were taken using an integrated scanner (Biograph mCT, Siemens, Germany). First, low-dose unenhanced CT using the 16 slice CT with acquisition parameters of 190 mA, 5 mm slice thickness, and 140

kV was performed for attenuation correction. Then, PET emission scanning in 8 or 9 bed positions with an acquisition time of 3 min per bed position from the skull base to the mid-thigh was acquired. For ^{18}F-FDG PET/CT imaging, all patients were asked to fast at least 6 h before the scanning, and blood sugar levels were confirmed to be lower than 200 mg/dL. All acquisitions were performed 60 min after the intravenous administration of 370 MBq ^{18}F-FDG and 1.8-2.2 MBq per kilogram/bodyweight of ^{68}Ga PSMA.

Image Interpretation and Semi Quantification

PET/CT images were analyzed and semiquantitative calculations of ^{18}F-FDG uptake and ^{68}Ga PSMA expression were performed on a Siemens Syngo.via PET/CT workstation. Images were analyzed regarding primary lesions and extraprostatic metastases. Radiopharmaceutical uptake higher than the surrounding background activity and distinct from physiologic sites were pathologic. In patients with solitary lesions showing radiopharmaceutical uptake, confirmation of metastases was performed with additional modality including CT or magnetic resonance imaging. Patients with metastatic disease were included in the study while the ones with synchronous tumors were excluded. Patients are then further classified as with MM or OM disease. OM disease was defined as having 3 or fewer metastases as suggested in the literature (9). Patients with more than 3 metastatic sites were classified as MM. Besides visual interpretation, semiquantitative analysis was performed in all patients by a single nuclear medicine physician. Region of interest (ROI) was drawn manually around the prostate gland or prostate site in those previously operated. In all patients, for the quantification of metastatic disease, ROI was drawn over the visually most radiopharmaceutical avid metastatic lesion to calculate the maximum SUV (SUV$_{max}$), which was normalized to body weight. Sites of physiological uptake were manually excluded while drawing ROI, and SUV$_{max}$ values were noted. In both OM and MM patients, after noting the SUV$_{max}$ values of the lesions, the highest value among them was considered for statistical analysis, for both radiopharmaceuticals. Clinical data of patients including GS and previous therapy history, were also collected from the files of the patients and the information system of our hospital.

Statistical Analysis

For statistical analyses, the software package SPSS v16.0 was used. Results of SUV$_{max}$ were expressed as a median. Mann-Whitney U test was used to compare the SUV$_{max}$ results of patients with OM and MM disease. Fisher's exact test was used for comparing frequency distributions between groups. Statistical analyses were performed separately in the calculation the significance of semiquantitative results for two different radiopharmaceuticals. The results were evaluated at the 95% confidence interval, and the significance level was taken as 0.05.

Results

A total of 145, age range 47-90 years with a mean age of 71. 46±9.26, were evaluated. In 59 of 145 patients (41%), ^{18}F-FDG PET/CT was performed; the remaining 86 (59%) patients had gone through ^{68}Ga-PSMA PET/CT examination. Thirty-seven of 145 patients (26%) were OM (Figures 1, 2). In 17 of these 37 patients, ^{18}F-FDG was used as a radiopharmaceutical, and in the remaining 20, ^{68}Ga PSMA was injected. The remaining 108 patients were MM (Figures 3, 4); 42 were in the ^{18}F-FDG group and 66 were in the group of ^{68}Ga PSMA.

Among all OM patients, 17 showed (46%) only bone metastases, 13 of 37 (35%) had lymph node metastases, and in 3 patients (8%) only soft tissue metastases including liver, lung, and the suprarenal gland was observed. In the same group with OM disease, bone and lymph node and bone and soft tissue metastases were seen in 3 (8%) and 1 (3%) patients, respectively. For both radiopharmaceuticals, in the OM group, metastatic disease was limited to the
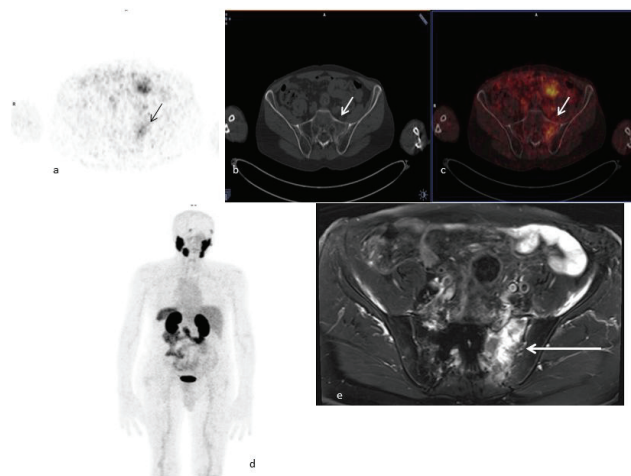
Figure 1. Transaxial (a: PET, b: CT, c: fused) and MIP (d) ^{68}Ga PSMA PET/CT images of a 42 year old patient with GS of 10. This patient, whose images depicted increased radiotracer accumulation and heterogeneous density in the left part of sacrum (a, b and c, respectively; arrows), was classified as oligometastatic. Calculated SUV$_{max}$ of the bone lesion was found as 7.26. Magnetic resonance imaging also revealed metastatic lesion in left part of sacrum with contrast enhancement (e, arrow)

PET: Positron emission tomography, CT: Computed tomography, ^{68}Ga: Gallium-68, PSMA: Prostate-specific membrane antigen, GS: Gleason scores, SUV$_{max}$: Maximum standardized uptake value, MIP: Maximum intensity projection

Figure 2. Transaxial (a-d: PET, b-e: CT, c-f: fused) and MIP (g) ^{18}F-FDG PET/CT images of a 69 year old oligometastatic patient with GS of 6. Sclerotic metastatic bone lesions were seen in the inferior part of right acetabulum and right ischium (b-e, arrows) with increased radiotracer uptake (a, c, d, f, g, arrows). SUV$_{max}$ of the lesion in acetabulum was calculated as 5.35

PET: Positron emission tomography, CT: Computed tomography, FDG: Fluorodeoxyglucose, GS: Gleason scores, SUV$_{max}$: Maximum standardized uptake value, MIP: Maximum intensity projection

Figure 3. Transaxial (a-d: PET, b-e: CT, c-f: fused) and MIP (g) ^{68}Ga PSMA PET/CT images of a 79 year old mulitmetastatic patient with GS of 7, revealed metastatic lymph nodes and sclerotic bone metaseses (b-e, arrows) with increased radiopharmaceutical uptake (a, c, d, f and g, arrows). SUV$_{max}$ of the right parailiac lymph node was calculated as 57.18 (c, thick arrow)

PET: Positron emission tomography, CT: Computed tomography, ^{68}Ga: Gallium-68, PSMA: Prostate-specific membrane antigen, GS: Gleason scores, SUV$_{max}$: Maximum standardized uptake value, MIP: Maximum intensity projection
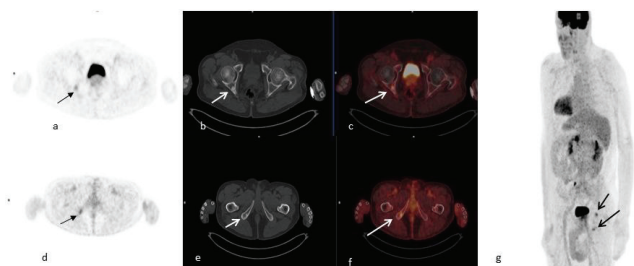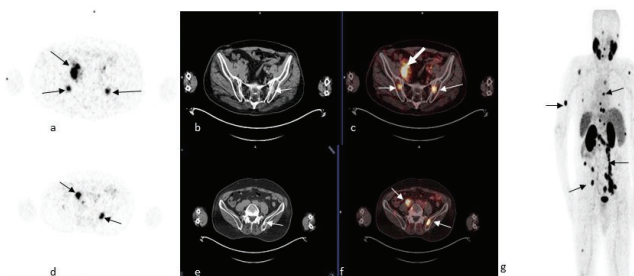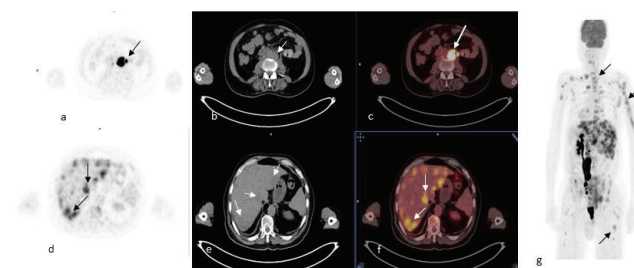

Figure 4. Transaxial (a-d: PET, b-e: CT, c-f: fused) and MIP (g) ^{18}F-FDG PET/CT images of a 77 year old patient. Multimetastases including bone (g, arrows), paraaortic lymph nodes (a, b, c, arrows) and liver (d, e, f, arrows) with increased ^{18}F-FDG uptake were observed. Calculated SUV$_{max}$ of lymph node was found as 56. 01 (c, arrow)

PET: Positron emission tomography, CT: Computed tomography, FDG: Fluorodeoxyglucose, SUV$_{max}$: Maximum standardized uptake value, MIP: Maximum intensity projection

pelvic region involving the pelvic bones and/or nodes in 25 of 37 (68%) patients. The most common sites of bone metastases were pelvic bones followed by the vertebrae (60% and 27%, respectively) in patients with OM patients. In MM patients, on the other hand, only bone metastases were observed in 33 of 108 patients (31%), only lymph node metastases were seen in 17 of them (16%), and only soft tissue metastases were present in 2 (2%). In the remaining 56 patients with MM disease, bone and lymph node, bone and soft tissue, and metastatic disease involving all mentioned sites were noted except 1 patient in whom only lymph node and soft tissue metastases were seen. Taken together, the bone was the most common site of extraprostatic metastases in patients with both OM and MM disease (57% and 81%, respectively). The highest SUV$_{max}$ was noticed in lymph node metastases in all patients except ones in OM disease of the ^{18}F-FDG group. The distribution of metastatic sites in patients with OM and MM disease and SUV$_{max}$ results of metastatic lesions are detailed in Tables 1, 2.

The median of the SUV$_{max}$ of metastatic lesions in OM and MM patients in the ^{18}F-FDG group was 5.60 (range: 1.72-17.40) and 9.51 (range: 4.13-56.01), respectively. The results of the calculated median SUV$_{max}$ values in OM and MM patients in the ^{68}Ga PSMA group were 13.44 (range: 3.72-60.34) and 29.84 (range: 4.29-88.80), respectively. Statistically, a significant difference was observed in the median SUV$_{max}$ results of metastatic lesions between patients with OM and MM disease for both radiopharmaceuticals (p=0.0001 and p=0.009 for ^{68}Ga PSMA and ^{18}F-FDG respectively, Mann-Whitney U test). Thirty-one of 86 patients (86%) in the ^{68}Ga PSMA group were *de novo* patients with PC (9 were OM, 22 were MM patients). The remaining ones were patients in whom therapy including, surgery, radiotherapy, or systemic therapy was used previously (11 were OM, 44 were MM patients). In the ^{18}F-FDG group, 12 of 17 OM patients were *de novo* PC, 5 patients were admitted at the post-therapy state; whereas 18 patients in MM disease had *de novo* PC and 24 of them were imagined after therapy. The presence of patients in the post-therapy state negatively affected the accumulation of the radiopharmaceutical in the prostate site that in the OM group; only 11 of 20 and 6 of 17 patients showed an accumulation of ^{68}Ga PSMA and ^{18}F-FDG, respectively. Similarly, in the MM group, 33 of 66 and 13 of 42 patients had radiopharmaceutical uptake for ^{68}Ga PSMA and ^{18}F-FDG, respectively, in the prostate site. Median values of SUV$_{max}$ calculated from the prostate site in patients with OM (range: 4.05-15.54) and with MM disease (range: 5.89-34.37) were 7.83 and 12.29 in the

Table 1. Distribution of metastatic sites in all patients with OM and MM disease

	Site of metastases							
Type of metastases	Bone only	Lymph node only	Soft tissue only	Bone + lymph node	Bone + soft tissue	Bone + soft tissue + lymph node	Soft tissue + lymph node	Total
OM	17	13	3	3	1	-	-	37
MM	32	15	2	40	6	12	1	108
Total	49	28	5	43	7	12	1	145

OM: Oligometastatic, MM: Multimetastatic

Table 2. Results of median SUV$_{max}$ values of radiopharmaceutical avid metastatic lesions in patients with OM and MM disease

Site of metastases	Patients with OM disease in ^{18}F-FDG group (n=17)	Patients with MM disease in ^{18}F-FDG group (n=42)	Patients with OM disease in ^{68}Ga-PSMA-11 group (n=20)	Patients with MM disease in ^{68}Ga-PSMA-11 group (n=66)
Lymph node	5.20	10.01	21.86	36.80
Soft tissue	6.20	9.20	17.13	18.57
Bone	5.35	8.15	11.48	27.65

n: Number, SUV$_{max}$: Maximum standardized uptake value, OM: Oligometastatic, MM: Multimetastatic, ^{68}Ga: Gallium-68, FDG: Fluorodeoxyglucose, PSMA: Prostate-specific membrane antigen

^{18}F-FDG group, respectively. In the ^{68}Ga PSMA group, on the other hand, nearly the same median SUV$_{max}$ values were reached in the prostate sites such as 26.23 and 26.74 in patients with OM (range: 5.96-122.04) and with MM disease (range: 8.34-76.15), respectively. Although a higher value was calculated in MM disease for ^{18}F-FDG, no statistically significant difference was found in the SUV$_{max}$ results of the prostate site between patients with OM and MM disease (p=0.136, Mann-Whitney U test). The results of semiquantifications of prostatic uptake and metastatic lesions in patients with MM and OM disease according to the radiopharmaceutical are summarized in Table 3.

When we looked for associating OM and MM disease with GS, we could not reach the scores of 13 patients in the ^{68}Ga-PSMA group, 1 in OM, and 12 in MM patients. In the ^{18}F-FDG group, GS of 14 patients were not available, 3 in OM and 11 in MM patients. For both radiopharmaceuticals, there were 45 patients with GS of <7 and 73 patients' GS was ≥7. The distribution of the patients according to the metastatic stage was 14 (31%) and 31 (69%) for OM and MM disease, respectively, in GS <7 patients. Among patients with GS above, 19 of them (26%) had OM and 54 (74%) had MM disease. No statistically significant difference was observed in the frequency distributions of OM and MM disease between patients with GS <7 and with GS ≥7 (p=0.673, Fisher's exact test). The distribution of the patients according to GS and type of metastases for the two radiopharmaceuticals is shown in Table 4.

Table 3. Median SUV$_{max}$ values calculated from prostatic site and metastatic lesions in all patients for two radiopharmaceuticals (range in parenthesis)

	^{68}Ga PSMA		^{18}F-FDG	
	Prostatic site	Metastatic lesion	Prostatic site	Metastatic lesion
OM	26.23 (5.96-122.04)	13.44 (3.72-60.84)	7.83 (4.05-15.54)	5.60 (1.72-17.40)
MM	26.74 (18.34-76.15)	29.84 (4.25-88.80)	12.29 (5.89-34.37)	9.51 (4.13-56.01)
p value (95% CI)	*	0.0001	0.136	0.009

*Statistical significance between the results of ^{68}Ga PSMA uptake of prostatic site in patients with OM and MM disease was not analyzed because of the nearly same results observed. CI: Confidence interval, ^{68}Ga: Gallium-68, FDG: Fluorodeoxyglucose, PSMA: Prostate-specific membrane antigen, OM: Oligometastatic, MM: Multimetastatic

Table 4. Distribution of the patients according to GS and type of metastases of patients with available score

Type of metastases			
GS	OM	MM	Total
<7	14	31	45
≥7	19	54	73
Total	33	85	118*

*GS scores of 4 patients with OM disease and 23 patients with MM disease were not available. GS: Gleason score, OM: Oligometastatic, MM: Multimetastatic

Discussion

The improvements in localized therapies that ablate the limited amount of metastatic disease and can even cure some patients highlighted once more the practical significance of the OM paradigm, which was first proposed in 1995 (10). Moreover, data suggesting the distinct biological differences between limited metastatic lesions and widely disseminated disease which is also supported by their different clinical settings for multiple primary cancers, including that of the prostate, have emerged (11).

Although no consensus exists, OM disease is generally defined as less than or equal to five metastatic sites on conventional imaging, including bone scintigraphy and CT, in patients with PC (7). Because of their limited sensitivities, which are in the 60%-80% range for a bone scan and 70%-80% for the CT, the functional imaging modality of PET/CT, which offers the ability to evaluate tumor metabolism with several radiotracers, have been increasingly used for detecting of PC metastases (3). It has been shown that ^{18}F-FDG PET/CT, may be useful in the diagnosis and staging of aggressive primary prostate tumors (12). The ability of ^{18}F-FDG PET/CT in the detection of metastatic disease in patients with biochemical failure and negative conventional imaging studies has been emphasized (12). Being highly specific, ^{68}Ga PSMA has been suggested as a new radiopharmaceutical that can detect prostate cancer relapses and metastases (2). The diagnostic sensitivity and reproducibility of ^{68}Ga PSMA PET/CT for the diagnosis and staging of patients with newly diagnosed PC have been noted as well (4). It is also been reported that SUV_{max}, which is the most widely used parameter for the quantification of radiotracer uptake of the tumor, may be used to differentiate malignant from benign lesions in the prostate gland, and correlation of SUV_{max} with PSMA expression is demonstrated (8,13). Increased ^{18}F-FDG uptake in primary cancers and eventually highly calculated SUV_{max} values showing proliferative activity of malignant tissue have also been reported in various tumors (14). Thus, the association of SUV_{max} with the biological aggressiveness of malignant tissue has been well established for both radiopharmaceuticals we used in our study.

To identify management strategies, it is crucial to answer the question of whether OM disease in PC is an indolent disease biology that the cancer is slow-growing and has limited metastatic potential or it is a result of existing metastatic disease, which is depicted with more sensitive imaging modalities an early time point (3). By Reyes and Pienta (15), the evolution of these two theories was summarized and it was underlined that the limited metastatic potential of OM disease could be attributable to less aggressive cancer

clones that can metastases to few organs in contrast to MM disease, which harbors aggressive cancer clones able to metastases to multiple organs. Although could not be analyzed in our cases, by Uppal et al. (16), biological markers related to the OM phenotype with limited potential to develop multimetastasis were investigated, and three miRNAs named miR-127-5p, miR-544a, and miR-655-39, were shown to be associated with cells of low malignant potential in a model of breast carcinoma lung colonization. Studies assessing the clonality and metastatic potential between prostate cancer cells demonstrated that Ki67 expression and phosphatase and tensin homolog protein losses have been correlated with poor prognosis (17).

Results of quantification in primary tumors with extraprostatic metastases than those without metastases were compared and higher SUV_{max} in former ones were reported previously (4). In the study by Erdoğan et al. (18), the role of SUV_{max} of the primary tumor as a predictor of OM and MM disease in patients with PC was also demonstrated with ^{68}Ga PSMA. The unusual point of our study was investigating the results of SUV_{max} values in MM and OM disease and comparing the results between them for two different radiopharmaceuticals. Interestingly, SUV_{max} values calculated from metastatic lesions of PC patients were found to be significantly higher in MM compared with OM disease for both ^{18}F-FDG and ^{68}Ga PSMA. Since the accumulation of former radiopharmaceuticals shows glucose metabolism and uptake of later is associated with receptor expression level, statistical analysis for comparing SUV_{max} values was performed separately. In the area of PC, a fair amount of genetic heterogeneity both between patients and between different disease sites in a single patient is observed (7). Taking into consideration the relation of SUV_{max} with tumor proliferation rate and its biological behavior, we thought that this difference may be secondary to the different aggressiveness of metastatic cells in OM and MM patients, which may support the hypothesis suggesting their distinct biological origin. Prostatic radiopharmaceutical uptake, on the other hand, was not found to be significantly different between these two diseases, which may be attributed to the low number of patients in subgroups and was discordant with the results of Erdoğan et al. (18). Besides, the highest SUV_{max} result calculated from the prostate site (122.04) was observed in the OM group, which might play a role as an extreme value and affect the statistical analysis in our study. However, GS, which is a marker of aggressiveness and risk for disease recurrence in PC, was not associated with the type of metastatic disease. We thought that whether it is OM or MM, the disease is metastatic; it has gained metastatic potential employing leaving primary tumor and evading

the immune system in contrast to non-metastatic PC. Since all patients were metastatic in our study, we could not observe any difference in the frequency distributions of OM and MM patients in terms of GS.

Concordant with the results of Afshar-Oromieh et al. (2), we found that both in patients with OM and MM disease, bones were the most commonly involved metastatic areas than the other sites. In the OM group, PSMA positivity was limited to the pelvis in 68% of our patients, which was also a similar result with the literature (19). When we looked at the results of semi quantification of metastatic sites, we saw those lymph node metastases presented with the highest contrast in most cases and this was also concordant with the results reported before (2,4).

Study Limitations

Because of consisting of patients who had gone through therapy for primary disease, accumulation of radiopharmaceutical in the prostate gland was observed in a limited number of patients in our study, which can be mentioned as a limitation as well. Most patients with prostatic uptake were the ones with *de novo* disease in our study. In the ^{18}F-FDG group, 15 of 30 patients with *de novo* disease did not show radiotracer uptake in the prostate gland (Table 3), which may be secondary to the low glycolytic activity of the primary tumor. Absent radiopharmaceutical uptake of the prostate site was recognized only in 1 patient with *de novo* disease in the ^{68}Ga PSMA group, which can be attributed to a small tumor mass that does not express adequate tracer uptake (20). Another limitation of our study is being heterogeneous, having both *de novo* and post-therapy patients and eventually a low number of patients in subgroups, especially in the OM group. A low number of patients with OM disease may also be evolved secondarily to the criteria we used for the number of metastatic lesions for the definition of OM disease. If we took patients with more than 3 but less than five lesions in the OM group, we would have more patients with OM disease. Finally, GSs were not available in all patients and this was also a limitation of our study. Taken together, the limitations of our study were specific to its retrospective origin.

Conclusion

In conclusion, molecular imaging with PET/CT may play a role in identifying the biology of OM and MM disease in patients with PC. SUV_{max} results of metastatic lesions are significantly higher in patients with MM than in patients with OM disease for both ^{18}F-FDG and ^{68}Ga PSMA, which

may be secondary to their different biological contents in terms of aggressiveness. Further studies with a larger number of presented *de novo* are needed to investigate whether prostatic uptake also differs or not between these two diseases, which may strengthen this hypothesis.

References

1. Sheikhbahaei S, Afshar-Oromieh A, Eiber M, Solnes LB, Javadi MS, Ross AE, Pienta KJ, Allaf ME, Haberkorn U, Pomper MG, Gorin MA, Rowe SP. Pearls and pitfalls in clinical interpretation of prostate-specific membrane antigen (PSMA)-targeted PET imaging. Eur J Nucl Med Mol Imaging 2017;44:2117-2136.

2. Afshar-Oromieh A, Avtzi E, Giesel FL, Holland-Letz T, Linhart HG, Eder M, Eisenhut M, Boxler S, Hadaschik BA, Kratochwil C, Weichert W, Kopka K, Debus J, Haberkorn U. The diagnostic value of PET/CT imaging with the (68)Ga-labelled PSMA ligand HBED-CC in the diagnosis of recurrent prostate cancer. Eur J Nucl Med Mol Imaging 2015;42:197-209.

3. Rao A, Vapiwala N, Schaeffer EM, Ryan CJ. Oligometastatic prostate cancer: a shrinking subset or an opportunity for cure? Am Soc Clin Oncol Educ Book 2019;39:309-320.

4. Basha MAA, Hamed MAG, Hussein O, El-Diasty T, Abdelkhalek YI, Hussein YO, Alasamer AF, Mohamed HAE, Deen DSE, Tantawy EF, Metwally MI, Zaitoun MMA, Aly SA, Altohamy JI, Mohamed AEM, Afifi AHM, Harb O. 68Ga-PSMA-11 PET/CT in newly diagnosed prostate cancer: diagnostic sensitivity and interobserver agreement. Abdom Radiol (NY) 2019;44:2545-2556.

5. Fraser M, Koontz B, Emmenegger U, De Meerleer G, Khoo V, Feng F, Corcoran NM, Hovens CM, Tran PT, Ost P, Boutros PC; GAP6 Consortium. What is oligometastatic prostate cancer?Eur Urol Focus 2019;5:159-161.

6. Kucharczyk MJ, Gravis G, Niazi T. The biology of oligometastatic prostate cancer: a different beast than polymetastatic prostate cancer. Eur UrolFocus 2019;5:117-118.

7. Joice GA, Rowe SP, Pienta KJ, Gorin MA. Oligometastatic prostate cancer: shaping the definition with molecular imaging and an improved understanding of tumor biology. Curr Opin Urol 2017;27:533-541.

8. Demirci E, Kabasakal L, Şahin OE, Akgün E, Gültekin MH, Doğanca T, Tuna MB, Öbek C, Kılıç M, Esen T, Kural AR. Can SUVmax values of Ga-

68-PSMA PET/CT scan predict the clinically significant prostate cancer? Nucl Med Commun 2019;40:86-91.

9. Gillessen S, Attard G, Beer TM, Beltran H, Bossi A, Bristow R, Carver B, Castellano D, Chung BH, Clarke N, Daugaard G, Davis ID, de Bono J, Borges Dos Reis R, Drake CG, Eeles R, Efstathiou E, Evans CP, Fanti S, Feng F, Fizazi K, Frydenberg M, Gleave M, Halabi S, Heidenreich A, Higano CS, James N, Kantoff P, Kellokumpu-Lehtinen PL, Khauli RB, Kramer G, Logothetis C, Maluf F, Morgans AK, Morris MJ, Mottet N, Murthy V, Oh W, Ost P, Padhani AR, Parker C, Pritchard CC, Roach M, Rubin MA, Ryan C, Saad F, Sartor O, Scher H, Sella A, Shore N, Smith M, Soule H, Sternberg CN, Suzuki H, Sweeney C, Sydes MR, Tannock I, Tombal B, Valdagni R, Wiegel T, Omlin A. Management of patients with advanced prostate cancer: the report of the advanced prostate cancer consensus conference APCCC 2017. Eur Urol 2018;73:178-211.

10. Hellman S, Weichselbaum RR. Oligometastases. J Clin Oncol 1995;13:8-10.

11. Tosoian JJ, Gorin MA, Ross AE, Pienta KJ, Tran PT, Schaeffer EM. Oligometastatic prostate cancer: definitions, clinical outcomes, and treatment considerations. Nat Rev Urol 2017;14:15-25.

12. Jadvar H. Is there use for FDG-PET in Prostate cancer? Semin Nucl Med 2016;46:502-506.

13. Woythal N, Arsenic R, Kempkensteffen C, Miller K, Janssen JC, Huang K, Makowski MR, Brenner W, Prasad V. Immunohistochemical validation of PSMA expression measured by 68Ga-PSMA PET/CT in primary prostate cancer. J Nucl Med 2018;59:238-243.

14. Gallamini A, Zwarthoed C, Borra A. Positron emission tomography (PET) in oncology. Cancers (Basel) 2014;6:1821-1889.

15. Reyes DK, Pienta KJ. The biology and treatment of oligometastatic cancer. Oncotarget 2015;6:8491-8524.

16. Uppal A, Wightman SC, Mallon S, Oshima G, Pitroda SP, Zhang Q, Huang X, Darga TE, Huang L, Andrade J, Liu H, Ferguson MK, Greene GL, Posner MC, Hellman S, Khodarev NN, Weichselbaum RR. 14q32-encoded microRNAs mediate an oligometastatic phenotype. Oncotarget. 2015;6:3540-3552.

17. Cuzick J, Yang ZH, Fisher G, Tikishvili E, Stone S, Lanchbury JS, Camacho N, Merson S, Brewer D, Cooper CS, Clark J, Berney DM, Møller H, Scardino P, Sangale Z; Transatlantic Prostate Group. Prognostic value of PTEN loss in men with conservatively managed localised prostate cancer. Br J Cancer 2013;108:2582-2589.

18. Erdoğan M, Özkan EE, Öztürk SA, Yıldız M, Şengül SS. The role of Ga-68 PSMA PET/CT scan on diffenetiating of oligometastatic and high risk prostate cancer. Mol Imaging and Radionucl Ther 2020;29:98-104.

19. McCarthy M, Francis R, Tang C, Watts J, Campbell A. A multicenter prospective clinical trial of 68 Gallium PSMA HBED-CC PET-CT restaging in biochemically relapsed prostate carcinoma: oligometastatic rate and distribution compared with standard imaging. Int J Radiat Oncol Biol Phys 2019;104:801-808.

20. Schreiter V, Gericke M, Beck M, Ghadjar P, Boening G, Schreiter NF. Usefulness of Ga-68 HBED-CC PSMA PET/CT for tumor staging in the initial diagnostic assessment of prostate cancer. J Nucl Med Radiat Ther 2016;7:291.

Leukocyte Labeling with Tc-99m-HMPAO: The Role of Leucocyte Numbers and Medication on the Labeling Efficacy and Image Quality

Tc-99m-HMPAO İşaretli Lökosit: Lökosit Sayısı ve İlaç Kullanımının Radyoişaretleme Verimi ve Görüntü Kalitesine Etkisi

 Emre Karayel[1,2], Meltem Ocak[3], A. Seher Birteksöz Tan[4]

[1]İstanbul University-Cerrahpaşa, Cerrahpaşa Faculty of Medicine, Department of Nuclear Medicine, İstanbul, Turkey
[2]İstanbul University, Institute of Graduate Studies in Health Sciences, İstanbul, Turkey
[3]İstanbul University, Faculty of Pharmacy, Department of Pharmaceutical Technology, İstanbul, Turkey
[4]İstanbul University, Faculty of Pharmacy, Department of Pharmaceutical Microbiology, İstanbul, Turkey

Abstract

Objectives: The aim of this study is to evaluation of Tc-99m-hexamethylpropyleneamineoxime (HMPAO)-labeled leukocytes in terms of radiochemical, biochemical, and microbiological quality controls and to examine the effect of leukocyte numbers of the blood obtained from patients and the medications currently used by the patients on the radiochemical yields of Tc-99m-HMPAO-labeled leukocytes, and imaging quality was evaluated.

Methods: Thirty paients were included in our study who applied to Istanbul University-Cerrahpasa, Cerrahpasa Faculty of Medicine, Department of Nuclear Medicine for Tc-99m-HMPAO-labeled leukocyte scintigraphy. Devices and chemicals used in the preparation of Tc-99m-HMPAO-labeled laukocytes were compared with other nuclear medicine clinics. Tc-99m-HMPAO-labeled leukocytes were evaluated in terms of radiochemical, biochemical, and microbiological quality controls. The effect of leukocyte numbers of the blood obtained from patients and the medications currently used by the patients on the radiochemical yields of Tc-99m-HMPAO-labeled leukocytes and imaging quality was evaluated.

Results: The pH range of Tc-99m-HMPAO was 6-8 and the radiochemical purity was 90±2.04% (n=30), the radiochemical yield of Tc-99m-HMPAO-labeled leukocytes was 51±2.18% (n=30), the radiolabeling yield of Tc-99m-HMPAO-labeled leukocyte increased as the amount of white blood cell in the blood increased and whether the patients used any antibiotic, blood thinners, insulin and blood pressure medications did not affect the radiolabeling yield of Tc-99m-HMPAO-labeled leukocytes. The number of erythrocytes were removed at a rate of >99% in LPR by starch solution (6% HES; in the hemocytometric examination of Tc-99m-HMPAO-labeled leukocytes performed zeroth and 4th h, living/dead cell ratio was found 97.5% and the product was sterile.

Conclusion: Tc-99m-HMPAO was labeled with leukocytes successfully, and Tc-99m-HMPAO-labeled leukocytes was safely injected to the patients as sterile without loss of vitality and aggregation.

Keywords: Tc-99m-HMPAO, Tc-99mHMPAO-labeled leukocytes, infection imaging

Öz

Amaç: Bu çalışmada; Tc-99m-heksametilpropilenaminoksim (HMPAO) ile işaretli lökositlerin radyokimyasal, biyokimyasal ve mikrobiyolojik açıdan kalite kontrollerinin incelenmesi ve hasta kanının ve lökosit süspansiyonunun ihtiva ettiği lökosit miktarı ile hastaların kullandıkları bazı ilaçların Tc-99m-HMPAO ile lökositlerin radyoişaretleme verimine etkisinin incelenmesi amaçlanmıştır.

Yöntem: Çalışmaya İstanbul Üniversitesi-Cerahhapaşa, Cerrahpaşa Tıp Fakültesi, Nükleer Tıp Anabilim Dalı'na Tc-99m-HMPAO ile işaretli lökosit sintigrafisi için başvuran 30 hasta dahil edildi. Radyoişaretleme sırasında kullandığımız alet ve kimyasallar literatürde belirtilenlerle diğer örneklerle karşılaştırıldı. Hazırlanan radyofarmasötiğin kalite kontrolleri radyokimyasal, biyokimyasal ve mikrobiyolojik açıdan incelendi. Hasta kanının ve lökosit süspansiyonunun ihtiva ettiği lökosit miktarları ile hastaların kullandıkları antibiyotik, kan sulandırıcı, insülin ve tansiyon ilaçlarının Tc-99m-HMPAO ile lökositlerin radyoişaretleme verimine etkisi SPSS-20 programı ile istatistiksel olarak değerlendirildi.

Bulgular: Tc-99m-HMPAO radyofarmasötiğinin pH aralığının 6-8 ve radyokimyasal saflığının %90±2,04 (n=30), Tc-99m-HMPAO ile işaretli lökositlerin radyokimyasal veriminin %51±2,18 (n=30), hastaların antibiyotik, kan sulandırıcı, insülin ve tansiyon ilacı kullanma durumunun Tc-99m-HMPAO ile işaretli lökositlerin radyokimyasal verimine etki etmediği, hasta kanında ve lökosit süspansiyonunda bulunan lökosit miktarı arttıkça Tc-99m-HMPAO ile işaretli lökositlerin radyokimyasal veriminin de arttığı, kullanılan nişasta çözeltisinin (%6 HES) kırmızı kan hücrelerinin %99'dan fazlasını ortamdan uzaklaştırdığı, işaretli lökositlerin hemositometrik yöntemle 0 ve 4. saatte yapılan analizleri sonucu lökositlerin %97,5 oranında canlılığını koruduğu ve son ürünün steril olduğu tespit edildi.

Sonuç: Tc-99m-HMPAO ile lökositler başarılı bir şekilde işaretlenmiş ve hastalara steril, canlılığını kaybetmemiş ve pıhtılaşma olmayan Tc-99m-HMPAO ile işaretli lökositlerin güvenle uygulanabileceği sonucuna varılmıştır.

Anahtar kelimeler: Tc-99m-HMPAO, Tc-99m-HMPAO işaretli lökosit, enfeksiyon görüntüleme

Introduction

Radiopharmaceuticals are drugs used in nuclear medicine paired with radiation sources. Radiopharmaceuticals with alpha or beta emissions are widely used for cancer treatment, while gamma ray emitters are used in diagnostic imaging. In the recent years, hybrid imaging systems such as single photon emission tomography/computed tomography (SPECT/CT), positron emission tomography/CT, PET/magnetic resonance have added significant progress in the use of diagnostic radiopharmaceuticals (1,2,3,4,5). Technetium-99m (Tc-99m) methylene diphosphonic acid, [67]Gallium-citrate, Tc-99m-nanocolloid, Tc-99m-human immunoglobulin, ^{18}F-fluorodeoxyglucose, Tc-99m-hexamethylpropyleneamineoxime-leukocyte (HMPAO-leukocyte) are the most common radiopharmaceuticals used for infection imaging. Due to differences in the uptake mechanisms, these radiopharmaceuticals can be used alone or together to increase specificity and sensitivity. Tc-99m-HMPAO-labeled leukocyte scintigraphy is a frequently preferred imaging method in infection imaging with its high specificity and sensitivity and can be used to determine various disorders such as occult site of infection, osteomyelitis of the appendicular skeleton, infected joint and vascular prosthesis, diabetic foot, fever of unknown origin, postoperative abscesses, lung infections, endocarditis, inflammatory bowel disease, neurological infections, infected central venous catheters or other devices (6,7,8,9).

Preparing Tc-99m-HMPAO-labeled leukocytes requires considerable and careful efforts in terms of radiation protection, and the blood may be infected with the pathogens. Moreover, the quality of the administered radiopharmaceutical is quite significant for mainting patient safety after administration.

In this study, we examined Tc-99m-HMPAO-labeled leukocytes in a cohort of 30 patients who applied to Istanbul University-Cerrahpasa, Cerrahpasa Faculty of Medicine, Department of Nuclear Medicine. The methods, devices and chemicals used in the preparation of Tc-99m-HMPAO-labeled leukocytes were compared with other nuclear medicine clinics in Europe. Additionally, it was assessed the possible effects of using different methods, devices and chemicals, the currently used medications by patients and the numbers of leukocytes [white blood cells (WBCs)] and erythrocytes [red blood cells (RBCs)].

Materials and Methods

Thirty paients were included in our study who applied for Tc-99m-HMPAO-labeled leukocyte scintigraphy (16 F, 14 M and age 62±15.1).

Primarily, patients were informed about Tc-99m-HMPAO-labeled leukocyte scintigraphy, and radiation protection instructions were provided. Patients' age, height, weight, gender, blood group, and history were noted before starting the procedure, in addition to whether they use certain medications such as antibiotics, insulin, blood pressure , and blood thinners.

The preparation of Tc-99m-HMPAO-labeled leukocytes was carried out under 2 main headings: "isolation of leukocytes", and radiolabeling and purification". All procedures were carried out under aseptic condition.

Isolation of Leukocytes

A total of 80 mL blood was taken from the patients with a butterfly needle (20 G) gently, 40 mL each into 2 sterile 50 mL syringes containing 0.5 mL anticoagulant (vasparin 1). 500 µL of 80 mL blood taken from the patients were separated to determine the number of leukocytes, erythrocytes, neutrophils, and lymphocytes in the blood. Samples with the number of WBCs >5.5 (10^3/uL) in the blood were compared with those with <5.5 (10^3/uL) through the change in the radiolabeling yield of Tc-99m-HMPAO-labeled leukocytes. 10 mL of 80 mL was

centrifuged (2000 g) and 3-5 mL volume of supernatant (cell free plasma, CFP) was used to dilute Tc-99m-HMPAO-labeled leukocytes just before the injection (6,10,11).

7 mL of PF polihes (HES 200/0.5) 6% starch solution was added to the remaining 50 mL syringes containing approximately 35 mL blood, and mixed slowly and left for erythrocyte sedimentation for 40-60 minutes. During sedimentation, the amount of supernatant (leukocyte-rich plasma, LRP) was visually checked. At the end of the sedimentation, the supernatant was transferred to a falcon tube before centrifuging (150 g, 5 min) 500 μL of the supernatant was separated again to determine the numbers of RBC and WBC in LRP by flow cytometry. Samples with the numbers of WBCs $>2\times10^8$ in the blood were compared with those with $<2\times10^8$ through the change in the radiolabeling yield of Tc-99m-HMPAO-labeled leukocytes. After centrifugation, the pellet was diluted with 2.5 mL vasparin-2 solution (6,10,12).

Vasparin-1 solution: 1.6 mL of heparin sodium (25.000 IU) + 8.4 mL NaCl (0.09%).

Vasparin-2 solution: 0.1 mL of vasparin-1 solution + 9.9 mL NaCl (0.09%).

Radiolabeling and Purification

Tc-99m-HMPAO was prepared by adding 40 mCi/2 mL freshly eluted (<30 min) Tc-99m to the HMPAO cold kit and incubated 10 min at room temperature. Afterward, leukocytes in 2.5 mL vasparin-2 solution and 20 mCi/1 mL Tc-99m-HMPAO were mixed into a 50 mL sterile falcon tube and incubated for 20 min at room temperature. During incubation, the mixture was shaken periodically. At the end of the incubation, the mixture was centrifuged (150 g, 5 min) and the supernatant was removed via pasteur pipette. Both pellet and supernatant were counted with a dose calibrator to calculate the radiolabeling yield of Tc-99m-HMPAO-labeled leukocytes (6,10,11).

Then, the pellet was diluted with 20 mL of sterile saline and 1 mL of 20 mL labeled leukocyte suspension separated for inoculation to sabouraud dextrose broth medium and 1 mL to fluid thioglycollate medium The remaining labeled leukocyte suspension was centrifuged over again (150 g, 5 min) and the supernatant was removed. The pellet was diluted with CFP. 100 μL of the patients' dose was separated for the hemocytometer method to determine the viability of leukocytes (6,10,11).

Quality Controls

Radiolabelling Efficiency of Tc-99m-HMPAO

The radiolabelling efficiency of Tc-99m-HMPAO was carried out with the paper chromatography method. Whatmann-3 paper was used as the stationary phase and ethyl acetate was used as the mobile phase (13,14). Lipo-Tc-99m-HMPAO showed an Rf value of 1.0. Hydro-Tc-99m-HMPAO and free Tc-99m showed an Rf value of 0.0. The strips were scanned with a scanner (Cyclone® Plus Storage Phosphor System, Perkin Elmer, Milan, Italy). The effect of the radiochemical purity on the radiolabeling yield of Tc-99m-HMPAO-labeled leukocytes was analyzed with SPSS-20.

Biochemical Analysis

The numbers of RBC, WBC, neutrophil and lymphocytes in the blood and numbers of RBC and WBC in LPR were determined by flow cytometry using a Beckman Coulter-LH780 device in a volume of 200 μL and manual method (15). The effect of the number of WBC in the blood and LPR on the radiolabeling yield of Tc-99m-HMPAO-labeled leukocytes was analyzed with SPSS-20.

Microbiological Quality Control of Tc-99m-HMPAO-labeled Leukocyte

1 mL samples obtained from 20 mL Tc-99m-HMPAO-labeled leukocytes, which diluted with 0.9% NaCl were kept until the amount of radioactivity fell below the limits allowed by the Nuclear Regulatory Authority, and then sterility test in accordance with European Pharmacopoeia was applied at Istanbul University, Faculty of Pharmacy, Department of Pharmaceutical Microbiology (6,16). Additionally, 100 μL samples obtained from the Tc-99m-HMPAO-labeled leukocyte were added to the Eppendorf tubes containing 100 μL methylene blue before the injection. The sample was shook gently and dripped onto a hemocytometry slide and examined under a light microscope to determine the viability of leukocytes at zeroth and 4th hours (6).

SPECT/CT Imaging Procedure and Calculation of Spleen/Liver Ratio

Scintigraphy images were acquired at 30 min and 4 h after Tc-99m-HMPAO injection. At 30 min, a static (planar) image was made for 10 min with 256x256 matrix size followed by a 1 minute spleen static image with the same matrix size. At the 4th h, static imaging was again conducted for up to 10 min with a 256x256 matrix, then SPECT/CT was performed with 32 frames, 45 second/frame, and 128x128 matrix size (17).

From 30 minutes images, spleen/liver uptake ratio, and lung uptake was derived and lung uptake was calculated at the 4th-hour via Image-J program (10.6 mCi, n=3).

This study Istanbul University-Cerrahpasa, Cerrahpasa Faculty of Medicine, Ethics Committee approval was obtained (number: 59491012-604.01.02), and all patients signed written informed consent.

Statistical Analysis

The effect of the blood thinners, insulin, antibiotics and blood pressure medications, and the amount of leukocytes in the blood and LPR were explored through the change in the radiolabeling yield of Tc-99m-HMPAO-labeled leukocytes using the SPSS-20 program. Mann-Whitney U test was used for comparing the means as the data showed no normal distribution.

Results

Isolation of Leukocytes

Any abnormalities, aggregates, clumps, or clots were not observed the during the isolation of leukocytes.

Quality Controls

Radiolabeling and Purification

The pH of Tc-99m-HMPAO was measured between 6 and 8 via a pH strip. The contents of the kit were completely dissolved and the radiochemical purity of Tc-99m-HMPAO was 90±2.04% (n=30) (Table 1).

During the radiolabeling and purification of Tc-99m-HMPAO-labeled leukocytes, it was observed that the leukocytes did not aggregate and the radiolabeling yield was found >40% for 28 patients, <40% for 2 patients, and 51±10.9% on average (Table 2).

Table 1. Radiochemical purity of Tc-99m-HMPAO			
Patient no	The radiochemical purity of Tc-99m-HMPAO (%)	Patient no	The radiochemical purity of Tc-99m-HMPAO (%)
1	93.4	16	91
2	91	17	89.5
3	91	18	89.5
4	95.7	19	91
5	87	20	93
6	87	21	93
7	91	22	89
8	91	23	89
9	91	24	91
10	91	25	91
11	91	26	90
12	91	27	90
13	86.4	28	92
14	86.4	29	92
15	93.4	30	90
HMPAO: Hexamethylpropyleneamineoxime			

Biochemical Analysis

The numbers of leukocytes, erythrocytes, neutrophils, and lymphocytes in the blood samples of patients and the numbers of erythrocytes in the LRP are shown in Table 3.

Microbiological Quality Control

No microbial growth was found in Tc-99m-HMPAO-labeled leukocytes, it was sterile. Additionally, in the hemocytometric examination of Tc-99m-HMPAO-labeled leukocytes performed zeroth and 4th hour, living/dead cell ratio was found 97.5%.

The Effect of the Medications Used by the Patients on the Radiolabeling Yield of Tc-99m-HMPAO-Labeled Leukocyte

The effect of whether the patients used any antibiotics, blood thinners, insülin, and blood pressure medications, as well as the quantity and duration of medications on the radiolabeling yield of Tc-99m-HMPAO-labeled leukocytes were analyzed with SPSS-20 (Table 4). It was revealed that the frequently used medications have no effect on the radiolabeling yield (p>0.05).

SPECT/CT Imaging

At SPECT/CT imaging, it was found that the spleen uptake was more than liver uptake and at 30th minute and 4th hour imaging there was no uptake in the lung.

Discussion

This study aimed to adapt the protocol specified as "Guidelines for the labeling of leucocytes with Tc-99m-HMPAO" (6) to our own conditions at Istanbul University-Cerrahpasa, Cerrahpasa Faculty of Medicine, Department of Nuclear Medicine. Also, the evaluation of Tc-99m-HMPAO-labeled leukocytes in terms of radiochemical, biochemical, and microbiological quality control. Furthermore, the effect of the medications currently used by the patients and leukocyte numbers in the blood obtained from patients and LPR on radiochemical yields of Tc-99m-HMPAO-labeled leukocytes and imaging quality was evaluated.

Frequent medications involving antibiotics, insulin, blood pressure, and blood thinners as well as the amount and duration of use were recorded. In despite of these results, the medications currently used by the patients did not affect the imaging quality and the radiolabeling yield of Tc-99m-HMPAO-labeled leukocytes statically (p>0.05). In line with these findings, it was concluded that patients can safely use these medications before the procedure as this is a crucial issue that impacts the quality of life of patients.

During the leukocyte isolation step, the patient's blood was taken into 50 mL injectors containing vasparin-1

Karayel et al. Leukocyte Labeling with Tc-99m-HMPAO

Mol Imaging Radionucl Ther 2023;32:28-34

Table 2. Radiolabeling efficiency of Tc-99m-HMPAO-labeled leukocytes

No	Tc-99m-HMPAO activity (mCi)	Tc-99m-HMPAO-labeled leukocyte activity (mCi)	Radiolabeling efficiency (%)	No	Tc-99m-HMPAO activity (mCi)	Tc-99m-HMPAO-labeled leukocyte activity (mCi)	Radiolabeling efficiency (%)
1	20	10,5	52.5	16	20	8.25	41.25
2	20	9	45	17	20	13.01	65.05
3	20	10	50	18	20	10.4	52
4	20	10.3	51.5	19	20	14.8	74
5	20	8.75	43.75	20	20	12.4	62
6	20	12.6	63	21	20	10.5	52.5
7	20	9	45	22	20	8.1	40.5
8	20	11.38	56.9	23	20	10.55	52.75
9	20	10.35	51,75	24	20	7.2	36
10	20	12.00	60	25	20	13.83	69.15
11	20	9.69	48.45	26	20	8.61	43.05
12	20	15.2	76	27	20	11.2	56.15
13	20	9.6	48	28	20	9.2	46
14	20	8.5	42.5	29	20	9.9	49.5
15	20	10.1	50.5	30	20	5.1	25.5

HMPAO: Hexamethylpropyleneamineoxime

Table 3. Analysis of cell numbers of leukocytes, erythrocytes, neutrophils and lymphocytes

Patient no	RBCs in blood (10⁶/uL)	RBCs in LRP (10⁶/uL)	WBC (10³/uL)	Neutrophils (%)	Lymphocytes (%)	Patient no	RBCs in blood (10⁶/uL)	RBCs in LRP (10⁶/uL)	WBC (10³/uL)	Neutrophils (%)	Lymphocytes (%)
1	4.65	0.03	5.1	77.4	16.1	16	5.36	0.02	3.8	56	39
2	4.78	0.04	5.1	45.6	46.1	17	4.76	0.02	10.3	59	29
3	6.35	0.04	5.4	70.6	20.7	18	4.53	0.04	6.4	58	35
4	3.9	0.03	7	53.2	37.4	19	4.86	0.03	5.5	45.8	34.3
5	5.49	0.03	5.1	67	25.4	20	4.21	0.03	5	61.3	33.3
6	5.85	0.03	3.4	52.4	42.6	21	4.89	0.03	10	82.5	12.1
7	4.72	0.04	4.5	62.1	32.1	22	4.66	0.03	3.8	43.7	41
8	5.9	0.04	5.3	73.8	19	23	4.77	0.03	7.4	49.5	36.1
9	5.11	0.04	9.2	85.9	11.7	24	6.29	0.04	6.2	65.2	28.7
10	6.45	0.02	2.9	69.5	23.3	25	5.68	0.03	6.3	54	33.6
11	5.67	0.02	4	64.7	28.7	26	5.01	0.02	2.8	56	40.7
12	3.99	0.03	5.8	70	19.9	27	7.63	0.03	3.3	67.5	25.9
13	4.59	0.03	3.7	66.3	21.2	28	4.1	0.02	4.4	86.9	8.7
14	4.85	0.05	5.1	56.4	37.5	29	4.62	0.01	3.5	82.5	6
15	4.71	0.03	3.7	55.5	40	30	4.1	0.02	4.4	86.9	8.7

RBC: Red blood cell, WBC: White blood cell, LRP: Leukocyte-rich plasma

Table 4. Medications currently used by patients and radiolabeling yield of Tc-99m-HMPAO-labeled leukocytes

	Antibiotics	Blood thinners	Insulin	Blood pressure
Number of patients using medications	7	9	10	9
Radiolabeling yield of Tc-99m-HMPAO-labeled leukocytes belongs patients using medications (mCi)	10.54	11.37	10.93	10.48
Number of patients not using medications	23	21	20	21
Radiolabeling yield of Tc-99m-HMPAO-labeled leukocytes belongs patients not using medications (mCi)	10.27	9.89	10.03	10.27
HMPAO: Hexamethylpropyleneamineoxime				

solution to prevent coagulation. In the guidelines (6), anticoagulant citrate dextrose solution (ACD-A) is used as an anticoagulant. In our study, since ACD-A is not available in our department, heparin sodium was used instead of ACD-A, and any coagulation problem was not experienced.

In the guidelines (6), it is stated that at least $2×10^8$ leukocytes must achieve a good labeling efficiency. In our study, the mean number of leukocytes in the blood and in the LPR was determined as $3.69±1.36×10^8$ and $2.89.88±×10^8$ respectively and these are above the numbers specified in the guidelines. The samples with the number of WBCs >5.5 (10^3/uL) in the blood were compared with those of <5.5 (10^3/uL). And the samples with the numbers of WBC >$2×10^8$ in the LPR were compared to those of <$2×10^8$. The radiochemical yield of the Tc-99m HMPAO-labeled leukocytes of the samples with the number of WBC >5.5 (10^3/uL) in the blood was higher than those of <5.5 (10^3/uL). The radiochemical yield of the Tc-99m HMPAO-labeled leukocytes of the samples with the number of WBC >$2×10^8$ in the LPR was higher than those of <$2×10^8$. For the first time in our study, the effect of the WBC numbers on the radiolabeling yield of Tc-99m-HMPAO-labeled leukocytes was compared.

According to guidelines (6), 10% HES (200/0.5 or 200/0.6) solution is recommended for getting LPR from the blood. In our study, we use 6% HES (200/0.5) solution, which was used by other groups (10,12). The erythrocyte numbers in the LPR determined with flow cytometer was found average $0.03±0.008*10^6$/uL. In other words, the number of erythrocytes were removed at a rate of >99% in LPR. This result is similar to the other group (11).

It is relevant to prepare Tc-99m-HMPAO during radiolabeling as it affects the radiolabeling yield of Tc-99m-HMPAO-labeled leukocytes. In our study, radiochemical purity of Tc-99m-HMPAO prepared with freshly eluted Tc-99m-pertechnetate, an average of 90%±2.04 was found and it falls within the limits specified in European Pharmacopeia.

While lipo- Tc-99m-HMPAO is labeled with leukocytes, it passes into the cell by passive diffusion and becomes trapped there. In the guidelines (6), it is stated that >40%

radiochemical yield is sufficient. In our study, the average radiolabeling yield of Tc-99m-HMPAO-leukocytes was found 51±10.9% and it was within the limits accepted by the guideline.

As with all other intravenously injected drugs, microbiological tests must be applied to Tc-99m-HMPAO-labeled leukocytes, which are classified as drugs by the Food and Drug Administration. In our study, a sterility test was applied to Tc-99m-HMPAO-labeled leukocytes in accordance with the European Pharmacopoeia. The samples were inoculated in liquid sabouraud medium and incubated for 14 days in an incubator at 25 °C and inoculated in thioglycolate liquid medium and incubated for 14 days in an incubator at 37 °C. Under normal conditions, at the end of the incubation period, the presence of growth in these media is evaluated according to the presence of turbidity with visual controls. However, since the samples contain leukocyte cells in both media, it is not possible to control the turbidity visually. At the end of the 14-day incubation period, the samples taken from the liquid sabouraud medium are cultured again into the sabouraud dextrose agar medium for 5 days, and the samples taken from the thioglycolate liquid medium are cultured again into the tryptic soybean medium for 3 days. At the end of the incubation periods, it was evaluated visually whether bacteria or fungal colonies grew on the media. Additionally, the samples were inoculated in sheep blood agar medium to grow other microorganisms and to determine hemolysis reactions, and were incubated for 3 days in an incubator at 37 °C. According to the sterility test, it was determined that there was no growth in all media and all the products were sterile.

Because of the visual controls, no clots or clusters were found. The results are similar to other studies (6,10,11).

While preparing Tc-99m-HMPAO-labeled leukocytes, the leukocytes must not lose their vitality during both labeling and after they are injected. Leukocytes that lose vitality are not labeled during the labeling process and the biodistribution is not like living cells after injection. In our study, the viability control leukocytes were performed with the hemocytometer and number of viable cells was found

Karayel et al. Leukocyte Labeling with Tc-99m-HMPAO

Mol Imaging Radionucl Ther 2023;32:28-34

97.5%. In the guidelines (6), it is stated that >96% viable cells are sufficient.

At SPECT/CT imaging, it was found that the spleen uptake was more than liver uptake and at 30th minute and 4th h scans, there was no uptake in the lung same as the guideline reported (6).

Conclusion

The protocol specified "Guidelines for the labeling of leucocytes with Tc-99m-HMPAO" (6) is successful and applicable at our site at Istanbul University-Cerrahpasa, Cerrahpasa Faculty of Medicine, Department of Nuclear Medicine. Tc-99m-HMPAO-labeled leukocytes was safely injected as sterile without loss of vitality and aggregation .

It was found that the medications currently used by the patients did not affect the radiolabeling yield of Tc-99m-HMPAO-labeled leukocytes and the radiolabeling yield of Tc-99m-HMPAO-labeled leukocytes increased as the leukocyte numbers increased.

Consequently, the protocol of preparing Tc-99m-HMPAO-labeled leukocytes and quality controls was installed in our department.

Ethics

Ethics Committee Approval: Istanbul University-Cerrahpasa, Cerrahpasa Faculty of Medicine, Ethics Committee approval was obtained (number: 59491012-604.01.02).

Informed Consent: All patients signed written informed consent.

Peer-review: Externally peer-reviewed.

Authorship Contributions

Concept: E.K., M.O., A.S.B.T., Data Collection or Processing: E.K., M.O., A.S.B.T., Analysis or Interpretation: E.K., M.O., A.S.B.T., Literature Search: E.K., M.O., A.S.B.T., Writing: E.K., M.O., A.S.B.T.

Conflict of Interest: No conflict of interest was declared by the authors.

Financial Disclosure: This research was supported by Istanbul University Scientific Research Projects (BAP) (project number: 25322).

References

1. Vermeulen K, Vandamme M, Bormans G, Cleeren F. Design and challenges of radiopharmaceuticals. Semin Nucl Med 2019;49:339-356.

2. Demir M. Nükleer Tıp Fiziği ve Klinik Uygulamaları (4. baskı). İstanbul, 2014.

3. Brugarolas P, Comstock J, Dick DW, Ellmer T, Engle JW, Lapi SE, Liang SH, Parent EE, Kishore Pillarsetty NV, Selivanova S, Sun X, Vavere A, Scott PJH; Society of Nuclear Medicine and Molecular Imaging Radiopharmaceutical Sciences Council. Fifty years of radiopharmaceuticals. J Nucl Med Technol 2020;48(Suppl 1):34S-39S.

4. Papagiannopoulou D. Technetium-99m radiochemistry for pharmaceutical applications. J Labelled Comp Radiopharm 2017;60:502-520.

5. Uhl P, Fricker G, Haberkorn U, Mier W. Radionuclides in drug development. Drug Discov Today 2015;20:198-208.

6. de Vries EF, Roca M, Jamar F, Israel O, Signore A. Guidelines for the labelling of leucocytes with (99m)Tc-HMPAO. Inflammation/infection taskgroup of the European Association of Nuclear Medicine. Eur J Nucl Med Mol Imaging 2010;37:842-848. Erratum in: Eur J Nucl Med Mol Imaging 2010;37:1235.

7. Govaert GAM, Bosch P, IJpma FFA, Glauche J, Jutte PC, Lemans JVC, Wendt KW, Reininga IHF, Glaudemans AWJM. High diagnostic accuracy of white blood cell scintigraphy for fracture related infections: results of a large retrospective single-center study. Injury 2018;49:1085-1090.

8. Granados U, Fuster D, Soriano A, García S, Bori G, Martínez JC, Mayoral M, Perlaza P, Tomás X, Pons F. Screening with angiographic images prior to (99m)Tc-HMPAO labelled leukocyte scintigraphy in the diagnosis of periprosthetic infection. Rev Esp Med Nucl Imagen Mol 2015;34:219-224.

9. Pijarowska-Kruszyna J, Karczmarczyk U, Jaroń AW, Laszuk E, Radzik M, Garnuszek P, Mikołajczak R. New synthesis route of active substance d,l-HMPAO for preparation technetium Tc99m exametazime. Nucl Med Rev Cent East Eur 2017;20:88-94.

10. Martinez T, Gallego Peinado M, Sanchez Catalicio J, Perez Angel F, Contreras Gutiérrez J. Validation of the leukocyte labeling procedure with a new kit for the preparation of technetium-99m exametazime injection. Nucl Med Commun 2016;37:432-434.

11. Kim EM, Jeong HJ, Lim ST, Sohn MH. Analysis of cell fraction of 99mTc-HMPAO radiolabeled leukocytes. Curr Radiopharm 2020;13:142-148.

12. Hung JC, Chowdhury S, Mullan BP. Use of stabilized technetium-99m-exametazime for radiolabeling leukocytes. J Nucl Med 1998;39:912-917.

13. Taşçı C, Ülker Ö, Ertay T, Taner MS, Soylu A, Berk F, Ünak P. Radyofarmasötikler için kalite kontrol yöntemleri kılavuzu. Turk J Nucl Med 2003;12:137-148.

14. Decristoforo C, Zolle I, Rakiás F, Imre J, Jánoki G, Hesslewood SR. Quality control methods of 99mTc pharmaceuticals. In: Zolle I (eds). Technetium-99m Pharmaceuticals. Springer, Berlin, Heidelberg, 2007. https://doi.org/10.1007/978-3-540-33990-8_9

15. Wongkrajang P. Comparison of leukocyte differential count by beckman coulter unicel DxH800, Beckman Coulter LH780 and Sysmex XE-5000. Siriraj Medical Journal 2015;67.

16. Owunwanne A. The handbook of radiopharmaceuticals. Springer, 2012.

17. O'Malley JP, Ziessman HA. Nuclear medicine and molecular imaging: the requisites e-book. Elsevier Health Sciences, 2020.

The Impact of Metabolic ¹⁸F-Fluorodeoxyglucose Positron Emission Tomography/Computed Tomography Parameters on the Prognosis of Resectable Pancreatic Adenocarcinoma

¹⁸F-Florodeoksiglukoz Pozitron Emisyon Tomografisi/Bilgisayarlı Tomografi Metabolik Parametrelerinin Rezektabl Pankreas Adenokarsinomunun Prognozu Üzerine Etkisi

 Özgül Ekmekçioğlu[1], Muharrem Battal[2], Özgür Bostancı[2], Banu Yılmaz Özgüven[3]

[1]University of Health Sciences Turkey, Şişli Hamidiye Etfal Training and Research Hospital, Clinic of Nuclear Medicine, İstanbul, Turkey
[2]University of Health Sciences Turkey, Şişli Hamidiye Etfal Training and Research Hospital, Clinic of Hepatobiliary Surgery, İstanbul, Turkey
[3]University of Health Sciences Turkey, Şişli Hamidiye Etfal Training and Research Hospital, Clinic of Pathology, İstanbul, Turkey

Abstract

Objectives: ¹⁸F-fluorodeoxyglucose (FDG)-positron emission tomography/computed tomography (PET/CT) is a useful staging method in pancreatic cancer. The prognosis of pancreatic adenocarcinoma is affected by the tumor stage and resectable state. Maximum standardized uptake value (SUV_{max}), metabolic tumor volume (MTV), and total lesion glycolysis (TLG) of primary tumors are related to prognostic parameters in pancreatic cancer. This study compared ¹⁸F-FDG PET/CT findings with prognostic factors and overall survival of patients with pancreatic cancer.

Methods: Patients with pancreatic adenocarcinoma, referred to our department between 2015 and 2022 for staging, were retrospectively evaluated. Head-to mid-thigh PET/CT images were obtained 1 h after ¹⁸F-FDG injection. Demographic data, survival, and clinical and pathological findings of 39 patients, who underwent surgery after PET/CT imaging, were collected. All primary tumor MTV, SUV_{max}, background SUV_{max}, and TLG data have were measured.

Results: The images of 39 patients (24 women and 15 men) with a mean age of 66.62±9.60 years were evaluated. The mean SUV_{max}, MTV 40%, and TLG of the primary tumors in the pancreatic tissue were 6.28±2.33, 19.33±9.77, and 66.56±45.99, respectively. The average survival after disease diagnosis was 18.97±11.47 (2-55) months. MTV and TLG were significantly higher in patients who died during our study. SUV_{max} has a significant effect on mortality.

Conclusion: ¹⁸F-FDG PET/CT metabolic parameters of SUV_{max}, MTV, and TLG could help predicting the prognosis of pancreatic cancer preoperatively and follow-up in patients with resectable tumors. Additionally, in our study group tumor grade and perineural invasion significantly affected overall survival.

Keywords: Positron emission tomography/computed tomography, pancreatic cancer, metabolic tumor volume, total lesion glycolysis, maximum-standardized uptake value

Öz

Amaç: ¹⁸F-florodeoksiglukoz (FDG)-pozitron emisyon tomografisi/bilgisayarlı tomografi (PET/BT), pankreas kanserinde yararlı bir evreleme yöntemidir. Pankreas adenokarsinomunun prognozunu, tümör evresi ve rezektabl olması etkilemektedir. Primer tümörün maksimum standartlaştırılmış alım değeri (SUV_{maks}), metabolik tümör hacmi (MTV) ve toplam lezyon glikolizisi (TLG), pankreas kanserinde prognostik parametrelerle ilişkili olduğu gösterilmiştir. Bu çalışma, pankreas kanserli hastaların ¹⁸F-FDG PET/BT bulgularının prognostik faktörler ve sağkalım ile arasındaki ilişkiyi araştırmayı amaçlamıştır.

Yöntem: 2015-2022 yılları arasında bölümümüze evreleme için sevk edilen pankreas adenokarsinomu tanılı hastalar retrospektif olarak değerlendirildi. ^{18}F-FDG enjeksiyonundan 1 saat sonra baş-uyluk ortası PET/BT görüntüleri elde edildi. PET/BT görüntüleme sonrası opere edilen 39 hastanın demografik bilgileri, sağkalım süreleri, klinik ve patolojik bulguları toplandı. Primer tümöre ait MTV, SUV$_{maks}$, arka plan SUV$_{maks}$ ve TLG verileri ölçülerek hesaplamalar yapıldı.

Bulgular: Yaş ortalaması 66.62±9.60 yıl olan 39 hastanın (24 kadın ve 15 erkek) görüntüleri değerlendirildi. Pankreas dokusunda primer tümörün ortalama SUV$_{maks}$, MTV %40 ve TLG'si sırasıyla 6.28±2.33, 19.33±9.77 ve 66.56±45.99 idi. Hastalık teşhisi sonrası ortalama sağkalım 18.97±11.47 (2-55) ay olarak bulundu. Çalışmamız sırasında ölen hastalarda MTV ve TLG anlamlı olarak daha yüksekti. SUV$_{maks}$'ın mortalite üzerinde önemli bir etkisi olduğu saptandı.

Sonuç: Preoperatif olarak elde edilen metabolik ^{18}F-FDG PET/BT parametreleri olan SUV$_{maks}$, MTV ve TLG rezektabl pankreas kanserinin prognozunu öngörmede ve takipte yardımcı olabilir. Ek olarak, tümör derecesi ve perinöral invazyon da genel sağkalımı önemli ölçüde etkilediği çalışmamızda anlaşılmıştır.

Anahtar kelimeler: Pozitron emisyon tomografisi/bilgisayarlı tomografi, pankreas kanseri, metabolik tümör hacmi, toplam lezyon glikolizis, maksimum standartlaştırılmış alım değeri

Introduction

Pancreatic cancer is one of the deadliest cancer types with high mortality rates, since it is usually detected with distant metastases. Due to the location of the tumor, it might not present symptoms in the initial stage. Even though the resection of the tumor has a curative effect, not every patient can gain the advantage of surgery. Mortality rates are almost 15% in a patient with an early stage (1,2,3).

The prognostic factors in pancreatic cancer are already been defined and mostly related to pathological findings such as tumor size, grade, lymph node metastases, tumor differentiation, perineural invasion, and lymphovascular invasion. These prognostic factors are proved to affect recurrence and survival (1,4).

^{18}F-fluorodeoxyglucose (FDG) positron emission tomography/computed tomography (PET/CT) is widely used in patients with pancreatic cancer. The contribution of PET/CT in clinical management is already known, particularly in staging. Detecting distant metastases could change the treatment decision, which also affects survival. A prospective multicenter study emphasized a 40% effect on management after ^{18}F-FDG PET/CT imaging on initial staging (5). Furthermore, ^{18}F-FDG PET/CT imaging could provide beneficial information about recurrence (6). The most commonly used parameter for metabolic activity is the maximum standardized uptake value (SUV$_{max}$) for defining the aggressiveness of the tumor and disease. Higher SUV$_{max}$ is well known for low differentiation and poor prognosis (7). PET/CT also allows volume measurement with the combination of metabolic parameters. Metabolic tumor volume (MTV) and total lesion glycolysis (TLG) are shown to be helpful in understanding the prognosis of the disease in many cancer types. MTV and TLG are the best volumetric data that provide information about the tumor mass burden on the whole body. These data provide valuable information about survival, which could even be a prognostic indicator of worse clinical behavior (8,9).

This study correlated the volumetric analyses and ^{18}F-FDG parameters with prognostic factors of patients, increasing the knowledge of the relationship between survival after the disease diagnosis and PET data.

Materials and Methods

Patients with biopsy-proven pancreatic adenocarcinoma that were referred to our department for staging with ^{18}F-FDG PET/CT between 2015 and 2022 were retrospectively evaluated. All patients underwent surgery after PET/CT. Patients who received treatment or underwent surgery before PET/CT were excluded from the study. The histopathology reports of patients had been received after surgery. All demographic data and pathological prognostic findings after surgery were obtained. Grade and size of the tumor, positivity for lymphovascular invasion, perineural invasion, and lymph node metastases were the data included in our study for the correlation. The tumor grade was classified as well or poor differentiated. Other the data besides tumor size were classified as positive or negative.

For the ^{18}F-FDG PET/CT protocol, all patients received approximately 111-370 Mbq (3-10 mci) of ^{18}F-FDG. After 45-60 min with an empty bladder, head to mid-thigh whole body CT (130kV, 50-80 mAs; slice thickness, 3 mm) and PET images were obtained (GE Healthcare, Wisconsin, USA). Oral contrast was used in all patients; in the meantime, intravenous contrast could not be performed in all patients. All PET/CT was were obtained using the same protocol; 1 h after injection of ^{18}F-FDG, head to mid-thigh images were obtained. All images were retrospectively evaluated again, and findings were noted. Patients with distant metastases were excluded from the study to understand the effect of

the measurements of only primary tumor burden. ^{18}F-FDG uptake >2.5 than background activity was accepted as pathological. The region of interest was drawn from the primary tumor location in the pancreatic tissue. SUV_{max}, MTV (cm³), and TLG (g/mL) of the primary tumor were measured using a GE Healthcare PET workstation (Figure 1). For MTV and TLG data, 40% cut-off value was defined as suggested in routine measurements. This threshold is most commonly used for measurements of metabolic volume parameters (10). Background SUV_{max} was also measured from the gluteal region where there was no pathological activity. The background SUV_{max} ratio was used in calculating the ratio with primary tumor SUV_{max} when necessary.

The survival data of the patients were obtained from the hospital system during the collection of the data of this study. The survival data were calculated as months after initial diagnosis and followed by ^{18}F-FDG PET/CT. The mortality rates were also collected from the patients who died during the data collection of the study. Ethical approval was obtained from the University of Health Sciences Turkey, Sisli Hamidiye Etfal Training and Research Hospital Ethics Committee no: 3105, date: 02.02.2021, and all patients provided written informed consent.

Statistical Analysis

All data were analyzed using the Statistical Package for the Social Sciences software for Windows (version 17.0; IBM, Armonk, NY, USA). Individual and aggregate data were summarized using descriptive statistics, including mean, standard deviations, medians (min-max), frequency distributions, and percentages. The Normality of the data distribution was verified by histogram graphs and the Kolmogorov-Smirnov test. For the variables that were not normally distributed, the Mann-Whitney U test was conducted to compare groups. The presence of correlation was analyzed with Spearman's rho test. For survival

Figure 1. Volumetric measurement of the primary lesion on the head of the pancreas with a 23.59 cm³ metabolic tumor volume and 112.1 g/mL of total lesion glycolysis

analyses, Kaplan-Meier analyses were used in the univariate analyses, and Cox regression was used in the multivariate analyses. Receiver operating characteristic (ROC) analysis was used to define cut-off values. P values <0.05 were considered statistically significant.

Results

Thirty-nine patients with histologically proven resectable pancreatic adenocarcinoma were included in this study. Of 39 patients, 24 were male, with a mean age of 66.62±9.60 (min-max: 41-80) years. The mean SUV_{max} of the primary tumor was 6.28±2.33, and the background to primary tumor SUV_{max} ratio was 8.09±3.50. The mean MTV and TLG values of the primary tumor were 19.33±9.77 cm³ and 66.56± 45.99 g/mL, respectively.

The mean tumor size of the primary tumor was 3.31±1.78 cm. Patients were divided into the well (n=32) or poorly (n=7) differentiated groups. Twenty-eight patients from the group had pathologically proven local lymph node metastases. Based on the pathology reports after surgery, 36 patients were positive for lymphovascular invasion, whereas 30 patients were positive for perineural invasion (Table 1).

The mean overall survival rate after diagnosis was 18.97±11.47 (2-55) months. Twenty-two patients were
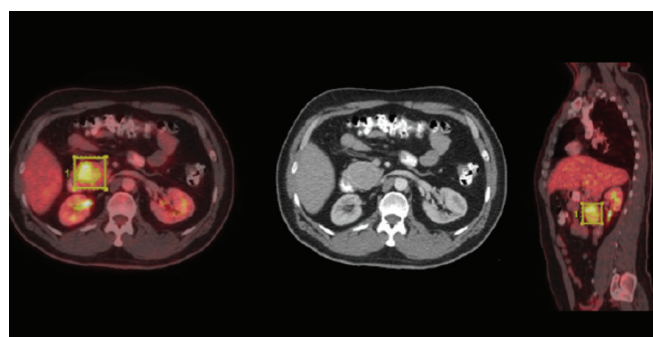
Table 1. Demographics of the patients enrolled to study	
Clinical characteristics	**Values**
Sex (n) Male Female	 24 15
Age mean ± SD (min-max)	66.62±9.60 (41-80)
Primary tumor size (cm)	3.31±1.78 (0.6-9)
Grade of the tumor (n) Well-differentiated Less-differentiated	 32 7
Lymph node metastases (n) Positive Negative	 28 11
Primary tumor SUV_{max} (min-max)	6.28±2.33 (2.8-13.9)
Metabolic tumor volume (cm³)	19.33±9.77
Total lesion glycolysis (g/mL)	66.56±45.99
Lymphovascular invasion (n) Positive Negative	 36 3
Perineural invasion (n) Positive Negative	 30 9
Overall survival after diagnosis (months)	18.97±11.47
SD: Standard deviation, min: Minimum, max: Maximum, SUV_{max}: Maximum standardized uptake value	

reported dead during the data collection of our study. In the Kaplan-Meier analyses, overall survival had a significant relationship with primary tumor grade and perineural invasion (p=0.026; p=0.005 respectively, Figure 2). Multivariate Cox regression analysis has shown that SUV_{max} has a significant effect as an independent factor on mortality (p=0.045, hazard ratio: 1.56, 95% confidence interval: 1.01-2.4, Figure 3). The TLG and MTV data of the patients who have died during the study were significantly higher than patients who were alive in the univariate analyses (p<0.001 and p<0.001, Figure 4).

Poorly differentiated tumor grade had a significant relationship with higher primary tumor SUV_{max} (p=0.031). Patients positive for lymph node metastases had significantly higher primary tumor SUV_{max} than the negative group. TLG

of the primary tumor was significantly higher in patients with perineural invasion (p=0.049).

ROC analysis was conducted for the cut-off values that were defined for the PET data that are statistically significant (Table 2). Primary tumor size with a cut-off value of 3.15 cm, sensitivity, specificity, positive predictive value, and negative predictive values were 59.09%, 88.24%, 86.67%, and 62.50%, respectively. The cut-off value for MTV was 13.80 cm^3 and sensitivity, specificity, positive predictive value, and negative predictive values were 95.45%, 70.59%, 80.77%, and 92.31%, respectively. The TLG cut-off value was 56.85 g/mL with sensitivity, specificity, positive predictive value, and negative predictive value of 77.27%, 94.12%, 94.44%, and 76.19% (Figure 5). Nonetheless, ROC analyses for SUV_{max} values did not show a significant result (p=0.854).
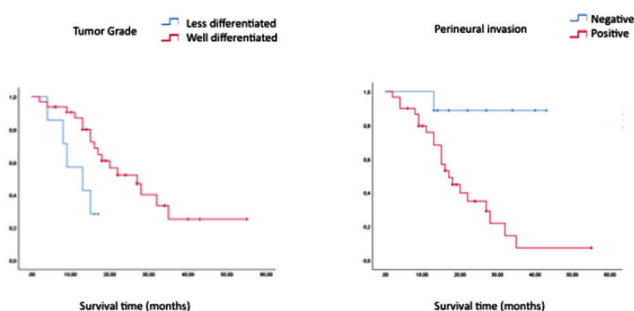
Discussion

SUV_{max} measurements have been successfully used and provided valuable information about the tumor's behaviour (11,12). Furthermore, SUV_{max} has been described as an independent prognostic factor in pancreatic cancer (13). Metabolic parameters of the tumor are shown to be as important as the anatomical information for the patient's prognosis. Nevertheless, as a drawback, the heterogeneous distribution of the ^{18}F-FDG inside the tumor could be deceptive. Other than in our routine daily practice, metabolic volume measurements are also available for evaluating tumor characteristics. In particular, studies have emphasized that metabolic volumetric data is helpful for understanding prognosis, tumor aggressiveness, and therapy assessment (9,14,15). The most useful volumetric parameters of MTV and TLG define additional and more detailed knowledge about tumor and metabolic function. Some studies have emphasized the effect of volumetric parameters on survival in pancreatic adenocarcinoma, more than SUV_{max} (16,17).

Patients who died had significantly higher MTV and TLG values than patients who were alive during the study. Another study similar to this study concept with 63 patients with resectable pancreatic adenocarcinoma reported a significant relationship between metabolic parameters and survival. The cut-off levels of MTV of 7.38 cm^3 and TLG

Figure 2. Kaplan-Meier curves of tumor grade and perineural invasion
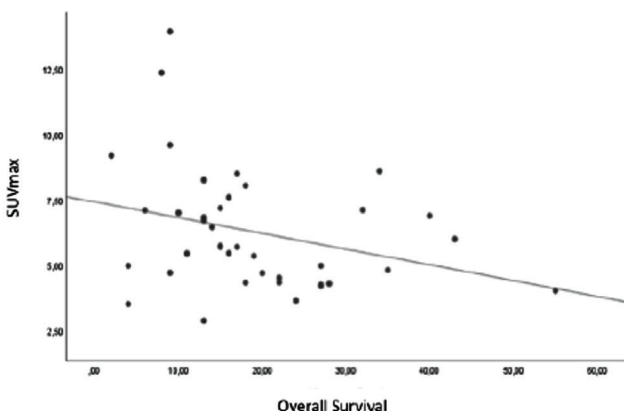
Figure 3. Effect of SUV_{max} as an independent factor on survival
SUV_{max}: Maximum standardized uptake value

| Table 2. ROC analysis and the cut-off values							
	Cut-off	Sensitivity	Specificity	PPV	NPV	CI (95%)	p
Tumor size	3.15	59.09%	88.24%	86.67%	62.50%	0.58-0.9	**0.010**
MTV cm³	13.80	95.45%	70.59%	80.77%	92.31%	0.79-0.9	**<0.001**
TLG g/mL	56.85	77.27%	94.12%	94.44%	76.19%	0.74-0.9	**<0.001**
ROC: Receiver operating characteristic, MTV: Metabolic tumor volume, TLG: Total lesion glycolysis, PPV: Positive predictive values, NPV: Negative predictive values, CI: Confidence interval							
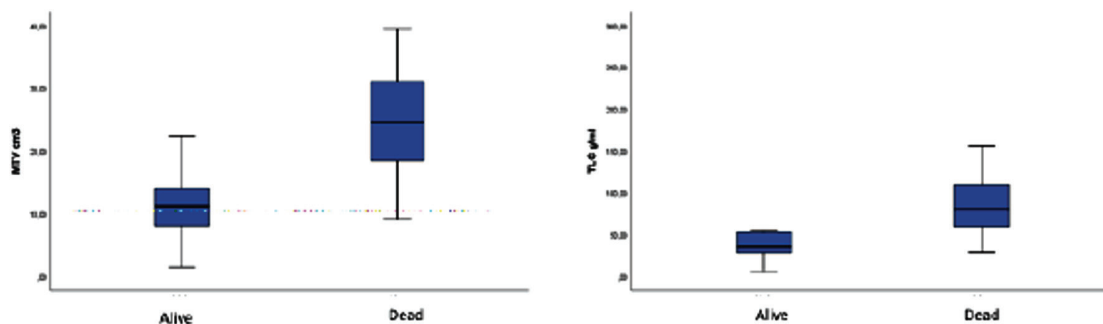
Figure 4. TLG and MTV data of the patients were significantly higher in patients who died during the study in univariate analyses
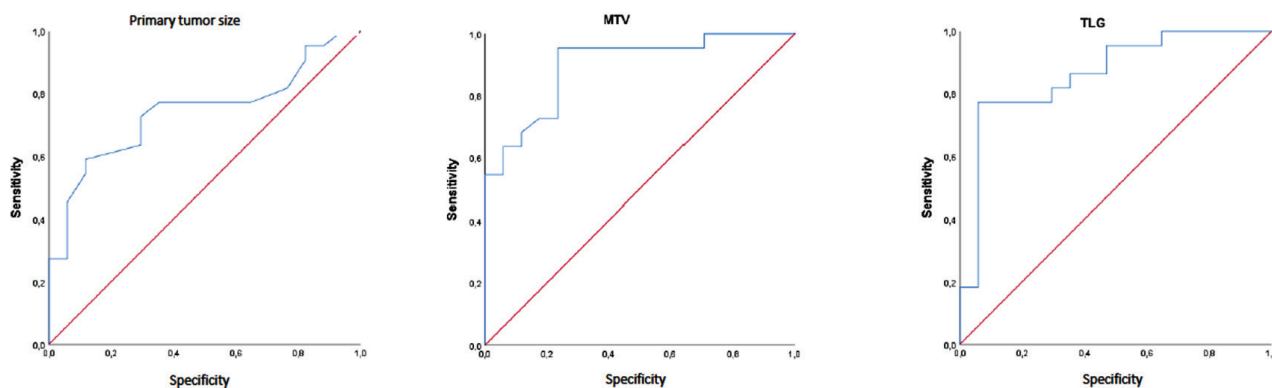MTV: Metabolic tumor volume, TLG: Total lesion glycolysis

Figure 5. ROC curves for the cut-off values of primary tumor size, MTV and TLG
ROC: Receiver operating characteristic, MTV: Metabolic tumor volume, TLG: Total lesion glycolysis

of 18.6 g/mL of this study were lower than our results found in the ROC analysis (18). Furthermore, one of the latest studies found a significant effect of MTV and TLG on survival. The median levels of MTV: 10 cm^3 and TLG: 55 were compatible with our cut-off levels (19). Likelihood, there is still no consensus on the volume thresholds of the measurements, and the results slightly differ also with other studies.

Compatible with other studies, we have found that higher primary tumor SUV$_{max}$ had a significant effect on mortality. Furthermore, tumor grade and perineural invasion were found to have a significant effect on overall survival in our patient group (7,20). Additionally perineural invasion was significantly correlated with TLG of the primary tumor in our study. Some other studies have reported no relationship between metabolic parameters and survival to either the lymphatic or perineural invasion (21,22). Another study emphasized a significant relationship between metabolic parameters and lymphovascular invasion (18). ^{18}F-FDG PET/CT findings are indicated for predicting tumor biology in pancreatic cancer. Perineural invasion is as a negative

prognostic factor and is related to tumor aggressiveness (22,23). The difference in our results from other studies could be caused by patients with metastases, who were excluded from our study, which could affect a more perineural positivity in the initial stage of these patients. Furthermore, we also believe that the results might be affected by the heterogeneous distribution or a small number of patients.

Daily practice of the ^{18}F-FDG PET/CT reports do not always include volumetric analyses. However, with the results of our study, we emphasized that the volumetric measurements and correlations should be considered for reporting. This would lead the clinician to decide on the next step after or even before surgery for operable patients, especially guiding for patient-specific treatment and follow-up of curative disease with being aware of early recurrence.

Study Limitations

This retrospective study has limitations. First of all this was a retrospective study. Since referral patients from other hospitals, not all patients were followed-up in our hospital.

Hence, we could not reach the detailed time to progression data. Furthermore, interobserver or intraobserver agreement of the ^{18}F-FDG PET/CT data analyses was not considered. Prospective trials with more patients should be conducted to evaluate predicting mortality with volumetric analyses and change rates of either overall survival or quality of life of the patient.

Conclusion

Metabolic volumetric parameters of ^{18}F-FDG PET/CT can provide beneficial prognostic information that could direct the treatment and follow-up strategy in staging resectable pancreatic adenocarcinoma. Additionally, SUV$_{max}$ has a significant effect on mortality, whereas tumor grade and perineural invasion has been shown to have a significant effect on overall survival.

Ethics

Ethics Committee Approval: University of Health Sciences Turkey, Sisli Etfal Training and Research Hospital Ethics Committee no: 3105, date: 02.02.2021.

Informed Consent: All patients provided written informed consent.

Peer-review: Externally peer-reviewed.

Authorship Contributions

Surgical and Medical Practices: M.B., Ö.B., Ö.E., B.Y.Ö., Concept: Ö.E., Design: Ö.E., M.B., Data Collection or Processing: Ö.E., B.Y.Ö., Analysis or Interpretation: Ö.E., Literature Search: Ö.E., Ö.B., Writing: Ö.E., Ö.B.

Conflict of Interest: No conflict of interest was declared by the authors.

Financial Disclosure: The authors declared that this study has received no financial support.

References

1. Bilimoria KY, Bentrem DJ, Ko CY, Ritchey J, Stewart AK, Winchester DP, Talamonti MS. Validation of the 6th edition AJCC Pancreatic Cancer Staging System: report from the National Cancer Database. Cancer 2007;110:738-744.

2. Li D, Xie K, Wolff R, Abbruzzese JL. Pancreatic cancer. Lancet 2004;363:1049-1057.

3. Grassetto G, Rubello D. Role of FDG-PET/CT in diagnosis, staging, response to treatment, and prognosis of pancreatic cancer. Am J Clin Oncol 2011;34:111-114.

4. Lewis R, Drebin JA, Callery MP, Fraker D, Kent TS, Gates J, Vollmer CM Jr. A contemporary analysis of survival for resected pancreatic ductal adenocarcinoma. HPB (Oxford) 2013;15:49-60.

5. Ghaneh P, Hanson R, Titman A, Lancaster G, Plumpton C, Lloyd-Williams H, Yeo ST, Edwards RT, Johnson C, Abu Hilal M, Higginson AP, Armstrong T, Smith A, Scarsbrook A, McKay C, Carter R, Sutcliffe RP, Bramhall S, Kocher HM, Cunningham D, Pereira SP, Davidson B, Chang D, Khan S, Zealley I, Sarker D, Al Sarireh B, Charnley R, Lobo D, Nicolson M, Halloran C, Raraty M, Sutton R, Vinjamuri S, Evans J, Campbell F, Deeks J, Sanghera B, Wong WL, Neoptolemos JP. PET-PANC: multicentre prospective diagnostic accuracy and health economic analysis study of the impact of combined modality 18fluorine-2-fluoro-2-deoxy-d-glucose positron emission tomography with computed tomography scanning in the diagnosis and management of pancreatic cancer. Health Technol Assess 2018;22:1-114.

6. Okamoto K, Koyama I, Miyazawa M, Toshimitsu Y, Aikawa M, Okada K, Matsuda H. Preoperative 18[F]-fluorodeoxyglucose positron emission tomography/computed tomography predicts early recurrence after pancreatic cancer resection. Int J Clin Oncol 2011;16:39-44.

7. Moon SY, Joo KR, So YR, Lim JU, Cha JM, Shin HP, Yang YJ. Predictive value of maximum standardized uptake value (SUVmax) on 18F-FDG PET/CT in patients with locally advanced or metastatic pancreatic cancer. Clin Nucl Med 2013;38:778-783.

8. Malek E, Sendilnathan A, Yellu M, Petersen A, Fernandez-Ulloa M, Driscoll JJ. Metabolic tumor volume on interim PET is a better predictor of outcome in diffuse large B-cell lymphoma than semiquantitative methods. Blood Cancer J 2015;5:e326.

9. Im HJ, Pak K, Cheon GJ, Kang KW, Kim SJ, Kim IJ, Chung JK, Kim EE, Lee DS. Prognostic value of volumetric parameters of (18)F-FDG PET in non-small-cell lung cancer: a meta-analysis. Eur J Nucl Med Mol Imaging 2015;42:241-251.

10. Su W, Ren S, Zhu X, Zhang H, Zuo C. Standardized thresholds of volume-based PET/CT parameters predicting survival of patients with pancreatic head cancer treated with stereotactic body radiation therapy. Ann Nucl Med 2020;34:379-387.

11. Lee SM, Kim TS, Lee JW, Kim SK, Park SJ, Han SS. Improved prognostic value of standardized uptake value corrected for blood glucose level in pancreatic cancer using F-18 FDG PET. Clin Nucl Med 2011;36:331-336.

12. Hwang JP, Lim I, Chang KJ, Kim BI, Choi CW, Lim SM. Prognostic value of SUVmax measured by fluorine-18 fluorodeoxyglucose positron emission tomography with computed tomography in patients with pancreatic cancer. Nucl Med Mol Imaging 2012;46:207-214.

13. Nakata B, Nishimura S, Ishikawa T, Ohira M, Nishino H, Kawabe J, Ochi H, Hirakawa K. Prognostic predictive value of 18F-fluorodeoxyglucose positron emission tomography for patients with pancreatic cancer. Int J Oncol 2001;19:53-58.

14. Byun BH, Kong CB, Park J, Seo Y, Lim I, Choi CW, Cho WH, Jeon DG, Koh JS, Lee SY, Lim SM. Initial metabolic tumor volume measured by 18F-FDG PET/CT can predict the outcome of osteosarcoma of the extremities. J Nucl Med 2013;54:1725-1732.

15. Han EJ, Yang YJ, Park JC, Park SY, Choi WH, Kim SH. Prognostic value of early response assessment using 18F-FDG PET/CT in chemotherapy-treated patients with non-small-cell lung cancer. Nucl Med Commun 2015;36:1187-1194.

16. Dholakia AS, Chaudhry M, Leal JP, Chang DT, Raman SP, Hacker-Prietz A, Su Z, Pai J, Oteiza KE, Griffith ME, Wahl RL, Tryggestad E, Pawlik T, Laheru DA, Wolfgang CL, Koong AC, Herman JM. Baseline metabolic tumor volume and total lesion glycolysis are associated with survival outcomes in patients with locally advanced pancreatic cancer receiving stereotactic body radiation therapy. Int J Radiat Oncol Biol Phys 2014;89:539-546.

17. Kim HS, Choi JY, Choi DW, Lim HY, Lee JH, Hong SP, Cho YS, Lee KH, Kim BT. Prognostic value of volume-based metabolic parameters measured by (18)F-FDG PET/CT of pancreatic neuroendocrine tumors. Nucl Med Mol Imaging 2014;48:180-186.

18. Im HJ, Oo S, Jung W, Jang JY, Kim SW, Cheon GJ, Kang KW, Chung JK, Kim EE, Lee DS. Prognostic value of metabolic and volumetric parameters of preoperative FDG-PET/CT in patients with resectable pancreatic cancer. Medicine (Baltimore) 2016;95:e3686.

19. Mohamed E, Needham A, Psarelli E, Carroll M, Vinjamuri S, Sanghera B, Wong WL, Halloran C, Ghaneh P. Prognostic value of 18FDG PET/CT volumetric parameters in the survival prediction of patients with pancreatic cancer. Eur J Surg Oncol 2020;46:1532-1538.

20. Yamamoto T, Sugiura T, Mizuno T, Okamura Y, Aramaki T, Endo M, Uesaka K. Preoperative FDG-PET predicts early recurrence and a poor prognosis after resection of pancreatic adenocarcinoma. Ann Surg Oncol 2015;22:677-684.

21. Myssayev A, Myssayev A, Ideguchi R, Eguchi S, Adachi T, Sumida Y, Tobinaga S, Uetani M, Kudo T. Usefulness of FDG PET/CT derived parameters in prediction of histopathological finding during the

surgery in patients with pancreatic adenocarcinoma. PLoS One 2019;14:e0210178.

22. Yoo MY, Yoon YS, Suh MS, Cho JY, Han HS, Lee WW. Prognosis prediction of pancreatic cancer after curative intent surgery using imaging parameters derived from F-18 fluorodeoxyglucose positron emission tomography/computed tomography. Medicine (Baltimore) 2020;99:e21829.

23. Ozaki H, Hiraoka T, Mizumoto R, Matsuno S, Matsumoto Y, Nakayama T, Tsunoda T, Suzuki T, Monden M, Saitoh Y, Yamauchi H, Ogata Y. The prognostic significance of lymph node metastasis and intrapancreatic perineural invasion in pancreatic cancer after curative resection. Surg Today 1999;29:16-22.

Attenuation Correction for Dedicated Cardiac SPECT Imaging Without Using Transmission Data

Transmisyon Verilerini Kullanmadan Özel Kardiyak SPECT Görüntülemede Atenüasyon Düzeltmesi

⊕ *Getu Ferenji Tadesse*[1,2,3], ⊕ *Parham Geramifar*[4], ⊕ *Mehrshad Abbasi*[5], ⊕ *Eyachew Misganew Tsegaw*[6], ⊕ *Mohammad Amin*[7], ⊕ *Ali Salimi*[2], ⊕ *Mohammad Mohammadi*[2], ⊕ *Behnoosh Teimourianfard*[8], ⊕ *Mohammed Reza Ay*[1,2]

[1]*Research Center for Molecular and Cellular Imaging (RCMCI), Advanced Medical Technologies and Equipment Institute (AMTEI), Tehran University of Medical Sciences (TUMS), Tehran, Iran*
[2]*Department of Medical Physics and Biomedical Engineering, Tehran University of Medical Sciences, Tehran, Iran*
[3]*St. Paul's Hospital Millennium Medical College, Department of Internal Medicine, Addis Ababa, Ethiopia*
[4]*Tehran University of Medical Sciences, Shariati Hospital, Research Center for Nuclear Medicine, Tehran, Iran*
[5]*Tehran University of Medical Sciences, Department of Nuclear Medicine, Vali-Asr Hospital, Tehran, Iran*
[6]*Debre Tabor University Faculty of Natural and Computational Sciences, Department of Physics, Debre Tabor, Ethiopia*
[7]*Shahed University Faculty of Science, Department of Computer Science, Tehran, Iran*
[8]*Tehran University of Medical Sciences, Postdoctoral Research Fellow, Tehran, Iran*

Abstract

Objectives: Attenuation correction (AC) using transmission scanning-like computed tomography (CT) is the standard method to increase the accuracy of cardiac single-photon emission computed tomography (SPECT) images. Recently developed dedicated cardiac SPECT do not support CT, and thus, scans on these systems are vulnerable to attenuation artifacts. This study presented a new method for generating an attenuation map directly from emission data by segmentation of precisely non-rigid registration extended cardiac-torso (XCAT)-digital phantom with cardiac SPECT images.

Methods: In-house developed non-rigid registration algorithm automatically aligns the XCAT- phantom with cardiac SPECT image to precisely segment the contour of organs. Pre-defined attenuation coefficients for given photon energies were assigned to generate attenuation maps. The CT-based attenuation maps were used for validation with which cardiac SPECT/CT data of 38 patients were included. Segmental myocardial counts of a 17-segment model from these databases were compared based on the basis of the paired t-test.

Results: The mean, and standard deviation of the mean square error and structural similarity index measure of the female stress phase between the proposed attenuation maps and the CT attenuation maps were 6.99±1.23% and 92±2.0%, of the male stress were 6.87±3.8% and 96±1.0%. Proposed attenuation correction and computed tomography based attenuation correction average myocardial perfusion count was significantly higher than that in non-AC in the mid-inferior, mid-lateral, basal-inferior, and lateral regions (p<0.001).

Conclusion: The proposed attenuation maps showed good agreement with the CT-based attenuation map. Therefore, it is feasible to enable AC for a dedicated cardiac SPECT or SPECT standalone scanners.

Keywords: Attenuation correction, cardiac, SPECT/CT, XCAT, emission data

Öz

Amaç: Transmisyon taraması benzeri bilgisayarlı tomografi (BT) kullanan atenüasyon düzeltmesi (AC), kardiyak tek foton emisyonlu bilgisayarlı tomografi (SPECT) görüntülerinin doğruluğunu artırmada standart yöntemdir. Son zamanlarda geliştirilen özel kardiyak SPECT BT'yi

desteklememektedir ve bu nedenle, bu sistemlerdeki taramalar atenüasyon artefaktlarına karşı savunmasızdır. Bu çalışmada, kardiyak SPECT görüntüleri ile birlikte rijit olmayan kayıt genişletilmiş kardiyak-gövde (XCAT)-dijital fantomun segmentasyonu yoluyla doğrudan emisyon verilerinden bir atenüasyon haritası oluşturmak için yeni bir yöntem sunulmaktadır.

Yöntem: Kendi geliştirdiğimiz rijit olmayan kayıt algoritması, organların dış hatlarını hassas şekilde bölümlere ayırmak için XCAT-fantomunu kardiyak SPECT görüntüsüyle otomatik olarak hizalar. Atenüasyon haritaları oluşturmak için verilen foton enerjileri için önceden tanımlanmış atenüasyon katsayıları atanmıştır. Otuz sekiz hastanın kardiyak SPECT/CT verilerinin dahil edildiği doğrulama için CT tabanlı atenüasyon haritaları kullanıldı. Bu veritabanlarından alınan 17 segmentli bir modelin segmental miyokardiyal sayımları, eşleştirilmiş örneklem t-testi ile karşılaştırıldı.

Bulgular: Önerilen atenüasyon haritaları ile CT atenüasyon haritaları arasındaki kadın stres fazının ortalama kare hatası ve benzerlik indeksi ölçüsü yapısal benzerlik indeksi ölçümünün ortalama ve standart sapması sırasıyla %6,99±1,23 ve %92±2,0 iken, erkek stres fazının değerleri %6,87±3,8 ve %96±1,0 idi. Mid-inferior, mid-lateral, bazal-inferior ve lateral bölgelerde ProAC ve CTAC ortalama miyokardiyal perfüzyon sayısı non-AC'ye göre anlamlı olarak yüksekti (p<0,001).

Sonuç: Önerilen atenüasyon haritaları BT tabanlı atenüasyon haritasıyla iyi bir uyum gösterdi. Böylelikle, kardiyak çalışmalar özel SPECT veya sadece SPECT tarayıcıları için AC'yi etkinleştirmek mümkün olmuştur.

Anahtar kelimeler: Atenüasyon düzeltmesi, kardiyak, SPECT/BT, XCAT, emisyon verileri

Introduction

Single-photon emission computed tomography (SPECT) is a non-invasive molecular imaging technique that can deliver the radio-tracer distribution images in the patient body by detecting gamma-ray photons (1). Photon attenuation is the most physical factor artifact that contributes to the quantitative and qualitative inaccuracy in cardiac SPECT and can lead to misinterpretation of images by the physicians (2). Thus, attenuation correction (AC) is important for reducing uncertainty in cardiac diagnosis.

van Dijk et al. (3) reported that after the implementation of cardiac AC, images interpreted as "normal" increased from 45 to 72% and the total images that are unequivocal went from 57 to 80%. Moreover, accurate cardiac AC can enhance in "true-positive" and significantly decrease in "false positive" results as confirmed by invasive coronary angiography, hence increase the diagnostic positive predictive value (4).

Non-uniform AC is obtained by measuring the attenuation distribution map in the patient's body, which can then be used along with iterative reconstruction algorithms to accurately compensate for the variable attenuation in the chest. Therefore, to ascertain the accurate correction, which in turn modifies the intensity of the cardiac image, it is essential to create a patient-specific attenuation map (5,6,7,8,9).

There are two methods for generating non-homogeneous attenuation map for AC of SPECT data: transmission-less method and transmission-based scanning using an external radionuclide or X-ray computed tomography (CT). The use of hybrid SPECT/CT systems and for generating non-homogeneous attenuation map is the most conventionally effective method. However, these systems are significantly more expensive than SPECT-only systems and need larger imaging housings and further room lead shielding. Additionally, it increases the radiation exposure dose to the patients and misregistreation between emission and transmission data can occur due to patient motion. According to the study (10) conducted with the myocardial perfusion SPECT/CT for 509 patients, the mean volume computed tomography dose index ($CTDI_{vol}$) received from attenuation CT was 1.34±0.19 mGy. Moreover, most of the systems used for cardiac imaging are either dedicated to cardiac scans that do not support transmission scanning or SPECT standalone due to the high cost of SPECT/CT (11). Around 80% of SPECT market share is stand-alone SPECT systems (12,13) and AC for these systems has paramount importance.

Currently, dedicated cardiac scanners have been developed by different vendor including a dedicated cardiac SPECT (called ProSPECT) with two detectors fixed 90° developed in our lab (Parto Negar Persia Co., Tehran, Iran) (14,15). The ProSPECT system is introduced as an optimized and low-cost design in nuclear cardiology. The gantry and table of the system are designed to comfortably accommodate patients and to provide dual patients positioning (supine and prone). We expect the major benefit of this research is to increase the diagnostic accuracy for such systems and the ~80% SPECT-only scanners to provide a healthy center community with the benefit of convenient and improved image quality.

Generally, there are three techniques for generating attenuation maps from SPECT emission data only. The first technique includes the segmentation of either the photopeak or the scatter data to generate the attenuation map (9,16,17,18,19). A coarse attenuation map can be obtained by segmenting different regions in SPECT images and assigning pre-defined attenuation coefficients. However, these methods are faced difficulty in defining

body outline and organs contour accurately from SPECT emission data. The second technique for generating an attenuation map is model-based methods that estimate the attenuation coefficients directly from the emission data (20,21,22,23,24). However, these models use simultaneous estimating SPECT emission and attenuation parameters; there were crosstalk between emission and attenuation parameters, and thus are inaccurate enough. These methods also suffer from high computation time and were applied only in a slice-by-slice manner. The third and recent technique is deep learning-based approaches that have been proposed to estimate images of one modality from those of another (1). CT attenuation maps were generated from SPECT data alone. This method though, it is more effective than the previous two technique; however, It requires a very large amount of data from another model to perform better than other techniques. It is extremely expensive to train due to complex data models, requiring expensive GPUs and hundreds of machines. This increases the cost to the users.

In this paper, we demonstrated that non-uniform attenuation map was generated from semi-automatic non-rigid registration of an emission reconstructed image with an extended cardiac-torso (XCAT) digital phantom (25) using an in-house developed algorithm and segmenting tissues to assign the respective linear attenuation coefficient to accurately correct the attenuation of the photons passing through the patient body. The use of a proposed map (ProMap) for the AC of the clinical data was evaluated, and the results were compared with CT-based attenuation map (CTMap). This study presented a new method for generating an attenuation map for cardiac AC directly from emission data by segmentation of precisely non-rigid registration XCAT-digital phantom with cardiac SPECT image.

Materials and Methods

This study included the following steps: a) generating the proposed attenuation map, b) developing a maximum-likelihood expectation-maximization (MLEM) algorithm for image reconstruction using MATLAB script (MATLAB 2019a version) and implementation of AC based on the proposed attenuation map, and c) clinical validation of the proposed method.

Ethics Committee Approval

The Tehran University of Medical Sciences Tehran, Iran, Vice-chancellor in research affairs approved the study protocol (approval ID: IR.TUMS.VCR.REC.1397.6355, date: 27.11.2018). All patients gave their informed consent before inclusion in the study.

Development of an Algorithm for Generating an Attenuation Map

The proposed attenuation map was synthesized by the segmentation of non-rigid registering of the simulated 3D XCAT digital phantom with the cardiac SPECT reconstructed image. The XCAT software includes a pair of highly detailed male and female anatomies defined using non-uniform rational B-sline and segmentation of the visible male and female anatomical patient datasets (25,26,27). XCAT non-rigid registration with emission image-based AC methods consist of differentiating the regions with different attenuation properties, assigning the pre-defined linear attenuation coefficients to them, and using the resultant attenuation map to correct the SPECT emission data during reconstruction.

The XCAT phantom is gained widespread importance in the low-resolution nuclear medicine imaging research and lacks the anatomical detail required for use in higher-resolution imaging modalities such as X-ray CT. Moreover, it has paramount importance for improving imaging instrumentation, data acquisition, techniques, image reconstruction, and processing methods, which in turn lead to enhance image quality and more accurate clinical diagnosis (28).

The in-house non-rigid registration algorithm developed in the MATLAB environment was used to perform automatically non-rigid registration of the simulated XCAT phantom of the thorax region with the SPECT image. Generally, the process of non-rigid registration involved in this study was finding the optimal geometric transformation that maximizes the correspondences across the simulated XCAT digital phantom and the SPECT reconstructed image.

The proposed attenuation map generated from non-rigid registration of emission image and simulated images were compared with the X-ray CT-based attenuation map by calculating similarity matrices such as root mean square, root mean square error (MSE), mean absolute error and similarity index measure (SSIM).

Generally, the procedure of generating the attenuation map involves the following: first, XCAT simulation for both male and females was performed. Second, matching the body outline was performed for the emission-reconstructed image and simulated XCAT phantom by non-rigid registration of slice by slice for the transversal view, and magnification parameters were used to fit the XCAT size with different sizes patients. Third, after the XCAT images were registered with the preliminary SPECT images, the thoracic region was segmented into soft tissue, lung, and bone. Fourth, according to the report by Okuda et al. (29), attenuation coefficients of 0.280/cm, 0.150/cm, and

0.053/cm were applied for segmented bone, soft tissue, and lung regions, respectively, for the gamma energy of 140 keV.

Development of the MLEM Algorithm

AC gets wide acceptance in routine clinics due to new reconstruction algorithms mentioned together as iterative algorithms (5,30,31,32). Iterative reconstruction algorithms offer a wide-ranging mathematical framework that allows the modeling of physical processes such as attenuation, scatter, and noise characteristics from the emission and detection processes (33). We adopted the ray-driven projector-backprojector technique, which integrates AC as described by Gullberg et al. (34).

System Matrix and Implementation of Attenuation Correction

The ultimate solution to the non-homogeneous attenuation problem in cardiac SPECT imaging could be solved using an iterative algorithm with a projector-backprojector that models the attenuation of photons along with projection and backprojection rays and that calculates attenuation factors for each pixel along each ray from the predetermined attenuation distribution (8,34). The system matrix or projection operator A has a vital role in the quality of the reconstructed images. Each element A (i,j) gives the contribution of photons emitted from the j'th image voxel in i'th measurement, which is detected by a specified detector's pixel in a certain position. There are several methods to approximate these contributions and even itis possible to use an unmatched projector-backprojector operator pair. Here, we assumed a matched projector and back-projectior operator and determined the contributions by calculating the intersection volume of each ray with each pixel. Considering the parallel hole collimator geometry, each intersection was calculated by finding the intersected area of each ray and pixels, then multiplying it by the slice thickness. The intersection point of each ray's side with each pixel is found and the area of the intersected polygon was calculated. Considering the relatively low resolution of nuclear medicine imaging and a small number of measurements, and the scarcity of the system matrix, we could calculate the system matrix once and store it on memory. Meanwhile the intersection area being calculated, the centroid of each polygon is found, and the distance between the centroid and the ray's detector was also calculated. For each ray, after finding the distance of all contributing pixels, the pixel's indices were sorted regarding their distance to the detector and then cumulative attenuation between the detector and each pixel was found. Then, the exponential correction is applied to the intersected volume and the final system

matrix was obtained. Based on this concept, the system matrix of SPECT was calculated using a MATLAB code. For the image reconstruction, A is a matrix of M x N, where N is the number of pixels, n^2 and $M = N_p D$ being the total number of projections of all detector elements, D, of the detector array in all projection directions, N_p. It is in this system that one includes the physics of imaging.

Clinical Validation

Study Protocol

To validate the proposed AC method, 38 subjects underwent 2-d Tc-99m-sestamibi stress-rest imaging protocol both normal and abnormal (17 males and 21 females, mean age 55±8 years, range 30-70) who were referred to our center for MPI for assessing coronary artery disease (CAD) were included. The mean body mass index was 26.2±3.7 kg/m^2 (range, 19.1-31.0 kg/m^2). Twenty participants (52.6%) underwent exercise, and 18 (47.4%) underwent pharmacological stress and rest studies. All patients underwent a standard MPI SPECT/CT scanner (Siemens Medical Solutions, Erlangen, Germany). In the pharmacological stress testing, stress was induced by the infusion of either dipyridamole at a rate of 140 μg^{-1}.min^{-1} for 4 min or of dobutamine with escalating 5 μg^{-1}.kg^{-1}.min^{-1} doses up to 40 μg^{-1}.kg^{-1}.min^{-1}. A standard dose of 750-900 MBq of Tc-99m sestamibi was injected 4 min after dipyridamole injection or at peak heart rate during dobutamine pharmacological stress and rest tests. Emission data were acquired by the use of parallel-hole, low-energy, high-resolution collimator, with the patient in the supine position. The acquisition orbits were circular over 180° arc (45° right anterior oblique to 45° left posterior oblique) with 32 steps (64 views), and emission data were acquired for 20 s per projection. The image acquisition matrix was, 64x64 and the pixel size was 6.4 mm. Images were acquired on the 140 keV photopeak with a 15% (129-151 keV) symmetrical window. Immediately after the acquisition of SPECT images for both stress and rest, CT imaging was performed for generating attenuation maps. CT scanning was performed using 140 kVp and 70 mAs in a 512×512 matrix (1.105 mm per pixel), with 5 mm slice thickness. The total acquisition time for the transmission study was 30 s.

The linear attenuation coefficient measured with CT is calculated at the X-ray energy. Rather than at the energy of the photon emitted by the radiopharmaceutical acquired during the radionuclide imaging study. It is therefore necessary to convert the linear attenuation coefficients obtained from the CT scan to match the energy of the radionuclide used in SPECT acquisitions. This is typically accomplished using the bilinear scaling method, relating

Tadesse et al. Attenuation Correction for Cardiac SPECT

Mol Imaging Radionucl Ther 2023;32:42-53

the μ value at the desired energy to the CT number measured at the effective energy of CT X-rays (35). The bilinear scaling method determines μ values via bilinear calibration lines, which are delimited at a CT number of zero Hounsfield units (HU) and are most commonly used in SPECT/CT scanners. This is performed using the system as designed by the manufacture (Siemens HealthCare).

For the administered activity of 750-900 MBq for SPECT and 0.9 mGy CTDI$_{vol}$. For CT, the mean effective doses for the patients considered in this study were 9 mSv for SPECT/CT, from this around 8 mSv for SPECT only. The effective dose for CT can be calculated using dose length product (DLP). It is the CTDI$_{vol}$ multiplied by the length of the scan. The units are mGy centimeters (mGy cm). The DLP can be used to calculate a rough estimate of the effective dose, and the effective dose for SPECT can be estimated using the activity-injected dose.

Patient Studies-reconstruction

Patients' data were reconstructed using an in-house developed MLEM (15 iterations) with and without AC and imported to Cardiac SPECT image reconstruction software (QPS/QGS, Cedars-Sinai Medical Center, Los Angeles, CA, USA) for quantitative analysis and to display standard short-axis, vertical, and horizontal long-axis views and polar maps. Scatter correction was performed on emission projection data obtained from the 15% lower scatter window. Two separate energy windows for the acquisition of the photopeak and the lower scatter according to the standard clinical protocol for Tc-99m (140 keV) were used for the scatter correction. The window widths were both set to 15% as recommended by the manufacturer (Siemens Healthcare), resulting in 108-129 keV for the lower scatter window and 129-151 keV for the photopeak window (36). Reconstructed stress and rest images were smoothed using a 3-dimentional Butterworth low-pass filter with a cutoff frequency 0.4 Hz with an order of 8.0. For AC, two different density maps were used: an attenuation map generated from the transmission study (CTMap) where the μ values were calculated from the CT numbers obtained (HU) and the ProMap generated from the emission data.

For the validation of the AC with ProMap, a QPS software algorithm was used to generate perfusion polar maps of 17 segments. Moreover, total counts of each segment attenuation corrected using ProMap and CTMap, were compared by paired t-test. Proposed attenuation correction (ProAC), computed tomography based attenuation correction (CTAC), and non-attenuation correction (NAC) databases were calculated on the basis of the QPS software for both genders.

Quantitative Evaluation

Percent of Variability and Relative Error

To quantitatively assess the homogeneity of radiotracer distribution in patient's image and the improvement inhomogeneity with AC, circumferential count profiles were generated from the apical, midventricular, and basal slices of NAC, ProAC, and CTAC. Image uniformity was assessed by the percentage variability (PV) of the count profiles defined by the following (11):

$$PV = \frac{SD}{Mean} \times 100 \quad (1)$$

where standard deviation (SD) and mean denote the values of the count profiles for each slice. For all slices, the mean percent variability can be calculated as follows:

$$MeanPV = \frac{1}{3}\sum_{i=1}^{3} \frac{SD(i)}{Mean(i)} \times 100 \quad (2)$$

where SD (i) and mean (i) denote the values of the count profiles for slice i (1, apical; 2, midventricle; and 3, basal).

We also used percentage of relative error (RE%) in the 17 segmented regions of the perfusion polar map between our proposed AC and the reference CTAC images:

$$RE\% = \frac{\Pr oAC - CTAC}{CTAC} \times 100 \quad (3)$$

The results of the comparative analysis are shown using box plots. In these plots, the box shows the median (horizontal line), with the lower (Q1) and upper quartiles (Q3) define the 25th and 75th percentiles, respectively.

Moreover, the proposed attenuation maps were then compared with the CT-based attenuation maps in terms of Voxelwise MSE and SSIM.

$$MSE = \frac{1}{vxl}\sum_{v=1}^{vxl} \left(\Pr oMap(v) - CTMap(v)\right)^2 \quad (4)$$

$$SSIM = \frac{\left(2Ave_{\Pr oMap}Ave_{CTMap} + c_1\right)\left(2\delta_{\Pr oMap,CTMap} + c_2\right)}{\left(Ave^2_{\Pr oMap} + Ave^2_{CTMap} + c_1\right)\left(\delta^2_{\Pr oMap} + \delta^2_{CTMap} + c_2\right)} \quad (5)$$

Where vxl stands for voxel, ProMap is the proposed attenuation map, and CTMap is CT-based attenuation map. In Equation (6), Ave$_{ProMap}$ and Ave$_{CTMap}$ stand for the mean value of the proposed attenuation map and CT-based attenuation map, respectively. δ^2_{ProMap} and δ^2_{CTMap} denote the variances of ProMap and CTMap, respectively, and $\delta_{ProMap,CTMap}$ the covariance of ProMap and CTMap images, respectively. The constants (C1: 0.01 and C2: 0.02) were set to avoid division by insignificant values.

Statistical Analysis

The proposed attenuation maps were further applied for AC on the cardiac SPECT images, and the AC-SPECT

using the ProMap were evaluated against the AC-SPECT images corrected with CTMap using RE%, MSE, and SSIM and statistical analysis of 17 segmental average values of myocardial counts. All continuous values were expressed as mean ± SD. The paired t-test was applied to determine statistically significant differences in the quantitative values; p values <0.05 were considered significant. GraphPad InStat version 3.06 for Windows (GraphPad Software, San Diego, CA, USA) and SPSS software (23.0; SPSS Inc.) was used for statistical analysis. Segmental values of the databases were expressed as the average and SD, which were calculated by QPS software.

Results

Patient Studies-reconstructed Images

Table 1 shows the mean, and SD of the MSE, and SSIM between the proposed attenuation maps and the CT attenuation maps. Among the generated attenuation maps, the lowest mean error metrics were resulted in the males' attenuation map, which are MSE: 0.06±1.11. The highest error metrics of males (MSE: 0.08 and 0.21 for rest and stress respectively). The highest error metrics of females (MSE: 0.11 and 0.10 for rest and stress respectively). The mean of SSIM for females were 0.92±0.02 for stress and 0.93±0.01 for rest, respectively, and for males 0.96±0.01 for stress and 0.97±0.02 for rest, respectively.

Clinical myocardial perfusion image (MPI) SPECT/CT data were used as a means of validating the proposed attenuation map approach compared with direct AC using a CT attenuation map. The qualitative analysis of the comparison between two attenuation maps was checked and approved by a well-experienced nuclear medicine physician.

Table 2 shows that the intraclass correlation coefficient for quantitative tracer uptake of images reconstructed using the synthesized attenuation map and CT-based attenuation map for attenuation-corrected images; the correlation coefficients for males were 0.93 [95% confidence interval (CI), 0.91-0.95] for stress images and 0.95 (95% CI, 0.93-0.96) for rest images and for females were 0.87 (95% CI,

0.84-0.89) for stress images and 0.92 (95% CI, 0.91-0.94) for rest images.

Although the clinical assessment of the method was not within the scope of our study in this phase, the impact of AC on clinical images was observed in some cases. Two sample studies male and female of reconstructed images from a SPECT myocardial perfusion study with and without AC using CTMap and ProMap are shown in Figure 1. The two patients were 73 and 62-year-old man and woman, respectively, were presenting with chest pain. The figure display depicts that without AC, low uptake in the in the inferior, inferoseptal, and inferolateral walls can be observed (yellow arrows), while this region becomes more homogeneous with AC using either CTMap or ProMap. Moreover, the result was interpreted as negative for appreciable stress-induced ischemia.

The CT-based attenuation maps, and proposed attenuation maps in the axial, coronal, and sagittal views at the upper left, MPI SPECT reconstructed images corrected using CT-based attenuation maps, proposed method and without AC in short axis, horizontal long axis and vertical long axis views and the polar map comparisons are shown in Figure 1.

The proposed method could generate consistent attenuation maps with the standard CT-based attenuation maps. The upper right images in Figure 1 for each subject show that the myocardial perfusion SPECT reconstructed images corrected using the CT-based attenuation map and the proposed attenuation map have good consistent, whereas obvious attenuation artifacts can be observed in the non-attenuation-corrected images, as pointed by

Table 2. Percentage segmental tracer uptake: correlation between proposed AC method and CT based AC method

AC				
	Male		**Female**	
Phase	**R**	**95% CI**	**r**	**95% CI**
Stress	0.93	0.91-0.95	0.87	0.84-0.89
Rest	0.95	0.93-0.96	0.92	0.91-0.94

r: Correlation coefficient, CI: Confidence interval, AC: Attenuation correction

Table 1. The mean and SD of the mean square error one, and structural similarity index measure one between proposed attenuation maps and the CT attenuation maps and MSE2 and SSIM2 between non-attenuation corrected image and proposed attenuation corrected image

Metric	MSE1				MSE2				SSIM1				SSIM2			
	Female		Male		Female		Male		Female		Male		Female		Male	
	Stress	Rest	Stress	Rest	Stress	Rest	Stress	Rest	Stress	Rest	Stress	Rest	Stress	Rest	Stress	Rest
Mean	0.07	0.07	0.07	0.06	0.23	0.21	0.20	0.19	0.92	0.93	0.96	0.97	0.69	0.75	0.77	0.79
SD	0.002	0.007	0.004	0.001	0.012	0.03	0.01	0.02	0.020	0.010	0.010	0.020	0.10	0.09	0.08	0.05

SD: Standard deviation, MSE: Mean square error one, SSIM: Similarity index measure, CT: Computed tomography

Tadesse et al. Attenuation Correction for Cardiac SPECT

Mol Imaging Radionucl Ther 2023;32:42-53

the yellow arrows. The 17-segment polar maps for each subject in Figure 1 (generated by Cedars-Sinai software package) of the SPECT images corrected by both CT-based and proposed attenuation maps are nearly consistent. In contrast, the polar maps without AC clearly show different patterns.

The new proposed method was also tested with the patients having fixed defects. Figure 2 shows that the proposed attenuation map works well not only with normal perfusion patients but also with patients having fixed defects. As shown in Figure 2 our result reveal that the proposed new

method for cardiac AC is even better than the CT-based AC. This might be because of the potential misregistration of SPECT and CT data because of they are obtained sequentially. Possible risk factors for misregistration include improper patient positioning, respiratory motion, patient motion, or mechanical misalignment of SPECT/CT device. To reduce this problem, before generating the results, the authors cross checked and corrected manually. Moreover, after applying ProMAP and CTMap for AC our finding showed that quantitatively better regional radiotracer distribution in the inferior, septal, and anterior walls with the new method than the CTMap-based method.

Polar plot presentation of nuclear MPIs from a male with a fixed left circumflex artery perfusion defect with attenuation (ProAC and CTAC) and NAC on a standard SPECT/CT camera.

Homogeneity of Cardiac Images with and Without AC

Figure 3 shows the mean PV of circumferential count profiles from short-axis patients images acquired with NAC, ProAC, and CTAC. With ProAC and CTAC the percent variability of circumferential count profiles was significantly reduced in both genders, indicating greater image homogeneity. The mean ± SD values for females were (8.0±0.96% and 7.6±0.8072%) for CTAC, (7.99±0.07% and 7.90±1.25%) for ProAC and (10.67±1.02% and 10.07±1.60%) for NAC, respectively, for stress and rest. The measures for males were CTAC (6.8±1.17%, 7.1±0.63%), ProAC (7.6±0.98%, 7.2±0.79%) and, (10.16±0.69%, 9.24±0.9%) respectively for stress and rest. There were statistically significant differences between ProAC and NAC values for females-

Figure 1. a) A 73-year-old male normal patient. b) A 62-year-old female, both have reversible cardiac perfusion defect in the right coronary arteries NAC: Non-attenuation correction, CTAC: Computed tomography based attenuation correction, ProAC: Proposed attenuation correction, SA: Short axis, HLA: Horizontal long axis, VLA: Vertical long axis

Figure 2. Polar plot presentation of nuclear myocardial perfusion images from a male with fixed left circumflex artery perfusion defect with attenuation (CTAC and ProAC) and without attenuation (NAC) on standard SPECT/CT camera
NAC: Non-attenuation correction, CTAC: Computed tomography based attenuation correction, ProAC: Proposed attenuation correction, SPECT/CT: Single-photon emission computed tomography/computed tomography
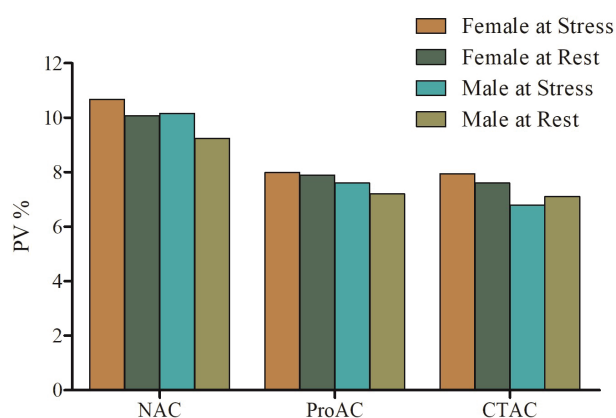

Figure 3. Circumferential percent variability, as a measure for image homogeneity, in basal, mid and apical regions. Percent variability improved significantly with the application of cardiac SPECT images with ProAC and CTAC compared with NAC
NAC: Non-attenuation correction, CTAC: Computed tomography based attenuation correction, ProAC: Proposed attenuation correction, SPECT: Single-photon emission computed tomography

stress and males-stress (p=0.034 and p=0.036), respectively, and there were statistically significant differences between CTAC and NAC for females-stress and males-stress (p=0.010 and p=0.035), respectively. Only for male stress that a significant difference between CTAC and ProAC (p=0.035) was observed.

Further quantitative analysis of the cardiac region was conducted by examining the percentage of RE% in the segmental region. Figure 4 shows box plots for the percentage of RE% of each segmental region between the ProAC and CTAC images for the cardiac regions across both genders. The graph shows that there was no significant median difference between the proposed AC and the standard transmission-based AC except in apical-anterior region in females in the rest phase (p<0.0001). 82% of male and 76% of female patients had studies where there was a segmental difference between ProAC and CTAC of less than ±5.

Statistical Differences in Database Analysis

In Table 3, clinical SPECT/CT data were used as a means of validating the ProMap approach compared with direct AC using CTMap and calculated segmental average and SD values in 17-segment models for stress, and rest are

shown. Figure 5 shows perfusion polar maps reconstructed images with and without AC using CTMap and ProMap. After applying AC as revealed on the polar maps, uniform count distribution was observed when the inferior and anterolateral counts were compared
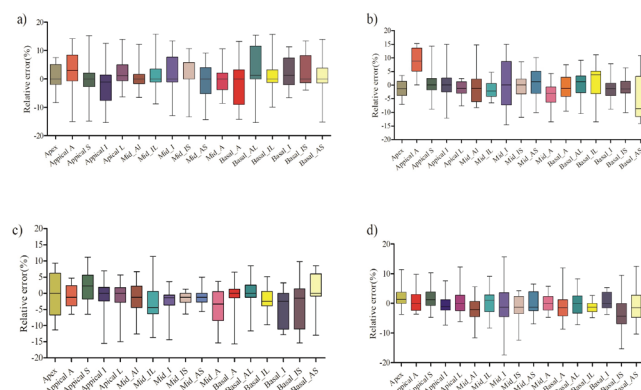

Figure 4. Box and whisker plots along with relative error percentage between images processed with ProAC and CTAC which were calculated for 17 segments of myocardial regions: a) female-stress, b) female-rest, c) male-stress, d) male-rest respectively

ProAC: Proposed attenuation correction, CTAC: Computed tomography based attenuation correction

Table 3. Segmental average and standard deviation values in the polar maps with non-attenuation correction, proposed attenuation correction and CT-based attenuation correction

	NAC				ProAC				CTAC			
	Stress		Rest		Stress		Rest		Stress		Rest	
	Female	Male	Female	Male	Female	Male	Female	Male	Female	Male	Female	**Male**
Apex	82±7.60	80±7.10	81±8.40	79±7.10	81±7.55	79±6.2	78±7.72	83±6.30	82±6.40	79 ±6.64	78±7.34	81±5.70
Apical-A	77±7.44	74±7.28	77±8.40	72±7.90	79±7.81	82±7.90	84±5.44	83±4.59	77±6.14	83±4.31	77±5.36	82±4.80
Apical-S	84±7.84	77±9.40	78±6.52	76±10.00	86±6.41	88±5.70	84±5.70	88±7.74	86±6.34	85±5.61	83±6.01	86±5.62
Apical-I	80±7.30	74±8.40	83±8.24	78±8.30	86±6.92	84±6.14	80±6.41	84±7.91	84±6.60	85±5.60	80±6.74	82±7.42
Apical-L	76±9.10	77±9.70	78±6.80	78±6.11	82±5.84	87±6.92	82±4.82	86±6.21	84±5.90	88±5.11	83±4.26	85±5.80
Mid-AL	78±6.63	77±7.08	81±6.80	74±9.10	85±5.70	88±5.00	87±5.33	87±7.30	86±5.41	89±4.50	88±6.30	88±7.30
Mid-IL	78±8.90	76±8.20	79±6.80	79±8.01	84±5.04	82±6.30	88±4.27	88±7.20	87±4.50	85±7.20	89±5.44	88±5.41
Mid-I	80±10.1	71±6.81	85±8.11	73±6.30	82±8.20	82±5.60	84±8.50	84±5.60	88±7.10	84±6.20	84±8.83	84±6.40
Mid-IS	80±7.20	71±8.30	78±4.12	72±6.20	85±7.20	80±5.80	85±6.50	81±5.00	84±5.40	79±6.33	85±6.90	81±5.44
Mid-AS	75±6.04	75±6.70	76±3.20	73±5.30	81±6.58	82±6.12	81±8.31	80±4.50	81±6.31	83±6.00	80±7.53	80±5.80
Mid-A	77±8.10	73±6.60	77±6.90	77±4.43	78±7.83	86±3.05	73±7.74	85±6.67	78±7.33	86±3.64	76±7.80	85±6.09
Basal-A	68±8.62	70±6.23	68±7.73	70±8.50	78±4.40	79±6.02	72±5.60	79±7.39	77±7.50	79±5.91	72±6.92	79±8.20
Basal-AL	72±8.02	68±9.91	71±6.24	69±9.50	74±6.91	80±5.41	78±6.61	78±5.30	77±8.01	89±6.03	78±8.20	79±6.02
Basal-IL	72±7.50	67±10.10	72±6.29	68±9.33	74±5.10	74±6.54	79±6.43	75±5.90	75±7.13	76±5.81	78±4.70	76±6.00
Basal-I	70±7.40	62±5.73	68±7.73	64±5.90	76±4.80	67±7.50	77±6.81	73±6.50	78±6.80	72±6.03	78±6.84	72±6.20
Basal-IS	68±7.91	62±6.40	67±8.04	65±6.90	72±6.16	64±6.60	72±6.61	65±5.91	75±6.83	67±7.10	73±4.70	68±5.60
Basal-AS	62±7.12	64±8.20	65±7.30	64±7.70	65±6.70	66±7.00	62±8.44	66±5.80	66±7.50	65±6.70	66±5.01	66±5.41

A: Anterior, S: Septal, L: Lateral, AL: Anterolateral, IL: Inferolateral, IS: Inferoseptal, AS: Anteroseptal, I: Iinferior, NAC: Non-attenuation correction, ProAC: Proposed attenuation correction, CTAC: Computed tomography based attenuation correction, CT: Computed tomography
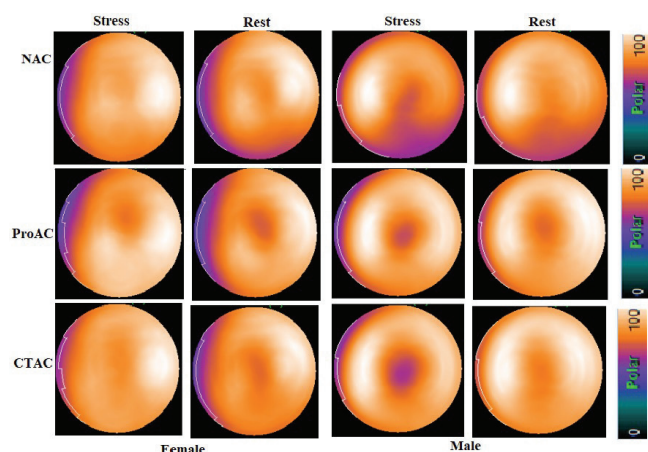
Tadesse et al. Attenuation Correction for Cardiac SPECT

Mol Imaging Radionucl Ther 2023;32:42-53

Figure 5. Comparison of the polar maps for NAC, ProAC and CTAC in female and male. The differences in the lateral and inferior counts between AC and NAC are shown

NAC: Non-attenuation correction, CTAC: Computed tomography based attenuation correction, ProAC: Proposed attenuation correction, AC: Attenuation correction

Paired t-test results for the comparison of ProAC and CTAC are shown in Table 4. As it was revealed, in the most cardiac regions, there is no significant difference between the two methods, which indicates that our proposed method is consistent with the standard method (CT based cardiac AC).

A paired sample t-test demonstrated that counts in the apical-lateral, mid-infrolateral, mid-anterolateral, mid-inferoseptal, basal-inferior, and basal-anterolateral were significantly higher than NAC in both genders and in both AC methods (Table 5). With AC using CTMap and ProMap, there were counted decreases in the apex for both genders but only CTAC female rest was statistically significant (p=<0.0001).

Regarding the gender difference analysis, for the stress condition basal-inferior and infroseptal showed significant differences in all ProAC (p=0.001 and p=0.001), CTAC (p=<0.0001 and p=0.015), and NAC (p=0.006 and p=0.006) respectively. Moreover, mid-anterior during the rest condition showed a significant difference between male and females in ProAC (p<0.0001) and in CTAC (p=0.001 and p=0.001) during stress and rest conditions, respectively. This might be caused by the anatomical difference between females and males.

Discussion

In this study, we proposed an effective method for generating an attenuation map directly from emission data using the segmentation of non-rigid registration of XCAT digital anatomical phantom with the emission image and assigning the tissue-based density map. Validation on real

patient studies revealed that the proposed method can generate attenuation maps nearly consistent with CT-based attenuation maps and were able to provide accurate AC for myocardial perfusion SPECT images. Also, in most of the regions, no significant segmental average values of myocardial count differences were observed between ProMap and CTMap (Table 4). This finding could be important for the studies acquired with dedicated cardiac SPECT or SPECT standalone scanners by providing AC without transmission data.

In Figure 5, it can be seen that our proposed AC achieved moreover similar results compared to the currently used standard approach. The proposed method reduced attenuation artifacts and changed the calculated segmental average values of myocardial counts compared with NAC databases. When AC is implemented optimally, the spread of radionuclide for the lateral, inferior and anterior and lastly septum received higher to lower perfusion. The attenuation-

Table 4. p values for comparison of proposed AC (ProAC) versus CT-based AC (CTAC)

| | P values for comparison of ProAC and CTAC | | | |
| | Stress | | Rest | |
	Female	Male	Female	Male
Apex	ns	ns	ns	ns
Apical-A	ns	<0.0001	ns	ns
Apical-S	ns	ns	ns	ns
Apical-I	ns	ns	ns	ns
Apical-L	ns	ns	ns	ns
Mid-AL	ns	ns	ns	ns
Mid-IL	ns	ns	ns	ns
Mid-I	ns	ns	ns	ns
Mid-IS	ns	ns	0.008	ns
Mid-AS	ns	ns	ns	ns
Mid-A	ns	0.001	ns	ns
Basal-A	ns	ns	ns	ns
Basal-AL	ns	ns	ns	ns
Basal-IL	ns	ns	ns	0.014
Basal-I	ns	ns	ns	ns
Basal-IS	0.016	ns	ns	ns
Basal-AS	ns	ns	ns	ns

A: Anterior, S: Septal, L: Lateral, AL: Anterolateral, IL: Inferolateral, IS: Inferoseptal, AS: Anteroseptal, I: Iinferior, NAC: Non-attenuation correction, ProAC: Proposed attenuation correction, CTAC: Computed tomography based attenuation correction, CT: Computed tomography, ns: Not significant, AC: Attenuation correction

Table 5. p values in comparison NAC, ProAC and CTAC

| | P values for female versus male | | | | | | p values for NAC versus ProAC | | | | p values for NAC versus CTAC | | | |
| | NAC | | ProAC | | CTAC | | Stress | | Rest | | Stress | | Rest | |
	Stress	Rest	Stress	Rest	Stress	Rest	Female	Male	Female	Male	Female	Male	Female	Male
Apex	ns	ns	0.014	<0.0001	0.003	0.004	ns	ns	ns	ns	ns	ns	<0.0001	ns
Apical-A	ns	ns	ns	ns	<0.0001	0.01	ns	0.001	0.001	<0.0001	ns	<0.0001	ns	<0.0001
Apical-S	ns	ns	ns	0.039	ns	ns	ns	0.002	0.004	<0.0001	ns	0.005	0.006	0.001
Apical-I	0.023	ns	ns	0.013	ns	ns	0.009	<0.0001	ns	0.034	0.035	<0.0001	ns	ns
Apical-L	ns	ns	0.009	ns	0.023	ns	0.004	0.002	0.031	0.001	0.001	<0.0001	0.012	<0.0001
Mid-AL	ns	ns	ns	ns	0.030	ns	0.001	0.002	0.001	0.006	<0.0001	<0.0001	<0.0001	0.003
Mid-IL	ns	ns	ns	ns	ns	ns	0.004	0.010	<0.0001	<0.0001	0.004	<0.0001	<0.0001	<0.0001
Mid-I	ns	<0.0001	ns	ns	ns	ns	ns	<0.0001	ns	<0.0001	0.02	<0.0001	ns	<0.0001
Mid-IS	0.025	0.008	0.035	ns	0.023	ns	0.039	<0.0001	0.005	<0.0001	0.01	<0.0001	0.008	<0.0001
Mid-AS	0.004	ns	ns	ns	0.028	ns	<0.0001	<0.0001	0.033	0.001	0.047	<0.0001	ns	0.003
Mid-A	ns	ns	ns	<0.0001	0.001	0.001	ns	0.001	<0.0001	0.001	ns	<0.0001	ns	0.001
Basal-A	ns	ns	ns	0.005	ns	ns	<0.0001	<0.0001	ns	<0.0001	<0.0001	<0.0001	0.033	0.01
Basal-AL	ns	ns	ns	ns	ns	ns	0.02	<0.0001	<0.0001	0.001	0.031	<0.0001	<0.0001	<0.0001
Basal-IL	ns	ns	ns	ns	ns	ns	ns	<0.0001	0.001	0.010	ns	<0.0001	0.001	0.004
Basal-I	0.006	ns	0.001	ns	0.002	0.018	<0.0001	<0.0001	<0.0001	<0.0001	<0.0001	<0.0001	<0.0001	<0.0001
Basal-IS	0.006	0.010	0.001	0.006	0.001	0.015	0.005	<0.0001	0.004	ns	0.049	<0.0001	0.002	0.002
Basal-AS	ns	ns	ns	ns	ns	ns	0.006	<0.0001	ns	ns	0.008	<0.0001	ns	0.041

A: Anterior, S: Septal, L: Lateral, AL: Anterolateral, IL: Inferolateral, IS: Inferoseptal, AS: Anteroseptal, I: Inferior, NAC: Non-attenuation correction, ProAC: Proposed attenuation correction, CTAC: Computed tomography based attenuation correction, CT: Computed tomography, ns: Not significant, AC: Attenuation correction

corrected myocardial perfusion counts using both ProMap and CTMap were more homogeneous than NAC images and the anterolateral, inferolateral and inferior counts were increased. We found an increase inhomogeneity in females than men after AC was applied. This is in agreement with the observations of Masood et al. (11). Moreover, to apply the proposed AC for clinical use, there is a need for creating attenuation-corrected databases for quantitative analysis.

MPIs most often suffer from attenuation artifacts in males and females due to attenuation from the diaphragm and breast (37,38). Although the clinical assessment of the proposed method was not within the scope of our study in this phase, there is a positive influence of AC on these attenuation artifacts. Figure 6, shows stress-only MPI performed with SPECT/CT in a female patient (body mass index 31 kg/m^2) shows a large clear perfusion defect in the anterolateral myocardial wall (arrows) on images obtained without attenuation correction (NAC), whereas attenuation-corrected images (ProAC) show no evidence of a defect at this site (arrowheads). These findings indicate a soft-tissue attenuation artifact that was eliminated with AC.

There were significant differences with and without AC average count in the inferior region for males (which is expected where diaphragm attenuation artifact is prominent, $p=<0.0001$ and <0.0001) and basal-anterolateral for females (where breast attenuation artifact prominent, $p=0.02$ and <0.0001) for stress and rest, respectively. This result is promising in terms of improving attenuation artifacts in the inferior segment in males and anterior segments in females because it provides a homogeneous count distribution in both genders. In a CT-based AC study by Grossman et al. (39), AC polar maps increased global uniformity of the count distribution.

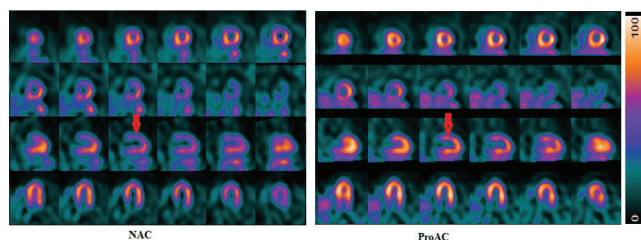As expected, there were significant count distribution differences between ProAC

Figure 6. Images obtained without attenuation correction (NAC) and with attenuation-correction (ProAC) and the effect of soft tissue attenuation artifact for large density breast was eliminated with the proposed attenuation correction

NAC: Non-attenuation correction, ProAC: Proposed attenuation correction

and NAC and between CTAC and NAC with stress and rest conditions for both genders. In most of the regions, both AC methods showed that gender differences were not statistically significant, which is consistent with the finding of Grossman et al. (39). However, our technique created a slightly higher bias on female subjects than male subjects, which is agreement with the finding of Shi et al. (1). This might be caused by the anatomical difference between females and males.

In our study, the quantitative analysis performed using MSE, and SSIM to assess the consistence of the proposed attenuation map with CT-based attenuation map (Table 1). The range of absolute RE in any 17 segmental region did not exceed 15%. More or less the percentage of RE was consistent over all regions.

The overall benefit of AC in clinical cardiac SPECT was beyond the scope of the current study. We expect a limited benefits in increasing the quality and quantitative analysis in the diagnosis of CAD. Moreover, avoiding the necessity of CT data for AC reduces the radiation exposure risk to the patient. The proposed method of AC is not intended to replace CT but rather to be viewed as a valid alternative when CT is not available. Also, there may be suspicious drawbacks concerning the reduction of accuracies in real clinical cases due to smearing or over correction, which should be further addressed in future clinical applications of the proposed AC method.

Study Limitations

Our study has several limitations: precisely registration of an XCAT digital phantom with emission image and assignment of attenuation values to the right region is not an easy task. Although non-homogeneous density of body tissue needs to assign continuous attenuation values, discrete attenuation coefficients are used for segmented XACT-emission image non-rigid registration-based AC. Therefore, analyzing the interindividual irregularity of tissue density and its effect on AC in cardiac SPECT is an

imperative issue. Moreover, an important limitation of this study is the interpatient variability of attenuation values, which can be the main cause of error in cardiac SPECT emission data. Mainly, based on the risk factors such as age, disease, and breathing patterns, lung density shows a high degree of interpatient variability of up to 10% (40). Image reconstruction and registration method used to obtain the final attenuation corrected of SPECT emission images also affect the final result.

Conclusion

The proposed attenuation maps show good agreement with the CT-based attenuation map. AC is feasible for myocardial perfusion SPECT images by only emission data as an alternative to the AC by CT-derived attenuation map. This could direct benefit studies acquired with dedicated cardiac SPECT or SPECT standalone scanners. There were significant count differences between ProAC and NAC, and the homogeneity of radioactivity distribution was increased with ProAC. Further studies in patients with CAD should be conducted to evaluate the clinical efficacy of the proposed AC method.

References

1. Shi L, Onofrey JA, Liu H, Liu YH, Liu C. Deep learning-based attenuation map generation for myocardial perfusion SPECT. Eur J Nucl Med Mol Imaging 2020;47:2383-2395.

2. Yamauchi Y, Kanzaki Y, Otsuka K, Hayashi M, Okada M, Nogi S, Morita H, Komori T, Ishizaka N. Novel attenuation correction of SPECT images

using scatter photopeak window data for the detection of coronary artery disease. J Nucl Cardiol 2014;21:109-117.

3. van Dijk JD, Mouden M, Ottervanger JP, van Dalen JA, Knollema S, Slump CH, Jager PL. Value of attenuation correction in stress-only myocardial perfusion imaging using CZT-SPECT. J Nucl Cardiol 2017;24:395-401.

4. Patchett ND, Pawar S, Sverdlov A, Miller EJ. Does improved technology in SPECT myocardial perfusion imaging reduce downstream costs? An observational study. Int J Radiol Imaging Technol 2017:3.

5. King MA, Tsui BM, Pan TS. Attenuation compensation for cardiac single-photon emission computed tomographic imaging: Part 1. Impact of attenuation and methods of estimating attenuation maps. J Nucl Cardiol 1995;2:513-524.

6. King MA, Tsui BM, Pan TS, Glick SJ, Soares EJ. Attenuation compensation for cardiac single-photon emission computed tomographic imaging: part 2. Attenuation compensation algorithms. J Nucl Cardiol 1996;3:55-64.

7. Manglos SH, Jaszczak RJ, Floyd CE, Hahn LJ, Greer KL, Coleman RE. Nonisotropic attenuation in SPECT: phantom tests of quantitative effects and compensation techniques. J Nucl Med 1987;28:1584-1591.

8. Tsui BM, Gullberg GT, Edgerton ER, Ballard JG, Perry JR, McCartney WH, Berg J. Correction of nonuniform attenuation in cardiac SPECT imaging. J Nucl Med 1989;30:497-507.

9. Zaidi H, Hasegawa B. Determination of the attenuation map in emission tomography. J Nucl Med 2003;44:291-315.

10. Abdollahi H, Shiri I, Salimi Y, Sarebani M, Mehdinia R, Deevband MR, Mahdavi SR, Sohrabi A, Bitarafan-Rajabi A. Radiation dose in cardiac SPECT/CT: an estimation of SSDE and effective dose. Eur J Radiol 2016;85:2257-2261.

11. Masood Y, Liu YH, Depuey G, Taillefer R, Araujo LI, Allen S, Delbeke D, Anstett F, Peretz A, Zito MJ, Tsatkin V, Wackers FJ. Clinical validation of SPECT attenuation correction using X-ray computed tomography-derived attenuation maps: multicenter clinical trial with angiographic correlation. J Nucl Cardiol 2005;12:676-686.

12. Rahman A, Zhu Y, Clarkson E, Kupinski MA, Frey EC, Jha AK. Fisher information analysis of list-mode SPECT emission data for joint estimation of activity and attenuation distribution. Inverse Probl 2020;36:084002.

13. https://www.technavio.com/report/. global-medical-imaging-global-spectmarket-2017-2021. Accessed 5 Nov 2019.

14. Fard BT, Sabet KA, Ay M. Introducing a dedicated cardiac SPECT imaging system: ProSPECT. Frontiers in Biomedical Technologies 2019;6:156-160.

15. Zeraatkar N, Sajedi S, Fard BT, Kaviani S, Akbarzadeh A, Farahani MH, Sarkar S, Ay MR. Development and calibration of a new gamma camera detector using large square Photomultiplier Tubes. J Instrum 2017;12:P09008.

16. Cade SC, Arridge S, Evans MJ, Hutton BF. Use of measured scatter data for the attenuation correction of single photon emission tomography without transmission scanning. Med Phys 2013;40:082506.

17. Núñez M, Prakash V, Vila R, Mut F, Alonso O, Hutton BF. Attenuation correction for lung SPECT: evidence of need and validation of an attenuation map derived from the emission data. Eur J Nucl Med Mol Imaging 2009;36:1076-1089.

18. Pan TS, King MA, De Vries DJ, Ljungberg M. Segmentation of the body and lungs from Compton scatter and photopeak window data in SPECT: a Monte-Carlo investigation. IEEE Trans Med Imaging 1996;15:13-24.

19. Pan TS, King MA, Luo DS, Dahlberg ST, Villegas BJ. Estimation of attenuation maps from scatter and photopeak window single photon-emission computed tomographic images of technetium 99m-labeled sestamib. J Nucl Cardiol 1997;4:42-51.

20. Gourion D, Noll D, Gantet P, Celler A, Esquerré JP. Attenuation correction using SPECT emission data only. IEEE Trans Nucl Sci 2002;49:2172-2179.

21. Krol A, Bowsher JE, Manglos SH, Feiglin DH, Tornai MP, Thomas FD. An EM algorithm for estimating SPECT emission and transmission parameters from emission data only. IEEET Trans Med Imaging 2001;20:218-232.

22. Nuyts J, Dupont P, Stroobants S, Benninck R, Mortelmans L, Suetens P. Simultaneous maximum a posteriori reconstruction of attenuation and activity distributions from emission sinograms. IEEET Trans Med Imaging 1999;18:393-403.

23. Rahman A, Zhu Y, Clarkson E, Kupinski MA, Frey EC, Jha AK. Fisher information analysis of list-mode SPECT emission data for joint estimation of activity and attenuation distribution. Inverse Probl 2020;36:084002.

24. Yan Y, Zeng GL. Attenuation map estimation with SPECT emission data only. Int J Imaging Syst Technol 2009;19:271.

25. Segars WP, Sturgeon G, Mendonca S, Grimes J, Tsui BM. 4D XCAT phantom for multimodality imaging research. Med Phys 2010;37:4902-4915.

26. Segars WP, Bond J, Frush J, Hon S, Eckersley C, Williams CH, Feng J, Tward DJ, Ratnanather JT, Miller MI, Frush D, Samei E. Population of anatomically variable 4D XCAT adult phantoms for imaging research and optimization. Med Phys 2013;40:043701.

27. Segars WP, Mahesh M, Beck TJ, Frey EC, Tsui BM. Realistic CT simulation using the 4D XCAT phantom. Med Phys 2008;35:3800-3808.

28. Segars WP, Tsui BMW, Jing Cai, Fang-Fang Yin, Fung GSK, Samei E. Application of the 4-D XCAT Phantoms in Biomedical Imaging and Beyond. IEEE Trans Med Imaging 2017;37:680-692.

29. Okuda K, Nakajima K, Motomura N, Kubota M, Yamaki N, Maeda H, Matsuo S, Kinuya S. Attenuation correction of myocardial SPECT by scatter-photopeak window method in normal subjects. Ann Nucl Med 2009;23:501-506.

30. Lange K, Bahn M, Little R. A theoretical study of some maximum likelihood algorithms for emission and transmission tomography. IEEE Trans Med Imaging 1987;6:106-114.

31. Lange K, Carson R. EM reconstruction algorithms for emission and transmission tomography. J Comput Assist Tomogr 1984;8:306-316.

32. Shepp LA, Vardi Y. Maximum likelihood reconstruction for emission tomography. IEEE Trans Med Imaging 1982;1:113-122.

33. King MA, Glick SJ, Pretorius PH, Wells RG, Gifford HC, Narayanan MV, Farncombe T. Attenuation, scatter, and spatial resolution compensation in SPECT. Emission tomography: the fundamentals of PET and SPECT. Academic 2004, 473-498.

34. Gullberg GT, Huesman RH, Malko JA, Pelc NJ, Budinger T. An attenuated projector-backprojector for iterative SPECT reconstruction. Phys Med Biol 1985;30:799-816.

35. Ay MR, Shirmohammad M, Sarkar S, Rahmim A, Zaidi H. Comparative assessment of energy-mapping approaches in CT-based attenuation correction for PET. Mol Imaging Biol 2011;13:187-198.

36. Zeintl J, Vija AH, Yahil A, Hornegger J, Kuwert T. Quantitative accuracy of clinical 99mTc SPECT/CT using ordered-subset expectation maximization with 3-dimensional resolution recovery, attenuation, and scatter correction. J Nucl Med 2010;51:921-928.

37. Munn S. The way to a man's heart is through his stomach: much "diaphragmatic" attenuation is likely gastric, and effervescent granules enhance cardiac imaging. Eur J Radiol 2004;52:271-275.

38. Goodgold HM, Rehder JG, Samuels LD, Chaitman BR. Improved interpretation of exercise Tl-201 myocardial perfusion scintigraphy in women: characterization of breast attenuation artifacts. Radiology 1987;165:361-366.

39. Grossman GB, Garcia EV, Bateman TM, Heller GV, Johnson LL, Folks RD, Cullom SJ, Galt JR, Case JA, Santana CA, Halkar RK. Quantitative Tc-99m sestamibi attenuation-corrected SPECT: development and multicenter trial validation of myocardial perfusion stress gender-independent normal database in an obese population. J Nucl Cardiol 2004;11:263-272.

40. Keereman V, Van Holen R, Mollet P, Vandenberghe S. The effect of errors in segmented attenuation maps on PET quantification. Med Phys 2011;38:6010-6019.

Metachronous Brain Tumor in 177Lu-PSMA Scan in a Patient with Metastatic Castration Resistant Prostate Cancer Mimicking Disease Progression

Metastatik Kastrasyon Dirençli Prostat Kanseri Olan Bir Hastada 177Lu-PSMA Görüntülemede Hastalık Progresyonunu Taklit Eden Metakron Beyin Tümörü

 Elahe Pirayesh, Mehrdad Tavakoli

Shahid Beheshti University of Medical Sciences School of Medicine, Shohadae Tajrish Medical Center, Department of Nuclear Medicine, Tehran, Iran

Abstract

A 66-year old man known case of metastatic castration resistant prostate cancer underwent successful 6 cycles treatment with 177Lu- prostate-specific membrane antigen. On the last post therapy whole body scan a new lesion in the skull was noted, suspected for disease progression. One week later, the patient complained from weakness of left upper extremity and brain magnetic resonance imaging revealed a brain tumor, confirmed as glioblastoma pathologically.

Keywords: PSMA, mCRPC, glioblastoma, prostate cancer

Öz

Metastatik kastrasyona dirençli prostat kanseri olan 66 yaşında bir erkek hasta, 177Lu-prostata özgü membran antijeni ile 6 kürlük başarılı bir tedavi gördü. Son tedavi sonrası tüm vücut taramasında, hastanın kafatasında yeni bir lezyon görüldü ve hastalığın progresyonundan şüphelenildi. Bir hafta sonra hasta sol üst ekstremitede güçsüzlük şikayeti ile başvurdu. Beyin manyetik rezonans görüntülemede beyin tümörü saptandı ve patolojik olarak glioblastom olarak doğrulandı.

Anahtar kelimeler: PSMA, mCRPC, glioblastom, prostat kanseri

Address for Correspondence: Elahe Pirayesh MD, Shahid Beheshti University of Medical Sciences School of Medicine, Shohadae Tajrish Medical Center, Department of Nuclear Medicine, Tehran, Iran
Phone: +989151710267 **E-mail:** elahe_pirayesh@yahoo.com ORCID ID: https://orcid.org/0000-0003-1354-6312
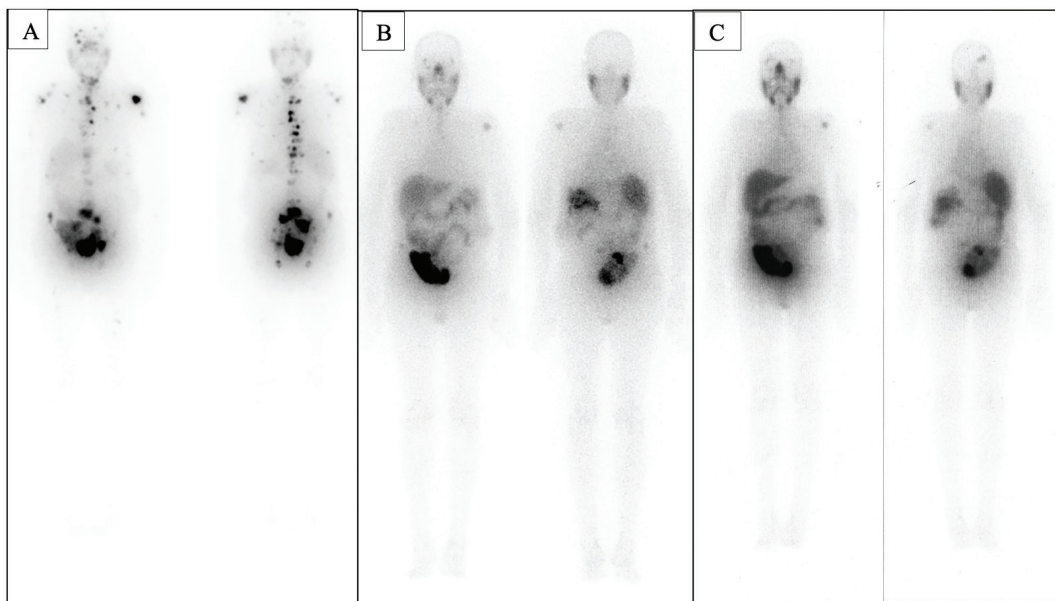
Figure 1. A 66-year-old man known case of transplanted kidney and prostate cancer (PC) (adenocarcinoma GS: 7/10) since 8 years ago received chemotherapy with docetaxel and different anti-androgen therapies including enzalutamide. Regarding the disease progression and serum prostate-specific antigen (PSA) rising, he was referred for radio ligand therapy with 177Lu- prostate-specific membrane antigen (PSMA).

At the time of the first examination, he had widespread skeletal metastases a PSA level of 139 mg/dL. He was an eligible candidate for radioligand therapy with 177Lu-PSMA, regarding the PSMA expression of the tumor, bone marrow reserve, renal function tests, and biochemical profiles.

He received 6 cycles of treatment (4 GBq in each cycle) with 2-3 months intervals and while the serial post therapies scans revealed gradual regression of metastases, a downward trend of PSA levels was noted throughout the entire course (139 ng/mL to 0.4 ng/mL), as well (1). (A) First and (B) 5th post therapy scan with 177Lu-PSMA. However, surprisingly on the 6th post therapy scan (C), a new lesion on the right side of the posterior skull was detected, suspected for new metastases and probable disease progression. Unfortunately, at the time of being aware of the comparison result of serial scans, the patient was not available anymore to obtain a single photon emission computed tomography study of the skull. One week later, the patient complained of progressive weakness of the left upper extremity and mild headache.
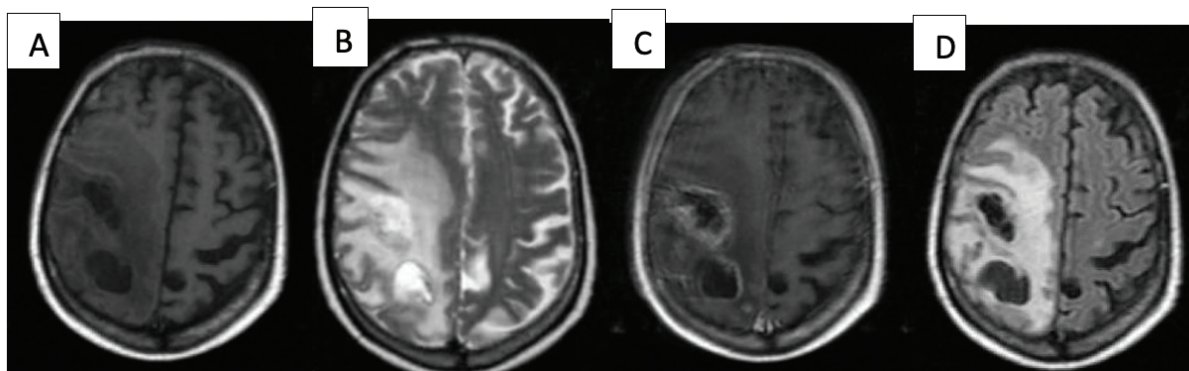
Figure 2. The patient underwent brain magnetic resonance imaging [(A) T1 weighted, (B) T2 weighted, (C) T1weighted with contrast, (D) fluid-attenuated inversion-recovery images] and it revealed a right frontoparietal necrotic mass with peripheral edema and incomplete ring enhancement with areas of patchy enhancement.
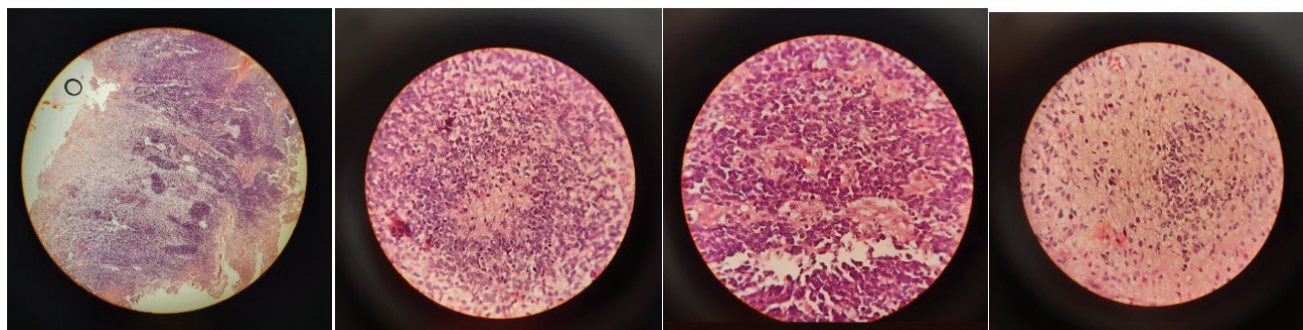
Figure 3. Stereotactic biopsy was performed and pathologic examination demonstrated a highly cellular and vascularized neoplasm with striking pleomorphism, composed of enlarged hyperchromatic nuclei and foci of palisading necrosis, compatible with glioblastoma multiforme (GBM).

Recent advances in the diagnosis and treatment of malignancies have resulted in improved survival of cancer patients, with increased chances of survivors being diagnosed with other primary malignancies. Multiple primary cancers (MPC), categorized as synchronous or metachronous, have an overall frequency of 2%-17% in the literature. MPCs have been reported in 1.14%-8.7% PC patients. The increased risk of some secondary tumors in PC, including bladder, colon, rectal, and urothelial cancers, could be related to radiation therapy. Some genetic factors (e.g. BRCA2) accounting for secondary primaries in PC have been recognized, as well, associated with pancreatic cancer or melanoma (2). Malignant brain tumors in PC patients is a very rare phenomenon, and no case has been found in case series studies (3,4). To our knowledge, it has been reported in a case report in the context of multiple neoplasms (5).

Since, GBM is one of the most vascularized tumors (6) and PSMA is overexpressed in the tumor vasculature of GBMs, PSMA-tracer uptake is seen in GBMs (7).

This case demonstrates a rare presentation of a metachronous brain glioblastoma in a PC patient. Additionally, it highlights the importance of careful interpretation of new PSMA-positive lesions in patients treating with 177Lu-PSMA.

Ethics

Informed Consent: The patient consent was obtained.

Peer-review: Externally and internally peer-reviewed.

Authorship Contributions

Surgical and Medical Practices: E.P., M.T., Concept: E.P., M.T., Design: E.P., M.T., Data Collection or Processing: E.P., M.T., Analysis or Interpretation: E.P., M.T., Literature Search: E.P., M.T., Writing: E.P., M.T.

Conflict of Interest: No conflict of interest was declare by the authors.

Financial Disclosure: The authors declared that this study received no financial support.

References

1. Norouzi G, Aghdam RA, Hashemifard H, Pirayesh E. Excellent response to lower dose of 177Lu-PSMA-617 in a metastatic castration-resistant prostate cancer patient with a transplanted kidney. Clin Nucl Med 2019;44:483-484.

2. Vogt A, Schmid S, Heinimann K, Frick H, Herrmann C, Cerny T, Omlin A. Multiple primary tumours: challenges and approaches, a review. ESMO Open 2017;2:e000172.

3. Hamza MA, Kamiya-Matsuoka C, Liu D, Yuan Y, Puduvalli VK. Outcome of patients with malignant glioma and synchronous or metachronous non-central nervous system primary neoplasms. J Neurooncol 2016;126:527-533.

4. Osman MM, Iravani A, Hicks RJ, Hofman MS. Detection of synchronous primary malignancies with 68Ga-labeled prostate-specific membrane antigen PET/CT in patients with prostate cancer: frequency in 764 patients. J Nucl Med 2017;58:1938-1942.

5. Grace S, Muzaffar R, Veerapong J, Alkaade S, Poddar N, Phillips N, Guzman M, Batanian J, Vogler C, Lai JP. Synchronous quadruple primary neoplasms: glioblastoma, neuroendocrine tumor, schwannoma and sessile serrated adenoma in a patient with history of prostate cancer. Anticancer Res 2015;35:2121-2127.

6. Neri D, Bicknell R. Tumour vascular targeting. Nat Rev Cancer 2005;5:436-446.

7. Salas Fragomeni RA, Amir T, Sheikhbahaei S, Harvey SC, Javadi MS, Solnes LB, Kiess AP, Allaf ME, Pomper MG, Gorin MA, Rowe SP. Imaging of nonprostate cancers using PSMA-targeted radiotracers: rationale, current state of the field, and a call to arms. J Nucl Med 2018;59:871-877.

Findings of I-131 SPECT/CT, 18F-FDG, and 68Ga-FAPI-04 PET/CT Imaging in a Patient Treated with Radioiodine Therapy for Metastatic Papillary Thyroid Carcinoma

Radyoiyot Tedavisi Alan Metastatik Papiller Tiroid Karsinomlu Bir Hastada I-131 SPECT/BT, 18F-FDG ve 68Ga-FAPI-04 PET/BT Görüntüleme Bulguları

 Gamze Tatar[1], Göksel Alçın[2], Özge Erol Fenercioğlu[2], Rahime Şahin[2], Tevfik Fikret Çermik[2]

[1]University of Health Sciences Turkey, İstanbul Bağcılar Training and Research Hospital, Clinic of Nuclear Medicine, İstanbul, Turkey
[2]University of Health Sciences Turkey, İstanbul Training and Research Hospital, Clinic of Nuclear Medicine, İstanbul, Turkey

Abstract

A 50-year-old man undergone total thyroidectomy and histopathology revealed papillary thyroid carcinoma with a tumor size of 4.5 cm. The patient was referred to a nuclear medicine clinic for radioiodine therapy. Since the thyroglobulin level before the treatment was 495 ug/L, low-dose (185 MBq) I-131 scan was performed. In addition to multiple liver metastases, bone metastases were detected in the sacrum and right 7th rib in I-131 whole body scanning and single photon emission computed tomography/computed tomography (CT) imaging at the time of initial staging. We present a case of multiple metastatic papillary thyroid carcinoma whose radioiodine treatment response and clinical outcome were evaluated with 18F-fluorodeoxyglucose and Gallium-68 FAPI-04 positron emission tomography/CT.

Keywords: Papillary thyroid carcinoma, liver metastasis, radioiodine therapy, I-131, 18F-FDG, 68Ga FAPI-04, PET/CT

Öz

Total tiroidektomi yapılan 50 yaşındaki erkek hastada histopatolojik incelemede tümör boyutu 4,5 cm olan papiller tiroid karsinomu saptandı. Hasta radyoiyot tedavisi için nükleer tıp kliniğine yönlendirildi. Tedavi öncesi tiroglobulin düzeyi 495 ug/L olduğundan düşük doz (185 MBq) I-131 taraması yapıldı. İlk evreleme sırasında I-131 tüm vücut taraması ve Tek foton emisyon tomografisi/bilgisayarlı tomografi (BT) görüntülemede çoklu karaciğer metastazlarına ek olarak sakrum ve sağ 7. kostada kemik metastazları saptandı. Klinik ve radyoiyot tedavi yanıtı 18F-florodeoksiglukoz ve Galyum-68-FAPI-04 pozitron emisyon tomografi/BT ile değerlendirilen multipl metastatik papiller tiroid karsinomu olgusu sunulmuştur.

Anahtar kelimeler: Papiller tiroid kanseri, karaciğer metastazı, radyoiyot tedavisi, I-131, 18F-FDG, 68Ga FAPI-04, PET/BT

Tatar et al. I-131, ¹⁸F-FDG, ⁶⁸Ga-FAPI Scan in Thyroid Cancer
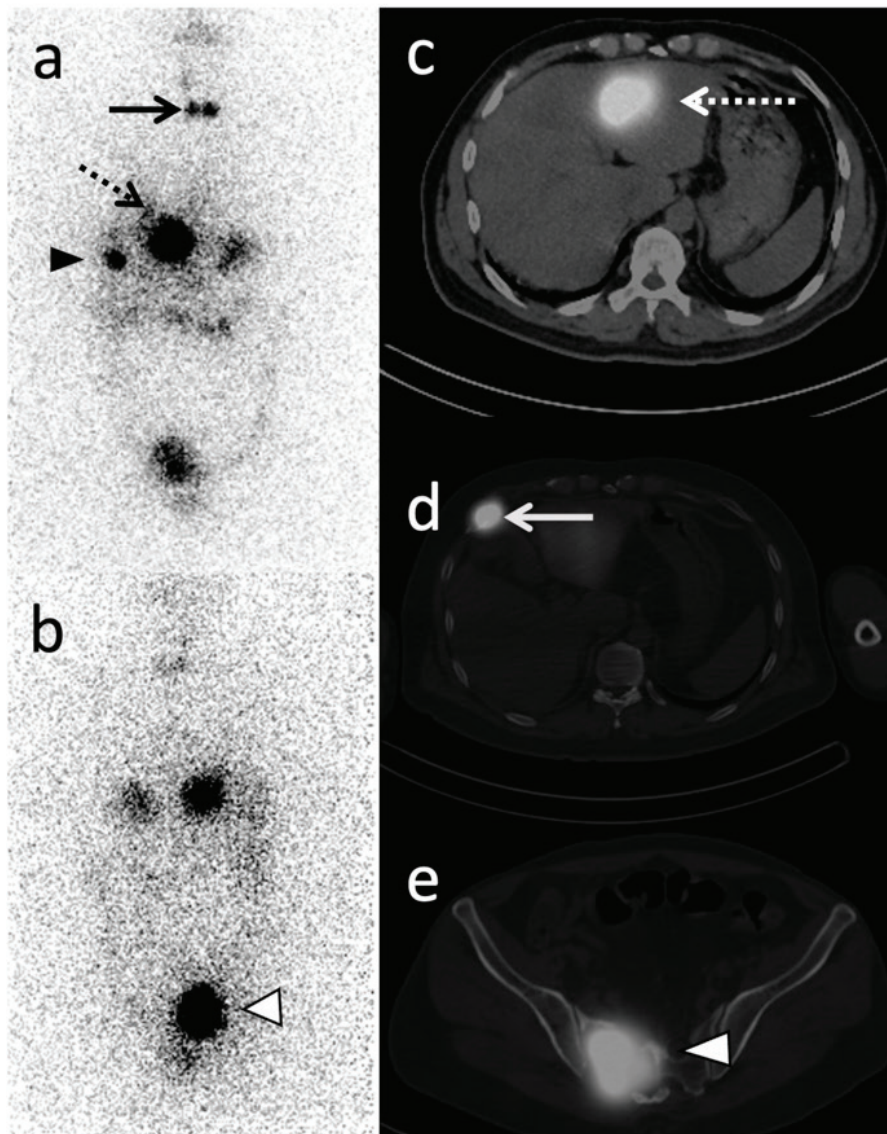
Mol Imaging Radionucl Ther 2023;32:57-61

Figure 1. Anterior (a) and posterior (b) view of whole-body scan (WBS) with 185 MBq (5 mCi) I-131 were performed due to elevated stimulated thyroglobulin (Tg) (higher than 495 ug/L, anti Tg: 1.7 IU/mL) and serum liver enzymes (alanine transaminase: 112 U/L and aspartate transaminase: 70 U/L). Remnant tissue uptake was observed in the thyroid bed (arrow), and four metastatic foci in the liver (dashed arrow), right half of the sacrum (arrowhead), and right anterior 7th rib of the thoracic skeleton (black arrowhead) were also observed. 9250 MBq (250 mCi) radioiodine therapy was applied. Post-therapy WBS and single photon emission computed tomography/computed tomography (CT) axial fusion images showed intense iodine accumulation in the metastatic lesions as described on low-dose WBS (c, d, e).
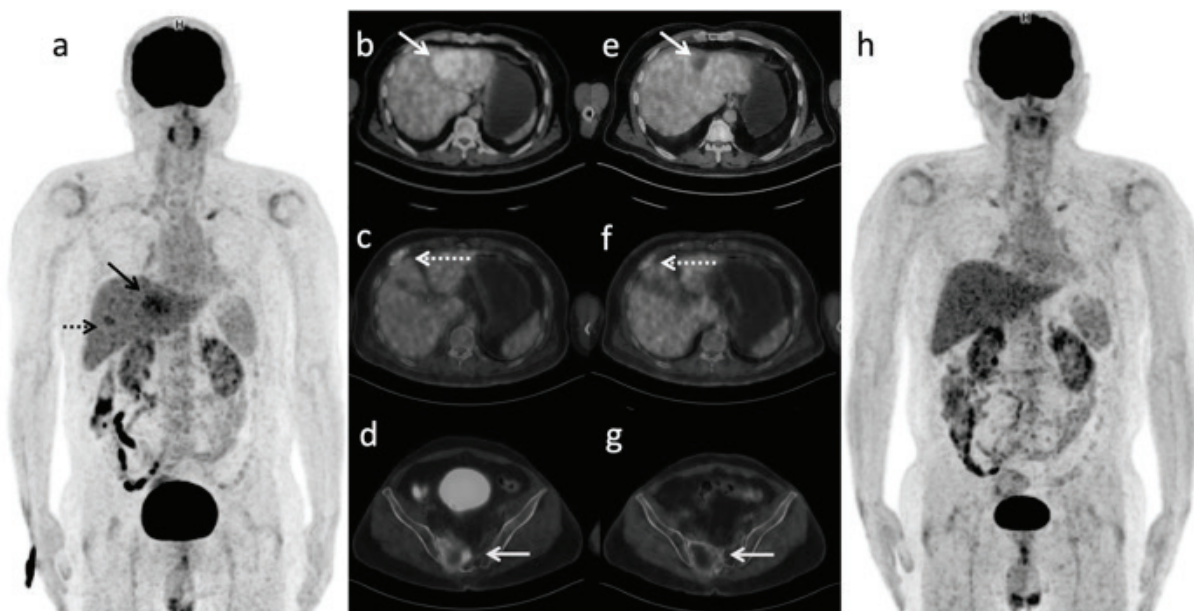
Figure 2. ^{18}F-fluorodeoxyglucose positron emission tomography (PET)/CT was performed 8 months after the radioiodine therapy to evaluate response and determine if there are other foci with ^{18}F-FDG positivity. Images of maximum-intensity projection (a) showed only one hypermetabolic metastatic mass-like lesion in the left lobe medial segment of the liver [maximum standardized uptake value (SUV$_{max}$): 6.5] (arrow), anterior part of the right 7th rib (dashed arrow), and lytic destructive hypermetabolic metastatic bone lesion with central necrosis (SUV$_{max}$: 4.0) in the right half of the sacrum (d) without additional lesions to the I-131 scan. Ten months after the first radioiodine therapy, the second therapy with 9250 MBq (250 mCi) was applied and radioiodine avid known metastasis was visualized in post-therapy I-131 scan. Four months after the second radioiodine therapy, the second ^{18}F-FDG PET/CT scan showed complete metabolic response in the liver (e) and partial response was observed in bone lesions (f, g). Serum Tg level decreased to 168 μg/L and liver enzymes returned to normal.
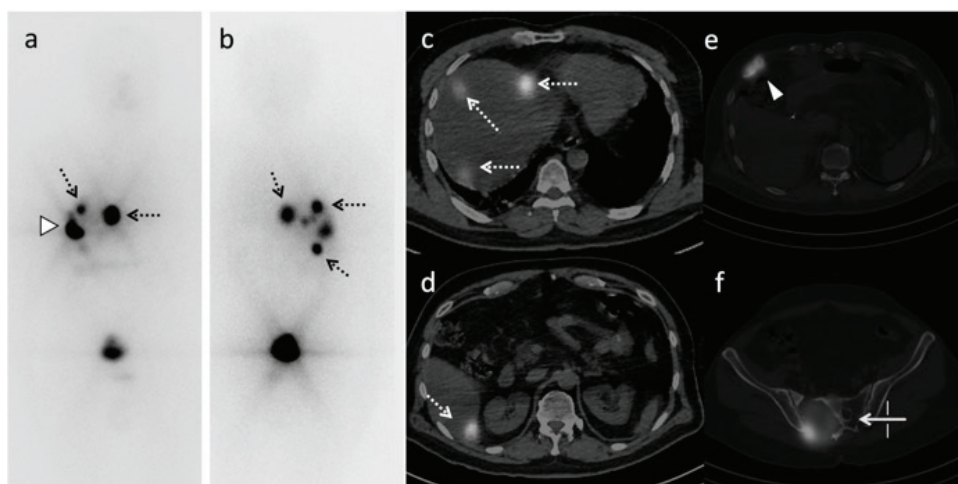
Figure 3. Eight months after 2nd radioiodine therapy, a third dose with 9250 MBq (250 mCi) I-131 was given (2750 MBq achieved) and multiple liver (a, b, c, d) and bone metastases were still iodine avid (e, f).
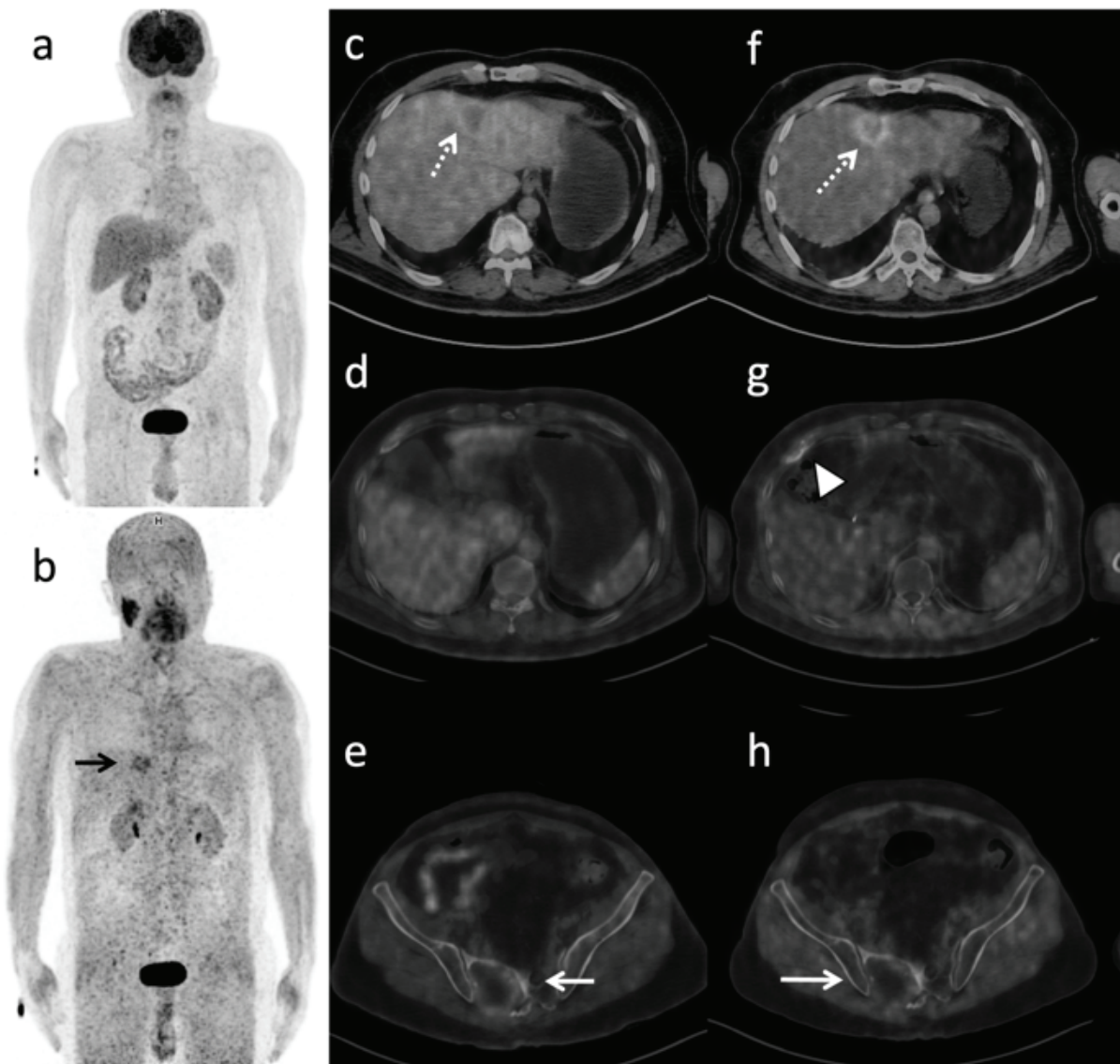
Tatar et al. I-131, ¹⁸F-FDG, ⁶⁸Ga-FAPI Scan in Thyroid Cancer

Mol Imaging Radionucl Ther 2023;32:57-61

Figure 4. ¹⁸F-FDG PET/CT was repeated 3 months after the third radioiodine therapy (a), and mild ¹⁸F-FDG uptake was detected in bone lesions (d, e) with continuing ¹⁸F-FDG negativity in the liver (c). In the same week, Gallium-68 (⁶⁸Ga)-FAPI-04 PET/CT imaging was performed (b) and moderate ⁶⁸Ga-FAPI-04 uptake was detected in hepatic metastases, while ¹⁸F-FDG was negative (f). Also, mild peripheral ⁶⁸Ga-FAPI-04 uptakes were seen in bone metastases (g, h) like as ¹⁸F-FDG. Four months later last ¹⁸F-FDG scan was performed and stable disease was detected with no signs of progression as to the previous scan. The last viewed Tg level decreased to 26.5 µg/L.

Distant metastatic disease at the time of diagnosis is rarely encountered in differentiated thyroid carcinoma (DTC) and usually occurs in the lungs and skeleton (1,2). Liver metastasis are seen even rarer (<1%). Radioiodine therapy is a valuable radionuclide in practice for treating DTC when they concentrate iodine (3,4). PET/CT serves a limited contribution to the diagnosis, but it has a significant impact in the management of DTC, especially at increased Tg levels (5,6). Response assessment can be investigated by PET/CT for an option to I-131 scan (7). As shown in the current case, ⁶⁸Ga-FAPI-04 may also take a place and add benefit in the restaging of metastatic DTC (8).

Ethics

Informed Consent: The patient gave written informed consent for imaging modalities and permitted publication of his medical data.

Peer-review: Externally peer-reviewed.

Authorship Contributions

Surgical and Medical Practices: G.T., Ö.E.F., R.Ş., T.F.Ç., Concept: G.T., G.A., T.F.Ç., Design: G.T., G.A., T.F.Ç., Data Collection or Processing: G.T., Ö.E.F., R.Ş., Analysis or Interpretation: G.T., G.A., T.F.Ç., Literature Search: G.T., Writing: G.T., T.F.Ç.

Conflict of Interest: No conflict of interest was declared by the authors.

Financial Disclosure: The authors declared that this study received no financial support.

References

1. Song HJ, Xue YL, Xu YH, Qiu ZL, Luo QY. Rare metastases of differentiated thyroid carcinoma: pictorial review. Endocr Relat Cancer 2011;18:165-174.

2. Madani A, Jozaghi Y, Tabah R, How J, Mitmaker E. Rare metastases of well-differentiated thyroid cancers: a systematic review. Ann Surg Oncol 2015;22:460-466.

3. Agriantonis DJ, Hall L, Wilson MA. Utility of SPECT/CT as an adjunct to planar whole body I-131 imaging: Liver metastasis from papillary thyroid cancer. Clin Nucl Med 2009;34:247-248.

4. Mohapatra T, Arora A, Bethune NN. Coexisting iodine avid and iodine nonconcentrating lesions with multiple distant soft tissue metastasis in papillary thyroid cancer. Indian J Nucl Med 2012;27:38-41.

5. Mosci C, McDougall IR, Jeffrey RB, Iagaru A. 18F-FDG PET/CT demonstration of a liver metastasis in a patient with papillary thyroid cancer. Clin Nucl Med 2012;37:234-236.

6. Palaniswamy SS, Subramanyam P. Diagnostic utility of PETCT in thyroid malignancies: an update. Ann Nucl Med 2013;27:681-693.

7. Verburg FA, Luster M, Cupini C, Chiovato L, Duntas L, Elisei R, Feldt-Rasmussen U, Rimmele H, Seregni E, Smit JW, Theimer C, Giovanella L. Implications of thyroglobulin antibody positivity in patients with differentiated thyroid cancer: a clinical position statement. Thyroid 2013;23:1211-1225.

8. Kratochwil C, Flechsig P, Lindner T, Abderrahim L, Altmann A, Mier W, Adeberg S, Rathke H, Röhrich M, Winter H, Plinkert PK, Marme F, Lang M, Kauczor HU, Jäger D, Debus J, Haberkorn U, Giesel FL. 68Ga-FAPI PET/CT: Tracer Uptake in 28 Different Kinds of Cancer. J Nucl Med 2019;60:801-805.

[11]C-Methionine PET/CT and ^{18}F-FDG PET/CT in the Evaluation of Adult Alveolar Rhabdomyosarcoma

Erişkin Alveoler Rabdomiyosarkomun Değerlendirilmesinde ^{11}C-Metionin PET/BT ve ^{18}F-FDG PET/BT

Ⓘ *Yuka Hiroshima,* Ⓘ *Yoichi Otomi,* Ⓘ *Takayoshi Shinya,* Ⓘ *Hideki Otsuka,* Ⓘ *Masafumi Harada*

Tokushima University, Department of Radiology, Tokushima, Japan

Abstract

A 70-year-old man with a tumor in the nasal and paranasal space, was pathologically diagnosed with an alveolar rhabdomyosarcoma, with right cervical lymph node metastasis. Magnetic resonance imaging revealed a primary tumor in the nasal and paranasal sinuses, with associated intracranial infiltration. ^{11}C-methionine positron emission tomography/computed tomography (PET/CT) revealed increased uptake in the primary tumor and right cervical lymph node metastasis. ^{18}F-fluorodeoxyglucose PET/CT also revealed increased uptake in the primary tumor and right cervical lymph node. However, the physiological brain uptake overlapped with the primary tumor uptake. Our case suggests the usefulness of ^{11}C-methionine PET/CT for accurately assessing the extent of alveolar rhabdomyosarcoma, especially in cases with intracranial infiltration or those approximating the brain.

Keywords: ^{11}C-methionine, ^{18}F-FDG, alveolar rhabdomyosarcoma, PET/CT

Öz

Nazal ve paranazal boşlukta tümörü olan 70 yaşında erkek hasta patolojik olarak sağ servikal lenf nodu metastazı olan alveolar rabdomiyosarkom tanısı aldı. Manyetik rezonans görüntülemede, nazal ve paranazal sinüslerde, intrakraniyal infiltrasyona da yol açan bir primer tümör görüldü. ^{11}C-metiyonin pozitron emisyon tomografisi/bilgisayarlı tomografi (PET/BT), primer tümörde ve sağ servikal lenf nodu metastazında artmış tutulum gösterdi. ^{18}F-florodeoksiglukoz PET/BT ayrıca primer tümörde ve sağ servikal lenf nodunda artmış tutulum gösterdi. Bununla birlikte, fizyolojik beyin tutulumu, primer tümör tutulumu ile üst üste gelmiştir. Bizim olgumuz, özellikle intrakraniyal infiltrasyonu olan veya beyne yakın yayılımı olan vakalarda alveolar rabdomiyosarkomun boyutunu doğru bir şekilde değerlendirmek için ^{11}C-metiyonin PET/BT'nin yararlı olduğunu düşündürmektedir.

Anahtar kelimeler: ^{11}C-metionin, ^{18}F-FDG, alveoler rabdomiyosarkom, PET/BT

Address for Correspondence: Yoichi Otomi MD, Tokushima University, Department of Radiology, Tokushima, Japan
Phone: +81-88-633-7173 **E-mail:** otomi.yoichi@tokushima-u.ac.jp ORCID ID: https://orcid.org/0000-0002-8960-3662
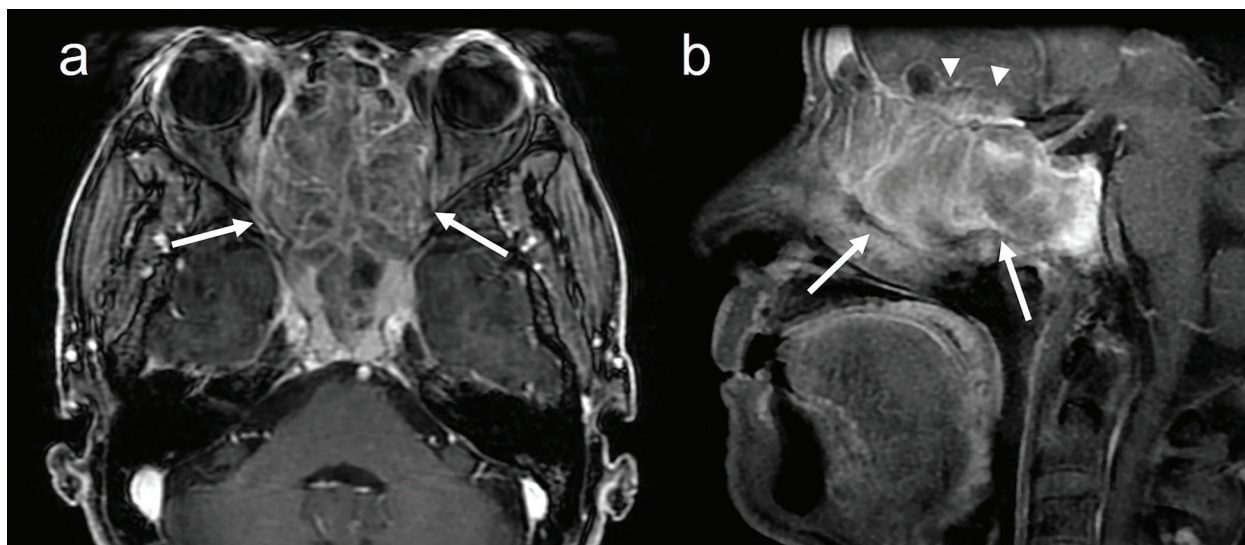
Figure 1. An axial gadolinium-enhanced T1-weighted magnetic resonance imaging (MRI) of a 70-year-old man with a tumor in the nasal and paranasal space. He was pathologically diagnosed with an alveolar rhabdomyosarcoma, with right cervical lymph node metastasis. The image shows a primary tumor in the nasal and paranasal spaces, located mainly in the ethmoid sinus (arrows) (a, b). The tumor extends into the anterior cranial fossa and the mid to the right frontal lobe (arrowheads) (b).
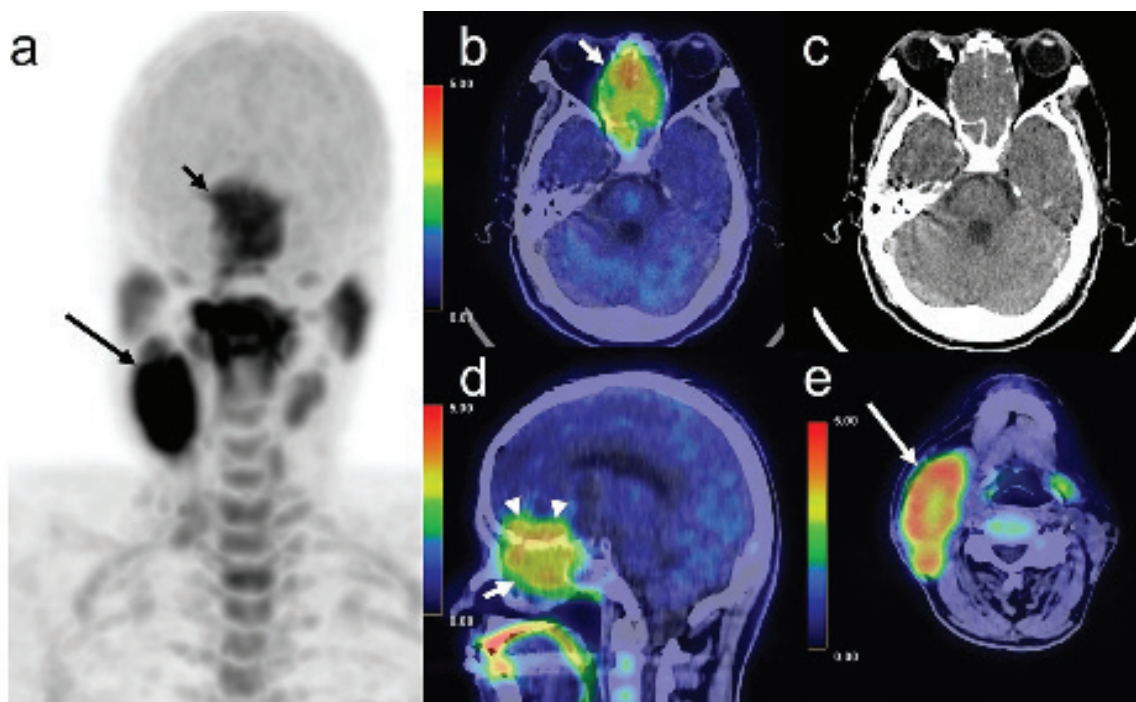

Figure 2. Maximum intensity projection 11C-methionine positron emission tomography (PET) image (a), axial 11C-methionine PET/computed tomography (CT) fusion image (b), CT image at the ethmoid sinus (c), sagittal 11C-methionine PET/CT fusion image at mid-tumor (d), and axial 11C-methionine PET/CT fusion image at the epiglottis level (e). The tumor, located in the nasal and paranasal sinuses, exhibited an increased 11C-methionine uptake, with a maximum standardized uptake value (SUV$_{max}$) of 3.89 (short arrows). Intracranial invasion of the tumor was observed (arrowheads). The tumoral extension, with high 11C-methionine uptake, can be differentiated from the normal brain area, which has a lower physiological 11C-methionine uptake. The enlarged right cervical lymph node also exhibited increased 11C-methionine uptake, with an SUV$_{max}$ of 4.94 (long arrows).
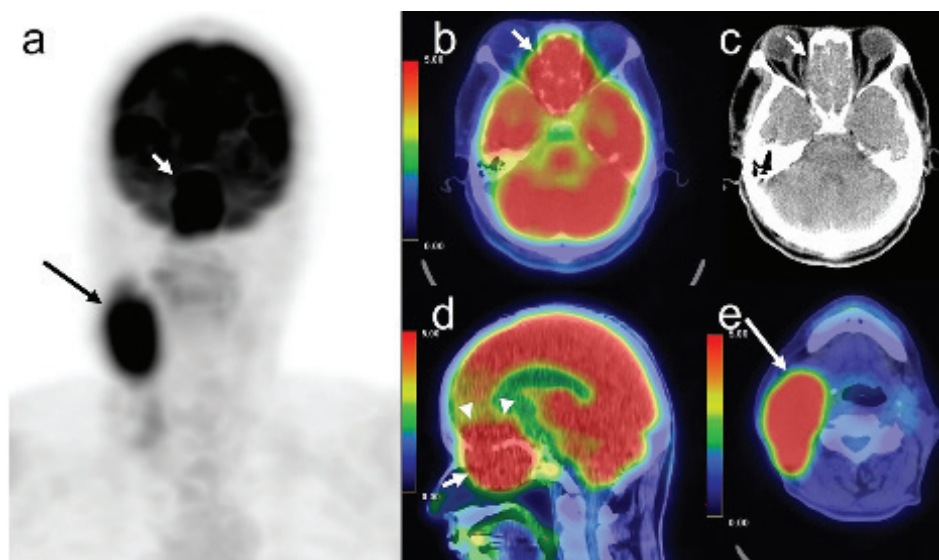
Figure 3. Maximum intensity projection ^{18}F-fluorodeoxyglucose (^{18}F-FDG) PET image (a), axial ^{18}F-FDG PET/CT fusion image (b), and CT image at the ethmoid sinus (c), sagittal ^{18}F-FDG PET/CT fusion image at mid-tumor (d), and an axial ^{18}F-FDG PET/CT fusion image at the epiglottis level (e). The ^{18}F-FDG PET/CT performed four days after ^{11}C-methionine PET/CT, showed an increased ^{18}F-FDG uptake in primary tumor with a SUV$_{max}$ of 8.63 (short arrows). Intracranial invasion of the tumor was also observed in (arrowheads), but it was challenging to differentiate the tumor ^{18}F-FDG uptake from physiological ^{18}F-FDG brain uptake. The enlarged right cervical lymph node also showed increased ^{18}F-FDG uptake with an SUV$_{max}$ of 10.42 (long arrows). No distal metastases were observed. Although alveolar rhabdomyosarcoma is a common soft tissue tumor in children, it rarely occurs in adults (1,2). ^{18}F-FDG PET/CT has been reported as a useful modality in detecting tumor and distant lesions, staging, and predicting outcomes in cases of pediatric rhabdomyosarcoma (3,4,5). In our case, the primary tumor in the nasal and paranasal sinuses was visualized using both ^{11}C-methionine PET/CT and ^{18}F-FDG PET/CT. ^{11}C-methionine PET/CT is a more useful modality in evaluating intracranial tumors (6,7) due to the low physiological brain uptake of ^{11}C-methionine. This allows ^{11}C-methionine PET/CT to delineate the tumor borders clearly. Cervical lymph node metastasis showed increased uptake of both tracers. ^{18}F-FDG PET/CT is a valuable modality to assess the local alveolar rhabdomyosarcoma other than the head and neck region and to evaluate regional lymph node metastasis and distant metastases. ^{11}C-methionine PET/CT may be a useful tool for patients with alveolar rhabdomyosarcomas, especially in the head and neck regions. Additionally, ^{18}F-FDG PET/MRI provides further improvements in the staging and assessment of soft tissue tumors (2,8). ^{11}C-methionine PET/MRI images from patients with rhabdomyosarcoma should be collected and discussed in future publications.

Ethics

Informed Consent: Written informed consent was obtained from the patient.

Peer-review: Externally peer-reviewed.

Authorship Contributions

Concept: Y.O., T.S., Design: Y.O., T.S., Data Collection or Processing: Y.H., Y.O., Analysis or interpretation: Y.O., T.S., H.O., M.H., Literature Search: Y.H., Y.O., Writing: Y.H.

Conflict of Interest: No conflict of interest was declared by the authors.

Financial Disclosure: The authors declared that this study received no financial support.

References

1. van der Graaf WTA, Orbach D, Judson IR, Ferrari A. Soft tissue sarcomas in adolescents and young adults: a comparison with their paediatric and adult counterparts. Lancet Oncol 2017;18:e166-e175.

2. Gennaro N, Marrari A, Renne SL, Cananzi FCM, Quagliuolo VL, Di Brina L, Scorsetti M, Pepe G, Chiti A, Santoro A, Balzarini L, Politi LS, Bertuzzi AF. Multimodality imaging of adult rhabdomyosarcoma: the added value of hybrid imaging. Br J Radiol 2020;93:20200250.

3. Federico SM, Spunt SL, Krasin MJ, Billup CA, Wu J, Shulkin B, Mandell G, McCarville MB. Comparison of PET-CT and conventional imaging in staging pediatric rhabdomyosarcoma. Pediatr Blood Cancer 2013;60:1128-1134.

4. El-Kholy E, El Nadi E, Hafez H, Ahmed S, Younes A, El-Kenanii N, Khalid E. Added predictive value of 18F-FDG PET/CT for pediatric rhabdomyosarcoma. Nucl Med Commun 2019;40:898-904.

5. Ricard F, Cimarelli S, Deshayes E, Mognetti T, Thiesse P, Giammarile F. Additional Benefit of F-18 FDG PET/CT in the staging and follow-up of pediatric rhabdomyosarcoma. Clin Nucl Med 2011;36:672-677.

6. He Q, Zhang L, Zhang B, Shi X, Yi C, Zhang X. Diagnostic accuracy of 13N-ammonia PET, 11C-methionine PET and 18F-fluorodeoxyglucose PET: a comparative study in patients with suspected cerebral glioma. BMC Cancer 2019;19:332.

7. Ito K, Matsuda H, Kubota K. Imaging Spectrum and Pitfalls of (11)C-methionine positron emission tomography in a series of patients with intracranial lesions. Korean J Radiol 2016;17:424-434.

8. Partovi S, Kohan AA, Zipp L, Faulhaber P, Kosmas C, Ros PR, Robbin MR. Hybrid PET/MR imaging in two sarcoma patients- clinical benefits and implications for future trials. Int J Clin Exp Med 2014;7:640-648.

Incidental Tc-99m MDP Uptake in Cortical-subcortical Parietotemporal Cerebral Area in a Patient with a History of Recent Ischemic Cerebrovascular Event who Underwent Whole-body Bone Scan

Yakın Zamanda İskemik Serebrovasküler Olay Öyküsü Olan ve Tüm Vücut Kemik Taraması Yapılan Bir Hastada Kortikal-subkortikal Parietotemporal Serebral Alanda Tesadüfen Saptanan Tc-99m MDP Tutulumu

🅾 *Demet Nak,* 🅾 *Sibel Göksel*

Recep Tayyip Erdoğan University Training and Research Hospital, Department of Nuclear Medicine, Rize, Turkey

Abstract

The authors present Tc-99m methylene diphosphonate (MDP) uptake in the right parietotemporal area at whole-body bone scan (WBBS) in 75 years male patient with prostate adenocarcinoma Gleason score 3+4 (pT2N0Mx). No residual or metastatic disease was detected in the patient's Gallium-68 prostate-specific membrane antigen positron emission tomography/computed tomography four months before WBBS. The patient had undetectable prostate-specific antigen levels and underwent WBBS to restage prostate cancer due to equivocal findings in previous WBBS. Current WBBS planar views revealed heterogeneous Tc-99m MDP uptake in the right parietotemporal area and the sphenoid bone in addition to equivocal uptake on the lower lumbar vertebrae. Single-photon emission computed tomography study to identify the MDP-avid lesion on the right cranial area revealed heterogeneous Tc-99m MDP uptake in the right parietotemporal area and sphenoid bone. The patient had a history of transsphenoidal surgery for a hypophyseal tumor two years ago and a recent cerebrovascular event (CVE). Diffusion-weighted magnetic resonance imaging revealed a cortical-subcortical patchy area of restricted diffusion in the parietotemporal region compatible with acute ischemia. Heterogeneous Tc-99m MDP uptake in the right parietotemporal area was attributed to recent CVE and secondary vascular-tissue change-related dystrophic calcification.

Keywords: Bone scan, cortical- subcortical, cerebral, MDP uptake

Öz

Yazarlar 75 yaşında prostat adenokarsinom Gleason skor 3+4 (pT2N0Mx) tanılı erkek hastanın çekilen tüm vücut kemik sintigrafisinde (TVKS) sağ parietotemporal bölgeye uyan alanda izlenen Tc-99m metilen difosfonat (MDP) tutulumunu sunmaktadır. Hastanın TVKS'den 4 ay önce çekilen Galyum-68 prostat spesifik membran antijeni pozitron emisyon tomografi/bilgisayarlı tomografide rezidü veya metastaz saptanmamıştı. Prostat spesifik antijen düzeyi ölçülebilir aralığın altında olan hastaya, önceki TVKS'de saptanan şüpheli bulguların aydınlatılması amacıyla yeniden evreleme amaçlı TVKS çekilmişti. Güncel TVKS'de sağ kraniyal bölgede saptanan Tc-99m MDP tutulumunu aydınlatmak için yapılan tek foton emisyonlu bilgisayarlı tomografi görüntülemede sağ parietotemporal bölgede heterojen Tc-99m MDP birikimi, sfenoid kemikte fokal tutulum ve lomber alt vertebralarda nospesifik tutulum izlendi. İki yıl önce hipofiz tümörüne yönelik transfenoidal cerrahi ve yakın tarihli serebrovasküler olay öyküsü mevcuttu. Diffüzyon ağırlıklı kraniyal manyetik rezonans görüntülerinde sağ parietotemporal bölgede kortikal-subkortikal alanda akut iskemi ile uyumlu yamasal difüzyon kısıtlılığı alanı saptandı. Sağ parietotemporal bölgede izlenen heterojen Tc99m-MDP tututlumu yakın tarihli iskemik serebrovasküler olaya ve vasküler-doku değişikliğine bağlı distrofik kalsifikasyona ikincil nitelikte değerlendirildi.

Anahtar kelimeler: Kemik sintigrafisi, kortikal- subkortikal, serebral, MDP tutulumu

---

Address for Correspondence: Demet Nak MD, Recep Tayyip Erdoğan University Training and Research Hospital, Department of Nuclear Medicine, Rize, Turkey
Phone: +90 464 213 04 91 **E-mail:** demet_nak@hotmail.com ORCID ID: https://orcid.org/0000-0002-9756-7788
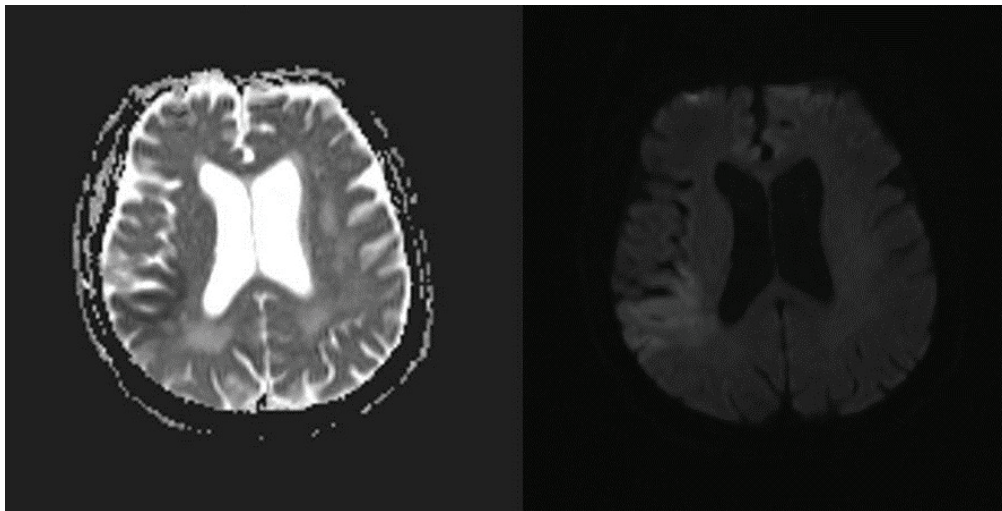
Figure 1. Axial apparent diffusion coefficient (ADC) (left) and diffusion-weighted (DWI) (right) magnetic resonance images (MRI) revealing cortical and subcortical patchy areas of restricted diffusion in parietotemporal region compatible with acute ischemia.
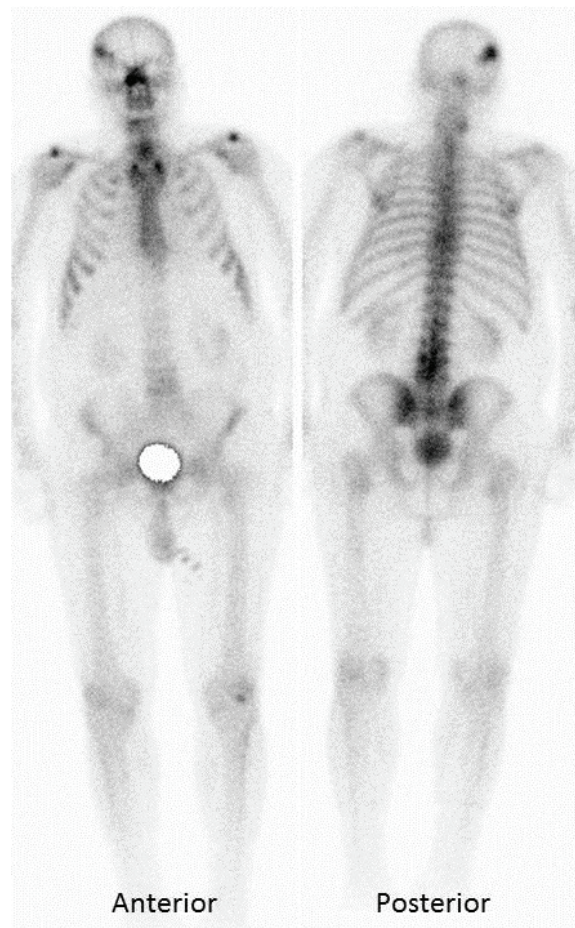

Anterior   Posterior

Figure 2. Tc-99m methylene diphosphonate (MDP) whole-body images show MDP avidity at the right cranial region, sphenoidal area, and equivocal activity at lower lumbar vertebrae. The equivocal activity in the lumbar region was attributed to disc herniation and accompanying degenerative changes.
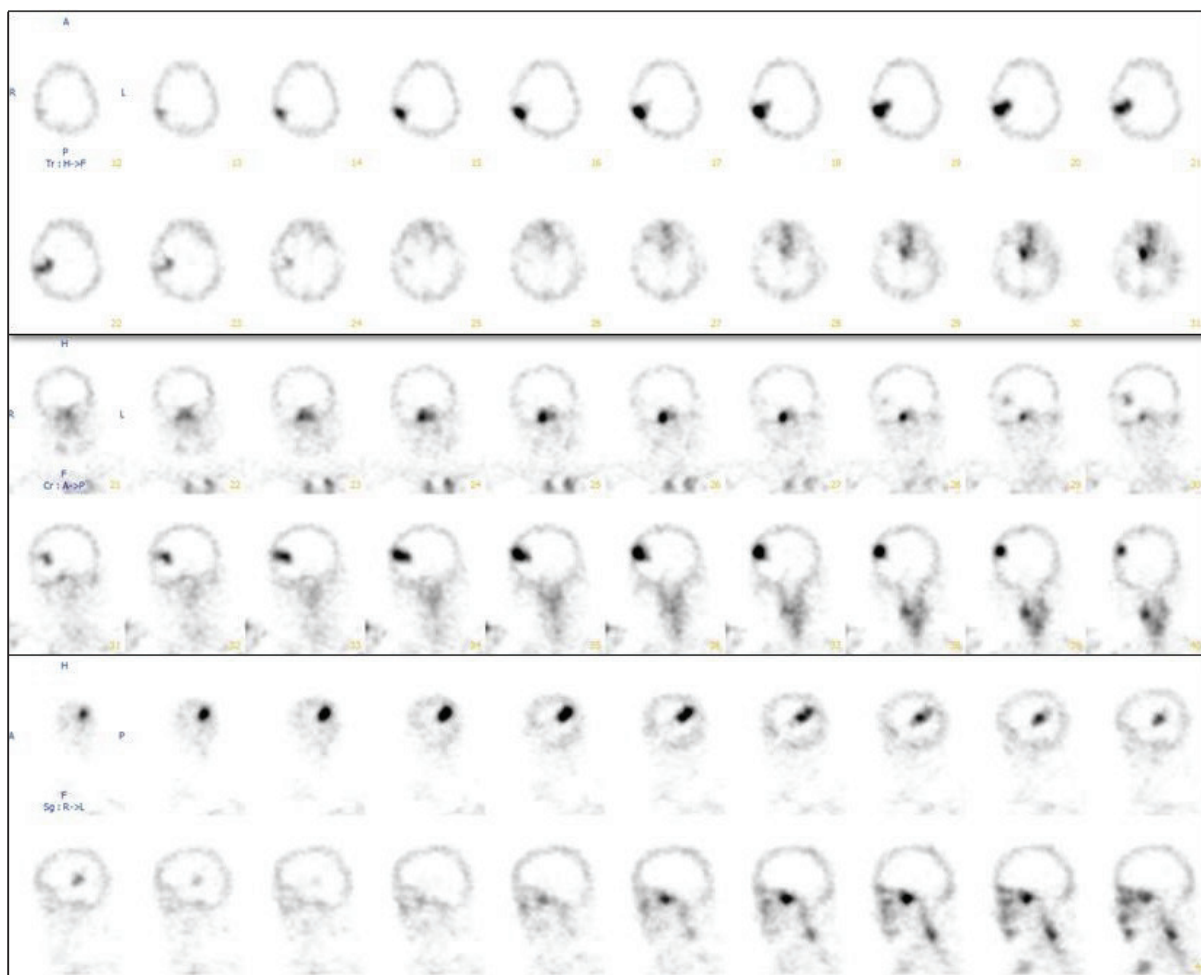
Figure 3. Axial (upper line) and coronal (midline) saggital (lower line) single-photon emission computed tomography images revealing heterogeneous Tc-99m MDP uptake of the parietotemporal cortical area matching with ADC and DWI MRIs, which showed restricted diffusion compatible with acute ischemia. Uptake on the right sphenoidal region was attributed to the patient's previous transsphenoidal surgery. In addition to primary and metastatic neoplasms, non-malignant and altered uptake of Tc-99m MDP can be seen due to various etiologies. Dystrophic calcification, defined as histologic disruption-induced calcium deposition in tissues after trauma, ischemia, cellular necrosis, or in the enzymatic necrosis of fat, occurs in patients with normal calcium and phosphorus levels (1). Cerebral, myocardial, and muscular infarction-related various Tc-99m MDP uptake patterns have been reported previously (1,2,3,4,5).

Ethics

Informed Consent: Oral and written informed consent of the patient was obtained.

Peer-review: Externally peer-reviewed.

Authorship Contributions

Concept: D.N., Design: D.N., Data Collection or Processing: D.N., S.G., Analysis, or Interpretation: D.N., S.G., Literature Search: D.N., Writing: D.N.

Conflict of Interest: No conflict of interest was declared by the authors.

Financial Disclosure: The authors declared that this study received no financial support.

References

1. Lionel Zuckier LS, Martineau P. Altered biodistribution of radiopharmaceuticals used in bone scintigraphy. Semin Nucl Med 2015;45:81-96.

2. Hung GU, Lee JD, Lee JK. Bilateral cranial Tc-99m MDP uptake due to hypoxic-ischemic encephalopathy. Clin Nucl Med 2007;32:328-329.

3. Kannivelu A, Padhy AK, Srinivasan S, Ali SZ. Extraosseous uptake of technetium-99m methylene diphosphonate by an acute territorial cerebral infarct in a classical biodistribution pattern. Indian J Nucl Med 2013;28:240-242.

4. Das J, Ray S. Incidental finding of technetium-99m methylene diphosphonate uptake in acute cerebral infarct. Indian J Nucl Med 2016;31:313-315.

5. Mackie GC. Tc-99m MDP uptake resulting from acute middle cerebral artery territory infarction. Clin Nucl Med 2003;28:851-852.

^{18}F-FDG PET/CT Imaging of a Grade 3 Lymphomatoid Granulomatosis in an Immunocompromised Pediatric Patient

Primer İmmün Yetmezliği Olan Evre 3 Lenfomatoid Granülomatozis Tanılı Pediatrik Bir Hastanın ^{18}F-FDG PET/BT Görüntülemesi

⊕ *Selin Kesim,* ⊕ *Feyza Şen,* ⊕ *Salih Özgüven,* ⊕ *Tunç Öneş*

Marmara University Pendik Training and Research Hospital, Department of Nuclear Medicine, Istanbul, Turkey

Abstract

Lymphomatoid granulomatosis is a rare extranodal Epstein-Barr virus-driven B-cell lymphoproliferative disease, involving predominantly lung, less often skin, kidney, and central nervous system. Here, we present a pediatric case with primary immunodeficiency, diagnosed with pathologically proven pulmonary grade-III lymphomatoid granulomatosis. ^{18}F-fluorodeoxyglucose (FDG) positron emission tomography/computed tomography (PET/CT) imaging demonstrated ^{18}F-FDG avid pulmonary masses with central air-bronchograms and cavitations. Although the definitive diagnosis depends on biopsy, ^{18}F-FDG PET/CT serves as a complementary imaging tool to evaluate the extent of the disease and response to treatment.

Keywords: Lymphomatoid granulomatosis, pulmonary involvement, ^{18}F-FDG PET/CT

Öz

Lenfomatoid granülomatozis, çoğunlukla akciğer, daha az sıklıkla deri, böbrek ve merkezi sinir sistemi tutulumu ile giden, nadir görülen ekstranodal Epstein-Barr virüsü ilişkili B-hücreli lenfoproliferatif bir hastalıktır. Burada, primer immün yetmezlikli, biyopsi ile pulmoner grade-3 lenfomatoid granülomatozis tanısı almış pediatrik bir olgu sunulmaktadır. ^{18}F-florodeoksiglukoz (FDG) PET/BT görüntülemesi, santral kesimde hava bronkogramları ve kavitasyonlar içeren ve ^{18}F-FDG tutulumu gösteren pulmoner kitleler göstermiştir. Kesin tanı biyopsiye bağlı olsa da ^{18}F-FDG PET/BT tetkiki hastalık yaygınlığının ve tedaviye yanıtın değerlendirilmesinde yardımcı bir görüntüleme yöntemidir.

Anahtar kelimeler: Lenfomatoid granülomatozis, akciğer tutulumu, ^{18}F-FDG PET/BT
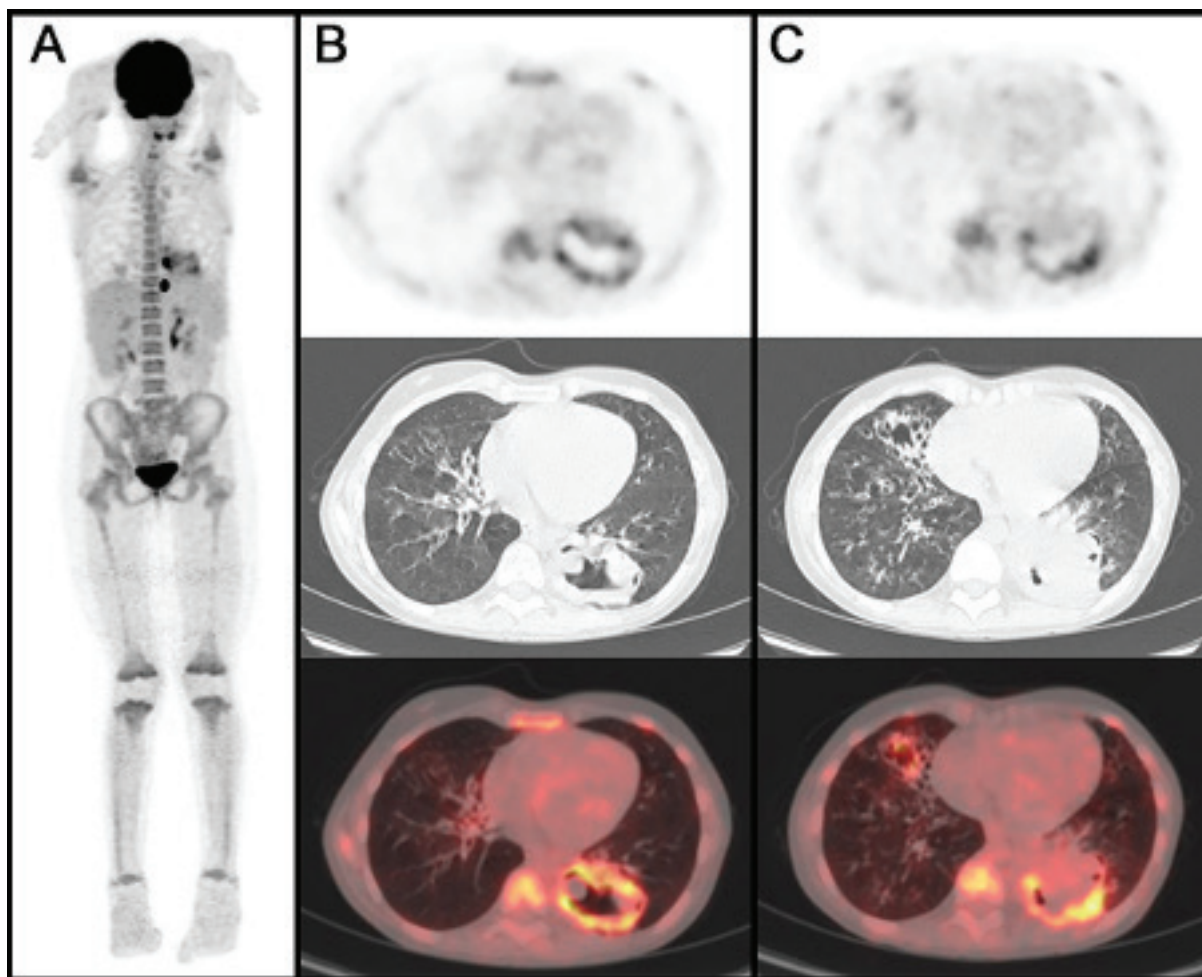
Figure 1. A 13-year-old girl, who has major histocompatibility complex class I deficiency, was presented with persistent cough, and computed tomography (CT) imaging revealed nodular lesions in both lungs. Biopsy was directed to the lesion in the left lower lobe of the lung, and histopathologic examination was consistent with grade 3 lymphomatoid granulomatosis (LG). A combination of chemoimmunotherapy was initiated and she was referred to ^{18}F-fluorodeoxyglucose (FDG) positron emission tomography/computed tomography (PET/CT) to evaluate the extent of the disease. ^{18}F-FDG PET/CT maximum intensity projection image showed ^{18}F-FDG avid pulmonary masses (A). Axial PET, CT, and fused PET/CT images demonstrated peripheral intense ^{18}F-FDG uptake with a maximum standardized uptake value of 19.2 in the pulmonary nodules/mass that have central cavitations, internal air-bronchograms, and subpleural distribution, in the left lower (B) and the mid lobe of the lung (C). No extrapulmonary lesions were identified. LG is a rare Epstein-Barr virus (EBV)-associated B-cell lymphoproliferative disorder, that involves extranodal sites, such as the skin, central nervous system, liver, and kidneys, with the lung almost always being affected (1). LG is classified into three histological grades depending on the number and density of atypical large EBV-positive B-cells, angio-invasive/angio-destructive reactive T-cell infiltration, and necrosis, which is essential in selecting appropriate treatment strategies (2). Corticosteroids and/or single-agent chemotherapy are used in low-grade (grade 1 and grade 2) LG, whereas high-grade (grade 3) LG, has an inferior outcome with a higher incidence of multisystem involvement and is best managed by chemoimmunotherapy (3). Most of the patients do not have underlying immunodeficiency, while immunosuppressed individuals have increased risk, as in our patient. LG typically presents in middle-aged adults, and reports of this disease in children are limited in the literature (4).

Pulmonary LG, which predominantly affects the mid to lower lung, presents with nodules and masses mostly in the peribronchovascular and subpleural regions, which corresponding to lymphatic dissemination, and central low attenuation, cavitation, and peripheral enhancement of the nodules/masses are related to the angio-invasive and angio-destructive nature of the disease (5). CT manifestations may mimic infection, bronchioloalveolar lung cancer, pulmonary lymphoma, sarcoidosis, or Wegener's granulomatosis, and LG should be considered a differential diagnosis while evaluating ^{18}F-FDG PET/CT images of pediatric patients with respiratory and/or B symptoms.

^{18}F-FDG PET/CT findings in patients with LG, involving the lung or central nervous system, were limited to case reports in the literature (6,7,8,9,10). Like other ^{18}F-FDG-avid high-grade lymphomas, ^{18}F-FDG PET/CT is reported to be an effective imaging tool for staging and monitoring response to treatment in patients with LG (9). With the ability to present both morphologic and functional information, whole-body ^{18}F-FDG PET/CT scan can assist in identifying the involved sites, guide high-yield biopsy, and help the management of the disease.

Kesim et al. Lymphomatoid Granulomatosis on PET/CT

Mol Imaging Radionucl Ther 2023;32:68-70

Ethics

Informed Consent: We have obtained all appropriate patient consent forms. In the form the patient has given her consent for her images and other clinical information to be reported in the journal.

Peer-review: Externally peer-reviewed.

Authorship Contributions

Surgical and Medical Practices: S.K., F.Ş., S.Ö., T.Ö., Concept: S.K., F.Ş., Design: S.K., F.Ş., Data Collection or Processing: S.K., F.Ş., Analysis or Interpretation: S.K., F.Ş., Literature Search: S.K., F.Ş., Writing: S.K., F.Ş.

Conflict of Interest: No conflict of interest was declared by the authors.

Financial Disclosure: The authors declared that this study received no financial support.

References

1. Roschewski M, Wilson WH. Lymphomatoid granulomatosis. Cancer J 2012;18:469-474.

2. Yang M, Rosenthal AC, Ashman JB, Craig FE. The Role and Pitfall of F18-FDG PET/CT in surveillance of high grade pulmonary lymphomatoid granulomatosis. Curr Probl Diagn Radiol 2021;50:443-449.

3. Melani C, Jaffe ES, Wilson WH. Pathobiology and treatment of lymphomatoid granulomatosis, a rare EBV-driven disorder. Blood 2020;135:1344-1352.

4. Tacke ZC, Eikelenboom MJ, Vermeulen RJ, van der Knaap MS, Euser AM, van der Valk P, Kaspers GJ. Childhood lymphomatoid granulomatosis: a report of 2 cases and review of the literature. J Pediatr Hematol Oncol 2014;36:416-422.

5. Chung JH, Wu CC, Gilman MD, Palmer EL, Hasserjian RP, Shepard JA. Lymphomatoid granulomatosis: CT and FDG-PET findings. Korean J Radiol 2011;12:671-678.

6. Sood A, Parihar AS, Malhotra P, Vaiphei K, Kumar R, Singh H, Mittal BR. Pulmonary recurrence of lymphomatoid granulomatosis diagnosed on F-18 FDG PET/CT. Indian J Nucl Med 2020;35:167-169.

7. Makis W, Deschenes J. Cerebral and pulmonary lymphomatoid granulomatosis and EBV positive oesophageal ulcer in an immunosuppressed renal transplant patient staged and followed with serial MRI and 18F-FDG PET/CT after rituximab therapy. BJR Case Rep 2016;2:20150503.

8. Nishihara H, Nakasato M, Sawa H, Murakami H, Yamamoto D, Moriyama K, Kato N, Hashimoto I, Kamada H, Tanaka S. A case of central nervous system lymphomatoid granulomatosis; characteristics of PET imaging and pathological findings. J Neurooncol 2009;93:275-278.

9. Kawai N, Miyake K, Nishiyama Y, Yamamoto Y, Sasakawa Y, Haba R, Kushida Y, Tamiya T, Nagao S. FDG-PET findings of the brain in lymphomatoid granulomatosis. Ann Nucl Med 2006;20:683-687.

10. Martínez-Esteve A, Álvarez-Pérez RM, García-Gómez FJ, Acevedo-Báñez I, Cuenca-Cuenca JI, Borrego-Dorado I. Paediatric grade-II lymphomatoid granulomatosis: (18)F-FDG PET/CT monitoring of disease activity. Rev Esp Med Nucl Imagen Mol 2016;35:131-132.

Incidental Detection of Pseudomembranous Colitis Through ¹⁸F-FDG PET/CT During the Restaging of Colorectal Cancer

Kolorektal Kanserin Yeniden Evrelenmesi Sırasında ¹⁸F-FDG PET/BT ile Psödomembranöz Kolitin Tesadüfen Saptanması

 Luca Filippi

Santa Maria Goretti Hospital, Department of Nuclear Medicine, Latina, Italy

Abstract

A 59-year-old man, previously submitted to anterior resection due to rectal cancer, underwent a contrast-enhanced computed tomography (ce-CT) for restaging before eventual chemotherapy. Because ce-CT showed a moderate enlargement of the descending colonic lumen, in despite the lack of symptoms, positron emission tomography (PET)/CT ¹⁸F-fluorodeoxyglucose (FDG) was carried out. ¹⁸F-FDG PET/CT demonstrated highly increased tracer incorporation along the colon walls. Two days after the PET/CT examination, complaints of diarrhea and abdominal pain began. Clostridioides difficile stool test resulted positiv; thus, thus he started antibiotic therapy without benefit. Because follow-up ce-CT demonstrated a megacolon condition, he was submitted to hemicolectomy. Histology revealed a diffuse condition of pseudomembranous colitis (PMC). This case highlights the potential of ¹⁸F-FDG PET/CT for detecting PMC morphological and functional features also in pre-symptomatic patients.

Keywords: Inflammatio, ¹⁸F-FDG, positron emission tomograph, colitis

Öz

Daha önce rektum kanseri nedeniyle anterior rezeksiyon uygulanan 59 yaşında bir erkek hastaya nihai kemoterapiden önce yeniden evreleme için kontrastlı bilgisayar tomografi (k-BT) uygulandı. K-BT'de, hastanın semptomu olmamasına rağmen inen kolonik lümende orta derecede genişleme görüldüğünden, ¹⁸F-florodeoksiglukoz (FDG) ile pozitron emisyon tomografi (PET)/BT çekildi. ¹⁸F-FDG PET/BT'de kolon duvarları boyunca artmış aktivite tutulumu görüldü. PET/BT incelemesinden iki gün sonra hastanın ishal ve karın ağrısı şikayetleri başladı. Clostridioides difficile'ye yönelik gaita testi pozitif sonuçlandı, antibiyotik tedavisine başlandı ancak hasta fayda görmedi. Takip k-BT bir megakolon durumunu gösterdiğinden, hasta hemikolektomiye gönderildi. Histoloji, yaygın bir psödomembranöz kolit (PMC) ile uyumlu idi. Bu olgu, ¹⁸F-FDG PET/BT'nin pre-semptomatik hastalarda da PMC'nin morfolojik ve fonksiyonel özelliklerini saptama potansiyelini vurgulamaktadır.

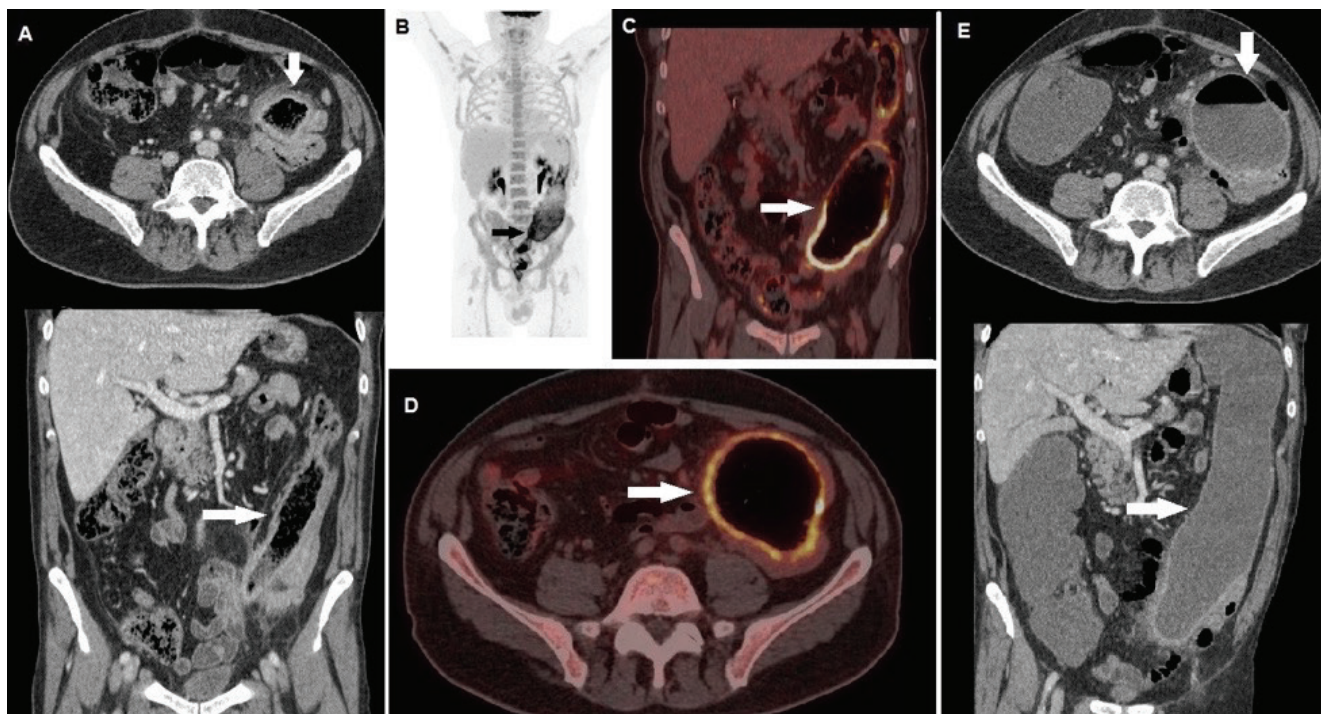**Anahtar kelimeler:** Enflamasyon, ¹⁸F-FDG, pozitron emisyon tomografi, kolit

Figure 1. In November 2020, a 59-year-old male was submitted to anterior resection due to rectal cancer, resulting in pT2 pN0 poorly differentiated adenocarcinoma at histological examination. In March 2021, he underwent contrast-enhanced computed tomography (ce-CT) for restaging and eventual therapeutic decision. Few days before the examination, he had completed one week course of oral amoxycillin due to oropharyngeal infection: ce-CT, at the venous phase (A), revealed abnormal enlargement of the descending colonic lumen (maximum diameter: 35 mm), coupled with parietal thickening and lymph adenopathies in the perivisceral fat, as well evident in the axial (top row, arrow) and coronal (lower row, arrow) images. The patient was completely asymptomatic. In the suspicion of tumoral peritoneal metastatization, five days later he was submitted to positron emission tomography (PET)/CT with 18F-fluorodeoxyglucose (FDG): whole body PET/CT (B) showed highly increased tracer incorporation (maximum standardized uptake value/maximum standard uptake value: 19.4) along the colonic walls (arrow), furthermore a diffuse, mild 18F-FDG uptake was evident in the blood marrow as for an inflammatory condition. Coronal (C) and axial (D) corresponding fused images well demonstrated tracer incorporation within the thickened walls of the descending colon, with a further enlargement of the lumen (arrow, maximum diameter 77 mm). The patient was promptly referred to the surgical department (SD) of our hospital for further clinical investigations. One day after admission to SD, he began experiencing abdominal pain and diarrhea: blood test was normal, except for an increased white blood cell' count (85% neutrophils), and stool test for Clostridioides difficile toxin resulted positive. He started antibiotic therapy with vancomycin at a high dose, without clinical benefits. Further ce-CT (E) demonstrated a worsening of colon enlargement (maximum diameter: 89 mm) and of the parietal thickening, as evident in the axial (top row, arrow) and coronal slices (lower row, arrow). The patient was submitted to left hemicolectomy. Post-surgical specimen showed typical features of pseudomembranous colitis (PMC). Nuclear medicine has a well-established role in the diagnosis of inflammation and infection through several technical approaches (1,2,3). Since activated lymphocytes and granulocytes overexpress glucose transporters and up-regulate hexokinase activity, PET/CT with 18F-FDG has been successfully applied to also the diagnosis and monitoring of infectious and inflammatory processes: PET/CT offers the advantage of being a whole body and single-day procedure, characterized by excellent spatial resolution (4,5). Although preclinical studies have suggested that the grade of 18F-FDG PET/CT in PMC may correlate with disease severity in animal models (6), there are few clinical reports on this topic (5,6,7,8]. The case we describe shows that 18F-FDG PET/CT scan can be applied to detect PMC typical features, consisting of increased glucose metabolism corresponding to diffuse bowel wall thickening and dilatation, also at a very early and still pre-symptomatic phase, therefore guiding clinicians to the more appropriate diagnostic and therapeutic approaches.

Ethics

Informed Consent: Patient consent was obtained before PET/CT examination.

Peer-review: Externally peer-reviewed.

Financial Disclosure: The author declared that this study has received no financial support.

References

1. Pijl JP, Nienhuis PH, Kwee TC, Glaudemans AWJM, Slart RHJA, Gormsen LC. Limitations and Pitfalls of FDG-PET/CT in infection and inflammation. Semin Nucl Med 2021;51:633-645.
2. Djekidel M, Brown RK, Piert M. Benefits of hybrid SPECT/CT for (111)In-oxine- and Tc-99m-hexamethylpropylene amine oxime-labeled leukocyte imaging. Clin Nucl Med 2011;36:e50-e56.
3. Filippi L, Biancone L, Petruzziello C, Schillaci O. Tc-99m HMPAO-labeled leukocyte scintigraphy with hybrid SPECT/CT detects perianal fistulas in Crohn disease. Clin Nucl Med 2006;31:541-542.
4. Vaidyanathan S, Patel CN, Scarsbrook AF, Chowdhury FU. FDG PET/CT in infection and inflammation–current and emerging clinical applications. Clin Radiol 2015;70:787-800.
5. Ahn BC, Lee SW, Lee J. Intense accumulation of F-18 FDG in colonic wall in adult onset still disease with pseudomembranous colitis. Clin Nucl Med 2008;33:806-808.
6. Cussó L, Reigadas E, Muñoz P, Desco M, Bouza E. Evaluation of Clostridium difficile Infection with PET/CT Imaging in a Mouse Model. Mol Imaging Biol 2020;22:587-592.
7. Hannah A, Scott AM, Akhurst T, Berlangieri S, Bishop J, McKay WJ. Abnormal colonic accumulation of fluorine-18-FDG in pseudomembranous colitis. J Nucl Med 1996;37:1683-1685.
8. Venkat R, Pandit V, Telemi E, Trofymenko O, Pandian TK, Nfonsam VN. Frailty predicts morbidity and mortality after colectomy for clostridium difficile colitis. Am Surg 2018;84:628-632.

A Rare Case and Atypical Metastatic Regions, Pulmonary Giant Cell Carcinoma

Nadir Olgu ve Atipik Metastatik Bölgeler, Pulmoner Dev Hücreli Karsinom

Ⓘ *Ceyda Nur Dündar Çağlayan,* Ⓘ *Müge Nur Engin,* Ⓘ *Adil Boz*

Akdeniz University Hospital, Department of Nuclear Medicine, Antalya, Turkey

Abstract

Sixty two years old man referred to our clinic due to suspicion of thymic mass. The hypermetabolic nodular lesion in the right lung upper lobe was seen in ^{18}F-fluorodeoxyglucose (FDG)-positron emission tomography/computed tomography (PET/CT) in addition to the mass in the anterior mediastinum which was found to without malignancy. The patient underwent wedge resection and final diagnosis was pulmonary giant cell carcinoma. In follow-up ^{18}F-FDG PET/CT multiple lesions with pathological activity were observed in the cerebrum, right postauricular region, bilateral adrenal, stomach, pancreas, pelvic soft tissue, mesenteric, left femur and bilateral lung parenchyma 6 months after. The pathology results of the right frontal, pelvic mass and the postauricular region were metastasis.

Keywords: Primary pulmonary giant cell carcinoma, ^{18}F-FDG PET/CT, atypical metastasis

Öz

Altmış iki yaşında hasta timik kitle nedeniyle kliniğimize başvurdu. Yapılan ^{18}F-florodeoksiglukoz (FDG)-pozitron emisyon tomografi/bilgisayarlı tomografide (PET/BT) anterior mediasten yumuşak doku kitlesine ek olarak sağ akciğerde hipermetabolik nodüler lezyon izlendi. Akciğer rezeksiyon sonrasında pulmoner dev hücreli karsinom tanısı aldı. Takip ^{18}F-FDG PET/BT'sinde beyin, sağ postauriküler, bilateral adrenal, mide, pankreas, pelvik yumuşak doku, mezenterik, sol femur ve bilateral akciğer parankiminde multipl patolojik aktiviteli lezyon gözlendi. Bunlardan sağ frontal, pelvik kitle ve postauriküler yerleşimli lezyonların histopatolojisi metastatik olarak sonuçlandı.

Anahtar kelimeler: Primer pulmoner dev hücreli karsinom, ^{18}F-FDG PET/BT, atipik metastaz

Address for Correspondence: Ceyda Nur Dündar Çağlayan MD, Akdeniz University Hospital, Department of Nuclear Medicine, Antalya, Turkey
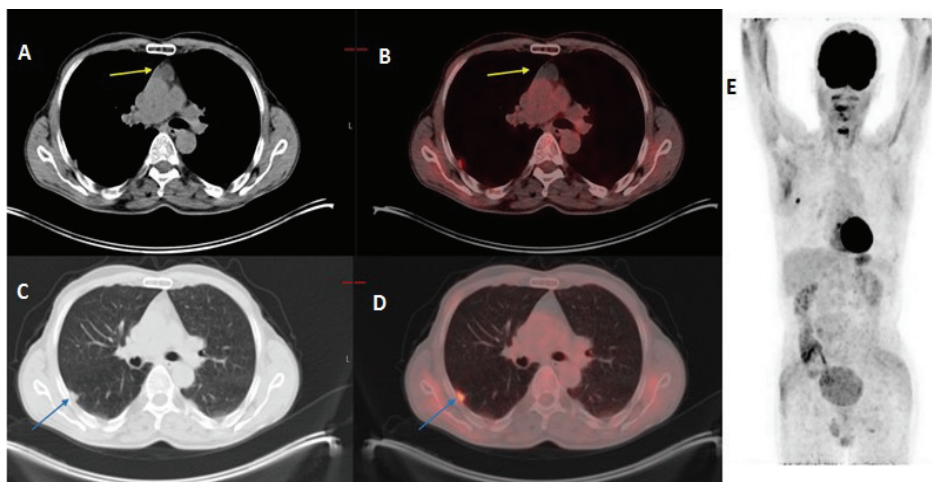**Phone:** +90 242 227 64 85 **E-mail:** ceydanurdundar@gmail.com ORCID ID: https://orcid.org/0000-0001-7467-4807

Figure 1. We present a case of a 62 years old man with a history of giant cell tumour of lung. 18F-fluorodeoxyglucose (FDG)-positron emission tomography/computed tomography (PET/CT) demonstrated abnormal uptake in the malignancy suspected nodular lesion in right lung upper lobe (C and D, blue arrow). The patient underwent right lung wedge resection and final diagnosis was pulmonary giant cell carcinoma with visceral pleural invasion. Axial thorax CT image (A), fused PET/CT images (B, D), axial parenchyma window CT image (C), wholebody maximum intensity projection (MIP) image (E).
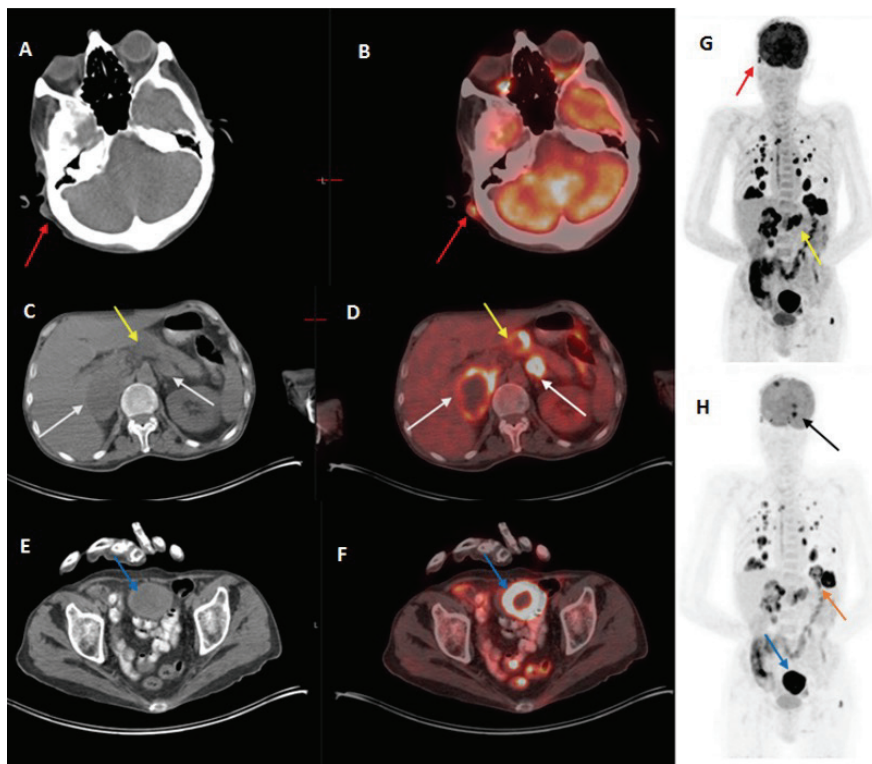

Figure 2. Six months after follow-up PET/CT, multiple metastatic lesions in the lung were noted. Multiple progressive metastatic lesions were seen around the brain (H, black arrow), bilateral adrenal (C and D, white arrows), pancreatic corpus (C, D, G, yellow arrows), pelvic soft tissue (E, F, H, blue arrows), right postauricular area (A, B, G, red arrows), left femur (G and H), and great curvature of stomach (H, orange arrow). The pathology of excisional biopsy proved that the right frontal, right postauricular and pelvic mass lesions were metastatic. Giant cell carcinoma of lung is a rare histological form of sarcomatoid carcinomas traditionally classified within the non-small cell lung carcinomas. Sarcomatoid tumors are an uncommon type of lung cancers (less than 1% of all lung cancers) and shows aggressive behavior (1,2,3,4,5). To the best of our knowledge, although there are reports of pulmonary giant cell carcinoma as a lung lesion in the literature (6,7,8), there are no reports of these atypical metastatic regions. Axial CT images (A, C, E), fused PET/CT images (B, D, F), wholebody MIP images (G, H).

Dündar Çağlayan et al. Metastatic Pulmonary Giant Cell Carcinoma

Mol Imaging Radionucl Ther 2023;32:74-76

Ethics

Informed Consent: Each patient must sign a written consent authorising the use of anonymous data for research purpose before performing PET/CT scan.

Peer-review: Externally peer-reviewed.

Authorship Contributions

Surgical and Medical Practices: C.N.D.Ç., M.N.E., A.B., Concept: C.N.D.Ç., M.N.E., Design: C.N.D.Ç., M.N.E., Data Collection or Processing: C.N.D.Ç., M.N.E., Analysis or Interpretation: C.N.D.Ç., M.N.E., A.B., Literature Search: C.N.D.Ç., M.N.E., Writing: C.N.D.Ç., M.N.E.

Conflict of Interest: No conflict of interest was declared by the authors.

Financial Disclosure: The authors declared that this study received no financial support.

References

1. Travis WD, Brambilla E, Nicholson AG, Yatabe Y, Austin JHM, Beasley MB, Chirieac LR, Dacic S, Duhig E, Flieder DB, Geisinger K, Hirsch FR, Ishikawa Y, Kerr KM, Noguchi M, Pelosi G, Powell CA, Tsao MS, Wistuba I; WHO Panel. The 2015 World Health Organization Classification of Lung Tumors: Impact of Genetic, Clinical and Radiologic Advances Since the 2004 Classification. J Thorac Oncol 2015;10:1243-1260.

2. Pabón-Carrasco S, Vallejo-Benitez AM, Pabón-Carrasco M, Rodriguez-Zarco E. Primary pulmonary giant cell tumor. Arch Bronconeumol (Engl Ed) 2019;55:60-62.

3. Alasio TM, Sun W, Yang GC. Giant cell carcinoma of the lung impact of diagnosis and review of cytological features. Diagn Cytopathol 2007;35:555-559.

4. Fishback NF, Travis WD, Moran CA, Guinee DG Jr, McCarthy WF, Koss MN. Pleomorphic (spindle/giant cell) carcinoma of the lung. A clinicopathologic correlation of 78 cases. Cancer 1994;73:2936-2945.

5. Baldovini C, Rossi G, Ciarrocchi A. Approaches to tumor classification in pulmonary sarcomatoid carcinoma. Lung Cancer (Auckl) 2019;10:131-149.

6. Plowman RS, Nguyen BD. Primary pulmonary giant cell tumor: (18)F-FDG PET/CT imaging. Rev Esp Med Nucl Imagen Mol 2016;35:274-276.

7. Seo JB, Im JG, Goo JM, Chung MJ, Kim MY. Atypical pulmonary metastases: spectrum of radiologic findings. Radiographics 2001;21:403-417.

8. Hayashi S, Kitada M, Ishibashi K, Matsuda Y, Miyokawa N. Combined large cell neuroendocrine carcinoma with giant cell carcinoma of the lungs: a case report. World J Surg Oncol 2013;11:205.

Snow Leopard Appearance of Subcutaneous Panniculitis such as T-cell Lymphoma on ^{18}F-FDG PET/CT

^{18}F-FDG PET/CT'de T-hücreli Lenfoma Benzeri Deri Altı Pannikülitin Kar Leoparı Görünümü

🆔 *Salah Nabih Oueriagli,* 🆔 *Laila El Asraoui,* 🆔 *Omar Ait Sahel,* 🆔 *Yassir Benameur,* 🆔 *Abderrahim Doudouh*

Mohamed V University Souissi, Mohammed V Military Teaching Hospital, Department of Nuclear Medicine, Rabat, Morocco

Abstract

Subcutaneous panniculitis such as T-cell lymphoma (SPTCL) is a very rare disorder. Patients usually present with multiple subcutaneous nodules on the extremities without visceral disease. Dissemination to extra-cutaneous sites is unusual. Only a few cases of SPTCL have been reported in the literature describing the findings of ^{18}F-fluorodeoxyglucose (FDG) positron emission tomography (PET). Here, we represent an interesting and unusual case of diffuse SPTCL with snow Leopard skin appearance on ^{18}F-FDG PET/computed tomography.

Keywords: Panniculitis-like T-cell lymphoma, snow Leopard skin, ^{18}F-FDG PET/CT

Öz

Subkütan pannikülit benzeri T-hücreli lenfoma (SPTCL) çok nadir görülen bir hastalıktır. Hastalar genellikle ekstremitelerde visseral hastalık olmaksızın çok sayıda subkütan nodül ile başvurdular. Ekstra-kutanöz bölgelere yayılım alışılmadık bir durumdur. Literatürde, ^{18}F-florodeoksiglukoz (FDG) pozitron emisyon tomografisi (PET) bulguları bildirilen yalnızca birkaç SPTCL olgusu bildirilmiştir. Burada, ^{18}F-FDG PET/bilgisayarlı tomografide kar Leoparı deri görünümü olan, diffüz SPTCL'li ilginç ve alışılmadık bir olguyu sunuyoruz.

Anahtar kelimeler: Pannikülit benzeri T-hücreli lenfoma, kar Leoparı derisi, ^{18}F-FDG PET/CT

Address for Correspondence: Prof. Salah Nabih Oueriagli MD, Mohamed V University Souissi, Mohammed V Military Teaching Hospital, Department of Nuclear Medicine, Rabat, Morocco
Phone: +212662101403 **E-mail:** salah.nabihoueriagli@gmail.com ORCID ID: https://orcid.org/0000-0001-7824-3158
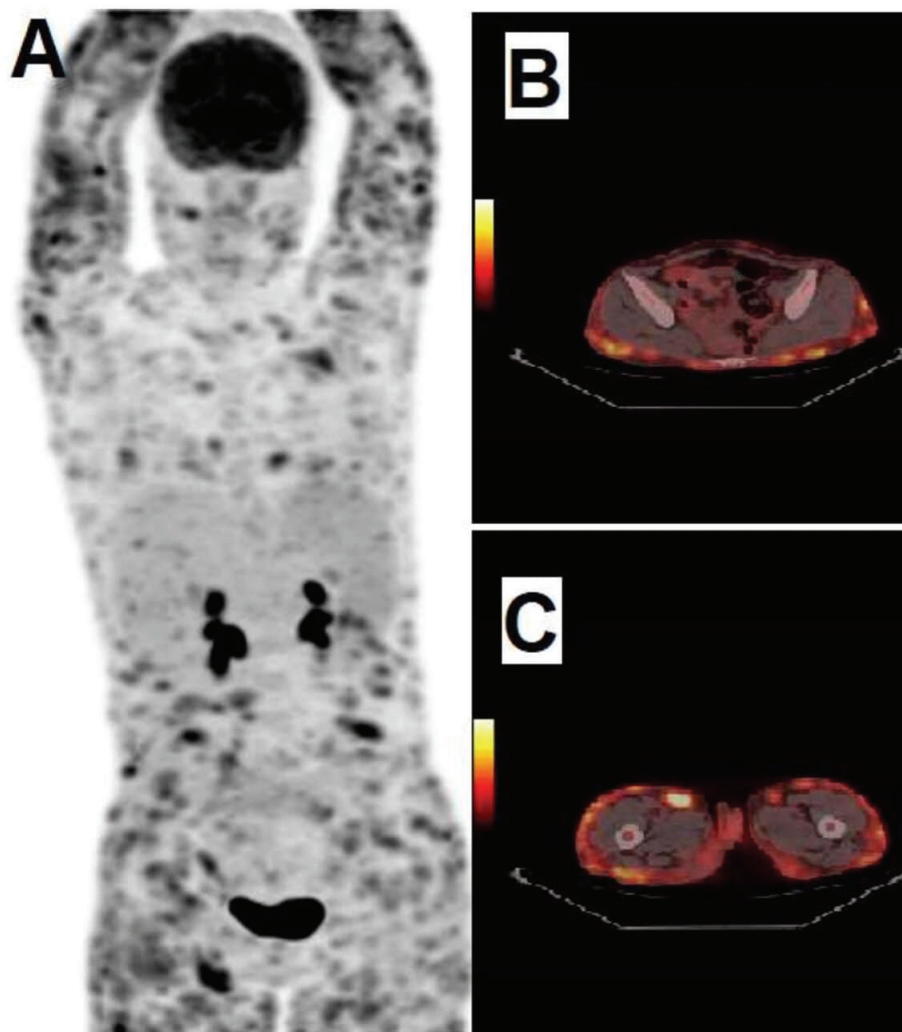
Figure 1. A 22-year-old female patient, presented with macrophage activation syndrome in the context of diffuse subcutaneous panniculitis such as T-cell lymphoma (SPTCL), was referred to our positron emission tomography (PET) unit to evaluate initial staging. Whole-body non-contrast-enhanced ^{18}F-fluorodeoxyglucose (FDG) PET/computed tomography (CT) was performed, and the 3D maximal intensity projection showed a snow Leopard skin appearance with multiple disseminated hot spots throughout the subcutaneous tissues (panel A). Fusion images in axial sections revealed areas of abnormal increased uptakes corresponding to diffuse subcutaneous ^{18}F-FDG multiple micronodular (panel B). Our PET/CT also showed nodal uptakes in right inguinal lymph-nodes with maximum standard uptake value: 8.6 (panel C). SPTCL is a very rare disorder in which all patients are usually presented with multiple subcutaneous nodules on the extremities and trunk without visceral disease (1). It represents 1% of cases of non-Hodgkin's lymphoma (2). Dissemination to extra-cutaneous sites is unusual, and SPTCL may be preceded for years by a seemingly benign panniculitis (3). In our knowledge, just a few cases have been reported in the literature, describing the appearance of SPTCL on ^{18}F-FDG PET (4). Without histology confirmation, snow Leopard skin appearance on ^{18}F-FDG PET/CT can be related to other origins such as: benign panniculitis, sarcoidosis, and cutaneous polyarteritis nodosa (5,6).

Ethics

Informed Consent: All appropriate patient consent forms were obtained. In this form, the patient gave consent for their pictures and other clinical information to be reported in the journal.

Peer-review: Externally peer-reviewed.

Authorship Contributions

Surgical and Medical Practices: S.N.O., Concept: S.N.O., L.E.A., O.A.S., Design: S.N.O., L.E.A., O.A.S., Data Collection or Processing: S.N.O., Y.B., Analysis or Interpretation: S.N.O., Literature Search: S.N.O., Writing: S.N.O., A.D.

Conflict of Interest: No conflict of interest was declared by the authors.

Financial Disclosure: The authors declared that this study received no financial support.

References

1. Willemze R, Jaffe ES, Burg G, Cerroni L, Berti E, Swerdlow SH, Ralfkiaer E, Chimenti S, Diaz-Perez JL, Duncan LM, Grange F, Harris NL, Kempf W, Kerl H, Kurrer M, Knobler R, Pimpinelli N, Sander C, Santucci M, Sterry W, Vermeer MH, Wechsler J, Whittaker S, Meijer CJ. WHO-EORTC classification for cutaneous lymphomas. Blood 2005;105:3768-3785.

2. Paulli M, Berti E. Cutaneous T-cell lymphomas (including rare subtypes). Current concepts. II. Haematologica 2004;89:1372-1388.

3. Weenig RH, Ng CS, Perniciaro C. Subcutaneous panniculitis-like T-cell lymphoma: an elusive case presenting as lipomembranous panniculitis and a review of 72 cases in the literature. Am J Dermatopathol 2001;23:206-215.

4. Kim JS, Jeong YJ, Sohn MH, Jeong HJ, Lim ST, Kim DW, Kwak JY, Yim CY. Usefulness of F-18 FDG PET/CT in subcutaneous panniculitis-like T cell lymphoma: disease extent and treatment response evaluation. Radiol Oncol 2012;46:279-283.

5. Bompard F, de Menthon M, Gomez L, Gottlieb J, Saleh NS, Chekroun M, Grimon G, Goujard C, Durand E, Besson FL. 18F-FDG PET/CT of sarcoidosis with extensive cutaneous and subcutaneous nodules: the snow leopard sign. Eur J Nucl Med Mol Imaging 2019;46:1980-1981.

6. Shimizu M, Inoue N, Mizuta M, Ikawa Y, Yachie A. Leopard skin appearance of cutaneous polyarteritis nodosa on 18Ffluorodeoxyglucose positron emission tomography. Rheumatology (Oxford) 2016;55:1090.

Significance of Clinico-radiological Correlation in a Patient with Pulmonary Intimal Sarcoma Simulating as Pulmonary Thromboembolism

Pulmoner Tromboembolizmi Taklit Eden Pulmoner İntimal Sarkomlu Bir Hastada Klinik-radyolojik Korelasyonun Önemi

🅾 *Stuti Chandola[1]*, 🅾 *Ekta Dhamija[1]*, 🅾 *Sameer Rastogi[2]*, 🅾 *Deepali Jain[3]*

[1]*All India Institute of Medical Sciences, Department of Radiodiagnosis, New Delhi, India*
[2]*All India Institute of Medical Sciences, Department of Medical Oncology, New Delhi, India*
[3]*All India Institute of Medical Sciences, Department of Pathology, New Delhi, India*

Abstract

Pulmonary intimal sarcoma (PAS) is a highly aggressive malignant mesenchymal tumor affecting the central pulmonary arteries. Similar clinical presentation and indeterminate laboratory parameters often result in misdiagnosis of this condition as pulmonary thromboembolism, which is a relatively common disease. Certain imaging features can however allow differentiation between these two diagnoses. We present one such case of PAS that was initially treated as pulmonary embolism; and briefly review the relevant imaging characteristics to avoid overlooking PAS especially in patients with an atypical clinical history for thromboembolism.

Keywords: Pulmonary intimal sarcoma, CT pulmonary angiography, pulmonary thromboembolism, wall eclipse sign

Öz

Pulmoner intimal sarkom (PAS), merkezi pulmoner arterleri etkileyen oldukça agresif bir malign mezenkimal tümördür. Benzer klinik tablo ve belirsiz laboratuvar parametreleri sıklıkla bu durumun, nispeten yaygın bir hastalık olan pulmoner tromboembolizm olarak yanlış teşhis edilmesine neden olur. Bununla birlikte, belirli görüntüleme özellikleri, bu iki durumun ayrımını sağlayabilir. Başlangıçta pulmoner emboli olarak tedavi edilen böyle bir PAS'li hastayı sunduk ve özellikle atipik klinik tromboembolizm öyküsü olan hastalarda PAS'yi gözden kaçırmamak için görüntüleme özelliklerini kısaca gözden geçirdik.

Anahtar kelimeler: Pulmoner intimal sarkom, BT pulmoner anjiyografi, pulmoner tromboembolizm, duvar tutulması belirtisi

Address for Correspondence: Assoc. Prof. Ekta Dhamija, All India Institute of Medical Sciences, Department of Radiodiagnosis, New Delhi, India
Phone: +9999725388 **E-mail:** drektadhamija.aiims@gmail.com ORCID ID: https://orcid.org/0000-0001-8265-9674
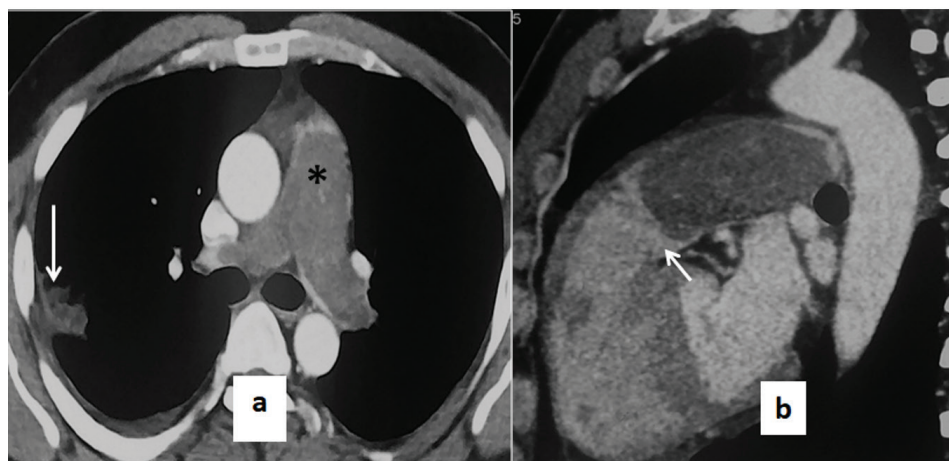
Figure 1. Pulmonary intimal sarcoma (PAS) is an aggressive malignant mesenchymal tumor originating from the subendothelial connective tissue lining of the central pulmonary arteries (i.e. main, right or left) (1,2). This rare condition is often misdiagnosed initially as pulmonary embolism and is followed by initiation of anticoagulation therapy which allows unbridled tumor growth (3,4). Although both diseases manifest as filling defects in pulmonary arteries, PAS is usually lobulated or nodular and forms an acute angle with the intimal surface with heterogeneous enhancement as compared to acute pulmonary embolism, which typically manifests as thin and thread-like defects (5,6). Vascular expansion with complete luminal occlusion is another distinctive feature of PAS and reflects the preferential intraluminal growth of the tumor.

Baseline computed tomography (CT) pulmonary angiography of a 35-year-old gentleman with complaints of non-productive cough and shortness of breath for 1 year with raised D-dimer levels (836 ng/mL, normal range <500 ng/mL) showed a lobulated heterogeneous intraluminal filling defect occluding the main pulmonary artery with extension into the right and left branches, mimicking a saddle embolus (asterisk in a). A small subpleural consolidation (arrow, a) seen in the right upper lobe represents pulmonary infarct. (b) Sagittal CT confirms the complete occlusion of the main pulmonary trunk with proximal extension of the filling defect into the region of the pulmonary valve (arrow). Although no obvious extravascular extension was seen, the lesion caused obscuration of the walls of the pulmonary arteries. With an initial diagnosis of massive pulmonary embolism, he was started on acenocoumarol but did not show any improvement.
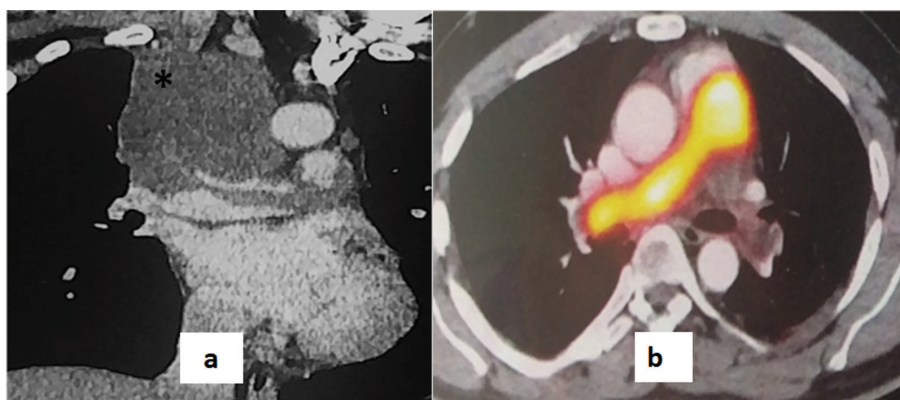

Figure 2. Coronal CT pulmonary angiography (a) performed after 7 months demonstrates the extension of the mass into the paratracheal location (asterisk) with the involvement of the superior vena cava. Such atypical features, including vascular expansion, complete occlusion of the pulmonary artery, and frank extravascular extension raised the suspicion of PAS. The patient underwent positron emission tomography (PET)/CT that showed avid radiotracer uptake (b) in the mass, which is not seen in embolism. The patient then underwent endobronchial ultrasound (EBUS) guided fine needle aspiration cytology (FNAC) of the lesion.

The most specific sign aiding in the detection of PAS is overt extravascular extension, which occurs in later stages (4). "Wall eclipse sign" is diagnostic of PAS and incorporates three criteria: (i) a low-density mass completely occupying the central pulmonary arteries, (ii) proximal protrusion of the mass into the right ventricular outflow tract, and (iii) obscuration of the one or both walls of the involved artery. All three are absent in thromboembolism (7). An acute angle of contact, presence of intratumoural vessels, absence of vessel tapering, and webs are helpful features for differentiating PAS from chronic thromboembolism (4,6). Although PAS does not show enhancement on CT, it however demonstrates avid uptake on ^{18}F-fluorodeoxyglucose PET, which reflects its increased metabolic activity; combined PET/CT is the most definitive modality of distinguishing PAS from non-neoplastic thromboembolic disease (5).
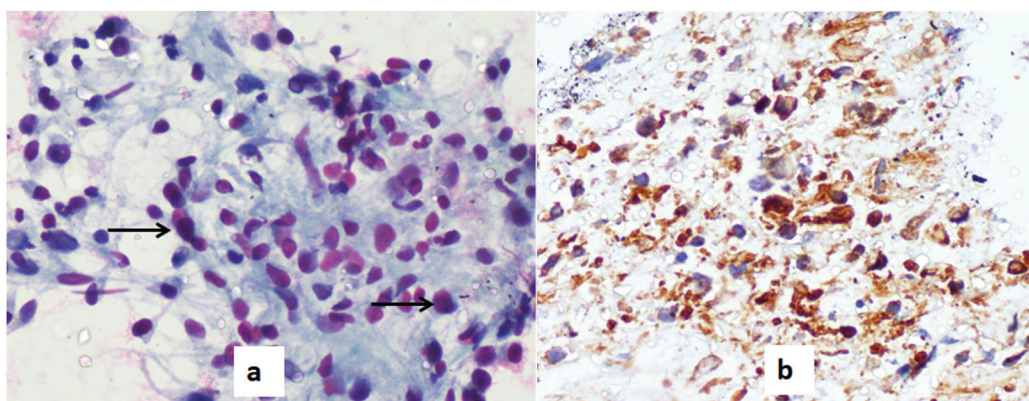
Figure 3. (a) EBUS-guided FNAC of the mass shows tumor cell fragments with pleomorphic oval to spindle cells showing high nucleo- cytoplasmic ratio (arrows in a) on high power photomicrograph (magnification 200x) with papanicolaou stain; (b) the tumor cells also showed strong positivity for smooth muscle actin (brown cells, same magnification), which was consistent with the diagnosis of PAS.
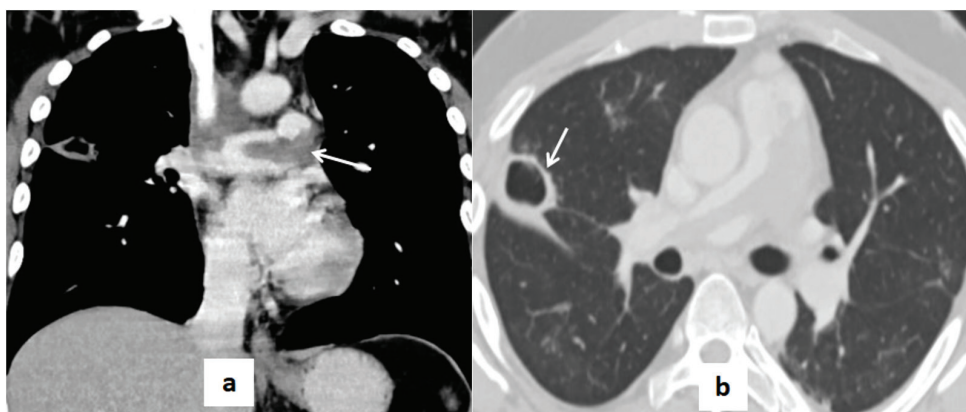

Figure 4. Coronal contrast-enhanced CT image post institution of cytoreductive chemotherapy revealed a reduction in the size of the mass (arrow in a) and cavitation in the pulmonary infarct (arrow in b) representing a partial response. However, the patient developed severe thrombocytopenia as a complication of chemotherapy with pulmonary hemorrhage and succumbed to the illness.

Ethics

Informed Consent: Obtained from the patient's attendant.

Peer-review: Externally and internally peer-reviewed.

Authorship Contributions

Surgical and Medical Practices: S.R., D.J., Concept: E.D., Design: E.D., Data Collection or Processing: S.C., Analysis or Interpretation: S.C., E.D., Literature Search: S.C., Writing: S.C., E.D., S.R., D.J.

Conflict of Interest: No conflict of interest was declared by the authors.

Financial Disclosure: The authors declared that this study received no financial support.

References

1. Scheidl S, Taghavi S, Reiter U, Tröster N, Kovacs G, Rienmüller R, Lang S, Klepetko W, Olschewski H. Intimal sarcoma of the pulmonary valve. Ann Thorac Surg 2010;89:e25-e27.

2. Burke A, Tavora FR, Maleszewski JJ, Fraizer AA. Tumors of the Heart and Great Vessels. In: AFIP Atlas of Tumor Pathology. 4th ed. Silver Spring, Md: American Registry of Pathology, 2015.

3. Mussot S, Ghigna MR, Mercier O, Fabre D, Fadel E, Le Cesne A, Simonneau G, Dartevelle P. Retrospective institutional study of 31 patients treated for pulmonary artery sarcoma. Eur J Cardiothorac Surg 2013;43:787-793.

4. Ropp AM, Burke AP, Kligerman SJ, Leb JS, Frazier AA. Intimal sarcoma of the great vessels. Radiographics 2021;41:361-379.

5. Kim C, Kim MY, Kang JW, Song JS, Lee KY, Kim SS. Pulmonary artery intimal sarcoma versus pulmonary artery thromboembolism: CT and clinical findings. Korean J Radiol 2018;19:792-802.

6. Cervilla-Muñoz E, Galeano-Valle F, Del-Toro-Cervera J, Calleja-Cartón E, Demelo-Rodríguez P. Differential diagnosis and treatment approach to pulmonary artery sarcoma: a case report and literature review. ERJ Open Res 2020;6:00124-2020.

7. Gan HL, Zhang JQ, Huang XY, Yu W. The wall eclipsing sign on pulmonary artery computed tomography angiography is pathognomonic for pulmonary artery sarcoma. PLoS One 2013;8:e83200.

Primary Isolated Breast Lymphoma Presenting as Primary Breast Cancer with ¹⁸F-FDG PET/CT

¹⁸F-FDG PET/BT'de Meme Kanserini Taklit Eden Primer Meme Lenfoması

 Özge Vural Topuz, *Özgür Omak,* *Burçak Yılmaz*

University of Health Sciences Turkey, Başakşehir Çam and Sakura City Hospital, Clinic of Nuclear Medicine, İstanbul, Turkey

Abstract

A 40-year-old woman with a palpable mass lesion in her right breast suggested as breast cancer was admitted to ¹⁸F-fluorodeoxyglucose (FDG) positron emission tomography/computed tomography (PET/CT) unit for the metabolic characterization of the lesion and for the staging of the disease. The patient had no fever and no evidence of weight loss or night sweats. ¹⁸F-FDG PET/CT revealed an isolated solid mass lesion with increased ¹⁸F-FDG uptake in the upper outer quadrant of the right breast and increased ¹⁸F-FDG uptake in the lymph nodes of the right axilla suspected as primary breast cancer and its local lymph node metastasis. There was no other pathological ¹⁸F-FDG uptake in the whole body. Excisional biopsy histopathology revealed diffuse large B-cell non-Hodgkin lymphoma.

Keywords: Breast, non-Hodgkin lymphoma, PET/CT, ¹⁸F-FDG

Öz

Sağ memede kitle saptanan meme kanseri ön tanılı 40 yaşında kadın hasta, lezyonun metabolik karakterizasyonu ve hastalığın evrelenmesi amacıyla ¹⁸F-florodeoksiglukoz (FDG) pozitron emisyon tomografisi/bilgisayarlı tomografi (PET/BT) ünitesine başvurdu. Hastanın ateş, kilo kaybı veya gece terlemesi yoktu. ¹⁸F-FDG PET/BT görüntülemesinde sağ meme üst dış kadranda artmış ¹⁸F-FDG tutulumu gösteren solid bir kitle lezyonu ile; sağ aksillada artmış ¹⁸F-FDG tutulumu gösteren lenf nodları izlenmiş olup ön planda primer meme kanseri ve aksiller lenf nodlarında metastaz şüphesi uyandırmıştır. Tüm vücudun geri kalan kısımlarında herhangi bir patolojik ¹⁸F-FDG tutulumu yoktu. Lezyonun eksizyonel biyopsi histopatolojisinde diffüz büyük B-hücreli non-Hodgkin lenfoma saptandı.

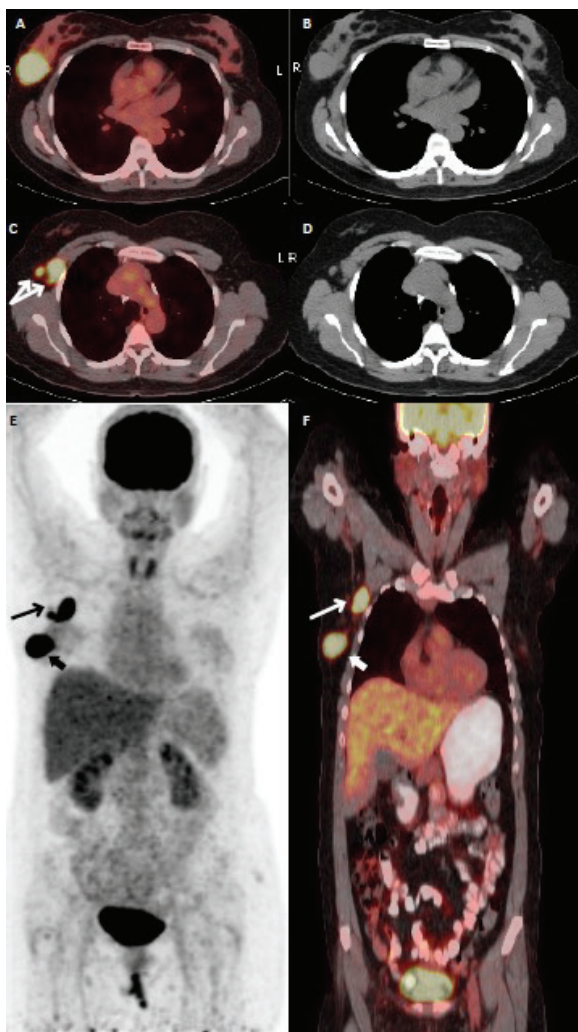**Anahtar kelimeler:** Meme, non-Hodgkin lenfoma, PET/BT, ¹⁸F-FDG

Figure 1. A 40-year-old woman with a palpable mass with an axial diameter of about 4 cm in her right breast suggested as primary breast cancer was admitted to our department for ^{18}F-fluorodeoxyglucose (FDG) positron emission tomography/computed tomography (PET/CT) imaging for metabolic characterization of the lesion. The patient had no fever and no evidence of weight loss or night sweats. The axial PET/CT and CT images of the chest (A, B, C, D) show a hypermetabolic lesion in the upper outer quadrant of the right breast with increased ^{18}F-FDG uptake (maximum standard uptake value: 19.3) and lymph node (arrows) involvement with increased ^{18}F-FDG uptake in the right axilla. Whole body maximum intensity projection (MIP) (E) and coronal PET/CT images (F) revealed hypermetabolic breast lesion (thick arrow) and axillary nodes (arrow) without other abnormal ^{18}F-FDG uptake in the entire body. Breast masses are common but are not usually caused by hematological malignancies. The breast is an uncommon site for developing malignant lymphomas. The small amount of lymphoid tissue in the breast may be the cause of the rarity of primary breast lymphoma (PBL) (1,2). Less than 1% of NHL involve the breast primarily and PBL accounts for 0.04%-0.5% of all breast malignancies (3,4) The most common histology of patients reported to have PBL is diffuse large B-cell non-Hodgkin lymphoma (DLBCL) (5). ^{18}F-FDG PET/CT has an important role in the staging of lymphoma, in the evaluation of treatment response and and in the detection of recurrence (6). Excisional biopsy result of the right breast lesion was reported as a DLBCL activated B-cell subtype. Immunohistochemical findings were CD3(+), CD5(+), CD10(-), CD20(+), CD38(+), CD44 (+),PAX5(+), Bcl-2(+), Bcl-6(+), and Ki-67 labeling index (80%-90%). The patient was then referred to the medical oncology department and received combination chemotherapy.
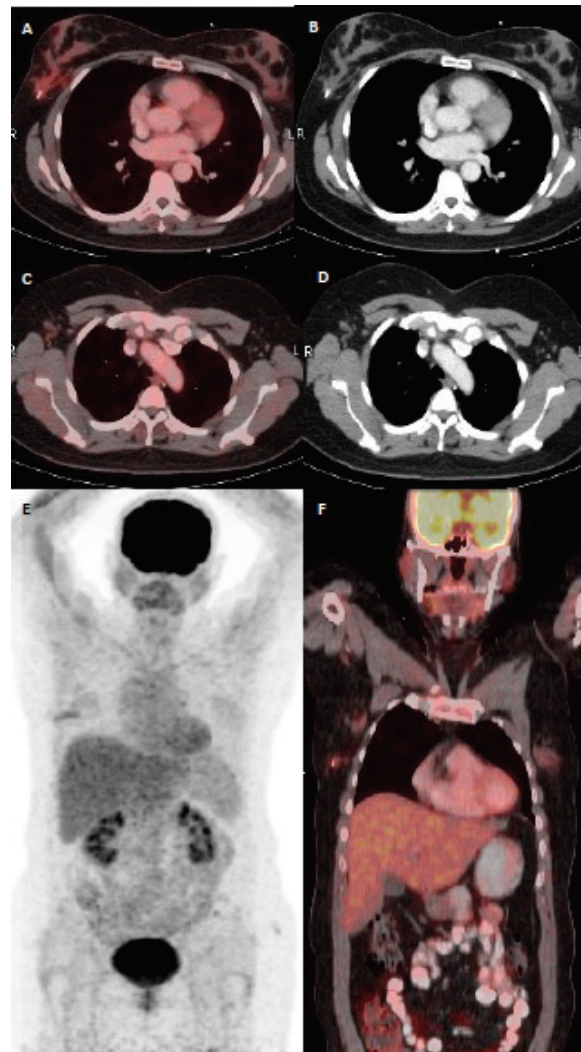
Mol Imaging Radionucl Ther 2023;32:83-86

Vural Topuz et al. Primary Isolated Breast Lymphoma

Figure 2. ^{18}F-FDG PET/CT was performed following appropriate chemotherapy, without any ^{18}F-FDG uptake in the whole body 4 months after the initial PET/CT study. The axial PET/CT and CT images (A, B, C, D) of the control PET/CT scan show no pathological ^{18}F-FDG uptake in the right breast and axilla. Whole-body MIP (E) and coronal PET/CT (F) images revealed complete regression of the disease.

Vural Topuz et al. Primary Isolated Breast Lymphoma

Mol Imaging Radionucl Ther 2023;32:83-86

Ethic

Informed Consent: Written informed consent was obtained.

Peer-review: Externally peer-reviewed.

Authorship Contributions

Surgical and Medical Practices: Ö.V.T., Ö.O., B.Y., Concept: Ö.V.T., B.Y., Design: Ö.V.T., B.Y., Data Collection or Processing: Ö.V.T., Ö.O., B.Y., Analysis or Interpretation: Ö.V.T., Ö.O., B.Y., Literature Search: Ö.V.T., Ö.O., Writing: Ö.V.T., Ö.O., B.Y.

Conflict of Interest: No conflict of interest was declared by the authors.

Financial Disclosure: The authors declared that this study received no financial support.

References

1. Woo OH, Yong HS, Shin BK, Park CM, Kang EY. Synchronous bilateral primary breast lymphoma: MRI and pathologic findings. Breast J 2007;13:429-430.

2. Lim H, Cho KR, Kim I, Hwang KW, Seo BK, Woo OH, Oh YW, Bae JW. Primary Peripheral T-cell Lymphoma of the Brexast: Radiologic and Pathologic Findings. J Breast Cancer 2010;13:318-322.

3. Domchek SM, Hecht JL, Fleming MD, Pinkus GS, Canellos GP. Lymphomas of the breast: primary and secondary involvement. Cancer 2002;94:6-13.

4. Jeanneret-Sozzi W, Taghian A, Epelbaum R, Poortmans P, Zwahlen D, Amsler B, Villette S, Belkacémi Y, Nguyen T, Scalliet P, Maingon P, Gutiérrez C, Gastelblum P, Krengli M, Raad RA, Ozsahin M, Mirimanoff RO. Primary breast lymphoma: patient profile, outcome and prognostic factors. A multicentre Rare Cancer Network study. BMC Cancer 2008;8:86.

5. Kong EJ, Cho IH. F-18 FDG PET/MRI findings of primary breast lymphoma in two cases: FDG PET/MRI findings of primary breast lymphoma. Clin Imaging 2015;39:682-684.

6. Chaushev B, Micheva I, Mechmed M, Balev B, Bocheva Y, Ivanova D, Krasnaliev I, Lozanova R, Klisarova A, Bochev P, Dancheva J. 18F-FDG PET/CT in the diagnosis of an extranodal relapse of diffuse large B-cell lymphoma (DLBCL): a clinical case with a literature review. Nucl Med Rev Cent East Eur 2016;19:11-13.

A Rare Hernia Mimicking Implant in a Patient with Rectal Adenocarcinoma: Internal Herniation

Rektal Adenokarsinomlu Bir Hastada İmplantı Taklit Eden Nadir Bir Fıtık: İnternal Herniasyon

⬤ *Sibel Göksel[1],* ⬤ *Mustafa Başaran[2],* ⬤ *Hasan Gündoğdu[2],* ⬤ *Cengiz Karaçin[3]*

[1]*Recep Tayyip Erdoğan University Faculty of Medicine, Department of Nuclear Medicine, Rize, Turkey*
[2]*Recep Tayyip Erdoğan University Faculty of Medicine, Department of Radiology, Rize, Turkey*
[3]*Dr. Abdurrahman Yurtaslan Training and Research Hospital, Clinic of Medical Oncology, Ankara, Turkey*

Abstract

Internal herniation may be seen more frequently in patients with intra-abdominal surgery and malignancy history. We presented a 58-year-old male patient diagnosed with rectal adenocarcinoma seven years ago with a history of surgery and pelvic radiotherapy. When the abdominal computed tomography (CT) image was taken during routine oncology follow-up, a lesion mimicking a serosal implant on the anterior abdominal wall was detected. ^{18}F-fluorodeoxyglucose (FDG) positron emission tomography (PET)/CT imaging was performed the suspicion of recurrence. It was concluded that the lesion, which was evaluated as an implant in abdominal CT with ^{18}F-FDG PET/CT imaging, was a spontaneously reducing internal herniation. ^{18}F-FDG PET/CT imaging in cancer patients is crucial in illuminating the suspicion of recurrent lesions in these patients and sheds light on the course of the patients in oncology practice.

Keywords: Internal hernia, mimicking implant, ^{18}F-FDG PET/CT, rectal adenocarcinoma

Öz

İnternal herniasyon karın içi cerrahi ve malignite öyküsü olan hastalarda daha sık görülür. Biz bu olgu sunumunda, 7 yıl önce rektal adenokarsinom tanısı almış, cerrahi ve pelvik radyoterapi öyküsü olan 58 yaşında erkek hastayı sunduk. Hastada rutin takiplerde çekilen abdomen bilgisayarlı tomografide (BT) karın ön duvarında serozal implant şüphesi olan lezyon saptandı. Nüks şüphesiyle çekilen ^{18}F-florodeoksiglukoz (FDG) pozitron emisyon tomografi (PET)/BT ile BT'de implant olarak değerlendirilen lezyonun, spontan redüksiyon yapan internal herniasyon olduğu sonucuna varıldı. Kanser hastalarında ^{18}F-FDG PET/BT görüntüleme bu hastalarda nüks şüphesinin aydınlatılmasında önemlidir ve onkoloji pratiğinde hastaların seyrine ışık tutar.

Anahtar kelimeler: İnternal herni, implant taklidi, ^{18}F-FDG PET/BT, rektal adenokarsinom
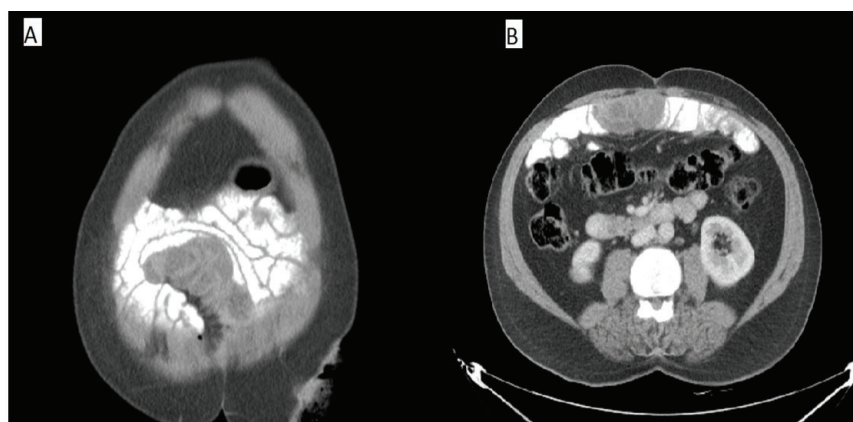
Figure 1. Internal hernia is mostly found incidentally, the literature has reported that sometimes accompanying malignancies cause herniation (1,2). In cases with an incidental internal hernia, atypical localization of the intestinal loops is often present without obstruction in the lumen. Internal hernias occasionally show spontaneous reduction and are often confused with many diseases (3,4). Contrast-enhanced coronal (A) and axial (B) sections of abdominal computed tomography (CT) imaging revealed a suspicious, cystic-necrotic appearing lesion mimicking the serosal implant on the anterior abdominal wall. The patient had a history of low anterior resection (LAR) after neoadjuvant chemoradiotherapy. The patient had no clinical symptoms, and tumor markers were at a normal level. The mesenteric fatty planes adjacent to the lesion were homogeneous, and no additional findings consistent with malignancy were found on the contrast-enhanced diagnostic abdominal CT.
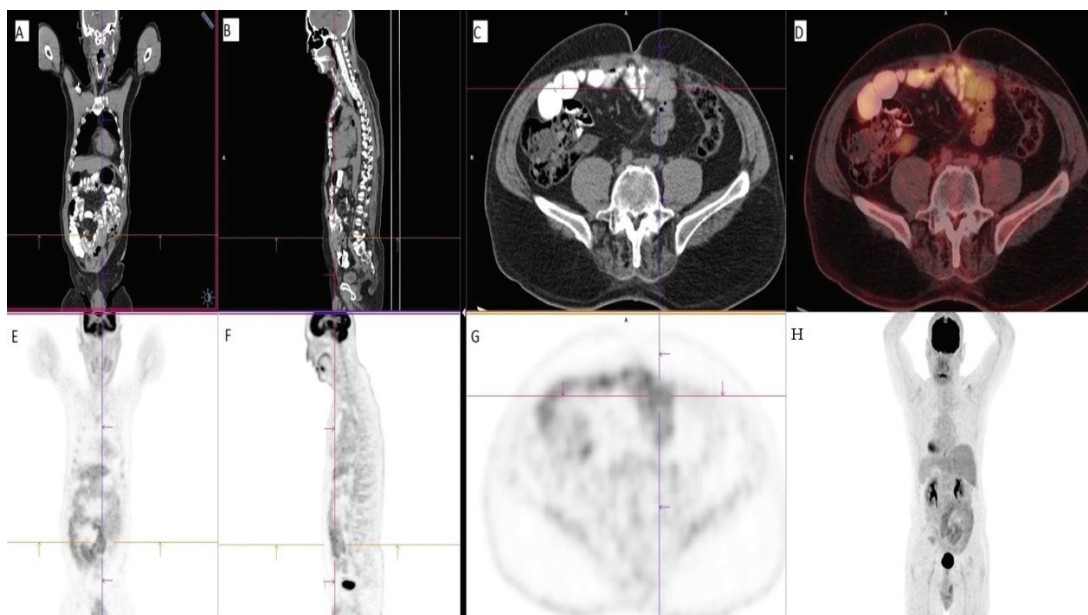

Figure 2. In patients with malignancy with a history of surgery, internal hernia should be considered in the differential diagnosis of lesions with suspected malignancy. Before making treatment decisions, the contribution of oncologic ¹⁸F-fluorodeoxyglucose (FDG) positron emission tomography (PET)/CT imaging, which reflects the metabolic status of suspicious lesions, is crucial (5,6). Findings that are not associated with malignancy but are detected incidentally on PET/CT scanning are becoming more common (7). Coronal (A)-sagittal (B) and axial (C) sections of CT images, axial section of fusion image (D), coronal (E)-sagittal (F) and axial (G) sections of PET images, and maximum intensity projection (H) image of PET/CT scan was performed patient with a suspicious implant lesion on the anterior abdominal wall. ¹⁸F-FDG PET/CT scan showed that the suspicious lesion, which seen on abdominal CT disappeared. It was observed that there was an oral contrast material passage in the existing intestinal loops in this region, and there was no pathological ¹⁸F-FDG uptake compatible with the implant on the anterior abdominal wall. Thus, thanks to PET/CT imaging, we excluded the diagnosis of implant and recurrent disease in our patient. When CT images of the abdomen were re-evaluated together with PET/CT images, it was seen that the suspicious lesion was observed as a sac on diagnostic CT, and it was compressing the small intestines in this state. Additionally, the convergence of adjacent mesenteric fatty planes and vascular structures into the sac was detected as supporting internal herniation. In a patient with rectal cancer with a history of LAR and radiotherapy, it was concluded that the image that was first evaluated as an implant on CT was internal herniation that was spontaneously reduced by ¹⁸F-FDG PET/CT scanning.

Ethic

Informed Consent: Patient consent was obtained.

Peer-review: Externally and internally peer-reviewed.

Authorship Contributions

Surgical and Medical Practices: S.G., M.B., H.G., C.K., Concept: S.G., Design: S.G., Data Collection or Processing: S.G., M.B., H.G., Analysis or Interpretation: S.G., M.B., H.G., Literature Search: S.G., M.B., Writing: S.G., M.B., H.G.

Conflict of Interest: No conflict of interest was declared by the authors.

Financial Disclosure: The authors declared that this study received no financial support.

References

1. Ghahremani GG. Abdominal and pelvic hernias. In: Gore RM, Levine MS (eds). Textbook of gastrointestinal radiology, 2nd ed. Philadelphia, PA: Saunders 2000; 1993-2009.

2. Liu PH, Kung WC, Wu YC, Chien ST, Chang WY, Hsu CW. Metastatic malignant gastrointestinal stromal tumor mimicking a right incarcerated inguinal hernia. Formosan Journal of Surgery 2014;47:189-192.

3. Doishita S, Takeshita T, Uchima Y, Kawasaki M, Shimono T, Yamashita A, Sugimoto M, Ninoi T, Shima H, Miki Y. Internal hernias in the era of multidetector CT: correlation of imaging and surgical findings. Radiographics 2016;36:88-106.

4. Hamimi AAH, Yunus TE. Internal mimics hernias and their mimics: how would radiologists help? Egypt J Radiol Nucl Med 2014;45:1071-1078.

5. Panagiotidis E, Datseris IE, Exarhos D, Skilakaki M, Skoura E, Bamias A. High incidence of peritoneal implants in recurrence of intra-abdominal cancer revealed by 18F-FDG PET/CT in patients with increased tumor markers and negative findings on conventional imaging. Nucl Med Commun 2012;33:431-438.

6. Elekonawo FMK, Starremans B, Laurens ST, Bremers AJA, de Wilt JHW, Heijmen L, de Geus-Oei LF. Can [18F]F-FDG PET/CT be used to assess the pre-operative extent of peritoneal carcinomatosis in patients with colorectal cancer? Abdom Radiol (NY) 2020;45:301-306.

7. Li Y, Behr S. Acute Findings on FDG PET/CT: key imaging features and how to differentiate them from malignancy. Curr Radiol Rep 2020;8:22.

¹⁸F-FDG PET/CT Findings Overlapping Lymphoma in a Patient with Systemic Juvenile Idiopathic Arthritis

Sistemik Jüvenil İdiyopatik Artritli Bir Hastada Lenfoma ile Örtüşen ¹⁸F-FDG PET/BT Bulguları

🄳 *Özlem Şahin¹*, 🄳 *Bülent Ataş²*, 🄳 *Özge Metin Akcan³*, 🄳 *Ahmet Eren Şen¹*

¹Necmettin Erbakan University, Meram Faculty of Medicine, Department of Nuclear Medicine, Konya, Turkey
²Necmettin Erbakan University, Meram Faculty of Medicine, Department of Pediatric Nephrology, Konya, Turkey
³Necmettin Erbakan University, Meram Faculty of Medicine, Department of Pediatric Infectious Diseases, Konya, Turkey

Abstract

Systemic juvenile idiopathic arthritis (sJIA) is an important autoinflammatory disease whose first symptom is usually fever, and life-threatening conditions such as macrophage activation syndrome can develop when diagnosis and treatment is delayed. sJIA is an exclusion diagnosis, and there is no specific test that distinguishes it from other febrile diseases. We report the positron emission tomography/computed tomography (PET/CT) findings of sJIA in a 12-year-old girl who presented with fever, rash, and arthralgia. ¹⁸F-fluorodeoxyglucose (FDG) uptake was observed in the spleen, bone marrow, and lymph nodes in ¹⁸F-FDG PET/CT performed to investigate the etiology of fever of unknown origin. The result of excisional biopsy performed with the suspicion of lymphoma from the left cervical lymph node with intense ¹⁸F-FDG uptake was reported as reactive hyperplasia. PET/CT is an alternative diagnostic method for patients with fever of unknown origin. In this case report, we emphasize that in patients with sJIA, there may be intense fluorodeoxyglucose-avid lymph nodes that may lead to the consideration of lymphoproliferative disease, and PET/CT findings along with spleen and bone marrow involvement may overlap with lymphoma.

Keywords: ¹⁸F-FDG, PET/CT, juvenile idiopathic arthritis, fever of unknown origin

Öz

Sistemik juvenil idiyopatik artrit (sJIA), ilk semptomu genellikle ateş olan önemli bir otoenflamatuvar hastalık olup tanı ve tedavi geciktiğinde makrofaj aktivasyon sendromu gibi hayatı tehdit eden durumlar gelişebilir. sJIA, diğer ateşli hastalıklardan ayıran spesifik testi olmayan bir dışlama tanısıdır. Ateş, döküntü, artralji ile başvuran 12 yaşındaki bir kız çocuğunda sJIA'nın pozitron emisyon tomografi/bilgisayarlı tomografi (PET/BT) bulgularını sunuyoruz. Nedeni bilinmeyen ateş etiyolojisini araştırmak için yapılan ¹⁸F-florodeoksiglukoz (FDG)-PET/BT'de dalak, kemik iliği ve lenf düğümlerinde ¹⁸F-FDG tutulumu gözlendi. Yoğun ¹⁸F-FDG tutulumu olan sol servikal lenf düğümünden lenfoma şüphesiyle yapılan eksizyonel biyopsi sonucu reaktif hiperplazi olarak rapor edildi. PET/BT, nedeni bilinmeyen ateşi olan hastalar için alternatif bir tanı yöntemidir. Bu olgu sunumunda, sJIA'lı hastalarda, lenfoproliferatif hastalık düşünülmesine yol açabilecek yoğun florodeoksiglukoz tutan lenf nodları olabileceğini, dalak ve kemik iliği tutulumu nedeniyle PET/BT bulgularının lenfoma ile örtüşebileceğini vurgulamaktayız.

Anahtar kelimeler: ¹⁸F-FDG, PET/BT, jüvenil idiyopatik artrit, nedeni bilinmeyen ateş

Introduction

Systemic juvenile idiopathic arthritis (sJIA) is an autoinflammatory disease that constitutes 10%-15% of children with JIA and has different pathogenesis and clinical features from other JIA subtypes. sJIA manifests itself with quotidian fever and arthritis. The evanescent rash, serositis, hepatosplenomegaly, and lymphadenopathy may be accompany (1,2). The diagnosis of sJIA is an exclusion diagnosis, and no specific test distinguishes it from other febrile diseases. Other causes of fever, such as infection, malignancy, systemic lupus erythematosus, and Kawasaki disease, should be ruled out. Arthritis may not be present at the beginning and may develop later. This complicates the diagnosis and identification may be difficult even for experienced physicians (2). 18F-fluorodeoxyglucose-positron emission tomography/computed tomography (18F-FDG PET/CT) can detect the underlying cause in about half of all children with fever of unknown origin (FUO) (3). Here, we report an adolescent patient with sJIA who presented with FUO, whose findings were compatible with lymphoproliferative disease in 18F-FDG PET/CT, but lymphoma was ruled out histopathologically.

Case Report

A 12-year-old girl presented to the pediatric emergency department with fever and joint pain. Her physical examination revealed fever that reached 40.5°C, an erythematous rash on her body, and tenderness in the right knee joint. There was no redness or temperature increase in the joint, and her other systemic examinations were normal. Her hemoglobin was 12.7 g/dL, the leukocyte count was 14100/µL, platelet count was 281.000/µL, erythrocyte sedimentation rate was 57 mm/hr, C-reactive protein was 81 mg/L, and ferritin was 5964 ng/mL. The microbiologic examinations (blood, urine, throat culture) of the patient were not diagnostic. Infective endocarditis and uveitis were excluded with echocardiography and ophthalmic examinations, respectively. A tuberculin skin test, thorax and abdominal CT, and immunologic tests were normal. No findings were found in the bone marrow aspiration biopsy. 18F-FDG PET/CT was performed after obtaining written consent from the family to determine the etiology of the fever in the patient whose biochemical parameters and fever did not regress despite broad-spectrum antibiotherapy. Conglomerated lymphadenopathies were observed in the bilateral cervical chain, more intensely on the left, on 18F-FDG PET/CT [maximum standardized uptake value (SUV$_{max}$): 31.80]. Additionally, there were several lymph nodes in the bilateral axillar and abdominal regions that showed increased metabolic activity. Diffuse

hypermetabolism was observed in the bone marrow and spleen. No 18F-FDG uptake suggestive of arthritis was detected (Figure 1). A histopathologic examination was recommended from the cervical lymph nodes to exclude lymphoproliferative disease according to PET/CT findings. The result of excisional biopsy from the left cervical lymph node was reported as reactive hyperplasia.

sJIA was considered with the presenting findings of fever, rash, arthralgia, no response to antibiotic therapy, increased acut-phase reactants, hyperferritinemia, and the exclusion of other diagnoses such as infections, malignancy, and hematologic disorders. The patient's symptoms resolved completely with appropriate therapy (steroid and methotrexate).

Literature Review and Discussion

sJIA is an important childhood disease that remains difficult to diagnose even for experienced physicians (2). The disease can manifest with quotidian fever, evanescent rash, serositis, hepatosplenomegaly, and lymphadenopathy. It
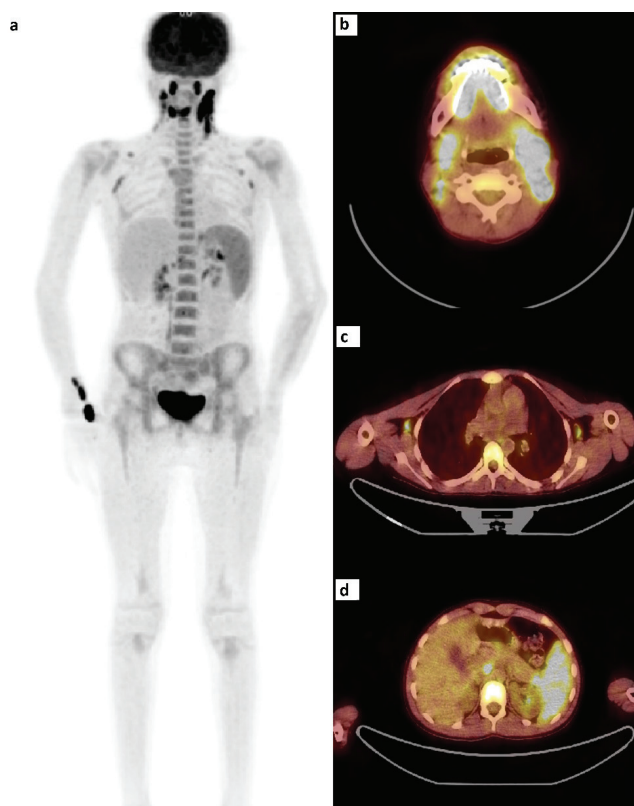
Figure 1. Increased 18F-fluorodeoxyglucose (FDG) uptake in the cervical, axillary lymph nodes, spleen, and bone marrow in the patient on maximum intensity projection positron emission tomography/computed tomography image (a); bilateral cervical and axillary lymph nodes with increased 18F-FDG uptake (b, c); intraabdominal lymph node with increased 18F-FDG uptake and intense 18F-FDG uptake in the spleen (d)

has also been thought for some time that sJIA is a polygenic autoinflammatory disease comprising several diseases of different clinical characteristics that have a common endpoint resulting in marked activation of the natural immune system. In nearly half of all cases, the disease is characterized by relapses following periods of remission; the arthritis usually resolves when systemic symptoms are controlled. As for the other half of the patients, the disease continues incessantly and chronic arthritis remains a life-restricting problem when systemic symptoms are eventually resolved. Moreover, there is a group of patients who show all other possible clinical systemic features in sJIA, but never develop arthritis (4,5).

In some articles published recently, the International League of Associations for Rheumatology (ILAR) classification criteria for JIA have been criticized as being inadequate, especially in the diagnosis of sJIA (5,6). Early and effective treatment of sJIA is important for preventing macrophage activation syndrome. It is especially important to make an accurate diagnosis before starting steroid therapy because it can temporarily mask malignancy (2). However, arthritis of at least of 6 weeks, as defined in the ILAR criteria is unrealistic and can cause a delay in diagnosis. It was determined that up to 50% of patients diagnosed with sJIA in Germany did not meet the ILAR criteria due to the absence of chronic arthritis (6).

The Pediatric Rheumatology International Trials Organization (PRINTO) criteria (2019) revising the ILAR classification criteria, removed the necessity for arthritis in the diagnosis of sJIA. The PRINTO criteria emerged because of the process initiated to distinguish the diseases seen only in children from diseases seen both in children and adults by identifying homogeneous disease groups found under the JIA umbrella term. Although the PRINTO criteria have yet to be validated, they were created with an international consensus (5). Our patient did not meet the ILAR criteria due to the absence of arthritis, but she could be defined as having sJIA according to the PRINTO criteria.

When the cause of fever of at least 8 days in a child cannot be explained with a cautious and detailed history, physical examination, and preliminary laboratory tests, it is defined as FUO (7). ^{18}F-FDG PET/CT is a valuable tool in the diagnosis of underlying causes in adult patients with FUO (8). As for children with FUO, most ^{18}F-FDG PET/CT data are limited, and a comprehensive study from 2020 provided the most detailed information. Pijl et al. (3) could identify the underlying true cause of fever with ^{18}F-FDG PET/CT in almost half (53 patients- 48%) of 110 pediatric patients with FUO. In this study, sJIA was the second most frequently diagnosed disease, with inflammatory

bowel diseases following endocarditis. The diagnosis was established based on ^{18}F-FDG PET/CT findings in three of five patients with sJIA (3).

Clinical practice guidance for JIA proposed ^{18}F-FDG PET as an imaging method for the diagnosis of sJIA in 2018 (9). It is important to recognize the ^{18}F-FDG PET findings of sJIA, one of the major causes of FUO, and remains a clinical exclusion diagnosis. However, to our knowledge, there is only one study in the literature investigating characteristic ^{18}F-FDG PET findings in sJIA (10). Kanetaka et al. (10) evaluated the ^{18}F-FDG PET findings of 59 patients with sJIA and they suggested that their evidence might be used as effective diagnostic tools in patients who do not receive a firm diagnosis. These researchers identified two different characteristic ^{18}F-FDG uptake patterns on ^{18}F-FDG PET in patients with sJIA. In the group defined as type 1, pathologic ^{18}F-FDG uptake in the spleen and bone marrow (especially red bone marrow reflecting systemic inflammation) was observed, and no pathologic uptake was detected in joint synovia. It is note worthy that the type 1 involvement pattern findings were similar to those of PET in adult-onset Still's disease, whose characteristic ^{18}F-FDG involvement has been defined in the bone marrow, spleen, and lymph nodes. Additionally, it was stated that findings similar to the type 1 involvement pattern in sepsis and bone marrow involvement in leukemia could be seen, so the diagnosis should be supported through serologic tests. As for patients in the group defined as type 2, characteristic ^{18}F-FDG uptake was observed, suggesting synovitis in inflamed joints, similar to patients with polyarticular JIA or rheumatoid arthritis. Pathologic ^{18}F-FDG uptake in the bone marrow and spleen has not been described previously.

Our case is compatible with the type 1 pattern due to the presence of bone marrow and spleen involvement and no joint involvement. However, our patient also had increased ^{18}F-FDG involvement in the lymph nodes in the cervical, axillary, and intraabdominal regions. The cervical lymph nodes in particular had very high SUV_{max} values (SUV_{max}: 31.80). We estimate that the reason for the absence of examples similar to our case in the article by Kanetaka et al. (10) was patients being included in the study according to the ILAR criteria. A case of sJIA has been reported previously with ^{18}F-FDG PET/CT findings mimicking lymphoma (11). Here, lymphadenopathies were more disseminated, but SUV_{max} values were more moderate (SUV_{max}: 4.5-10.7). There are also cases of lymphoma mimicking JIA in the literature (12,13).

Based on the findings in our case, we emphasize that there may be lymph nodes with increased metabolic activity that can reach high SUV_{max} values in ^{18}F-FDG PET findings of

sJIA, and a differential diagnosis with lymphoma should be made in such patients presenting with FUO.

Ethics

Informed Consent: Informed consent was obtained from the patient's family.

Peer-review: Externally peer-reviewed.

Authorship Contributions

Surgical and Medical Practices: B.A., Ö.M.A., Concept: Ö.Ş., Design: Ö.Ş., Data Collection or Processing: Ö.Ş., Analysis or Interpretation: Ö.Ş., A.E.Ş., Literature Search: Ö.Ş., Writing: Ö.Ş.

Conflict of Interest: No conflict of interest was declared by the authors.

Financial Disclosure: The authors declared that this study received no financial support.

References

1. Behrens EM, Beukelman T, Gallo L, Spangler J, Rosenkranz M, Arkachaisri T, Ayala R, Groh B, Finkel TH, Cron RQ. Evaluation of the presentation of systemic onset juvenile rheumatoid arthritis: data from the Pennsylvania Systemic Onset Juvenile Arthritis Registry (PASOJAR). J Rheumatol 2008;35:343-348.

2. Shenoi S, Wallace CA. Diagnosis and treatment of systemic juvenile idiopathic arthritis. J Pediatr 2016;177:19-26.

3. Pijl JP, Kwee TC, Legger GE, Peters HJH, Armbrust W, Schölvinck EH, Glaudemans AWJM. Role of FDG-PET/CT in children with fever of unknown origin. Eur J Nucl Med Mol Imaging 2020;47:1596-1604.

4. Martini A. It is time to rethink juvenile idiopathic arthritis classification and nomenclature. Ann Rheum Dis 2012;71:1437-1439.

5. Martini A, Ravelli A, Avcin T, Beresford MW, Burgos-Vargas R, Cuttica R, Ilowite NT, Khubchandani R, Laxer RM, Lovell DJ, Petty RE, Wallace CA, Wulffraat NM, Pistorio A, Ruperto N; Pediatric Rheumatology International Trials Organization (PRINTO). Toward New Classification Criteria for Juvenile Idiopathic Arthritis: First Steps, Pediatric Rheumatology International Trials Organization International Consensus. J Rheumatol 2019;46:190-197.

6. Hinze CH, Holzinger D, Lainka E, Haas JP, Speth F, Kallinich T, Rieber N, Hufnagel M, Jansson AF, Hedrich C, Winowski H, Berger T, Foeldvari I, Ganser G, Hospach A, Huppertz HI, Mönkemöller K, Neudorf U, Weißbarth-Riedel E, Wittkowski H, Horneff G, Foell D; PRO-KIND SJIA project collaborators. Practice and consensus-based strategies in diagnosing and managing systemic juvenile idiopathic arthritis in Germany. Pediatr Rheumatol Online J 2018;16:17.

7. Cherry JD, Harrison GJ, Kaplan SL, Steinbach WJ, Hotez PJ. Feigin and Cherry's textbook of pediatric infectious diseases. 8th ed. Philadelphia, Elsevier 2019; 608-610.

8. Wang Q, Li YM, Li Y, Hua FC, Wang QS, Zhang XL, Cheng C, Wu H, Yao ZM, Zhang WF, Hou QY, Miao WB, Wang XM. 18F-FDG-PET/CT in fever of unknown origin and inflammation of unknown origin: a Chinese multi-center study. Eur J Nucl Med Mol Imaging 2019;46:159-165.

9. Okamoto N, Yokota S, Takei S, Okura Y, Kubota T, Shimizu M, Nozawa T, Iwata N, Umebayashi H, Kinjo N, Kunishima T, Yasumura J, Mori M. Clinical practice guidance for juvenile idiopathic arthritis (JIA) 2018. Mod Rheumatol 2019;29:41-59.

10. Kanetaka T, Mori M, Nishimura K, Nozawa T, Kikuchi M, Sakurai N, Hara R, Yamazaki K, Yokota S. Characteristics of FDG-PET findings in the diagnosis of systemic juvenile idiopathic arthritis. Mod Rheumatol 2016;26:362-367.

11. Lord M, Allaoua M, Ratib O. Positron emission tomography findings in systemic juvenile idiopathic arthritis. Rheumatology (Oxford) 2011;50:1177.

12. Del Torto M, Breda L, Di Marzio D, De Sanctis S, La Barba G, Chiarelli F. Hodgkin's lymphoma mimicking juvenile arthritis. Clin Exp Rheumatol 2010;28:143.

13. Jesus AA, Jacob CM, Silva CA, Dorna M, Pastorino AC, Carneiro-Sampaio M. Common variable immuno deficiency associated with hepatosplenic T-cell lymphoma mimicking juvenile systemic lupus erythematosus. Clin Dev Immunol 2011;2011:428703.